EPFL

Thèse n° 9916

# Bringing casting to microfabrication: processing and deformation of microcastings

Présentée le 24 février 2023

Faculté des sciences et techniques de l'ingénieur
Laboratoire de métallurgie mécanique
Programme doctoral en science et génie des matériaux

pour l'obtention du grade de Docteur ès Sciences

par

**Luciano BORASI**

Acceptée sur proposition du jury

Dr A. Hessler-Wyser, présidente du jury
Prof. A. Mortensen, Prof. Y. Bellouard, directeurs de thèse
Prof. R. Spolenak, rapporteur
Prof. G. Dehm , rapporteur
Prof. R. Logé, rapporteur

École
polytechnique
fédérale
de Lausanne

2023

# Acknowledgements

During my time at EPFL, I have had the chance to discuss and work with many people.

First, I would like to express my sincere gratitude to my director, Andreas Mortensen, for being always available and for his exceptional guidance and support throughout my doctoral journey. His always useful advices, encouragement, and detail reviews have contributed to the successful completion of this thesis. I am also grateful to him for being a wonderful mentor and person.

I would like to acknowledge my co-director Yves Bellouard for being always available and willing to offer valuable insights and recommendations. Despite not sharing much time together, I have learned significantly from our meetings.

I am grateful to the esteemed members of the thesis examination committee, Prof. G. Dehm, Prof. R. Spolenak and Prof. R. Logé, for their time and dedication. Thank you all for your constructive and interesting discussions.

A huge thanks to R. Charvet and C. Dénéréaz, the LMM experimental dream team, for all the invaluable help and impressive work during these years. I am truly thankful for all the time they both dedicated in our designs and experiments. Their help is reflected in each step of this thesis.

I am indebted to my dear micromolding teammates, now Doctors, Enrico Casamenti and Simone Frasca. This work could not have been done without them. I thank them for always being positive, for all the time, and for your great desire to go for more.

I also thank all the undergraduate students that I had the pleasure to work with, for all the valuable help and work: François, Francesca, Pranav, Olivier, Leanna and Félix.

I am beyond grateful for all my current and past colleagues, as well as all my friends around Lausanne, with whom I have enjoyed many memorable activities. The experience outside the lab has also exceeded all of my expectations and has been a truly enriching one.

Lastly, I would like to express my gratitude to all my family and friends in Argentina for their and unwavering belief in my abilities throughout my life. Specially to Ale, for all her support, every day help inside and outside the lab, and our endless discussions about experiments. Being able to make all this journey side by side it has been a real pleasure. Finally, to my parents Silvana and Juan José, who have always been supportive in all my endeavors. Their love and understanding have been a constant source of strength and motivation.

# Abstract

This work extends the range of pathways for the production of metallic microcomponents by downscaling metal casting. This is accomplished by using either of two different molding techniques, namely femtosecond laser micromachining or lithographic silicon microfabrication, in combination with metal pressure infiltration followed by solidification and mold leaching. Structures produced in this work, of size ranging from a few tens of micrometer to a few millimeters and with features of size down to around 2 μm, are cast out of engineering metals (silver, copper, gold, and their alloys). Femtosecond laser machining, on one hand, enables the fabrication of freeform structures that are difficult or impossible to produce by any other means. On the other hand, combining silicon microfabrication with metal pressure casting allows the production of 2D and 2.5D microcomponents with massive parallelization. Microcasting is shown with both molds to feature excellent dimensional control, high reproducibility, the potential for full density, the possibility to alloy with great freedom the infiltrant alloy composition, and a capacity to replicate essentially any continuous shaped hollow with micrometric precision.

Microcasting, in both forms developed here, provides a new way to efficiently produce micron-scale single-crystalline specimens that are amenable to tensile testing. By conducting *in-situ* displacement-controlled tensile tests under the scanning electron microscope at room- and elevated temperatures (200 °C and 400 °C), it is demonstrated that the mechanical response of microcast silver or copper, either bare or coated with ceramic, shows attractive strength and ductility values, indicating in turn the high microstructural quality of the material produced while providing insights into small-scale plasticity. The latter are achieved by investigating the influence of size, crystal orientation, and temperature on the deformation, yield, strain burst statistics, and strain hardening of these micrometric dense metal samples and comparing data with bulk counterparts that are cast to have a diameter near 1 mm. Results show clear evidence of small-scale plasticity. The yield stress of microcastings is affected by both size and temperature and shows evidence of the presence of a scale-dependent density of geometrically necessary dislocations in the cast metal, while no effect of the crystal orientation is measured. The decrease in yield stress at elevated temperatures can fully be attributed to the concomitant decrease in shear modulus, suggesting that the mechanisms that govern the initiation of plastic flow in microcast silver are likely the same from 20 °C up to 400 °C. The work hardening rate also decreases with increasing temperature; however, it does so faster than do elastic properties. The complementary cumulative distributions of strain burst amplitudes agree with an exponentially truncated power-law distribution that has the expected power-law exponent. There is, within error, no measured dependence of the cutoff intensity on sample diameter or test temperature.

Keywords: micro-manufacturing, microcasting, plasticity size-effects, micro-tensile testing, single crystal deformation, intermittent plasticity.

# Résumé

Ce travail augmente la palette des moyens de produire des microcomposants métalliques en réduisant l'échelle à laquelle on peut couler les métaux. Pour ce faire, deux techniques différentes de micro-moulage sont étudiées, à savoir le micro-usinage par laser femtoseconde ou la micro-fabrication lithographique sur silicium, en combinaison avec l'infiltration du métal sous pression suivie de sa solidification et de la dissolution sélective du substrat. Les pièces ainsi réalisées ont une taille qui peut varier de quelques micromètres à quelques millimètres et sont fabriquées à partir de métaux comme l'argent, le cuivre, l'or et leurs alliages. Le micro-usinage par laser femtoseconde, d'une part, permet la fabrication de structures ayant des caractéristiques géométriques complexes et qui sont difficiles, voire impossibles à produire en utilisant d'autres méthodes de fabrication. D'autre part, la combinaison des procédés de gravure sur silicium et de la coulée sous haute pression, ouvre la voie à la fabrication en série de microcomposants 2D et 2.5D par parallélisation massive des étapes d'élaboration. Le procédé de micro-coulée, dans les deux cas, présente un excellent contrôle dimensionnel, une reproductibilité élevée, le potentiel d'obtenir des pièces en métal de pleine densité, la possibilité de définir avec une grande liberté la composition de l'alliage, ainsi que la capacité de produire des pièces de géométrie complexe avec une précision micrométrique.

Les procédés de micro-coulée développés au cours de ce travail offrent en particulier un nouveau moyen de fabrication permettant de produire efficacement des échantillons monocristallins à l'échelle du micron pouvant être sollicités par traction uniaxiale. En effectuant des essais de traction contrôlés par le déplacement, in-situ sous le microscope électronique à balayage à température ambiante et élevée (200 °C et 400 °C), il est démontré que l'argent ou le cuivre micro-coulés, nus ou revêtus de céramique, présentent des propriétés mécaniques attrayantes. Les données reflètent la haute qualité microstructurale du matériau produit, tout en fournissant de nouvelles données sur la plasticité à petite échelle. L'influence de la taille, de l'orientation des cristaux et de la température sur leur déformation plastique sont étudiées, notamment pour ce qui concerne les statistiques de chute soudaine de charge et le taux d'écrouissage de ces échantillons métalliques micrométriques. Les résultats obtenus sont comparés avec ceux de cristaux du même métal produits de manière analogue pour leur donner un diamètre proche de 1 mm. Les données indiquent clairement la présence d'effets d'échelle dans la déformation des métaux microcoulés. La limite d'élasticité est influencée à la fois par le diamètre des échantillons et la température, et montre les signes d'une présence dans le métal micro-coulé de dislocations géométriquement nécessaires dont la densité dépend de l'échelle. Aucun effet de l'orientation cristalline sur la limite d'élasticité n'est mesuré. La diminution de cette dernière à des températures élevées peut être entièrement attribuée à la baisse simultanée du module de cisaillement, ce qui suggère que les mécanismes gouvernant l'initiation de la plasticité dans l'argent micro-coulé sont probablement les mêmes de 20 °C à 400 °C. Le taux d'écrouissage diminue également avec l'augmentation de la température, mais ici la diminution est à vitesse plus élevée que les propriétés élastiques. Les fonctions cumulatives de distribution complémentaires des amplitudes des chutes de charge coïncident avec une

distribution de type loi puissance suivie d'une coupure exponentielle. La loi puissance présente l'exposant attendu, alors que la valeur de l'amplitude de coupure ne montre pas de dépendance mesurable par rapport au diamètre de l'échantillon ou à la température de l'essai.

Mots clés : micro-fabrication, microcoulée, effet de taille, test de micro-traction, déformation de monocristaux, plasticité intermittente.

# Contents

# Chapter 1 Introduction

The trend toward miniaturization of electromechanical systems has led to the development of innumerable miniaturized devices that are now present in our everyday lives. Many domains of technological progress, including microelectromechanical systems (MEMS), microsensors, metamaterials, integrated optical devices, microfluidic, medtech micro-components, or microelectronic devices, rely on the availability of geometrically complex structures made to micrometric resolution. Despite remarkable progress made in recent years in advanced micromanufacturing, current means for producing truly three-dimensional metallic micro-components with non-trivial shapes are often either too slow to be economically viable, not adapted to metals of interest for engineering applications, or produce porous or otherwise imperfect metal microstructures because a straightforward downscaling of systems and technologies is often not possible. This has encouraged scientists and engineers to develop new materials processing techniques.

Since the mechanisms ruling the deformation of metals are altered if one confines the external (extrinsic) dimensions of the specimen to a scale roughly below 100 μm, the same trend towards miniaturization and the rapid evolution of micromechanical systems have also triggered a large volume of research on the subject of small-scale plasticity, meaning the plastic deformation of small specimens. This is most often conducted by focused ion beam (FIB) milling micropillar shaped samples that are tested in compression; such tests have been used to generate an extensive bank of data, but have limitations, namely artefacts introduced into the material close to the surface during ion-milling (including implanted gallium and/or dislocations together with internal stresses) and the fact that tests are generally conducted in compression (leading to barreling, buckling, and an inhomogeneous, non-uniaxial stress distribution).

This work aims, first, to provide new means for the production of metallic microcomponents by downscaling metal casting. This is accomplished by using either of two different molding techniques, namely femtosecond laser machining or silicon microfabrication, in combination with metal pressure infiltration followed by solidification and, if free-standing metal samples are desired, mold leaching. Results represent an advance in the art of metallurgical processing but are also likely to have direct impact in microtechnology by providing a pathway for the production metal micro-parts with considerable freedom in terms of part geometry.

A second goal of this work is to explore the mechanical properties of microcast metals, produced to have selected uniform diameters from a few to several tens of micrometer and of sufficient length to be tested in uniaxial tension within a scanning electron microscope. The tensile behavior of microcast silver and copper is thus examined by conducting displacement-controlled *in-situ* microtensile tests at room-temperature, 200 °C, and 400 °C. Data are compared with bulk counterpart samples cast to have a diameter near 1 mm. The results provide new insights into small-scale plasticity since the influence of multiple parameters, namely size, crystal orientation, and temperature can be investigated in uniaxial tension within samples free of artefacts

introduced by FIB milling. Those tests furthermore demonstrate the capabilities of microcasting in terms of materials performance.

Chapter 2 of the thesis is dedicated to outline micro-manufacturing methods and general considerations of crystal plasticity that are relevant to this work and place in context the process and investigations detailed in subsequent chapters. Chapter 3 and 4 introduce each of the two forms of microcasting developed here, namely metal pressure infiltration in combination with either femtosecond laser micromachining (Chapter 3) or lithographic silicon microfabrication (Chapter 4). The mechanical properties of microcastings are evaluated at room- (Chapter 5) and elevated temperatures (Chapter 6). General conclusions and perspectives for future development are discussed in Chapter 7.

Supplementary videos are available for download from the Zenodo website at https://zenodo.org/ under the following digital object identifier (DOI): 10.5281/zenodo.7624068.

# Chapter 2 Literature Review

The purpose of the present chapter is to describe the literature that underlies topics of specific relevance to this thesis, namely micromanufacturing processes, their advantages, limitations and new areas for exploration. Attention then turns to general concepts of crystal plasticity with focus on confined plasticity, as a preamble to studies of the mechanical properties of microcastings presented in subsequent chapters.

## 2.1 Fabrication methods of components in the microscale

Microelectromechanical systems (MEMS), which are devices or components that convert a stimulus (physical, chemical, biological, optical, etc.) into a useful output (electrical, mechanical motion, etc.), represent a good example of how microfabrication techniques may have a great impact in daily life [1]. Different techniques have been developed in order to fabricate micrometer scale devices and, for metallic parts in particular, suitable fabrication methods capable of producing different shapes at a small scale might be divided into three groups, namely (i) those where the metal grows in layers, (ii) those where the shape is achieved by removing material or manipulating a form such a wire or foil and (iii) new casting techniques.

A concise overview of available techniques for the production of metallic microstructures is given below, together with their limitations and influence in the final component. First, techniques employed to study microplasticity with limited potential for industrial application are introduced, and subsequently, fabrication methods enabling high production rates and/or three-dimensional (3D) microstructures are described. Present coverage aims to cover both the micron and submicron scale; reviews covering in depth 3D metal micromanufacturing at the submicron scale can be found in [2,3].

### 2.1.1 Focused ion beam milling

Focused ion beam (FIB) milling is a technique initially established in microfabrication that has gradually evolved toward high-resolution FIB microscopes [4]. A focused beam is made of accelerated ions, normally $Ga^+$; four main physical interactions are manifested when ions bombard a solid surface: (i) sputtering of substrate atoms, (ii) emission of secondary electrons, (iii) implantation of ions near the surface, and (iv) heating due to emission of phonons. The sputtering of atoms from the surface enables localized milling, allowing the fabrication of pieces with sub-micron resolution and with a geometry only restricted by the accessibility of the beam [5,6]. The sputtering rate depends on the number of ions hitting the surface (FIB current) as well as the nature of the material; still, essentially any material can be milled. Secondary electrons emitted from the materials surface can be used for high-resolution imaging; yet, nowadays "dual-beam" FIB-SEM instrument are conventionally employed for imaging, milling and deposition due to the increased versatility afforded by the presence of both beams.

Uchic *et al.* [7–9] introduced focused ion beam milling as a new method enabling the preparation of standing micropillars amenable to uniaxial compression testing. These pillars are produced from bulk material and remain linked to it, which facilitates micromanipulation (Figure 2-1a). Due to the top-down machining method, micropillars generally exhibit some degree of taper, generally between 2 ° and 5 °, which leads to a non-uniform geometry along their length and a non-uniform applied stress upon pillar compression. Implications of tapered pillars are inaccuracies in defining the flow stress, and the displaying of artificial work hardening rates, since for instance a taper angle of 4.5 ° results in stresses 55 % lower at the base with respect to the top of the pillar in pillars displaying usual aspect ratio values, which can for example cause yield to spread from top to bottom across the sample [10–12]. Further automatization of the process [8] has since enabled the fabrication of taperless pillars, and provides a path for proper milling of polycrystalline specimens, which otherwise show different milling rates depending on the crystal orientation.

The main drawback of FIB milling is related to the damage that is induced by the beam on the machined materials microstructure close to the surface, due to the various modes of interaction of the machined material with the accelerated ions [13]. Formation of intermetallic compounds, ion implantation, creation of point defects, introduction of dislocation loops, and liquid metal and grain boundary embrittlement constitute some defects induced by FIB milling that are reported in the literature [14–21]. Annealing of FIB-milled components has been used to partially reduce the amount of implanted Ga ions, but this may alter the material microstructure, *e.g.,* by changing the initial distribution and density of dislocations [15]. The magnitude of damage depends on the nature of the substrate and the milling conditions (namely incident angle and ion energy among others). Usually final polishing steps are conducted with low milling currents to minimize or remove surface damage [17]. Since the thickness of the damaged layer remains fixed to the milling conditions, such that the damaged material layer represents an increasing proportion of the tested volume as sample dimensions decrease, this intrinsically creates size effects and influences the behavior of pillars under stresses. Numerous studies employing various materials show that size-effects are inherent to the microscale, regardless of the fabrication method [22–25]; still, defects introduced by FIB directly impact conclusions drawn from FIB-pillars investigations, such that other fabrication methods have been proposed to overcome these concerns.

Another limitation of FIB microfabrication is the milling speed, in that the manufacture of samples with diameters above 10 μm may take up to a day, resulting in high sample production costs. That also limits the fabrication of complex shapes, namely dog-bone specimens. A more recent technique, namely $Xe^+$ plasma FIB (PFIB) micromachining, enables high-throughput milling for large volume characterization, enabled by the use of higher currents [26–28]. Furthermore, PFIB micromachining eliminates problems linked with $Ga^+$ contamination in the sample and was shown to introduce less amorphization in silicon [19,28]. A comparison of the behavior of ultrafine-grained and monocrystalline aluminum micropillars prepared by gallium and xenon ion milling shows effects of the micromachining ion used on both the mechanical strength and mode of deformation exhibited (Figure 2-1b) [19,29]. In aluminum, furthermore, the segregation of gallium at grain boundaries reduces the strength of micropillars and higher doses exacerbate the drop.

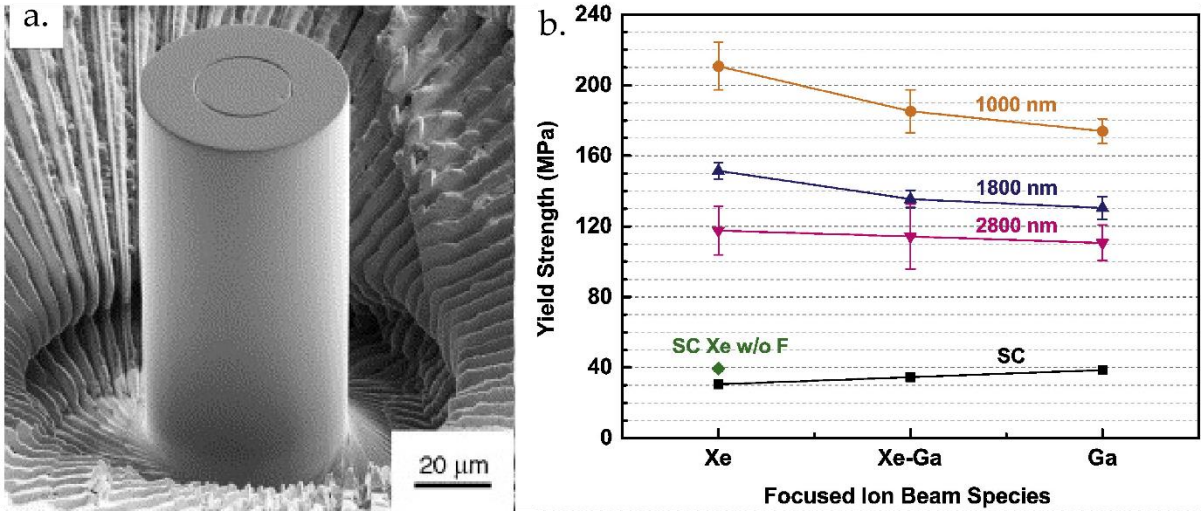


**Figure 2-1** a) A micropillar machined into a $Ni_3(Al, Hf)$ single crystal. The circle on the top surface is a fiducial mark for automated machining. b) Effects of the use of different ions during FIB milling on the yield strength of aluminum micropillars. a-b). Images reprinted from [8] and [19] respectively, with permission from Elsevier.

### 2.1.2 Selective etching

Micrometric samples can be produced by means of directional solidification of a rod eutectic followed by selective etching of the matrix. Ingots of a eutectic alloy are molten and directionally solidified in a Bridgman furnace imposing a vertical thermal gradient, to create well-aligned rod-like eutectic microstructures [30–33]. The size of each rod is determined by the cooling rate, which limits diffusion distances (*i.e.*, the higher the solidification rate, the smaller the rods and their spacing). Following solidification, the eutectic alloy is submerged into an etchant that selectively etches away the matrix, exposing fibers as free-standing microsamples amenable to mechanical testing.

Bei *et al.* [30,31] fabricated monocrystalline molybdenum pillars (D 360-1400 nm) out of a NiAl-Mo alloy, which exhibit a mechanical behavior corresponding to that of defect-free whiskers. The dislocation density of such pillars can be tuned by subjecting the long fibrous composite to deformation after solidification, prior to etching of the matrix. In addition, oriented aluminum sheets can also be produced by selective etching of a $Al/Al_2Cu$ alloy [33]. These fibers show a yield strength in tension that depends on both the fiber section and dislocation density.

This elegant method enabled fruitful studies on microplasticity; however, it is restricted in terms of feasible sample chemical compositions and shapes since samples are limited to eutectic or near-eutectic compositions.

### 2.1.3 Microfabrication and hot-embossing

*Hot embossing* or metal *nanoimprinting* refer to the process of reproducing a design with dies of similar pattern, one the negative of the other, as in forging or coining. For metals, this fabrication technique relies on the plastic deformation of soft and ductile metals into a structured rigid mold. Precise mold manufacturing at the micron scale can be achieved using widespread silicon microfabrication techniques, which are nowadays available for structuring silicon substrates (these techniques are detailed in following sections as we use them

in our work). The filling of silicon etched templates via hot-embossing has been demonstrated to fabricate sub-micron structures out of silver, gold and a gold-tin alloy, which if needed can subsequently be freed from the template by selectively etching the mold after processing [34–37].

Forming parameters include sample set up, vacuum, applied force, temperature ramps, among others, and they are essential to accomplish a complete filling of cavities. For instance, a gold interlayer is deposited in [37] to enhance wettability before embossing a molten gold-tin alloy at 320 °C. Similarly, the imprinting of pure silver and gold into silicon is conducted under high vacuum at elevated temperature (400 °C) and using mechanical pressures in the order of 300 MPa. Since the metal embossing process occurs above the recrystallization temperature of the embossed metal and involves deformation, monocrystalline metallic microstructures can be fabricated. Micro-compression tests on pillars produced this way (with diameters $D$ in the range 130–3000 nm) cross the threshold from bulk to dislocation-nucleation governed plasticity [36]. In addition, mechanical twinning is reported as an important deformation mechanism in sub-micron silver pillars, possibly triggered by preexisting twins.

The use of silicon microfabrication enables rapid and scalable prototyping, as well as simple tailoring of dimensions and aspect ratios; however, nanoimprinting is limited to simple shapes because intricate (*e.g.*, expanding) structures are challenging to fill. It is also restricted in terms of materials since it requires metals that flow at low pressure and temperatures, and that are compatible with silicon.

### 2.1.4 The LIGA process: microfabrication and electroplating

*Electroplating* is based on the electrochemical reduction of metallic ions and their deposition on a surface. LIGA is an acronym from the German words 'Lithographie, Galvanoformung und Abformung' (Lithography, electroplating, molding), and refers to the combination of lithographic processes with electroplating. This technique, which has some common features with hot-embossing, is employed to fill by electrodeposition small cavities that have been previously patterned into polymeric resins, namely polymethyl methacrylate (PMMA) or SU-8, by lithographic processes. LIGA was first developed using X-ray lithography to generate high-aspect ratio components [38], but this requires expensive synchrotron sources. Alternatively, UV-LIGA, spawned from a collaboration between EPFL and IBM, uses SU-8, an epoxy-based resin sensitive to near-ultraviolet light [39,40]. Nowadays, a large number of variants of the process exist, with well-established companies fabricating micromechanical parts.

The conventional LIGA process is outlined in Figure 2-2a. It begins with the deposition of a seeding layer (*i.e.*, gold) onto a substrate (generally silicon), and continues with a spin coating of a photoresist layer with a thickness close to the intended height of structures. The shape of the final components is defined in the resist by means of exposure (*i.e.*, photolithography [41,42], X-rays [38], electron beam [43]) and development. Metal is then electrodeposited onto the substrate, and the resin is removed to expose freestanding metal structures.

The outcome from electroplating generally consists of nano-twinned or nanocrystalline microstructures that can be further annealed to obtain monocrystalline samples. Electroplated dislocation-containing pillars (with diameters $D$ in the range 750-25 nm, Figure 2-2b) have been tested in compression or tension, exhibiting localized deformation and strong size-effects [23,43–46]. One of the main drawbacks when testing in tension is that pillars do not adhere well to the substrate, such that specific anchoring or gluing strategies are needed (such as focused electron beam deposition).

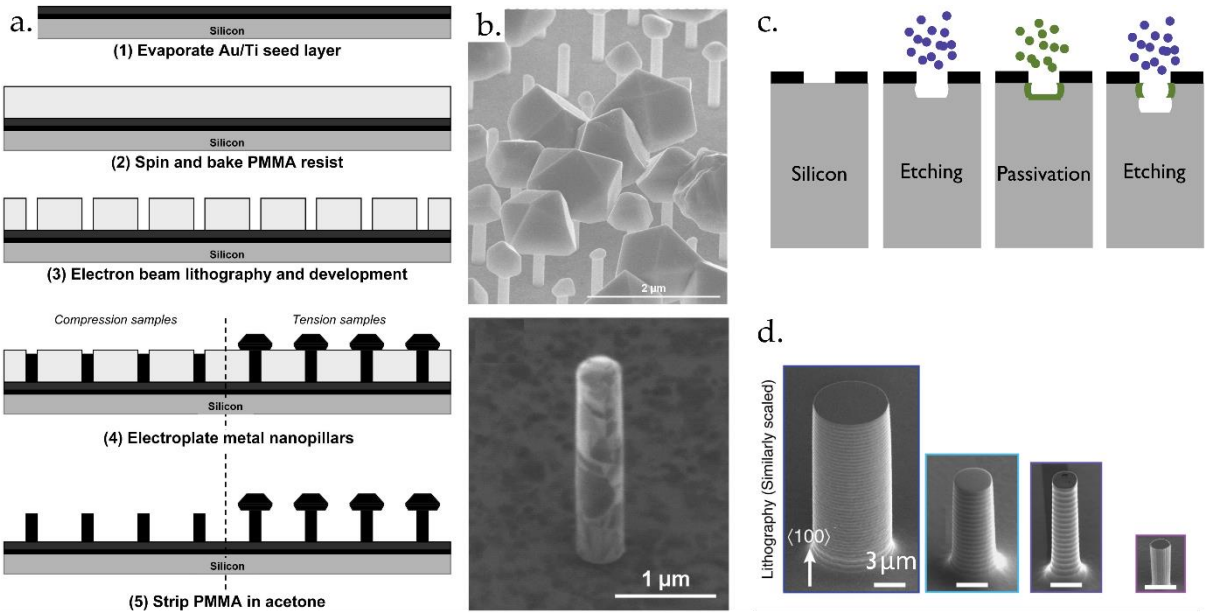


**Figure 2-2** Lithographic processes and the fabrication of pillars. a) Schematic illustration of a e-beam lithography in combination with electroplating. b) Copper mono- and nanocrystalline pillars of copper produced via a). c) Schematic illustration of deep reactive ion etching (DRIE). d) Silicon pillars obtained by lithography. a-b) Adapted from [43]. d) Adapted from [47].

Lithographic cleanroom processes are available to etch cavities into silicon. In this case, after photoresist development, the pattern is transferred to the silicon generally by deep reactive ion etching (DRIE). This process is used to etch deep features and consists of periodically switching gases to alternately etch and protect the surface (*i.e.*, $SF_6$ and $C_4F_6$ plasmas respectively, Figure 2-2c) [48]. Silicon pillars produced in this manner (Figure 2-2d); when tested in compression these achieve yield strengths nearly matching ideal limits, reaching values significantly higher than their FIB-milled counterparts [47,49,50].

Lithography-based techniques provide excellent dimensional control while enabling the fabrication of many components simultaneously and to a high level of precision; however, fabricated structures are essentially 2D or at most 2.5D in geometry, with the inability to fill high-aspect ratio or reentrant cavities due to clogging. Also, when combined with electroplating, lithography-based approaches are limited in alloy compositions that can be deposited, and feature comparatively low deposition rates.

### 2.1.5 Microstamping

Conventional manufacturing methods such as stamping have successfully been extended to produce small-scale metallic parts. In "*microstamping*", the machine, tools and sheets are miniaturized in order to get final

features in the micrometer range [51]. This technique is suitable for high-volume part production with low unit prices, but it has several limitations. For example, the design of the component is limited to relatively simple 2D forms, due to the need for a sheet as a starting point, and the metal sheet should withstand critical deformation levels.

### 2.1.6 Wire electro-discharge machining

*Wire electro-discharge machining* (WEDM) is an example of processes that involve removal at high spatial resolution of material from the workpiece. An electrical discharge produced between a wire and a workpiece generates a controlled spark that melts and vaporizes a microscopic area of the material. Dielectric fluid in between the two electrodes (wire and workpiece) is continuously provided in order to remove eroded particles and to cool down both the wire and the machined part [52]. Although WEDM is a versatile process due to its ability to machine a large number of materials delivering 3D shapes, the minimum conceivable feature is limited by the wire diameter (typically around 0.05-0.3 mm [52,53]).

### 2.1.7 Laser micro-manufacturing

In metal-manufacturing, conventional laser cutting and ablation is for instance employed together with electropolishing for the fabrication of cardiovascular stents. Recently, femtosecond lasers, which are lasers that emit ultrashort pulses (*e.g.*, shorter than 1 ps = $10^{-12}$s), can manufacture components of diverse materials, with minimal to non-existent collateral effects on the immediate surrounding to the laser-exposed region due to the absence of heat diffusion beyond the focal volume as a direct consequence of the combined extreme brevity and peak intensity of the pulse characterizing this peculiar laser-matter interaction. Several articles are available on femtosecond laser machining [54–57]. Worth noticing, femtosecond lasers can be nowadays employed for rough sectioning in-situ in the SEM in combination with FIB milling [58,59].

The advantage of femtosecond laser micromachining of laser-transparent materials, usually fused silica, is that it can be used in a non-ablative regime and thanks to the ultra-high-peak power it may trigger non-linear absorption events (*e.g.,* multiphoton absorptions) in the bulk transparent material. The femtosecond exposure may then lead to changes that are confined to a focal volume, which implies that an internal volume is modified without alterations of the remaining material or the sample surface. At low applied energies, when no ablation occurs, exposing the material to the focused femtosecond laser spot leads to structural changes that locally increase the refractive index and enhance the susceptibility of glass to wet chemical etching. Experimental evidence suggests that the structure is locally densified, in part due to a decrease in the Si-O-Si angles, which implies the presence of a field of high-stresses around the machined region [56,60]. If in a subsequent step the substrate is submerged in a low-concentration etchant (typically solutions of aqueous diluted hydrofluoric acid (HF), potassium hydroxide (KOH), or sodium hydroxide (NaOH) [61]), the laser-exposed regions are selectively removed at rates about 100 times faster than unexposed regions. Furthermore, the etching rate depends on the deposited energy or exposure dose (which is a function of the LAZ, scanning speed, repetition rate and energy per pulse) [54–57,60–62]. Patterned glass etching can take from one to

several hours depending on the area to be etched. Two main features of the process should be pointed out: i) the shape of the pattern is only restricted by the accessibility of the etchant and ii) surface features of the hollows thus carved into glass are linked with the etchant and the exposure pattern. The surface roughness (Ra) and typical waviness of HF-etched channels have been estimated to be in the range of 100 to 250 nm and 0.5 μm respectively, but they depend on the patterns writing strategy [56].

The method has also been used to micromachine samples for testing at the microscale. Fused silica specimens fabricated by means of femtosecond laser machining and tested in both compression [63] or tension [64], exhibit high strength in the gigapascal range (8 to 10 GPa in compression, and around 2 GPa in tension).

### 2.1.8 Advanced additive manufacturing techniques

When it comes to non-transparent substrates such as metals, none of the aforementioned techniques provides full geometrical design freedom in all three dimensions. Recent years have seen the addition of a wide range of novel advanced additive manufacturing processes; still, conventional powder-based printing processes are typically limited to the size of the powder particles (*i.e.*, ≈ 20 μm) [65]. Novel approaches that can produce metal structures at the micro and/or nanoscale are based on the reduction of metal ions present in solution and are usually known as *advanced additive manufacturing* techniques, comprehensive reviews can be found in [2,3].

Wu *et al.* [66] fabricated silver 3D structures composed of aggregations of silver nanoparticles embedded within a sol-gel matrix. Despite the low diameter of the silver particles (around 40-50 nm), at the end of the process, particles are not interconnected and hence the final structures are not electrically conductive. This process was extended to produce silver and gold (electrically conductive) structures on top of glass substrates [67]; however, it was found to be difficult to produce complex 3D shapes and the surface quality was rather low. A printing process based on nanoparticle dispersions followed by sintering was used to produce complex 3D metallic architectures such as microlattices with truss elements having diameters in the range of 20 μm [68]. Porosity is controlled by varying the sintering conditions. Another remarkable multiscale additive process based on electrochemical reduction of metallic ions was recently introduced to manufacture copper structures [69]. The advantage of this technique relies on the fact that it is a single-step fabrication process, affording good surface quality and multiscale freeform capability. Electrohydrodynamic redox printing (EHD-RP) is also a novel technique able to print metallic structures at the submicron scale [70]. This consists in the dissolution of a metal anode in a liquid solvent enclosed within a nozzle. By means of an applied DC voltage, droplets of the solvent containing metal ions are ejected and guided from the nozzle towards a substrate where the metal is reduced. A major advantage of EHD-RP is its capability for on-the-fly control of the chemistry of the deposited metal. This enables the production of chemically architected structures.

Novel metal microprinting processes are, thus, appearing that might also have tangible technological impact in microtechnology; however, there are limitations associated with printed structures, such as porosity or microstructural features that are highly dependent on the processing conditions and might, therefore, be hard

to control. Exceptions are techniques based on freeform electrodeposition [69–71] that manufacture complex and smooth structures made of dense metal. An inherent limitation of bottom-up approaches is linked with the point-by-point building of structures, which renders such processes inherently slow.

## 2.2 Microcasting

Metal casting is one of the oldest manufacturing processes and has been an essential vehicle for technological progress through millennia. Cast products are estimated today to be present in up to 90 % of all durable goods [72]. Reasons are multiple: casting affords the production of shapes with high geometrical complexity and is extremely flexible in terms of both fabrication volume, ranging from a single piece to mass-produced components, and also in terms of alloy chemistry. In addition, casting delivers nearly-net and dense products with a multiscale capability, meaning that large products may contain features defined at diverse scales.

Casting comprises, in general, three stages: (i) mold manufacturing, (ii) casting of the molten metal, and (iii) demolding. Metal casting has resisted miniaturization down to the fabrication of micrometric components due to several challenges present across the three stages of the process. Some of those limitations are:

i. Precision molding affording freeform processing at these scales is not simple and processes to create micrometric features in materials that withstand metal casting temperatures are scarce. In addition, any imperfection along the mold surface such as grain boundaries or interfaces, which are insignificant in conventional casting, may result in comparatively large and detrimental imperfections along the cast metal surface at the microscale.
ii. Ceramic materials are generally more suitable for mold manufacturing due to high stability and lower reaction with metals at elevated temperatures; however, the filling of micrometer cavities in a ceramic mold with molten metal is not spontaneous because of the non-wetting nature of nearly all metal/ceramic systems, which results in capillary forces opposing the metal ingress [73].
iii. Most materials shrink as they solidify; this volume change is usually compensated in casting by locally supplying liquid metal through *risers* or *feeders* in the last areas solidifying. This may be difficult at the microscale; furthermore, removing such small risers may introduce additional challenges when dealing with small components.
iv. Demolding complex metal structures embedded in a substrate without any damage to the cast may be extremely difficult at small-scale, where samples are weak and, therefore, mechanical means are not a good alternative.

A downscale version of investment casting is reported in the literature for the fabrication of metal components with sizes on the order of some hundred microns (Figure 2-3a) [74–78]. Instead of wax, a polymeric (PMMA) pattern is replicated in a LIGA structure and is submerged into a ceramic slurry (or investment) to reproduce the external shape and generate the mold. After drying, the investment is sintered and the pattern pyrolyzed in a subsequent step. It is clear that the investment compound has a major impact on the surface roughness of the casting. A mixture of a fine $SiO_2$-power and 6 μm phosphate powder has been employed as investment.

Demolding is achieved by selective etching the mold; for this, a mixture of silica-phosphate powder and hydrofluoric acid (HF) is utilized, which restricts the process to precious metals, since they are the only to be resistant to such an etchant [76,77]. A modified plaster bonded investment that dissolves in water was used for casting alloys such as aluminum-bronze [75]. Note that sintering of powder-based investment impedes the definition of mold features smaller than the powder particles and leads to polycrystalline molds. Grain boundaries create, by capillary force equilibration, depressions along the mold surface, which can subsequently be reproduced by the metal and result in surface defects. The values of roughness ($R_a$) reported in microcastings produced by investment casting are reported to be between 1.13 μm and 0.27 μm [74]. To enhance the surface quality and prevent chemical reactions between the melt and the mold, a new microcasting process based on permanent molds is proposed in [79]. The negative of the piece is milled in two halves out of steel or graphite plates, which can be opened to extract the cast after solidification. Both processes, however, are highly restricted by the manufacturing of the mold since there is no process to machine free 3D sub-micron features and fabricating polymeric patterns by LIGA may provide, at most, 2.5D structures.

When filling either investment or permanent molds, as mentioned above, capillary forces play a major role and need to be overcome by external pressure. The pressure ($P$) necessary to drive the molten metal into cavities of radius $R$ can be estimated for a highly non-wetting fluid by the Young-Laplace equation ($P \approx \frac{2cos(\theta)\sigma_{LV}}{R}$) where $\sigma_{LV}$ the surface tension of the liquid-vapor interface, which for most metals can be approximated as 1 $Jm^{-2}$, while $\theta$ is the wetting angle of the fluid on the solid being infiltrated [73]. This implies that pressures on the order of 2 MPa will fill cavities ≈ 2 μm wide. This simple back-of-the-envelope analysis only considers the effect of capillary forces in an evacuated hollow cylinder. The effect of any pressure within the cavity due to trapped gas can only be neglected if the mold is under vacuum or if the porosity in the mold allows the gas to pass through the walls. Experimental results show that the required pressure to completely fill rough channels can be higher, both because roughness will increase the apparent wetting angle in non-wetting systems, and also because higher pressures might be required to fill all asperities along the solid surface [74]. In the investment and permanent mold microcasting approaches detailed above the driving pressure was applied by centrifugal casting, in which an increase in the centrifugal forces is achieved by increasing the revolutions per minute or extending the radius of rotation [76].

Alternatively, a microcasting process that is painstaking but pushed the state-of-the-art down to smaller dimensions for the production of samples amenable to tensile testing has been developed within our laboratory (the Laboratory of Mechanical Metallurgy, LMM) at EPFL. Mold manufacturing consists of growing monocrystalline NaCl salt molds around organic patterns by slowly evaporating a slightly undersaturated water solution (Figure 2-3b). This process only occurs in the absence of external vibrations and the evaporation of the water bath can take up to a couple of months. Subsequently, the pattern is pyrolyzed by heating molds in an air atmosphere. Hollow cavities in NaCl molds are created from pyrolizable (polymeric) fibers and employed to cast thin aluminum wires down to ≈7 μm with an excellent surface

roughness of around 50 nm [80–85]. The infiltration of such cavities is conducted by gas pressure infiltration. For that, molds are heated up in vacuum and surrounded by metal, which when it melts seals the cavities and ensures a differential pressure driving the metal into the cavity when the ensemble is pressurized. This variation of microcasting has been used to study the deformation of metals at the microscale (Figure 2-3c). It is limited, however, in the shapes that it can produce and by the melting temperature of NaCl (801 °C). Recently, a method to fabricate salt-based structures by 3D printing, with possible features down to 100 μm, using resins loaded with salt particles has been introduced in [86], and employed to produce aluminum and magnesium lattices by metal pressure infiltration (the process was developed at ETH in Zürich and the metal infiltration was conducted in our laboratory).

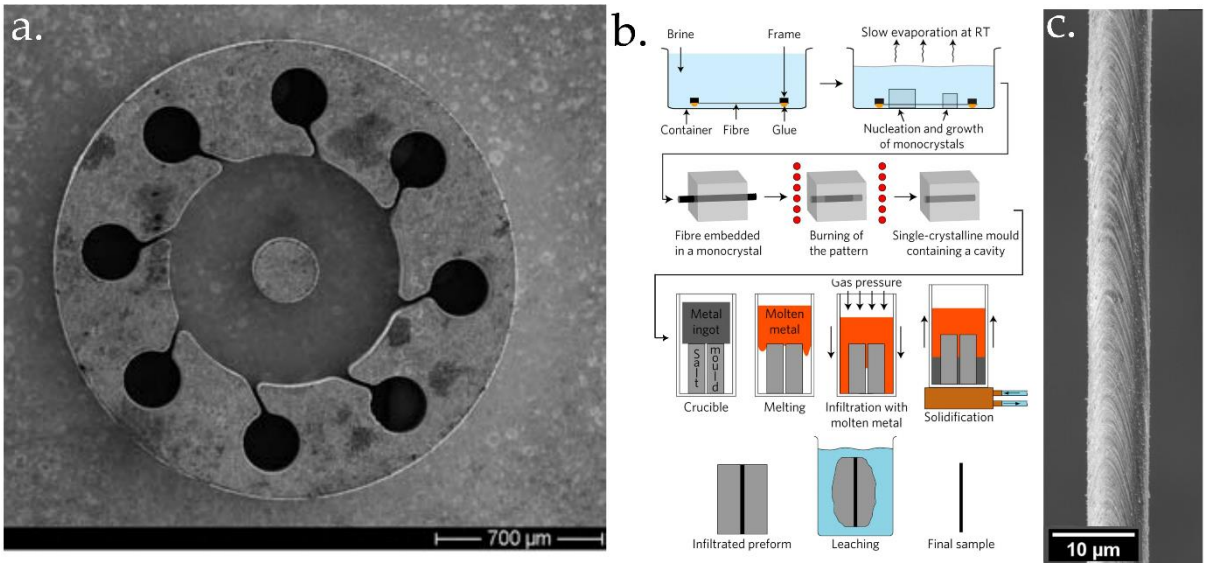


**Figure 2-3** Structures produced by microcasting. a) A nozzle plate made out of a gold alloy. b) Schematic illustration of the microcasting process into salt molds. c) A SEM image of a magnesium wire produced by microcasting into salt mold after being tested in tension. a) Reproduced from [77], with permission from Springer Nature. b-c) Images taken from [81].

The properties of metal microcomponents are directly impacted by the fabrication method, *i.e.*, through the surface state, porosity, microstructure, grain size, chemical composition, together with external dimensions of the component. Thus, structures produced by microcasting strategies, which are introduced in the present work, have been evaluated by mechanical testing. Towards interpretation of results some considerations of crystal plasticity are detailed in what follows.

## 2.3 The deformation of single crystals – general considerations

The plasticity of single crystals has been of particular interest during the early to mid XX$^{th}$ century. These investigations spawned many of the theories employed nowadays to describe the mechanical deformation of metals. One of the reasons for working with single crystals is that this sidesteps the role of grain boundaries and also because mechanical and sometimes physical properties vary with the crystal orientation in interesting and insightful ways.

When subjecting a polished crystal to uniaxial tension, it is possible to evidence the appearance of one or more sets of parallel fine lines along the surface of the specimen. These lines, referred to as *slip lines*, *slip steps*,

or *slip traces*, are physical steps on the surface that are usually developed from the microscopic sliding of crystal blocks over one another along well-defined crystallographic planes [87–89]. The planes on which slip occurs are called slip or *glide planes*, while the shear directions are known as slip or *glide directions*. The presence of slip traces implies that slip is inhomogeneous on the atomic scale and occurs in discrete systems, called *slip systems*. These systems are usually those with the closest atomic packing, and for the case of a face-centered cubic (FCC) crystal 12 slip systems are recognized, which comprise four slip planes ({111}) with three slip directions in each (<110>).

One variable playing a significant role when evaluating single crystal properties is the crystallographic orientation. The *stereographic projection* is generally used to visualize the crystallographic orientation of each crystal. It consists of reducing by one dimension the geometry of crystallographic planes and directions to be able to draw in two-dimensions (2D) three-dimensional (3D) data [90]. Planes and directions can be seen as great circular lines and points respectively (Figure 2-4). A standard stereographic projection usually refers to a stereographic projection with an important crystallographic direction or pole plane lying at its center (Figure 2-4 b-c). In Figure 2-4c it is also possible to observe the great circles that correspond to {100} and {110} planes: these divide, for FCC metals, the standard projection into 24 crystallographically equivalent spherical triangles [89], formed in all cases with a <111>, <110>, and <100> directions at each corner of the triangles. This, for instance, indicates that lattice directions shown in Figure 2-4d as $a_1$, $a_2$ and $a_3$ are crystallographically equivalent since they are located at the same relative positions inside the triangles. For straightforward visualization of crystallographic features, the mechanical data of single crystal deformation is therefore usually complemented with a stereographic triangle, in which the crystal orientation relative to the crystal rod axis of one or several specimens is displayed (as in Figure 2-4e).

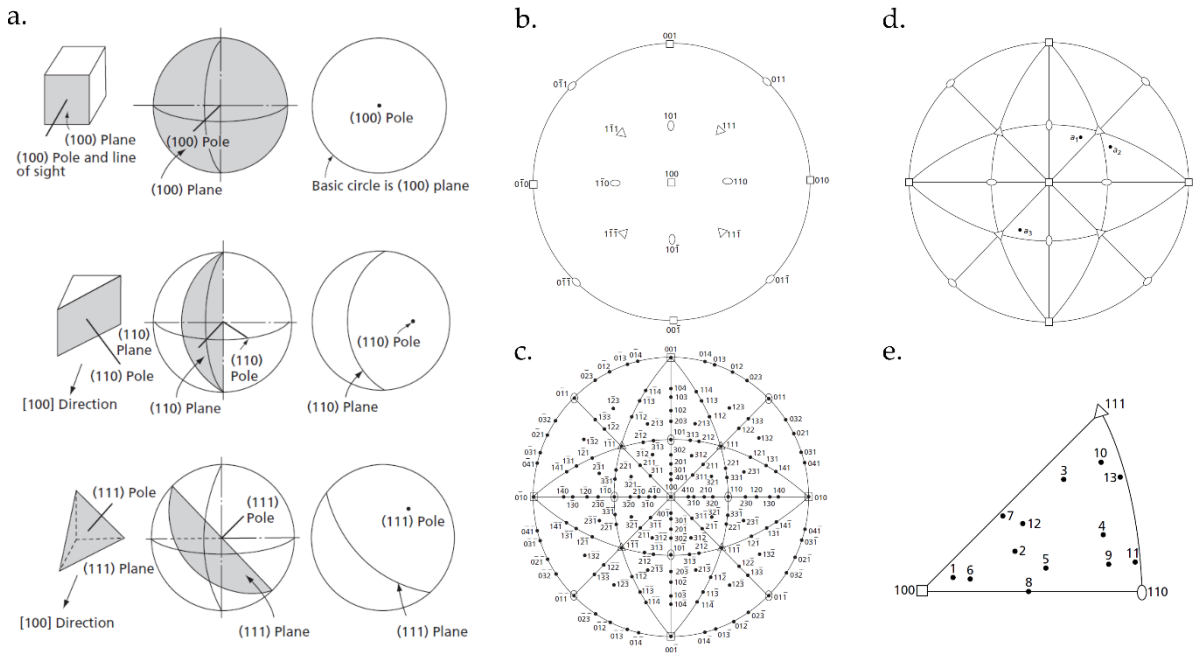


**Figure 2-4.** a) Stereographic projections of several planes and directions. b) A simple 100 standard stereographic projection and an identical projection showing additional poles c). d) Represents three equivalent crystallographic directions $a_1$ $a_2$ and $a_3$ displayed in a specific stereographic projection. e) A stereographic triangle in which the crystal orientations relative to the crystal rod axis for different specimens are displayed. Images adapted from [90].

Metals, at intermediate temperatures, most often deform by the movement of dislocations, and slip begins when the shear stress reaches a specific value, usually known as the critical resolved shear stress (CRSS). The Schmid and Boas equation (Equation 2-1) can be used to relate a uniaxial stress (σ) state to the resolved shear stress (τ) along a specific slip system (*s*) as follows [87,90]:

$$\tau^s = \sigma \cos\theta \cos\emptyset = \sigma \cdot S \qquad \text{Equation 2-1}$$

where $\theta$ represents the angle between the tensile axis and the normal to the slip plane, $\emptyset$ is the angle between the tensile axis and the slip direction and the product of their cosines is known as the Schmid factor (*S*) and is in the range of 0.27 to 0.5 (Figure 2-5).

Similarly, the shear strain in the slip system ($\gamma$) is related to the uniaxial strain ($\varepsilon$). According to the conservation of energy the mechanical work of the applied stress $dW = \sigma \cdot d\varepsilon$ is equal to the work of the resolved shear stress along the slip plane and direction: $\tau^s d\gamma = \sigma \cdot S \cdot d\varepsilon$, and therefore, $d\varepsilon = S \cdot d\gamma$ [91].

Schmid showed that the flow in a single crystal initiates when the shear stress resolved on the primary slip system reaches a critical value that is independent of the crystal orientation but is affected by the temperature, chemical composition and defect content of the crystal [87,89]. The primary slip system is that with the highest Schmid factor, and its nature depends on the orientation of the crystal with respect to the tensile axis (Figure 2-5b). The number of slip systems initially activated varies as a function of the crystal orientation (Figure 2-5c); for FCC metals, the deformation of crystals with an initial orientation laying in the inner region of the stereographic triangle begins via slip in a single system, while orientations at the corners or edges of the stereographic triangle are prone to slip in multiple systems. When those are not coplanar (as is the case between [111] and [011]), this is manifested as a set of two or more intersecting slip lines visible along the sample surface [89]. These two situations are usually termed as *single* or *multiple slip (or glide)*, respectively. In practice, for FCC metals, orientations that are only some degrees away from the boundaries of the elementary triangle may still exhibit multiple slip and evidence resolved shear stresses higher than would be expected for single glide [87,91].

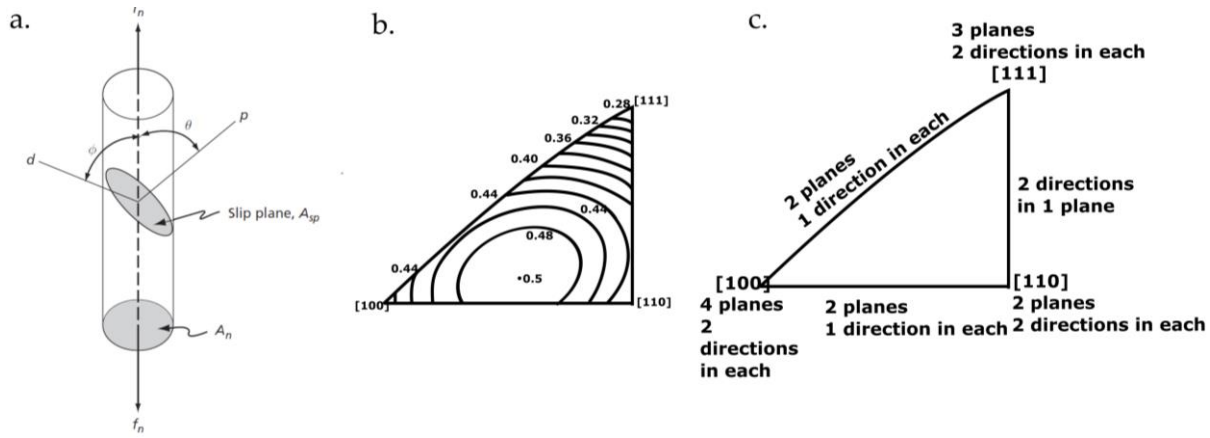


**Figure 2-5** a) Schematic representation of the determination of the critical resolved shear stress (adapted from [90]). b) Representation of the values of Schmid factor for FCC metals as a function of the crystal orientation (Redrawn from [92]). c) Stereographic triangle displaying the amount of operative slip systems along boundaries for FCC metals (Redrawn from [89]).

During the uniaxial plastic deformation of a crystal oriented for single slip, the movement of one end of the sample relative to the other, which would be a consequence of shearing the crystal in any direction (Figure 2-6a), may be prevented due to mechanical constraints if sample ends are not free to move laterally to accompany the motion of gliding planes [88]. If it can be accommodated (by bending or grip rotation) this constraint leads, in tension, to a rotation of slip planes towards the tensile axis, as schematically represented in the stereographic projection by the grey dashed lines in Figure 2-6c [89]. This rotation of the crystal causes an evolution of the Schmid factor with tensile strain. If slip initially takes place along a single glide system, the ensuing rotation of the crystallographic axes tends towards, and eventually reaches, the [001]-[$\bar{1}$11] edge, where the onset of slip in a second (conjugate) slip system is initiated; thereafter, the crystal continues its deformation in multiple (duplex) slip. The duplex slip further rotates the crystal along the [001]-[$\bar{1}$11] boundary towards the [$\bar{1}$12] pole, which is located mid-way between the two operative slip directions. Once it has reached this point, the specimen finally interrupts its rotation and remains there until tensile necking and fracture occur [87,89]. It is important to point out that other crystals, such as hexagonal crystals (HCP) do not exhibit duplex slip; their rotation thus continues over large strain spans, which can produce extensive sample deformation by single glide, and hence extensive crystal rotation prior to fracture [88]. On the contrary, FCC crystals with initial orientations at the [001] or [111] corner do not rotate since the number of potential slip systems, 8 and 6 respectively, enable uniaxial tensile deformation along those two directions [91]. Here too, in practice samples oriented close to, but not at, these two corners, which are expected to undergo rotation, also experience from the onset similarly stable deformation with several operative slip system [87,91]. This area, usually referred to as the "*basin of attraction*" of the [001] or [111] poles in the literature, is larger in the case of the [111] corner.

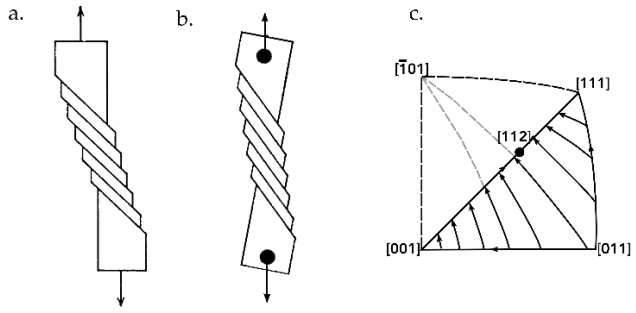


**Figure 2-6** Schematic illustration of a uniaxial plastic deformation of a crystal. a) Shear of the crystal with a movement of one end relative to the other. b) Constrained situation due to the tensile grips. c) Rotation of the crystallographic axes during tensile deformation. a-b) Redrawn from [89]. c) Redrawn from [91].

## 2.4 Dislocations in face-centered cubic metals

### 2.4.1 Partial dislocations and stacking faults

Crystal defects influencing the deformation of FCC metals are well-known; these are detailed here; comprehensive descriptions can be found in [87,89,93,94].

As mentioned above, in face-centered cubic systems, slip takes place along {111} planes and with <110> as the observed slip direction. As schematically illustrated in Figure 2-7a, the movement of the first row of white atoms towards the right by distance *b*, with *b* representing the Burgers vector of the dislocation ($\frac{1}{2}$ [$\bar{1}$10 ]), shifts the dislocation one unit atomic spacing to the left, leaving behind a perfect crystal, as expected from a perfect dislocation [93]. This displacement of a dislocation in FCC crystals occurs in fact in two steps, where the consecutive movement of atoms in a zigzag manner reaches the same final location, as illustrated in (Figure 2-7b). The dislocation (*b* in Figure 2-7a) thus dissociates into two *Shockley partial dislocations* (of vectors *c* and *d* in Figure 2-7b, of vector $\frac{1}{6}$<112>); such a dissociation is energetically favorable since, according to Frank's (simplified) rule, the energy of each dislocation is proportional to the square of the Burgers vector [91,93] with in the present case is such that $b^2 < c^2+d^2$.

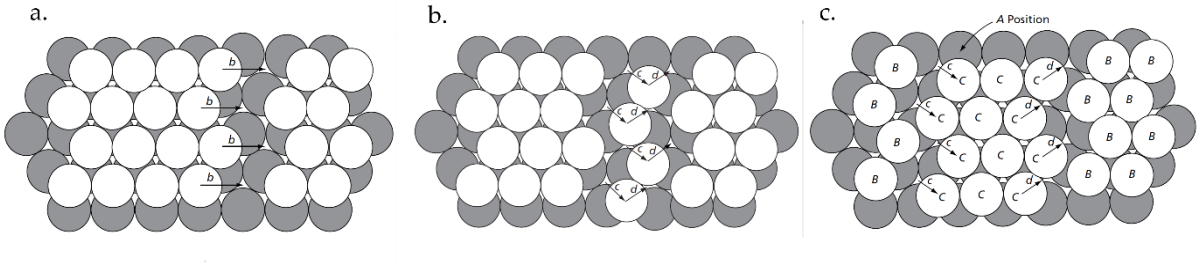


**Figure 2-7** Schematic illustration of the movement of a dislocation in a face-centered cubic metal. a) A perfect dislocation of Burgers vector *b*. b) Shockley partial dislocations of Burgers vector *c* and *d*. c) An extended dislocation with an associate stacking fault. Images adapted from [90].

The elastic interaction between two dislocations creates a force that can be calculated by means of the Peach-Koehler equation [93]. The repulsive force between partial dislocations leads to an increase in their separation distance (*d*) by adding additional rows of atoms to the zigzag (Figure 2-7c), creating what is known as an *extended dislocation* [90] separated by a *stacking fault* [87,93,94]. The stacking fault has an associated extra *stacking fault energy* (SFE or ϒ) [in $Jm^{-2}$ or $Nm^{-1}$], which creates an attractive force between partials dislocations [93]. Balancing the repulsive ($F_r$) and attractive ($F_a$) forces between partial dislocations provides the equilibrium separation distance between them ($d_{eq}$). Considering the angle between partial dislocations as 60°, the same magnitude of the Burgers vector ($\frac{a}{\sqrt{6}}$ with *a* the interatomic distance), and for the special case of $\nu = 0$ [93]:

$$F_r = \frac{\mu b_1 \cdot b_2}{2\pi d} = \frac{\mu |b_1||b_2| \cos 60°}{2\pi d} = \frac{\mu b^2}{4\pi d} \qquad \text{Equation 2-2}$$

$$F_a = -\frac{d(\gamma x)}{dx} = -\gamma \qquad \text{Equation 2-3}$$

$$F_r + F_a = 0 \rightarrow \; d_{eq} = \frac{\mu b^2}{4\pi\gamma} \qquad \text{Equation 2-4}$$

Equation 2-4 shows that the separation distance between partial dislocations, in other words, the width of the stacking fault between two Shockley partials, is inversely proportional to the SFE, γ [87]. This intrinsic characteristic of the material, which varies significantly from one FCC metal to another, has a major impact on the plasticity of FCC metals, as described in following sections. The estimation of the SFE for different materials can be performed by measuring the width of the stacking fault in transmission electron microscopy

(TEM). For instance, for aluminum, copper, and silver, γ is on the order of 140, 40 $mJm^{-2}$, and 20 $mJm^{-2}$ respectively, which corresponds to a width of *a*, 5*a* and 7*a*, respectively.

### 2.4.2 Cross slip

Dislocations generally glide in FCC metals along a well-defined plane, as mentioned before, but under certain circumstances they are able to switch plane while gliding. This is referred to as *cross slip* [93] (as schematically illustrated in Figure 2-8. For cross-slip to occur, both the dislocation Burgers vector and the dislocation line must be contained in the new plane; only screw dislocations may therefore undergo cross slip [90], and planes onto which a dislocation may cross-slip are restricted. For instance, for a screw dislocation with $b = \frac{1}{2}[\bar{1}01]$ moving in (111), the only potential slip plane that contains its vector is $(1\bar{1}1)$. If, for any reason, the dislocation prefers this latter system, it can switch glide planes. If this process repeats and the dislocation moves back to the original slip plane, the process is known as *double cross slip* (Figure 2-8a-(3)) [93]. An important feature of this mechanism is the new configuration created on the original system (from point b to c in Figure 2-8a-(3)); this resembles a Frank-Read source configuration (see 2.4.5 Frank-Read and single-arm dislocation sources), which is able to generate new dislocations if the two arms in the cross-slip plane are pinned.

Since the Burgers vector of a partial dislocation ($\frac{1}{6}$<112>) lies only in one of the {111} slip planes, it cannot cross slip; yet, dislocations in FCC metals are known to cross-slip [93]. Different mechanisms exist to explain the cross slip of extended dislocations [95–97]. The first is the Fleischer model [98] (Figure 2-8b), which proposes that the leading partial, for instance $b = \frac{1}{6}[\bar{2}11]$ moving in a (111) plane, dissociates to create two new dislocations following the reaction: $\frac{1}{6}[\bar{2}11] \rightarrow \frac{1}{6}[\bar{1}21] + \frac{1}{6}[\bar{1}\bar{1}0]$. The first of the new dislocations is a glissile partial contained in the $(11\bar{1})$ cross slip plane while the latter is a sessile dislocation remaining behind, usually known as a *stair-rod* dislocation [90], which is necessary for the stacking fault to move from one slip plane over into another. This stair-rod attracts the trailing partial and is removed when the latter arrives [90] (Figure 2-8b-(4)). In this model the dislocation remains dissociated during cross slip; it has been demonstrated that this requires more energy than an alternative scenario, which involves the temporary recombination of partials and is due to Escaig and Friedel.

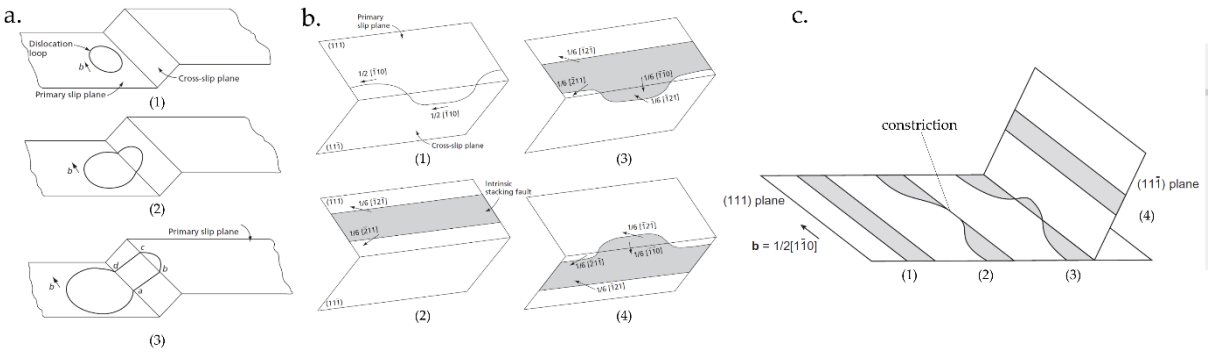


**Figure 2-8** Schematic illustration of different cross slip mechanism. a) Sequence of a double cross slip of a perfect dislocation. b) Sequence proposed by Fleischer for cross slip of an extended dislocation. c) The Friedel -Escaig mechanism of cross slip of an extended dislocation. a-b) Adapted from [90]. c) Adapted from [93].

The Friedel-Escaig model (Figure 2-8c), detailed in [91,93,95], comprises the formation of a point constriction in the stacking fault, thus creating locally a perfect dislocation able to switch slip planes and thus cross slip. Forming such a constriction requires extra energy; this may be the result, for instance, of dislocation interactions when the applied stress tends to push partials together [91]. From this model, it is evident that metals with a high SFE may cross slip more easily, since the distance between partials, and the work required to recombine them, is smaller. Therefore, the smaller the SFE is, the greater is the difficulty of dislocations to change plane while they glide, and hence the greater is the effect of dislocation interactions in arresting the dislocation [87]. The formation of constrictions being a thermally activated process, an increase in temperature leads to a higher probability of cross slip. The higher or lower capacity of metals to cross-slip drastically affects the deformation process and is detailed in following sections.

### 2.4.3 Climb-Jogs and Kinks

Contrary to screw dislocations, the movement out of the glide plane of dislocations with an edge component is nonconservative; for a dislocation other than a screw dislocation to switch slip planes, diffusion is therefore required. The process is called *climb* and is schematically illustrated for a pure edge dislocation in Figure 2-9a [93,95]. Climb requires removing or adding atoms at the dislocation core in order to move the dislocation line normal to the glide plane. This mechanism requiring diffusion, it is thermally activated [89]. Similarly to what occurs in cross slip, during climb the dislocation moves gradually, along a portion of its length rather than shifting all at once, since this would require a complete row of atoms being added or removing simultaneously [95]. When a small segment of a dislocation climbs, the junction created between the upper and lower part of the dislocation is called a *jog* (Figure 2-9b).

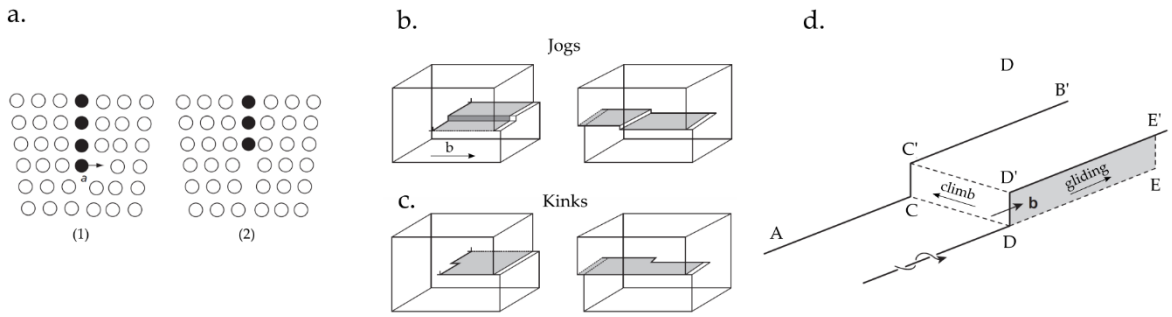


**Figure 2-9** a) Schematic illustration of climb in an edge dislocation. b) Jogs formation in an edge and screw dislocation, the shaded area represents a slip plane. c) Kinks formation in an edge and screw dislocation. d) The sessile character of a jog in a screw dislocation. Reprinted from [99,100], with permission from Elsevier.

Climb is thus performed by the motion of jogs. When steps on the dislocation are produced on its slip plane, the junction is called a *kink* (Figure 2-9c). Since kinks are contained in the same slip system as the dislocation line, they do not interfere with dislocation glide. The case of jogs is more complex; jogs on a pure edge dislocation do not affect glide either. On the other hand, a jog on a screw dislocation has an edge character, and thus it is only capable of glide in the plane containing both its line and Burgers vector, *i.e.*, along the axis of the screw dislocation (plane defined as DD'-EE' in Figure 2-9d). Movement of the screw dislocation in other planes, for example towards ACC'B', therefore requires diffusion to enable climb of the jog; hence,

the movement of such screw dislocations in planes other than the glide plan if their jogs will be temperature-dependent [93]. Jogs can be produced during plastic deformation, when two dislocations intersect [93].

### 2.4.4 Force on a dislocation

When a resolved shear stress (τ) is applied to move a dislocation of Burgers vector *b*, the resulting glide force (*F*) per unit length of dislocation can be expressed as [93]:

$$F = \tau \cdot b \qquad \text{Equation 2-5}$$

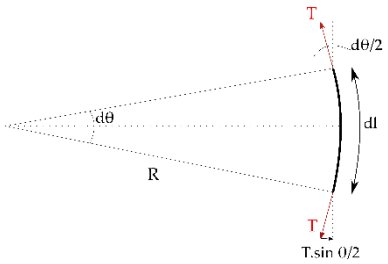


**Figure 2-10** Curved dislocation under a line tension *T*. Redrawn from [93].

A dislocation line, being a defect in the crystal, has an associated energy which is minimized by reducing its length. Thus, in order to increase the length of a dislocation, work has to be performed. The resulting *line tension* (T), has units of energy per unit length, and, if one assumes it not to depend on the dislocation line orientation and treats the crystal using isotropic linear elasticity, equals [93]:

$$T = \zeta \mu b^2 \qquad \text{Equation 2-6}$$

with $\zeta \approx 1$ and where μ is the shear modulus; an appropriate value for μ in anisotropic crystals (treated here in the framework of isotropic linear elasticity) is the Reuss average [91,101]. Ignoring the orientation dependence of the linear dislocation energy, the (hence isotropic) line tension will create a force on a dislocation curved to radius *R*, which at equilibrium can be compensated by an applied shear stress ($\tau_0$). From a force balance in Figure 2-10 one has [91]:

$$2T \sin\frac{\theta}{2} = \tau_0 b dl \qquad \text{Equation 2-6}$$

with $dl = Rd\theta$

which, if $d\theta$ <<1 and $\sin\theta \approx \theta$, implies:

$$\tau_0 = \frac{\zeta \mu b}{R} \qquad \text{Equation 2-7}$$

Such that the stress needed to bow a dislocation to radius *R* increases as *R* decreases. At a higher level of sophistication than what precedes, one can consider the fact that the value of $\zeta$ depends on the nature of the dislocation: it decreases with increasing screw character of the dislocation; this causes variations in the shear stress given by Equation 2-7 with the orientation of the dislocation, and also causes torque terms to act on the dislocation line. The value of $\zeta$ also decreases with increasing dislocation field overlap, and hence with both increasing dislocation density and curvature of the dislocation. In the former case $\zeta$ is generally taken to

depend on the dislocation density; in the latter case, a frequently used approximation is to take the value of $\zeta$ to be:

$$\zeta = \frac{ln\left(\frac{R}{b}\right)}{4\pi} \qquad \text{Equation 2-8}$$

assuming that the inner cut-off radius in calculations of the dislocation energy equals *b*.

### 2.4.5 Frank-Read and single-arm dislocation sources

When a dislocation pinned at two points and extending from those points outside of the glide plane bows out under applied stress, the stress required to move it forward increases up to the point where the radius of curvature *R* of the dislocation is minimum, which is reached when $R=L/2$, with *L* the distance between pinning points (Figure 2-11a-(3)) [94]. Further expansion of the dislocation line from this point causes an unstable development since *R* decreases. Once the dislocation reaches the point shown in Figure 2-11a-(5), and assuming there is no jog formation in its expansion, the two segments *m* and *n* (having the same Burgers vector but opposite line sense) annihilate [94]. The resulting dislocation loop expands out, and at the same time, the initial dislocation segment is restored and may repeat the process. This mechanism is known as a *Frank-Read source* and is a well-known process for dislocation multiplication within crystals and, therefore, for the initiation of significant plastic deformation.

In a small crystal, a similar mechanism can be identified if a dislocation is pinned at only one point and from there on part of the dislocation lies in a slip plane, with the resulting dislocation arm intersecting the sample free surface, (Figure 2-11b). In this case, under applied stress, the source pivots around its pinning point, taking the shape of a spiral, and by pivoting slips crystal within the glide plane that contains the pinned and exiting arm. Such a process of dislocation multiplication is known as *single-ended source* or *single-arm source*; each revolution of the arm implies a displacement equal to one Burgers vector [93]. This mechanism is of particular interest at the micrometer scale, and can for example be created if a Frank-Read source is truncated at the surface during sample micromachining for example [102–104].

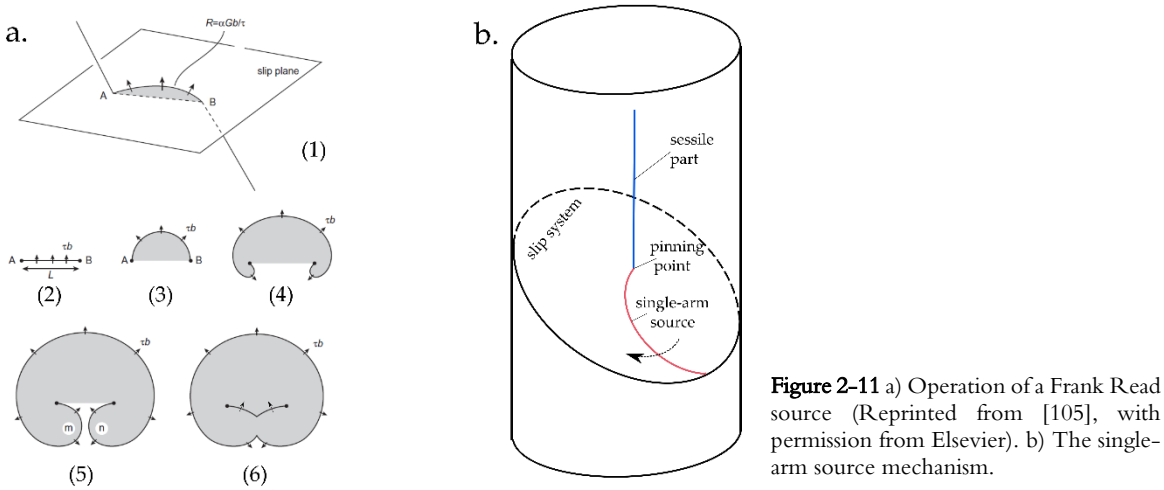


**Figure 2-11** a) Operation of a Frank Read source (Reprinted from [105], with permission from Elsevier). b) The single-arm source mechanism.

### 2.4.6 Dislocation Pile-ups

When dislocations emitted from a source encounter a hard obstacle such as a hard-incoherent particle, a grain boundary or an oxide layer, they tend to pile up against it. Since these dislocations have the same Burgers vector, they repel each other. The resultant stress on the dislocation closest to the barrier ($\tau_n$) can be shown to be equal to the total number of dislocations in the pile-up ($n$) times the applied stress ($\tau$), so that $\tau_n = n\tau$. If a dislocation pile-up forms starting from a Frank-Read source, it gradually exerts a *back stress* on the dislocation source, which opposes the applied stress. This implies that, to continue plastic deformation of the crystal, the applied stress must increase, which might in turn activate smaller sources situated elsewhere within the crystal [94,106].

### 2.4.7 Intersection of dislocations

The interaction between moving dislocation may result in the formation of barriers to dislocation motion, such as attractive junctions, jogs, Hirth locks or Lomer-Cotrell locks, to name a few. These obstacle formation mechanisms play a significant role in the work hardening of crystals. A convenient tool for visualizing dislocation reactions in FCC crystals is *Thompson's tetrahedron* (Figure 2-12a). This consists of representing four gliding {111} systems parallel to the faces of a tetrahedron; each corner of the tetrahedron is denoted by A, B, C, D and the mid-points by $\alpha, \beta, \gamma, \delta$. The Burgers vector of perfect dislocations are represented by the edges of the tetrahedron (AB, BC, CD, etc.) while partial dislocations are defined by a line from a corner to the mid-point of a face that meets that corner, namely A$\beta$ or A$\gamma$ [93].

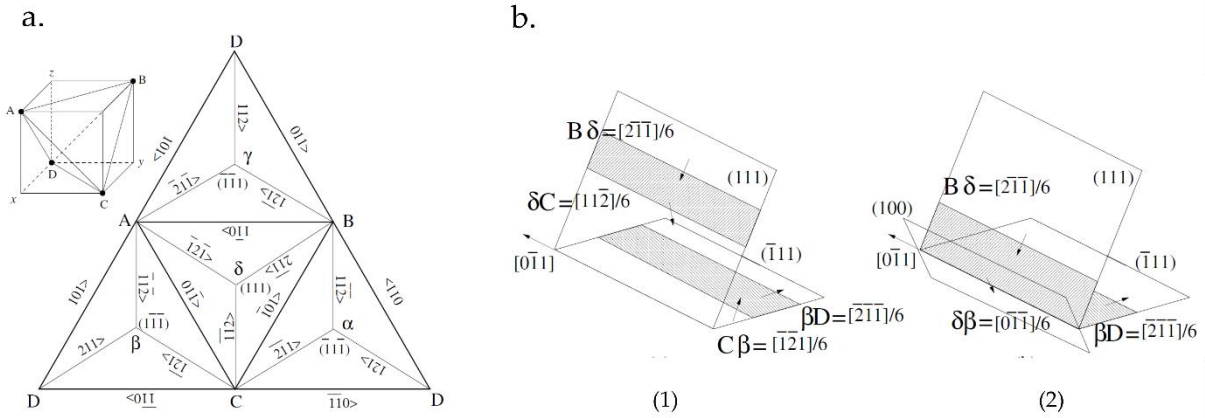


**Figure 2-12** a) The Thompson's tetrahedron notation. b) The Lomer-Cotrell junction formation mechanism. Reprinted from [107] with permission from Elsevier.

If slip eventually occurs on two different {111} systems, when leading partials meet at the intersection line, they may repeal or attract each other depending on the particular direction of the Burgers vectors. Considering the case in which a BC dislocation ($\frac{1}{2}[10\bar{1}]$) dissociates (BC→B$\delta$+ $\delta$C) and moves on the (111) system, and at the same time, a CD dislocation ($\frac{1}{2}[\bar{1}\bar{1}0]$) gliding on the ($1\bar{1}\bar{1}$) plane as CD→ C$\beta$ + $\beta$D (Figure 2-12b-(1)), when the leading partials $\delta$C and C$\beta$ meet, the following reaction takes place as it minimizes the energy:

$$\delta C + C\beta \rightarrow \delta\beta \qquad \text{Equation 2-9}$$

$$\frac{1}{6}[11\bar{2}] + \frac{1}{6}[\bar{1}\bar{2}1] \rightarrow \frac{1}{6}[0\bar{1}\bar{1}] \qquad \text{Equation 2-10}$$

The resulting Burgers vector $\delta\beta$ (Figure 2-12b-(2)) does not lie in either of the two slip planes and thus it represents a sessile dislocation, which exerts repulsive forces on the remaining partials B$\delta$ and $\beta$D. This type of junction with a stair-rod sessile arrangement is known as *Lomer-Cottrell lock* and constitutes an important mechanism that provides, particularly in low stacking-fault metals a barrier to dislocation motion [93,94,108].

## 2.5 Flow stress and work hardening of single crystals

When a single crystal is tested in uniaxial tension, the experimental data are conventionally represented by means of the resolved shear-strain curves (Figure 2-13a). Typically, different stages can be distinguished in such curves, which are described by changes in the work hardening rate (WHR-$\theta$)[87,109], defined as the slope of the curve:

$$\theta = \left.\frac{\partial\tau}{\partial\gamma}\right|_{T,\dot{\gamma}} \qquad \text{Equation 2-11}$$

with both the temperature ($T$)and strain rate ($\dot{\gamma}$) held constant throughout the tensile test. Up to five different stages, or domains, of deformation have been recognized to be present in FCC crystals [109–112]. A number of intrinsic and extrinsic parameters directly affect not only the extension and slope of the stages of deformation, but also the flow stress (or CRSS) of single crystals; these include the crystal structure, chemical

composition, crystallographic orientation, SFE, surface condition, size, deformation mode, strain rate, and temperature [87,109].

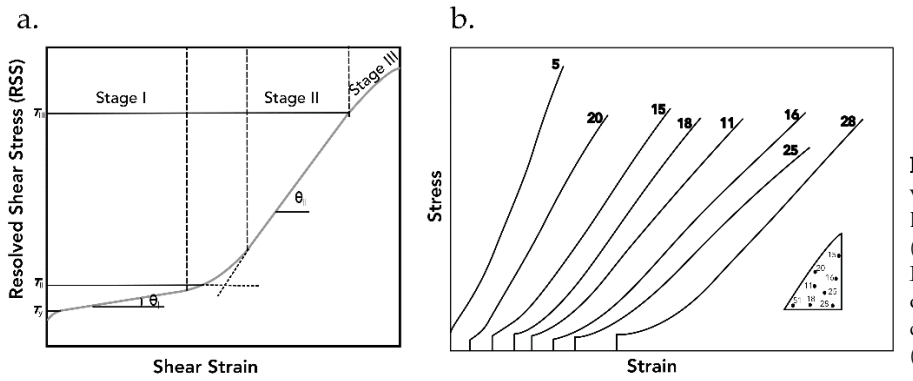


**Figure 2-13** a) The stage of work hardening of an ideal FCC single crystal (Redrawn from [110]). b) Effect of the crystal orientation on the deformation of silver crystals (Redrawn from [113]).

The flow stress is often associated with the stress necessary to sustain the long-range propagation of dislocations through the structure of the material, which generally comprises obstacles of variable strength [109]. In the case of pure FCC crystals, where the lattice resistance is negligible, the flow stress is controlled by dislocation-dislocation interactions. When forest dislocations intersect a moving dislocation line, the latter will bow between intersection points to an extent dictated by the applied stress according to Equation 2-7. In such a scenario, the distance between forest dislocations ($l$) can be estimated through the dislocation density ($\rho$) as $l \approx \frac{1}{\sqrt{\rho}}$ and thus:

$$\tau_c = \alpha \mu b \sqrt{\rho} \qquad \text{Equation 2-12}$$

This equation, introduced by Taylor in 1934 [114], describes forest hardening. It has been shown to remain valid for a large range of dislocation density values, regardless of the dislocation arrangement [109]. Parameter $\alpha$ is a dimensionless number expressing the average strength of interactions between gliding and forest dislocations; it is known to vary slowly with the dislocation density as a result of variations in the average line tension. From experimental data and DD simulations, with FCC metals an appropriate value when the Taylor relation is written in resolved shear stress-strain coordinates is:

$$\alpha = 0.35 \frac{\ln\left(b\sqrt{\rho_f}\right)}{\ln\left(b\sqrt{\rho_o}\right)} \qquad \text{Equation 2-13}$$

where $\rho_o$ is a reference dislocation density equal to $10^{12}$ m$^{-2}$ [91]. This gives for the more usual dislocation densities $\alpha$ values on the order of 0.3-0.5.

In addition to the dislocation density, evidence of a significative impact of the crystal chemical composition on the CRSS and the shape of the resolved shear-strain curves has been demonstrated for FCC metals [113]. No major change of the CRSS for the initiation of flow with crystal orientation has been observed for fully annealed FCC crystals.

Beyond the initial flow stress, once plasticity has begun, normally at least two stages of deformation are evidenced. Characteristics of the first three among those, namely Stage I to Stage III of FCC crystal deformation (relevant for the present work; Stages IV and V are for very heavily deformed metals), are:

- Stage I-Easy glide: In this stage, exhibited in crystals that initially deform in single slip, deformation of the crystal is accomplished with a low WHR, usually in the range of $2\ 10^{-4}\mu$ to $5\ 10^{-4}\mu$ [115]. Different factors influence the extension of this stage. It is evident, due to the low work hardening rate, that this stage of deformation is associated with a low rate of dislocation storage; dislocations move over long distances before interacting with obstacles. The microstructure develops low-angle walls of primarily edge dislocations [115–118]. The impurity content has been shown to both increase or decrease Stage I of deformation, depending on the nature of the impurity. When they tend to form a second phase, impurities reduce and may completely suppress Stage I since these obstacles create stress inhomogeneities that may trigger the activation of dislocations in another slip system. On the contrary, when impurities are in solid solution they tend to extend Stage I, decreasing the WHR of both Stage I and II of deformation [113]. The crystallographic orientation also represents a factor influencing the extension and rate of work hardening of this stage, which is ascribed to the level of activity on the secondary system. Orientations near or on the edges of the stereographic triangle, where more than a single slip can be operative, exhibit a minor or absence of Stage I deformation, Figure 2-13b [88,113]. The surface condition also affects the mechanical behavior of single crystals; an extensive review can be found in [118]. In particular, in the presence of an oxide layer, the rate of work hardening and the flow stress were shown to increase for silver [119], while the extension of Stage I was reduced due to dislocation pile-ups and the early onset of slip on secondary systems [118]. The crystal size also influences the extent of Stage I [120], with a reduction in crystal size leading to an extension of Stage I and a lower WHR. This has been ascribed to a lower rate of dislocation multiplication due to dislocation escape at the surface. Among FCC metals, those with a low SFE and low tendency for cross slip show larger extensions of Stage I of deformation.

- Stage II represents, by far, that which has received most attention during the early work. The WHR during this stage is in the range of $3\ 10^{-3}\mu$ to $6\ 10^{-3}\mu$ [110], *i.e.*, roughly ten times higher than in Stage I. It varies with the orientation, similar to what occurs in Stage I [87]. The Stage II WHR is the highest in crystals initially oriented close to the (001)-(111) boundary, where multiple slip systems are operative. The increase in RSS with deformation is ascribed to an increase in the forest dislocation density, following Equation 2-12 [87]. The microstructure shows high dislocation densities, with a network of interacting primary and secondary dislocations. A predominance of widely extended and stable Lomer-Cotrell locks at low SFE or temperature is evidenced in this stage [87,109]. The WHR in Stage II has a mild dependence on temperature, and similar findings were found for its dependence on the strain rate [87,109,112]. The slight decrease with temperature of the Stage II WHR has been linked to the drop in elastic modulus [87]. The transition from Stage II towards Stage III of deformation is usually associated with the activation of cross slip; thus, metals with a low SFE usually display an extensive Stage II of deformation [87,109]. Furthermore, a significant drop in the WHR of this stage has been observed in copper crystals with diameters below 200 μm; this is explained by a lower rate of dislocation multiplication due to dislocation annihilation at the surface when the external size of the crystal is reduced [109].

- Stage III is characterized by a gradual decrease in the WHR and is associated with dynamic recovery [87,121]. As previously mentioned, this stage of deformation is associated with cross slip, which is responsible for the onset of dynamic recovery and can explain the parabolic hardening exhibited in Stage III of FCC crystal deformation. Its onset is usually known to be triggered by a critical stress, namely that which provides the driving force for constriction processes that enable cross slip [110]. This stress is in the range of $3\ 10^{-3}\mu$, and decreases exponentially with temperature [109]. Models that have been proposed to describe the WHR of single crystals in Stage III assume that the rate of dislocation multiplication of Stage II still holds but is reduced by a rate of recovery that increases with deformation. A frequently used hypothesis is that the rate of dislocation annihilation is proportional to the dislocation density ($\frac{\partial \rho}{\partial \gamma} = -L\rho$) [110].

## 2.6 The influence of temperature

Some characteristics of the impact of temperature on the deformation of single crystal are described in preceding sections; yet, a few aspects merit being detailed.

The deformation of crystals, at intermediate temperatures, usually involves gliding, interactions of dislocations and the rearrangement of previously stored dislocations. Gliding, in particular, involves two consecutive processes: its initiation and its propagation, the velocity of the plastic flow being determined by the most difficult step of a sequence of processes. An expression by Orowan [122] links the rate of macroscopic deformation ($\dot{\gamma}$) with the (mobile) dislocation density ($\rho$), the average velocity ($\bar{v}$) and the Burgers vector:

$$\dot{\gamma} = \rho b \bar{v} \qquad \text{Equation 2-14}$$

It therefore correlates an experimental variable, such as the strain rate, with characteristics of the internal microstructure. This equation also implies that the stress dependence of $\dot{\gamma}$ can be related to the stress dependences of $\rho$ and $v$. Different equations associate the average dislocation velocity with the resolved shear stress [95,123]. Assuming that dislocation motion follows an Arrhenius form:

$$v = v_o \exp\left[\frac{-\Delta G(\tau)}{kT}\right] \qquad \text{Equation 2-15}$$

where the frequency at which dislocation segments overcome barriers and the average distance covered by this segment between barriers is contained in $v_o$, and $\Delta G(\tau)$ is the change of Gibbs free energy required to overcome the energy barrier, assumed to depend on the shear stress ($\tau$), while $k$ and $T$ are the Boltzmann constant and absolute temperature respectively. According to Equation 2-15 and 2-14, and defining $\gamma_o = v_o \rho b$, at fixed dislocation density $\rho$ the resulting plastic shear strain rate can be written as:

$$\dot{\gamma} = \gamma_o \, exp\left[\frac{-\Delta G(\tau)}{kT}\right] \qquad \text{Equation 2-16}$$

The identification of dislocation mobility mechanisms consists of determining experimentally the value of $\Delta G$ [95], which is the energy barrier to be overcome for the thermally activated deformation mechanism to operate. Even though there may be different relations for $\Delta G(\tau)$, in the case of a mechanism with a constant

activation volume, typically a linear form in which the energy barrier can be reduced by the application of stress is assumed:

$$\Delta G(\tau) = \Delta G_o - \tau V \quad \text{Equation 2-17}$$

Here $\Delta G_o$ denotes the stress-free energy barrier and $V$ represents an *activation volume* ($V = -(\partial \Delta G/\partial \tau)_T$), usually defined (for reasons that have to do with the physics and measurement of activation volumes) as the *effective activation volume*. An *activation area* ($\Delta a = V/b$) is also used to refer to this quantity, on the reasoning that this is the more physically significant quantity [124]. In simple terms, the activation area is the area swept by the dislocation while overcoming, with a contribution form thermal activation, the energy barrier that opposes its motion. The activation volume or area vary significantly with the microscopic mechanisms governing plastic deformation [125]. For instance, the activation volume displays small values (on the order of 10 $b^3$) for the kink pair mechanism, while somewhat larger values are obtained for dislocation-solute interactions, and values in the range of 1000 $b^3$ are found for the forest mechanism [95,125].

Furthermore, considering a constant structure (this implying that parameters involved in $\gamma_o$ do not change) [126]:

$$\Delta G(\tau) = kT \ln \frac{\gamma_o}{\dot{\gamma}} = AkT \quad \text{Equation 2-18}$$

It has been shown that, for certain values of mobile dislocation density and area swept by a dislocation in an activation event, $A$ ~21 [126]. Consequently, by combining Equation 2-17 with Equation 2-18 under this approximation one obtains:

$$\tau = \frac{\Delta G_0}{V} - \frac{AkT}{V} \quad \text{Equation 2-19}$$

This equation has two main implications. First, it allows to recognize that a rapid or slow decrease of the stress with temperature will occur for mechanisms with a small or large activation volume respectively [95]. On the other hand, it implies that the flow stress of a material can be decoupled into two parts (Equation 2-20), namely an athermal or internal stress ($\tau_i$), and an effective or thermal stress ($\tau^*$):

$$\tau = \tau_i(\gamma) + \tau^*(T, \dot{\gamma}) \quad \text{Equation 2-20}$$

The temperature-independent stress ($\tau_i$) arises from long range stresses opposing dislocation movement [95,127], namely the internal stress field developed by other dislocations and the Peierls or *lattice friction stress*, the latter being negligible for FCC metals at intermediate temperatures. Then, the stress field developed by other dislocations is mostly athermal, yet varies with temperature but does so only through the temperature dependence of the shear modulus [128]. On the other hand, the thermal stress ($\tau^*$) has a strong dependence on temperature, because thermal fluctuations redistribute energy and thus help dislocations to overcome obstacles at a level of stress lower than the stress needed at absolute zero temperature [80,129].

Cotrell and Stokes evaluated the influence of the temperature on the flow stress by deforming single crystals up to different levels of deformation at a certain temperature $T_1$, recoding the flow stress ($\tau_{T1}$). Subsequently, the crystal was unloaded, the temperature modified to $T_2$ and the new flow stress ($\tau_{T2}$) was measured. A constant ratio $\tau_{T2}/\tau_{T1}$ was found, regardless of the level of deformation (or dislocation structure). This states that the thermal and athermal contributions to the stress remain proportional as the microstructure evolves;

this is usually known as the Cotrell and Stokes, of Cotrell-Stokes, relation. Similar findings were reported for the strain rate at fixed stress [130].

It is thus apparent that temperature has a major influence on the deformation of crystals, affecting not only the flow stress but also the rate of hardening, notably through the rearrangement of stored dislocations.

## 2.7 Small-scale plasticity

In previous sections the crystal is assumed sufficiently large that dimensions involved be those defined by the microstructure (*e.g.*, the dislocation density in the Taylor hardening law or the grain size in polycrystalline materials). These intrinsic microstructural dimensions govern the mechanical behavior of materials on the macroscopic scale, meaning in materials sufficiently large for their microstructural development not to be altered by free surface effects. When the external (extrinsic) dimensions of the specimen are small and approach the intrinsic microstructural dimensions, the mechanisms ruling deformation are generally altered; this is called the plasticity size effect. Size effects have been evidenced in whiskers (dislocation-free crystals), single- and polycrystalline thin films, and dislocation-containing micropillars. This section does not intend to entirely describe the characteristics of small-scale plasticity, as this has been the subject of a large volume of research, but to give a general overview of its main features with emphasis on questions that are relevant to present results. Comprehensive and extended reviews can be found in Refs [13,102,131–133].

Over the past decades, after the introduction of a uniaxial microcompression testing method to study the plasticity of micro- and nanopillars produced by FIB micromachining, interest in plasticity size effects reached a high intensity [7–9]. Unlike the plastic deformation of a bulk metal, which takes place through what is measured as smooth and homogeneous flow, uniaxial tests on micro- and nanoscale metallic samples generally present a drastic increase in both the flow stress and its scatter, and the manifestation of a serrated stress-strain behavior. These characteristics are detailed in subsequent sections.

### 2.7.1 The flow stress

Despite a large fluctuation among pillars of the same diameter, an increase in yield strength with decreasing pillar size has been demonstrated when the sample diameter $D$ becomes roughly $< 100$ μm. Most studies focus their attention on FCC crystals, but this trend is extended to body-centered cubic (BCC), HCP, shape-memory and high entropy alloys, and metallic glasses.

Expressing the relationship between the yield strength ($\tau$) and the sample diameter ($D$) as a power-law was proposed in [134] and employed by many studies to fit measured data as follows:

$$\tau = \tau_0 + AD^n \qquad \text{Equation 2-21}$$

where $\tau_0$ is the bulk strength of the same material, $A$ is a constant, and $n$ is the (empirical) power-law exponent. After analyzing a significant amount of data, a universal power-law exponent for FCC metals of $n \approx 0.6$ was proposed in [134], suggesting that only a particular mechanism governs the deformation. Contradicting this, diverse investigations reported power-law exponents ranging over a wide range,

extending from 0.3 up to 1 (*e.g.*, [14,135,136]). This suggests the presence of multiple mechanisms; also, the variety of exponents observed leads to question whether a power-law relationship extracted from a double-logarithmic plot has fundamental validity. Numerous factors have furthermore been found to affect the observed scaling behavior, which are not explicitly considered in Equation 2-21, namely the aspect ratio [14,137], geometry [138], and the initial dislocation density [139,140] of samples tested.

Different models have attempted to explain the reasons behind the increase in yield strength with decreasing sample diameter. *Dislocation starvation* [22,44] assumes that when the external size of the sample is reduced, dislocations that travel through the crystal will annihilate at free surface before breeding new ones. There is then a higher probability for dislocations to exit before multiplication at decreasing sample diameter, or in other words one observes a higher rate of dislocation escape, causing source depletion and the need for new dislocations to nucleate for deformation to continue, leading in turn to an increase in the value of applied stress required to deform the crystal. This model may explain the basic mechanisms involved in sub-micron specimens where the number of dislocations initially present is highly limited (*i.e.*, one dislocation in a volume of 10 $\mu m^3$ if the dislocation density is $10^{10}$ $m^{-2}$). In this range, where a substantial number of dislocations exit, the number of mobile dislocations is exhausted due to mutual interaction and the applied stress must be raised to sustain deformation. This is known as *exhaustion hardening* [141].

The deformation of specimens with diameters of some tens of microns is probably ruled by the collective behavior of dislocations and the presence of a significant density of sources. An analytical expression, corresponding to Equation 2-7*,* is developed in [142] for thin films to predict a variant of Equation 2-7giving the critical stress required to bow out a dislocation of length *L*, presented in [143] as:

$$\tau = \frac{\mu b}{2\pi}\frac{1}{L}\ln\left(\frac{a\,L}{b}\right) \qquad \text{Equation 2-22}$$

where *a* is a constant, $\mu$ and *b* are the shear modulus and Burgers vector respectively. In this study, *L* is reported to be between a third and a fourth of the limiting dimension, namely half the thin film thickness or the micropillar diameter. Parthasarathy *et al.* [144] propose that double-pinned Frank-Read sources, initially present in micropillars, rapidly evolve towards single arm dislocations due to interactions with the free surface, a process termed *source truncation* and observed in [145]. The longest single-arm-source (SAS) then defines the flow stress. The stress to activate such a source is similar to that required to activate Frank-Read sources (see Section 2.4.5 Frank-Read and single-arm dislocation sources and Equation 2-7), and is thus inversely proportional to a characteristic length *L.* An analytical expression to evaluate *L* is given in [144]; in samples containing several dislocations across the sample cross-section it is reasonable to estimate it as $L \approx D/3$, as described earlier for thin films. From this, Parthasarathy *et al.* [144] propose that the critical resolved shear stress, as given by the SAS model, can be computed as:

$$\tau_{SAS} \approx \frac{\alpha G b}{L} + 0.5 G b\sqrt{\rho} \qquad \text{Equation 2-23}$$

Similar expressions, which vary depending on prefactors that are adopted for either term, are reported in [81,146,147]. For instance, according to [81]:

$$\tau_{SAS} \approx \frac{0.12G\ln\left(\frac{L}{b}\right)}{\frac{L}{b}} + 0.44Gb\sqrt{\rho} \qquad \text{Equation 2-24}$$

The SAS model also predicts that, for essentially dislocation-free sub-micron pillars, the flow stress corresponds to the stress needed to nucleate a dislocation from the free surface. This stress differs from the flow stress estimated for whiskers because of surface imperfections; it is expected to equal the stress required to move isolated partial dislocations across the pillar [144]. Thus, the maximum CRSS possible depends on the stacking fault energy and is capped by $\tau_{SAS}^{max} \approx SFE/b$.

The single-arm-source model has been shown to properly reflect trends in experimental data over a wide range of pillar sizes (Figure 2-14a) (even though in its derivation it introduces the forest contribution as a back stress, which is not legitimate since both the size-independent and size-dependent terms are based on the same Orowan bowing mechanism). Being generally applied to interpret FIB-milled nanopillar data, the structure of which is assumed to be unaltered during sample preparation (thus ignoring FIB-related damage), it assumes that the forest dislocation density does not vary with *D*.

El Awady [140] analyzed the influence of the dislocation density ρ on the mechanisms governing the deformation at small scale and proposed regions for each mechanism (Figure 2-14b). In addition, a generalized size-dependent Taylor-strengthening law is proposed on the basis of extensive discrete dislocation simulations, similar to Equation 2-23, with a characteristic length scaling with both the dislocation density and the sample diameter, as $L = D\sqrt{\rho}$.

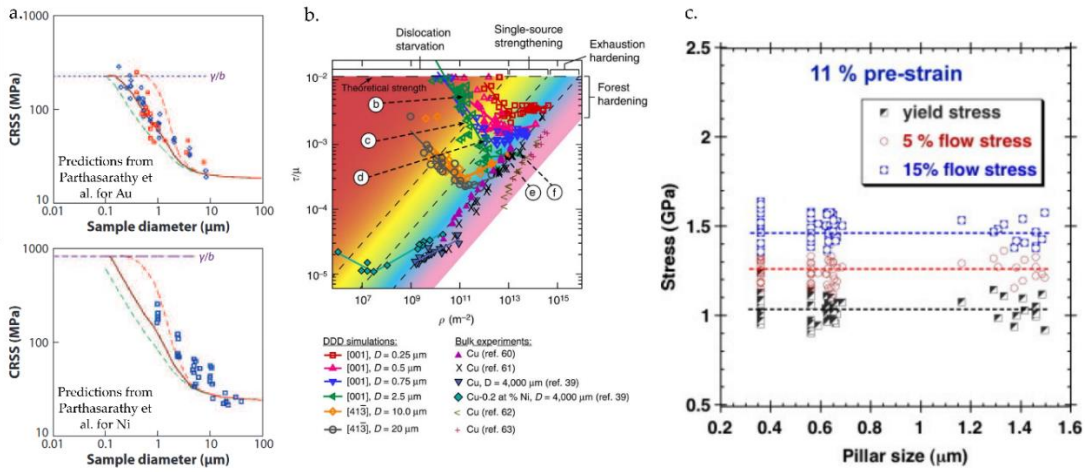


**Figure 2-14** a) Predictions of Equation 2-23 for Ni and Au in comparison with experimental data. b) Dimensionless flow stress as a function of dislocation density, colors highlight regions of different deformation mechanism c) Flow-stress versus sample-size for Mo(Ni,Al) microcrystals of variable initial dislocation density. a-c) Reprinted from [144] and [30], with permission from Elsevier. b) Image adapted from [140].

Bei *et al.* [30] also investigated the effect of the initial dislocation density on the flow stress employing molybdenum pillars produced without FIB milling (Figure 2-14c). Different pre-strain levels are imposed on several pillars and a drop in the yield strength and its scatter on subsequent loadings is reported. This is ascribed to the fact that dislocations must nucleate in pristine pillars, and thus a high yield strength is observed, while the gradual introduction of dislocations leads to bulk-like behavior with less variability and lower flow stresses.

Likewise, annealing heat treatments modify the initial dislocation density, reducing the number of dislocations available in the crystal (note that annealing is also commonly applied to remove defects introduced by focused ion milling; see 2.1.1 Focused ion beam milling). Experiments on annealed cast aluminum and FIB milled copper specimens led to report a considerable increase in yield strength with respect to their non-annealed counterparts [15,82]; this is attributed to dislocation source depletion after heat treatment. Beyond the flow stress, copper pillars experience a softening down to stress levels comparable with non-annealed specimens. On the contrary, cast aluminum wires do not exhibit such softening and continue their deformation with a highly serrated behavior.

### 2.7.2 The work hardening rate

Unlike the flow stress, characterization at the microscale of the work hardening rate has been more occasional, in particular in samples free of stress gradients. Most available studies are conducted by microcompression of pillars, with its associated limitations (see Section 2.7.3 Testing considerations). In Ref. [141], interpretation places focus on the work of Gil Sevillano *et al.* [148] and postulates that according to percolation theory the work hardening rate must scale proportionally to $D^{1/3}$. WHR rate measurements are also made difficult due to the sudden strain-bursts, which hinder quantitative analysis. Similarly, a strong size effect is also observed on the work hardening rate when reducing the diameter of the pillars, particularly in the sub-micrometer range [139,141,149,150]. As an example, an extremely high work hardening rate is reported on copper pillars oriented for multiple slip with diameters below 2 μm, reaching up to 4.6 GPa with a breakdown of the Taylor hardening law [150]. This characteristic is explained by a change in deformation mechanism, proposed by different theories, in which the stress needs to be increased abruptly in order to reactivate or nucleate a new source after source exhaustion or extinction [139,151,152]. Instead, single crystals oriented for single slip with sizes in the micrometer range evidence an essentially nil WHR and an extended Stage I of deformation [141]. This lack of work hardening, with essentially no dislocation storage, has been described as one of the main mechanisms indicating the onset of confined plasticity, particularly of micrometer samples where dislocation annihilation leads to a stationary dislocation network rather than a dislocation-starved material, as is the case in sub-micrometer samples [149].

### 2.7.3 Testing considerations

Determining the mechanical properties at the micrometer scale differs from conventional testing due to a considerable number of associated challenges; still, such experiments have been practiced as far back as the 1950s [153,154]. In-situ scanning electron microscopy and transmission electron microscopy experiments, together with the rapid evolution of micromechanical testing systems have assisted in overcoming several of the challenges, namely positioning, alignment, and sensitivity, among others. At the same time, many different approaches in terms of sample shape and loading conditions have been employed, many of them developed to study thin film [155–157]. Main techniques are nanoindentation [158,159], microbeam bending [160–

163], compression testing [7,44,141,152], tensile testing [23,81–83,164,165], and a few other non-conventional testing methods [166,167].

Uniaxial compression testing of pillars consists of squeezing pillars of aspect ratio (length-to-diameter) ≈ 2.5 : 1 with flat-punch tips, generally of diamond. Since pillars are linked to bulk material, this strategy avoids difficulties arising from sample manipulation. Yet, in microcompression testing it is crucial to establish the real contact area, to avoid any strain localization, and therefore to ensure a good alignment throughout the experiment [16]. *Buckling* or a lateral shift of the loaded surface, count among the main intrinsic limitations of this technique; this plays an essential role above 5 % of plastic deformation. Buckling may lead to an underestimation of the yield strength [13,102]. Similarly, friction forces between the punch and the pillar together with the fact that it is attached to the substrate at its other end prevent the lateral expansion of the specimen while it is compressed. This results in *barreling*, which causes deviations from a state of uniaxial stress state and also hinders a meaningful computation of work hardening rates [13].

Most limitations exhibited by microcompression can be overcome by uniaxial microtensile testing. Kiener *et al.* [168] developed an in-situ tensile testing procedure for FIB-milled specimens, which enables the mechanical testing in tension of high aspect ratio specimens. The low lateral stiffness of such samples eliminates restrictions associated with lateral movement of the load application point, while buckling is absent as are constraints originated from the sample base [13,168]. These features allow the specimen to deform extensively in single slip [150]. A similar approach is employed to test FIB-milled gold and molybdenum crystals [23,169], as well as electroplated copper [23]. In uniaxial tensile testing clamping the sample and applying a load represent some of the main challenges. Kiener *et al.* [168] produced a wider region at the end of the specimen such that it can be grabbed by an appropriately machined mechanical grip, and reported lower yield strength values measured in tension than in compression [14]. A similar strategy is conducted in [23], where copper specimens glued to the base by amorphous tungsten are pulled out by a custom-fabricated tensile grip. Krebs *et al.* [81,84] produce much longer wires and employ glue to fixate them at either end to the load train of a custom-built tensile testing rig.

### 2.7.4 The influence of temperature

The examination of the mechanical behavior of microsamples at elevated temperatures has its experimental difficulties, namely thermal drift, temperature calibration of both specimen and indentor/grip, temperature match between the two, and surface degradation to name some of the challenges [170,171]. Yet, a large number of investigations are now available that study the influence of thermally activated mechanisms at elevated temperature in the presence of strain gradients, *i.e.*, by means of nanoindentation, on a wide range of materials [172–177]. Early attempts prevented oxidation by testing under a protective atmosphere, namely argon, but still experienced considerable thermal drift. This was improved by heating both specimen and indenter tip and developing different approaches to measure and match their temperatures. Uniaxial micromechanical studies on the behavior of materials at elevated temperatures are more occasional. Korte *et*

*al.* [178] carried out compression at temperatures up to 400 °C of $MgAl_4O_4$ spinel micropillars, in which it is possible to observe significant plasticity with increasing temperature, a linear decrease in yield strength, and activation volumes equivalent to those exhibited by BCC metals, which are ascribed to the lattice resistance. Subsequently, micropillar compression investigations at elevated temperatures have mostly focused on the behavior of BCC metals, initially studying tantalum [179] and molybdenum [180] due to their comparatively low critical temperature [181], and extending investigations to tungsten [182]. Body-centered cubic metals generally exhibit a weak size dependence at room temperature associated with the influence of lattice friction [183–185]. Above room temperature, BCC metals display a transition towards strong size dependence with increasing temperature due to thermally activated mechanisms (Figure 2-15a), namely an increased mobility of screw dislocations, which also leads to a lower yield strength. In addition, Mo micropillars manifest signs of significant slip at elevated temperatures [180], similar to W pillars that show a change from homogeneous to localized deformation with increasing temperature, and an increase in fracture toughness [182,186] (Figure 2-15b). Equivalent results are reported for LiF FCC microcrystals [187], with a bulk strength governing the behavior at room temperature when no size-effects are evidenced and a size-dependence contribution which becomes gradually predominant at high temperatures. Silicon FIB-milled pillars also exhibit an influence of temperature on their deformation, showing a brittle-to-ductile transition in fracture at around 300 °C together with considerably lower yield strength values with increasing temperature [188]. Similar drops in yield strength with increasing temperature are reported on gallium nitride grown by epitaxy tested up to 500 °C; in this study, plasticity parameters are measured through compression strain rate jump tests [189]. A Zr-based bulk metallic glass shows on the other hand a constant flow stress up to temperatures around 400 °C [190]. A few microcompression studies at high temperature on FCC metals are available, namely on a nickel superalloy [191], nanocrystalline nickel [192], polycrystalline copper [193], and single crystalline annealed copper pillars [194]. No variation in the size dependence nor in the yield strength is observed on copper micropillars compressed at temperatures as high as 400 °C (Figure 2-15c), while the slip traces are more distributed at elevated temperatures; this is ascribed to the activation of extra dislocation sources at elevated temperature [194].

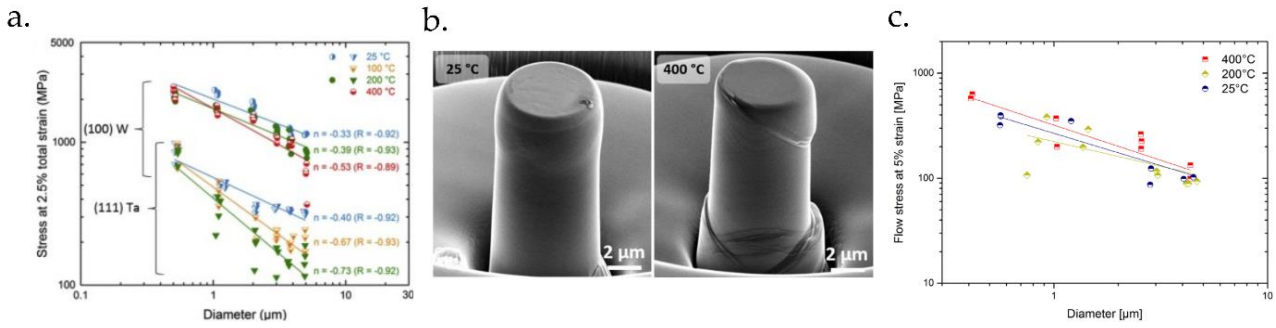


**Figure 2-15** a) The effect of temperature on the size effect in tantalum (Ta) and tungsten (W) micropillars. b) A change from homogeneous to localized deformation in W pillars with increasing temperature. c) No signs of change in the size dependence nor in the yield strength exhibited in copper micropillars with increasing temperature. a-b) Adapted from [182]. c) Image from [194].

### 2.7.5 Intermittency

Flow intermittency, or in other words a stochastic burst-like progression of plastic deformation, also characterizes confined plasticity. This is generally observed through the presence of either sudden strain jumps in load-controlled experiments or large rapid load drops under displacement-controlled conditions (producing a serrated stress-strain curve). These events arise from the collective motion of dislocations or from the activation of sources capable of generating large and rapid strain increments, which lead to those rapid avalanche-like, large-amplitude, slip events, leaving a surface step along the crystal surface. Statistics of such *dislocation avalanches* show that the probability ($p(s)$) of an event of size $s$ follows a power-law ([195]) at small event sizes, potentially over several orders of magnitude, depending on the precision of measurements and their nature [135,149,196–205]:

$$p(s) = As^{-\lambda} \qquad \text{Equation 2-25}$$

where $A$ is a normalization constant and $\lambda$ is the power-law exponent. Some studies conclude that the existence of a power-law is linked with dislocations displaying a self-organized critical (SOC) process in which the structure, after deformation, rapidly evolves to a critical jammed configuration independent of the initial state. The collapse of such jammed configurations leads to a collective avalanche-like progression of deformation. The concept of self-organized criticality was introduced to describe more generally dynamical systems that develop towards a second-order phase transition at which interaction between entities results in scale-invariant events [206]. The presence of a power-law distribution thus suggests a scale-free behavior of dislocations, with the expected formation of structures that, at diverse scales, are equivalent in statistical sense, similarly to fractal patterns [149,197,198,207–211]. This approach also applies in descriptions of other physical instabilities, namely sand piles avalanches or earthquakes [197,205,212]. Also, according to the literature, this power-law scaling at small event sizes is not affected by temperature [204,213].

The measurement of dislocation avalanche events has been performed by different methods, namely acoustic emission (AE) [205,207,213–215], image-based analysis [216–218], as well as analyzing the duration time or axial displacement during the event [201,219,220], or by examining the magnitude of the load drops [81,149,204].

The energy detected by acoustic emission is associated with the release of elastic energy due to the local rearrangement of the dislocation network within the crystal [221]. Signal extracted by transducers is similar to crackling noise [222], comprising intermittent events with a broad range of amplitudes (Figure 2-16a). Acoustic emission investigations on ice single crystals [207,223], together with measurements of burst size distributions in metallic micropillars [205,215,224,225] report, similar to Equation 2-25, avalanches that follow a power-law distribution with a universal power-law exponent ≈ 1.6-2 independent of the material and temperature [213].

A simple and direct method to assess the size of slip events is to analyze the magnitude of the axial displacement or load drop during an avalanche. This is done, for instance, in Refs. [80,81,197,199,201,204]. In this case, a universal power-law exponent for Equation 2-25 of $\lambda \approx 1.4 - 1.6$ is reported, independently

of the material, sample diameter, and testing conditions. The latter does not affect the scaling behavior, but it influences the extent of an avalanche, being larger in load-controlled experiments than in displacement-controlled conditions [226,227]. For BCC metals, the magnitude of strain bursts scales with the strain rate [228]. Slip events generally span from a few angstroms up to a few micrometers. Furthermore, diverse modeling methods reach similar power-law exponents [198,202,214].

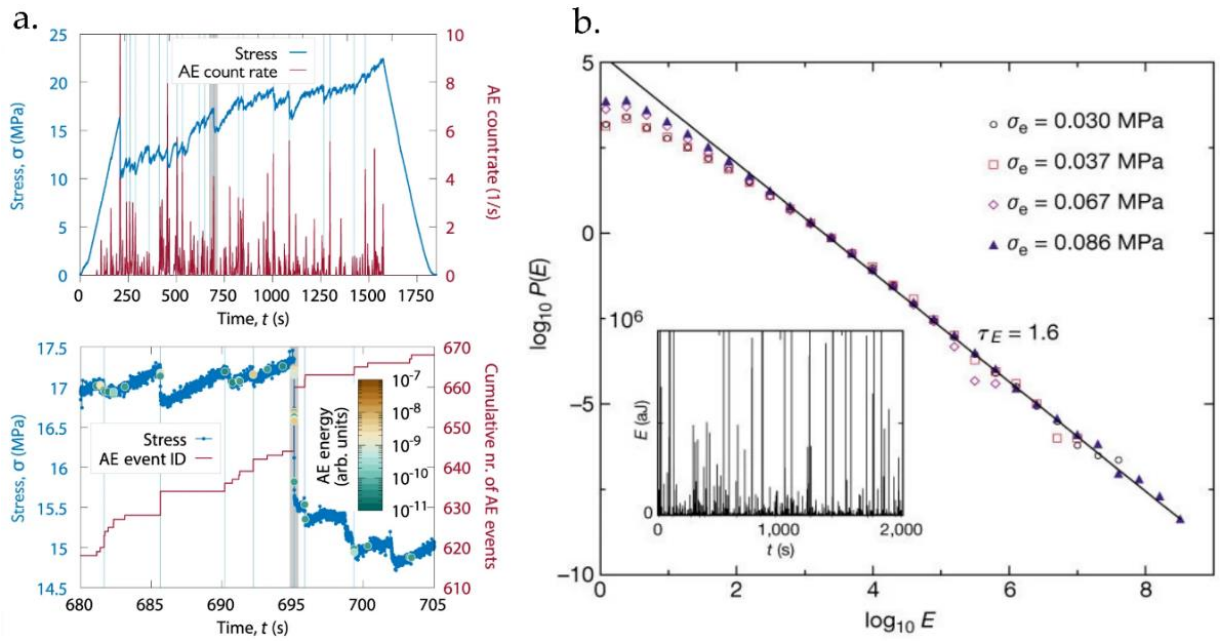


**Figure 2-16** a) Stress-time (blue) and acoustic emission (AE) count rate-time (top-red), as well as the cumulative number of AE counts vs. time (bottom-red). b) The probability distribution of energy bursts following a power-law distribution of exponent 1.6, for diverse loading steps. The inset shows a normal acoustic emission signal. Images adapted from [205] and [207] respectively.

Statistical studies including large slip events generally display a truncation of the power law distribution around a *cut-off* value ($s_c$) that limits the size of avalanches [198,200,201,204,220]. Richeton *et al.* [213,229] observed by compressing ice polycrystals that SOC breaks down in the presence of grain boundaries and that grain boundaries restrict the size of the avalanche at large amplitudes. They then found that the complementary cumulative distribution function (CCDF=P(s≥ $s_0$)), defined as:

$$P(s \geq s_0) = \int_{s_0}^{\infty} p(s)ds \qquad \text{Equation 2-26}$$

of the experimental data could be fitted by:

$$P(s \geq s_0) = Ds^{-\kappa}\exp^{\left(-\frac{s}{s_c}\right)^m} \qquad \text{Equation 2-27}$$

where a universal power-law exponent $\kappa = \lambda - 1$ characterizes the complementary cumulative distribution function at small slip events, $D$ is a normalization constant and $m = 1$, corresponding to an exponential cutoff of the CCDF [81,204,229] (Figure 2-17a displays such a distribution with data from another study).

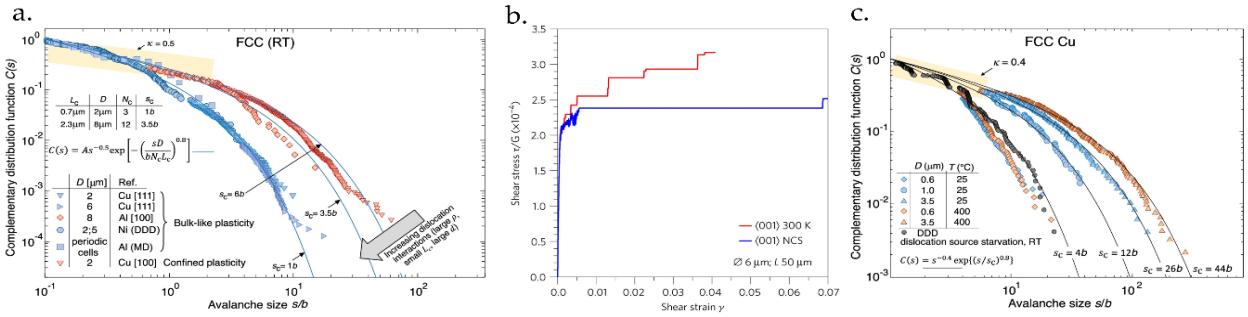


**Figure 2-17** a) Complementary distribution function ($C$(s)) of the individual slip events in different FCC micropillars from compression experiments displaying a power-law behavior at small event sizes together with an exponential cut-off. b) The effect of no cross slip (NCS) in the size of displacement bursts according to simulations. c) Complementary distribution function vs. avalanche size for different [100]-oriented copper pillars tested at room- and elevated temperature. a) and c) Adapted from [204], b) from [81].

Zaiser *et al.* [198,200,202] proposed an alternative truncated power-law model in which the (non-complementary, binned) probability ($p$(s)) shows the same scaling form as in Equation 2-27 with $m = 2$, namely $p(s) = As^{-\lambda}\exp^{\left(-\frac{s}{s_c}\right)^2}$ (note that, since a probability $p$(s) with $m = 2$ does not lead to a complementary distribution truncated by an exponential as in Equation 2-27; see Appendix 1- *Zaiser-Nikitas expression for the complementary cumulative distribution function*, the two expressions differ significantly). According to the model introduced by Zaiser *et al.* [198,200,202] the cut-off value $s_c$ arises from avalanches being influenced by the rate of decrease in applied stress (or similarly increase in flow stress) with increasing strain during a strain burst. More specifically, two parallel mechanisms reduce the effective stress driving dislocations motion, namely (i) the intrinsic hardening ($H$) of the specimen due to dislocation storage or other sources of back-stress, and (ii) under displacement-controlled conditions the system relaxes the applied (resolved shear) stress with increasing strain $\Delta\gamma$ according to $\Delta\tau = M\Delta\gamma$, where $M$ is the strain-based stiffness [MPa]. This stiffness $M$ is linked to the system-*cum*-sample stiffness $J$ [μN/μm] as reported in [81], $M = \frac{J\,D\,S}{A_o}$; where $D$ is the specimen diameter, $S$ is the Schmid factor and $A_o$ the initial sample area. Note that these expressions do not consider the increase in effective stress due to the decrease in cross-sectional area during/after a deformation. The maximum length increment ($\Delta l_{max}$) that can be produced by a dislocation avalanche according to this model is roughly given by:

$$\Delta l_{max} = \frac{C\,b\,\mu\,S}{M + H} \qquad \text{Equation 2-28}$$

where $C \approx 5$, and $b$ and $\mu$ are the Burgers vector and shear modulus respectively.

Cross-slip was reported as a mechanism that can induce cessation of dislocation motion, thus limiting the size of sudden slip events. In Ref. [81] a correlation between the increase of shear stress on the cross-slip plane with lower slip event sizes is observed, as well as clearly larger displacement bursts when cross slip is not considered in 3D discrete dislocation simulations (Figure 2-17b). For comparison, microcompression experiments on FIB-machined copper pillars tested at room temperature and at 400 °C exhibit no noticeable variations in the cut-off values [204] (Figure 2-17c). Both of these two works report an exponential cut-off of the CCDF, following Equation 2-27. This can be observed in [81] by a linear trend of the CCDF vs. event size in semi-logarithmic coordinates (such that $m = 1$), and was found in [204] to fit Equation 2-27 best with $m = 0.8$, while being also compatible with $m = 1$ [J. Alcalá, J. Očenášek private communications].

# Chapter 3 Freeform Microcasting

In this chapter a novel microcasting technique that combines femtosecond laser micromachining with metal casting is introduced. The process exposed here is a truly three-dimensional microfabrication process. Virtually any interconnected 3D shape can be produced in etchable laser-transparent material, and then infiltrated with a metal. In addition, the process inherits attributes from conventional casting, namely the fabrication of nearly-net and fully dense microstructures – and also some of its challenges, notably feeding solidification porosity.

Disclaimer: This chapter contains literal reproduction of full paragraphs and figures of the following publication: [230]-***L. Borasi****, E. Casamenti, R. Charvet, C. Dénéréaz, S. Pollonghini, L. Deillon, T. Yang, F. Ebrahim, A. Mortensen, Y. Bellouard, 3D metal freeform micromanufacturing, Journal of Manufacturing Processes. 68 (2021) 867–876* to which the author has contributed. Specifically, the author conducted the infiltration of the molds and the characterization of components after demolding. The author also contributed to the design of the embedded cavities, while the femtosecond laser micromachining was performed by Dr. Enrico Casamenti (EC) and Mr. Sacha Pollonghini (SP). Four of the article authors (CD, RC, YB and AM) are inventors on awarded European and US patents, application numbers of which are: US 2018304352 - WO 2017081635, awarded to the École Polytechnique Fédérale de Lausanne (EPFL) [231]. Both the author and EC equally contributed in generating the figures and writing the first draft of the manuscript.

In addition, Section "3.2.4 Glass-in-glass composites" contains results of the article [232] *E. Casamenti, G. Torun,* ***L. Borasi****, M. Lautenbacher, M. Bertrand, J. Faist, A. Mortensen, Y. Bellouard, Glass-in-glass infiltration for 3D micro-optical composite components, Opt. Express, OE. 30 (2022) 13603–13615.* The author worked on the strategy to infiltrate such glass and contributed to relevant preliminary experiments. Only basic information is reproduced here, while further findings are detailed in reference [232].

## 3.1 Freeform microcasting: combining femtosecond laser machining with metal casting

Process steps that lead to produce 3D structures of dense engineering noble metal with sub-micron resolution are detailed in Figure 3-1. As an illustration, we show the production of a micrometric classroom containing a series of miniature chairs and desks. Step 1 in Figure 3-1 consists in exposing quartz glass to femtosecond (fs) laser irradiation according to a freely designed interconnected geometrical pattern that defines the material to be removed by altering locally the glass structure. This alteration causes the glass to be preferentially etched where it has been exposed to laser irradiation.

This glass micromachining process is based on nonlinear absorption phenomena that occur in laser-transparent substrates when the incoming laser beam locally exceeds a peak irradiance level (typically around the $GW/mm^2$), triggering a chain of events leading to the ionization of the matter. As the effect is non-linear and depends on a threshold value, the effective size of the ionized volume can be smaller than both the beam waist itself and the laser wavelength [233–235]. In addition, given the extremely short plasma life time, the absorbed energy remains confined in the focal volume and no heat is transferred to the surroundings, which thus remain largely unaffected [236,237]. Combined with the possibility to define with high-accuracy the beam trajectory thanks to the use of high precision motorized stages (PI Micos with a repeatability of 200 nm over a centimeter motion range and a micron over the full travel range), this process enables the engraving of arbitrary 3D-shapes made of single voxel sizes, the geometry and resolution of which depends chiefly on the confocal parameters and the pulse energy. In our case, the beam waist was focused to 1.9 μm and we used a moderately focused beam with an energy of about 240 nJ. As a result, a voxel of laser-modified volume has an ellipsoid shape with 1.9 μm and 8 μm on the short and long axis, respectively. Smaller voxel sizes can be achieved by lowering further the pulse energy.

In Figure 3-1 step 2 wet chemical etching of the substrate preferentially removes those regions that were modified by the laser along a continuous path that intersects the mold free surface. The etching-rate contrast between pristine and modified mold material depends on the chemistry used (namely, with fused quartz, etching with a basic – KOH [238] – or with an acidic – HF [234,235] – solution), on the deposited energy (or net fluence), and on other laser-related parameters such as the laser-beam polarization or the pulse duration [239]. By precisely controlling the exposure and the etching steps, it is thus possible to achieve micrometric resolutions in the mold manufacturing. As the etching front progresses inward from the mold surface through the exposed pattern, the final shape of the etched volume becomes diffusion-limited and shows a dependence on the etching rate contrast between pristine and exposed material. This may lead to a dependence of the etched geometry on the time of exposure to the chemical solution, to be compensated for in the design of the path followed by the fs-laser beam.

Filling of the cavities with the metal, steps 3 to 5 (Figure 3-1), is performed by applying on the liquid metal external pressure sufficient to overcome capillary forces at play and force the metal to flow into the mold. This is achieved using pressurized gas. In experiments reported here, the metal to be infiltrated is placed on top of the substrate, over all exposed cavities. The chamber is evacuated, then kept under a low vacuum and heated up to slightly above the melting point ($T_m$) of the metal to be cast. Once it is molten, the metal covers and seals all mold entries along the upper mold surface. At this point, a non-reactive gas, typically argon, is bled into the chamber. As the gas pressure builds up, the pressure it exerts on the metal eventually drives the latter to flow into the (evacuated) cavities of the mold, filling them. Once the mold is full, mold and metal are cooled to solidify the metal. In doing this, particular consideration must be given to feed metal solidification shrinkage, a classical challenge in casting also present at the microscale. To this end, directional metal cooling is used; this is done by placing a chill in contact with the apparatus along the substrate side opposite to the metal drop. One must also avoid the formation of cracks that may appear in the brittle glass substrate under the action of thermal stresses associated with the difference in coefficients of thermal expansion (CTE) between metal (typically ~10-20 μm $m^{-1}K^{-1}$) and substrate (~0.5 μm $m^{-1}K^{-1}$). Such cracks were observed in some of our experiments through standard and cross-polarized optical microscopy; they are avoided by means of slow cooling after infiltration.

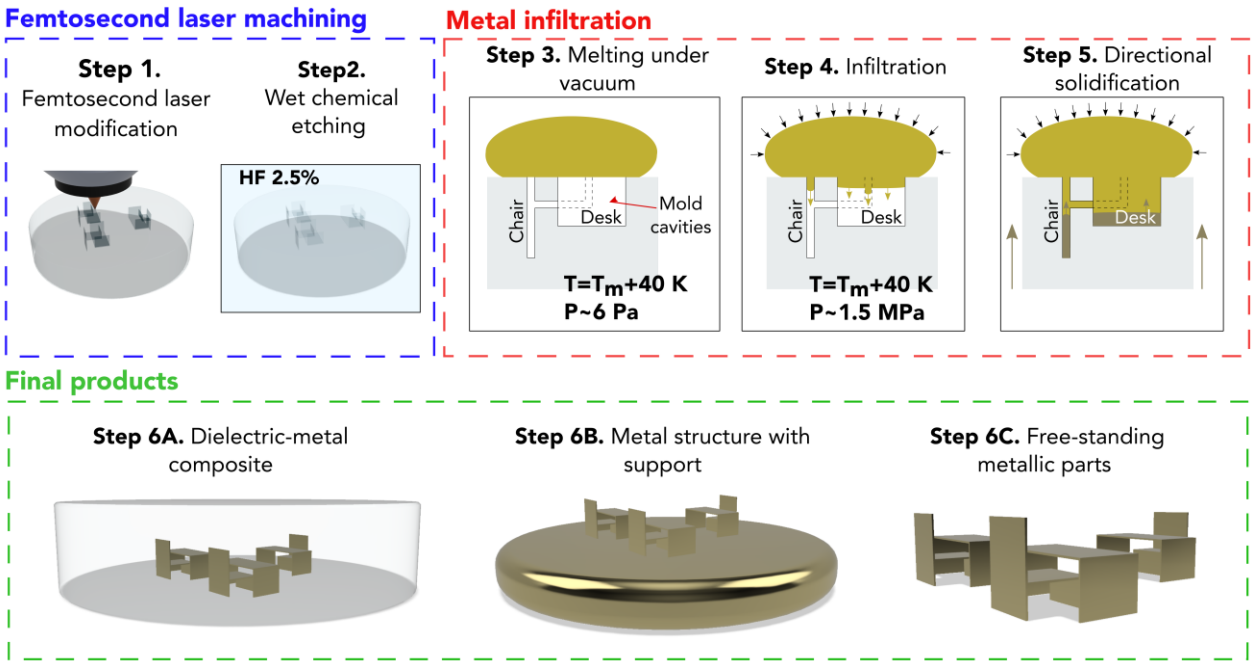


**Figure 3-1** Schematic of the microcasting process. The process comprises two main sequences, one being fs-laser 3D micromachining, and the second being metal pressure infiltration. Step 1 – a pattern defining the 3D structure is inscribed within a fused quartz substrate using a fs-laser. Step 2 - the substrate undergoes wet chemical etching to dissolve interconnected laser-patterned regions that intersect the substrate surface, thus turning the fused quartz substrate into a mold to be filled with metal. Step 3 - the fused quartz mold is positioned in the infiltration chamber, together with a metal load placed over the exposed cavities; the chamber is evacuated and the temperature is raised to melt the metal. Step 4 - pressurized inert gas pushes the metal against capillary forces, driving it to fill the pre-evacuated hollows. Step 5 - while maintaining the pressure, the chamber is put in contact with a chill to promote directional solidification. Step 6 - different final microscopic products can be obtained by varying final steps in the process.

After solidification (Figure 3-1 step 6), a substrate-metal composite is produced. The excess metal can be removed to obtain a microscopic fused quartz/metal composite structure that can, in itself, be of interest in

microengineering device fabrication (Figure 3-1 step 6A). Alternatively, to produce a loose metal casting, the glass mold is dissolved in an etchant to which the metal is inert (for example, an aqueous HF solution when casting silver). Demolding -in the terminology of casting- can either produce miniature structures that are linked to a bulk metal base (Figure 3-1 step 6B), or if Steps 6A and 6B are combined, it will yield many separate miniature metal castings (Figure 3-1 step 6C).

### 3.1.1 Experimental implementation of the process

The glass molds were fabricated at the Galatea Laboratory by Dr. Enrico Casamenti and Mr. Sacha Pollonghini using fs-laser micromachining followed by wet chemical etching according to a process described in the literature [235]. An ytterbium-fiber amplifier laser (Yuzu, manufactured by Amplitude, Bordeaux, France) emitting 270 fs pulses at a wavelength of 1030 nm at a repetition rate of 800 kHz, with an energy of 240 nJ (average power after the objective of about 190 mW) was used. The laser is focused in the specimen using a 0.4-numerical aperture objective to a measured waist of 1.9 μm at the focal point. The substrate used is a UV-grade fused quartz plate (Heraeus HOQ 310), 800 μm-thick, and 25 mm-square. The substrate is moved with linear stages (Micos - UPS 150). Following laser exposure, the specimen is etched for several hours in a 2.5 % HF acid bath at room temperature. In order to fit the dimensional requirements of the chamber used for metal infiltration, the substrates are cut into circular disks of 6 mm diameter to produce the molds into which the desired shapes to be injected are laser-patterned and subsequently etched.

The setup used for pressure infiltration consists of a refractory stainless steel (UNS S31400) chamber in which an alumina crucible prevents contact of the steel chamber with a graphite crucible that contains both the mold and the metal (Figure 3-2). Once mold and metal are placed within the graphite crucible, the infiltration chamber is bolted shut at its top. The top of the chamber contains a carbon foil to seal the closure and is connected to a vacuum pump and an argon bottle through a pipe, in which a K-type thermocouple is also introduced in order to monitor the temperature during infiltration by placing the thermocouple tip 1 mm above the melt. The chamber is evacuated (usually to ~0.06 mbar) and positioned within an induction coil using an overhead crane. A GMF12 CELES (Lautenbach-France) induction furnace is utilized to heat up the ensemble, to 1000 °C in the case of silver and 1100 °C for infiltration with copper or gold. Once the target temperature is reached, the chamber is pressurized with an inert gas (Argon N48, typically at ~1.5 MPa for structures of minimum feature size exceeding 1.5 μm, or 5 MPa otherwise). Subsequently, the chamber is lowered until its bottom is in contact with a water-refrigerated copper chill, maintaining the pressure and also with the induction furnace turned on, in order to create a vertical temperature gradient to promote directional solidification (Figure 3-2). Once the solidification temperature is reached on the thermocouple reading, the chamber is cooled further and then kept at ~ 600 °C during 1h in order to relieve internal stresses caused by differential shrinkage between the mold and the metal (Figure 3-2). Heating is then stopped and the substrate-metal component is retrieved once it has reached room temperature. To produce cast metal structures released from their mold, in a final step the fused quartz mold is dissolved in high concentration

HF during approximately 12 hours. Pure silver, gold or copper, all of 99.99 wt.% purity, were utilized as infiltrant metals as well as a silver-copper alloy (79Ag-21Cu (wt.%)).

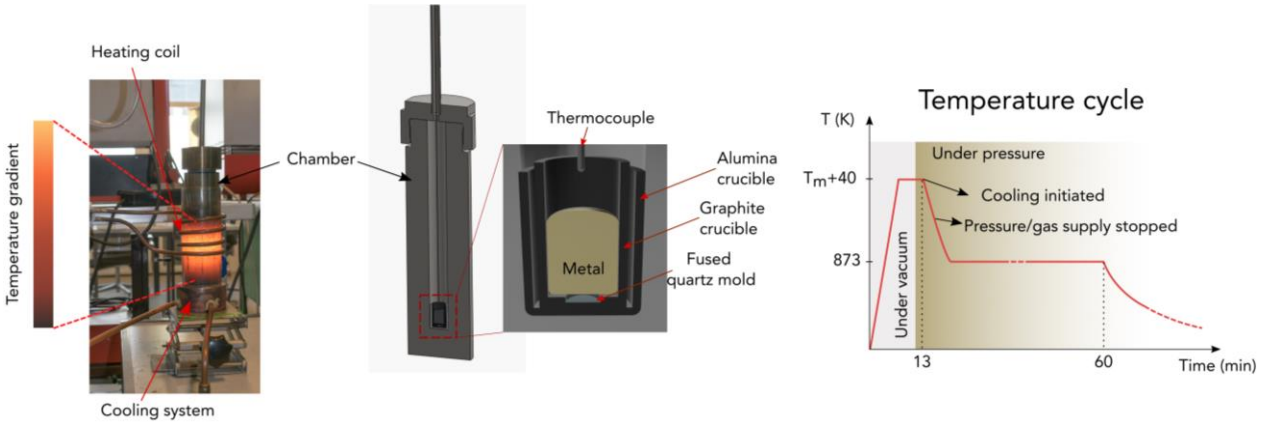


**Figure 3-2** Image of the experimental setup (left), schematic representation of the chamber (middle) and thermal cycle applied during infiltration (right).

## 3.2 Results

### 3.2.1 Fabrication of 3D metal microstructures

Figure 3-3 displays images of a micron-scale classroom composed of desks and chairs, all made of pure silver. This particular assembly demonstrates the ability of the present process to produce, at the microscale, complex 3D structures with a shape that is not amenable to metal micromachining. The cast structures have a thickness near 2 μm. The similarity of chair/table pairs shows the reproducibility of the technique, and its resolution is shown by the micron-scale surface roughness of the mold or casting. In this illustration, to allow for observation in the scanning electron microscope, the fused quartz substrate was dissolved after solidification; this left the final metal chair and table structures linked to the silver that remained above the substrate (as in Figure 3-1 step 6B). Figure 3-3c and 3-3d show a close inspection of one of the chairs in two different perspectives, to exhibit its thickness and contours. A rough and wavy finishing of the top edge is observed. This feature is associated with the progressing etching front after laser machining during mold preparation and is later on reproduced by the metal during infiltration and solidification. Specifically, such imperfections are found if the etching is interrupted before the entire laser-affected region is removed. It is in fact not seen on the other edges of the structures of Figure 3-3 (or in subsequent figures). On the other hand, the slight roughness on the lateral edges of the chair (in Figure 3-3d) derives from the laser machining trajectory followed during mold preparation; it can be avoided by optimizing both the laser trajectory and the deposited energy. As shown in Figure 3-3e, the metal grain size far exceeds that of casting features, such that chairs and tables are essentially all monocrystalline – this parallels what was found with cast aluminum microwires cast using molds of grown NaCl single crystal [81].

The process is also used to fabricate a set of suspended ('H-shape') beams made of pure gold, Figure 3-4. The suspended beams in Figure 3-4 have a 45 x 45 $\mu m^2$ square-cross section and a length of 900 μm, demonstrating an aspect ratio (AR) – cross-section over length - as high as 20. Furthermore, in this experiment the AR was not maximized: higher values are likely achievable. Indeed, fs-laser micromachining has demonstrated AR values that exceed 500 with only two entrance points for the etchant [240]; it has no theoretical aspect ratio limit if multiple entries can be included [235]. Close inspection of the mold surface along a longitudinal cut through an un-infiltrated mold along the length of the suspended-beams (Figure 3-4c) reveals features typical of fs-laser exposed silica glass etched with hydrofluoric acid [60]: note how those are later on reproduced by the gold (Figure 3-4b). This demonstrates that the pressure infiltration process used here can replicate shapes with a sub-μm-scale resolution, similar to what is obtained in polymer molding [241]. Even though the overall surfaces of the suspended beams are easily correlated to features on the mold, some peculiarities can be distinguished in some structures (red delimited areas in Figure 3-4d). These depressions are particularly smooth and they interrupt surface patterns present on the fused quartz surface; hence, they may have been produced by metal solidification shrinkage or the presence of trapped gas.

Figure 3-4e shows a cross section through a similar structure made of pure silver, still embedded in fused quartz and exposed by conventional grinding and polishing of infiltrated beams. As seen, the metal is dense, or in other words exempt of pores. To check that there is no significant chemical interaction between the mold and the metal, composition gradients near the interface of the host substrate/metal were performed by Energy-dispersive X-ray spectroscopy (EDS) in the scanning electron microscope operated at 10 kV (Figure 3-4f). The X-ray intensity at the metal-silicon dioxide boundary was modeled with CASINO Monte Carlo software v2.5 (Sherbrooke, Canada) assuming a 10 kV electron beam, beam size 5 nm and 10000 electrons (Figure 3-4f). No new phase, and no traces of metal within the fused quartz host, were detected.

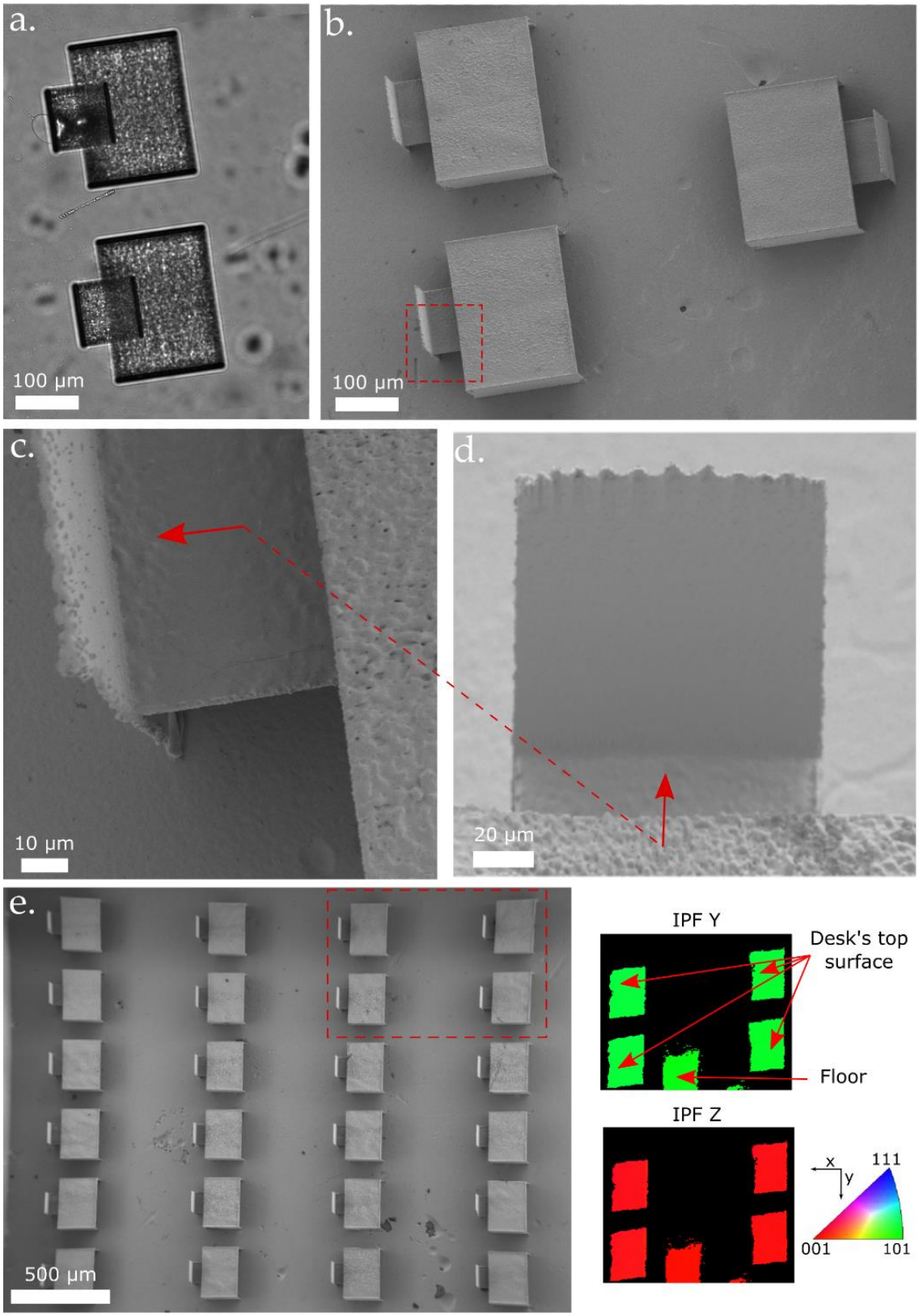


**Figure 3-3** Images of a cast silver miniature classroom. (a) reveals the fused quartz substrate (*i.e.*, the mold) after etching and before metal infiltration (Step 2 in Figure 3-1). In (b) the metal structure is shown after dissolution of the mold (Step 6B in Figure 3-1). (c) and (d) details at higher magnification the area delimited by the dashed rectangle in (b), the arrow indicates the orientation of (d) with respect to (c). (e) An array of 6x4 "chairs" and "desks" and inverse pole figures (IPF) of the four "desks" contained in the red dashed rectangle, evidencing that these, as well as the "floor" (*i.e.*, the support), are single-crystalline metal structures. (a) Optical microscopy taken through fused quartz, (b), (c), (d) and (e) scanning electron microscopy (SEM) and (e) electron backscatter diffraction (EBSD).

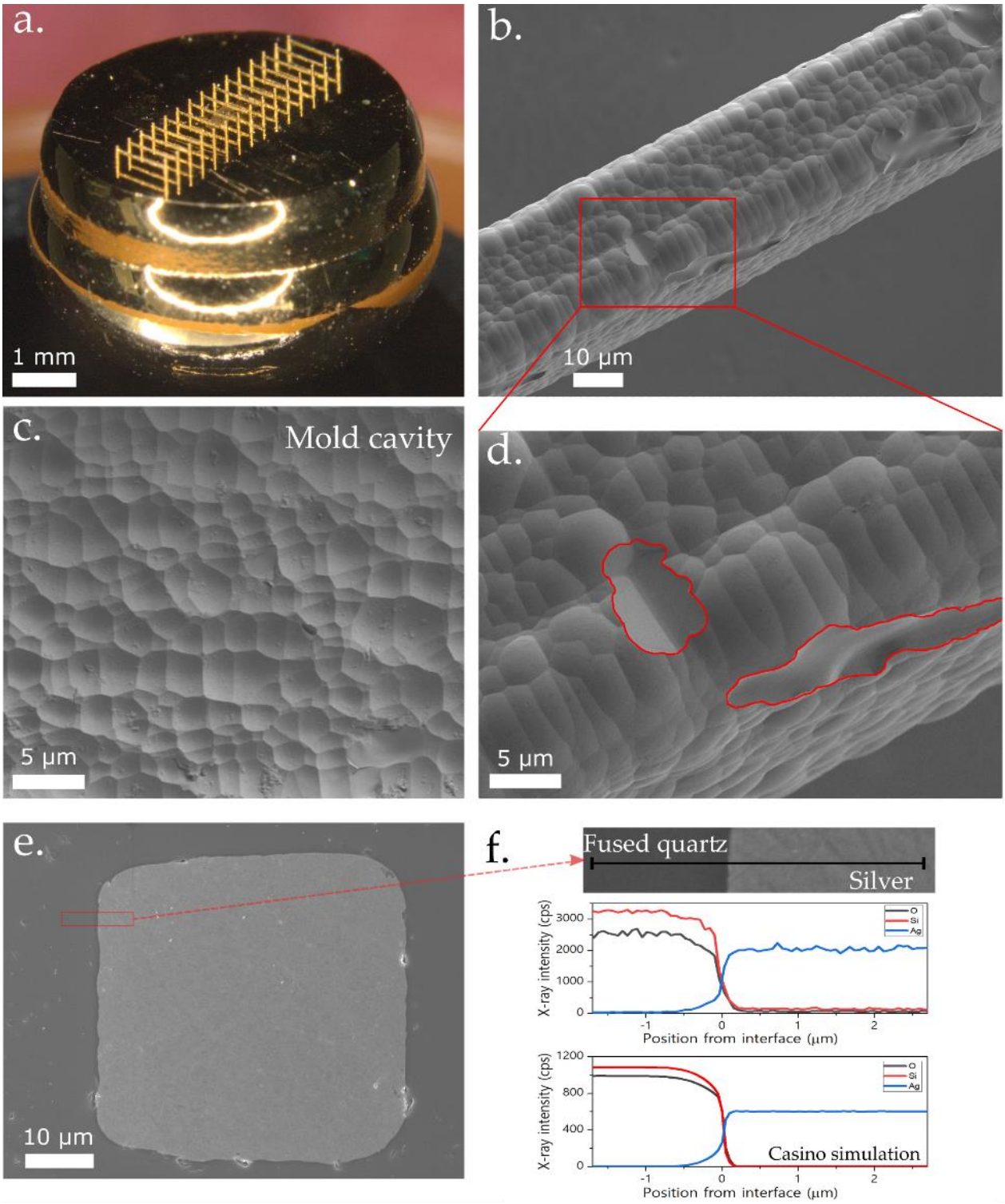


Figure 3-4 Images of suspended beams made of gold and left connected to the bulk metal. (a) overall view of the piece after dissolution of the fused quartz mold. (b) SEM close-up image of a single suspended beam showing features typical of a silica glass etched with hydrofluoric acid. (c) SEM images of the internal surface of an etched, un-infiltrated mold cavity. In (d) a portion of the beam in (b) is shown to highlight likely surface casting defects in red. (e) SEM image of a cross section of a similar silver structure while it was still embedded in the fused quartz mold, showing that the beams are made of pore-free, dense metal. (f) Chemical composition analysis normal to the silver/silicon dioxide interface of the sample shown together with a CASINO Monte Carlo simulation of X-ray intensity from a sharp SiO2/Ag boundary.

Local properties of the metal were measured by nanoindentation. A TI 950 Triboindenter (Hysitron® Corporation, Minneapolis, MN) with a load cell of 10000 μN and a diamond Berkovich indenter tip was used to measure both the hardness and elastic modulus of the cast from cross-sections of trusses still embedded in the fused quartz substrate (similar to what is seen in Figure 3-4e). Quasi-static indentations were made to a maximum load of 8000 μN for silver and to 3000 μN for copper, the loads being selected in correlation with the trusses' cross-sections (150x150 μm for Ag silver and 25x25 μm for copper) to minimize the elastic influence of the substrate and to be able to indent 4 times on each specimen. The loading-holding-unloading sequence was of 5-2-5 seconds and the data were analyzed according to the Oliver-Pharr procedure [158]. Table 3-1 shows values of Young's modulus for pure silver and copper. Data yield a Young's modulus of 84 ± 1.2 GPa for silver, and 132 ± 6 GPa for copper. These values are to be compared with 83 GPa and 128 GPa for bulk silver and copper respectively [242,243], in accord with the observation that the microcast metal is fully dense. This shows that the process produces metallurgically sound metal, the flow stress of which can be tailored by alloying.

**Table 3-1** Measured elastic modulus (E) for silver and copper trusses produced by microcasting. STD describes the standard deviation measured on each sample, and orientation refers to the crystallographic orientation along which the sample was indented.

| Ag | | | Cu | | |
|---|---|---|---|---|---|
| Orientation | E measured [GPa] | STD | <Orientation> | E [GPa] | STD |
| 1< 112> | 82.4 | 0.8 | 1< 304> | 135 | 3.0 |
| 2< 213> | 84.0 | 0.5 | 2< 101> | 137 | 2.5 |
| 3< 213> | 84.3 | 0.4 | 3< 113> | 122 | 2.6 |
| 4< 213> | 86.0 | 0.8 | 4< 113> | 132 | 6.1 |
| 5< 213> | 84.5 | 0.8 | 5< 304> | 134 | 3.6 |
| 6< 212> | 83.4 | 0.9 | | | |
| **Mean** | **(Ag) 84** | | | **(Cu) 132** | |
| STD | 1.2 | | | 6 | |

## 3.2.2 Fabrication of embedded microstructures

Figure 3-5a exhibits an array of silver pyramids embedded in the fused quartz mold, each ending in a much thinner filament, 30 μm-long and ~2 μm in diameter. The remaining silver after solidification was removed by mechanical grinding in order to obtain, as in Figure 3-1 step 6A, a final product consisting of the 6 mm-diameter, 800 μm-thick, fused quartz substrate containing an array of embedded silver pyramids each topped by this thin, antenna-like, coaxial filament. This demonstrates that the combination of laser-patterning and infiltration characteristic of the process provides a pathway for the production of multiscale 3D structures that would be difficult if not impossible to achieve by other means. As another prototype giving an example of the innovation potential of the technology, Figure 3-5b-d show a 3D-array of high-aspect ratio multiscale silver-copper alloy micro-electrodes that are left embedded in the fused quartz mold (visualized here by observation through the glass). The minimum distance between electrodes is about 6 μm and the total structure length is 5 mm (leading to an aspect ratio of the glass slit between electrodes that exceeds 800).

Being able to produce such arbitrarily shaped 3D highly conductive electrodes embedded in a high dielectric constant material host is interesting in numerous fields of microtechnology: *e.g.*, implantable devices in medicine, or components for high-voltage, high-frequency electronics.

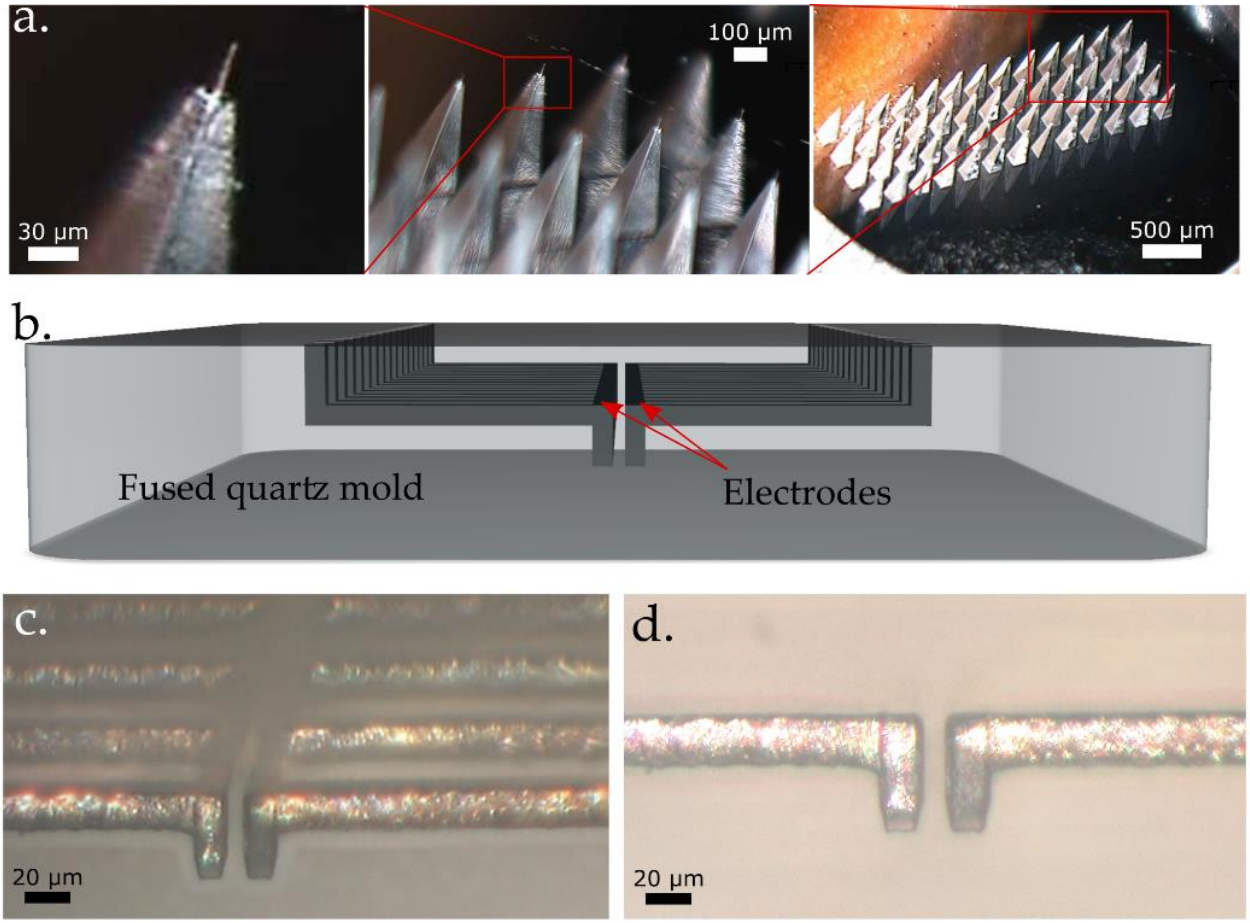


**Figure 3-5** (a) Optical micrograph of a silver pyramid array embedded in fused quartz, each pyramid ending with a thin antenna-like filament extending from its tip, illustrating the multiscale and multi-material capability of the process. (b), (c) and (d) are images of a row of electrode pairs embedded in fused quartz. (b) CAD model of the design (for the sake of clarity, the drawing is out of scale). (c) and (d) are optical micrographs of the resulting structures of 79wt%Ag-21wt%Cu alloy embedded in fused quartz.

Figure 3-6 shows a larger, geometrically complex, 3D (Maltese cross) structure fabricated out of copper or silver. Figure 3-6a-c show the structure still embedded within fused quartz, whilst Figure 3-6d shows the self-standing structure (here made of silver) extracted out of its mold. The beams composing the truss structure have a diameter around 50 µm, while the entire Maltese cross fits within an area of two-by-two millimeters. In this larger casting, there was a higher probability for solidification to nucleate and propagate from different locations of the mold, leading to a polycrystalline structure. Grain boundaries are indeed revealed by the trough that capillary forces have created along the beams composing the structure (Figure 3-6d). This is confirmed by EBSD, which shows the presence of three crystals in the imaged structure, grain boundaries of which are consistent with the location of grain boundary grooves visible in the SEM micrograph. Figure 3-6c shows a larger version (~4 x 4 mm) of the same design, this time infiltrated with pure copper and left embedded in fused quartz.

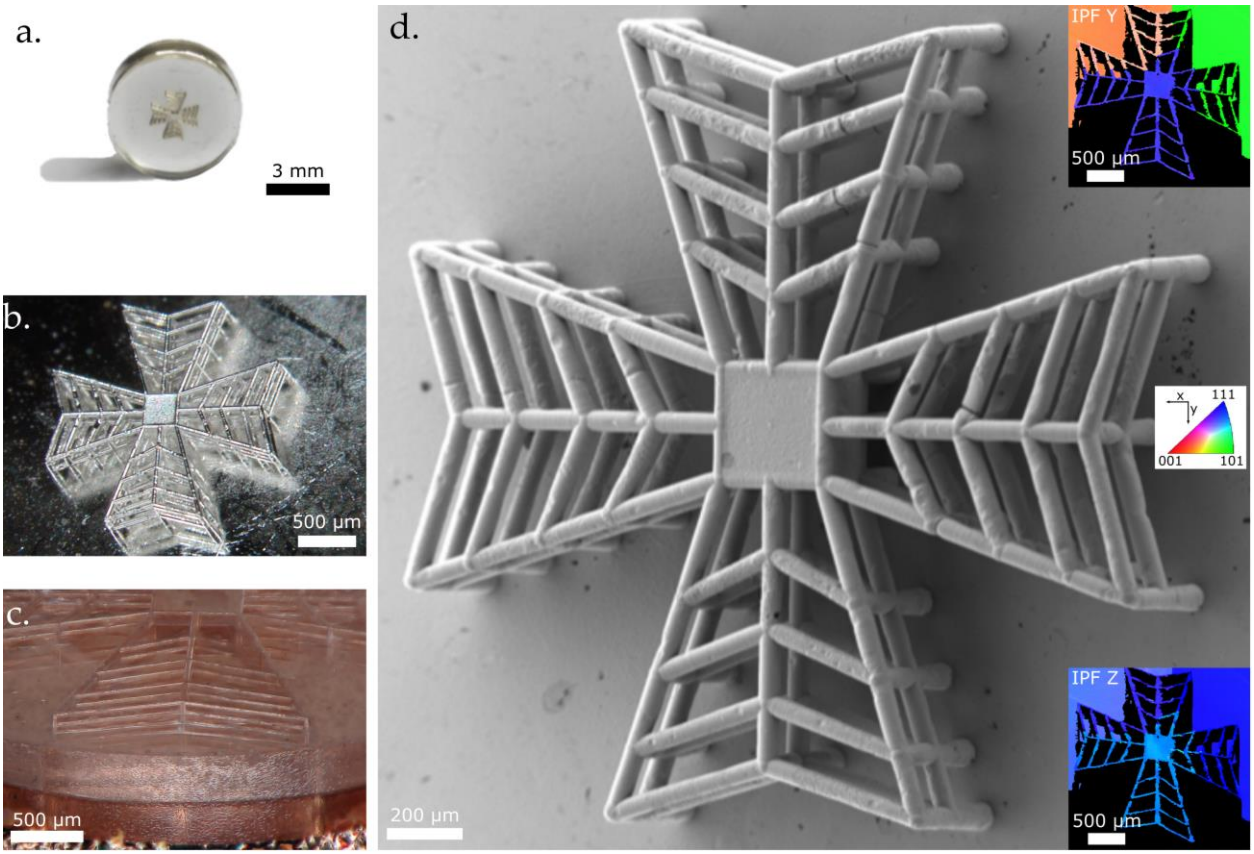


**Figure 3-6** Complex (Maltese cross) 3D structure produced in pure silver and pure copper. a-b) optical images of a silver cross embedded within its fused quartz mold (a) and after demolding (b). (c) Macroscopic image of a larger version of the same design produced in copper, also still contained within its fused quartz mold. (d) SEM image of the silver cross in (a) and (b) after mold removal. The related IPF images show the presence of 3 distinct grains, whose boundaries are made visible in the SEM image by the typical groove they have created along the casting surface.

### 3.2.3 Eliminating surface defects due to solidification shrinkage

As aforementioned, castings usually present surface defects, characterized by surface depressions, generally smooth and with a random shape, which are likely associated with solidification shrinkage. Feeding solidification shrinkage has been the main challenge encountered in processing, and different trials have been conducted with the purpose of addressing this issue. One of the methods pursued, which is classically used in casting, is to impose a finite temperature gradient across the thickness of the mold, to accomplish directional solidification and, with a proper orientation of the structure, to continuously maintain, above the area that is solidifying, a reservoir of liquid that feeds the change in volume at the solidification front. Another approach is to develop metal alloys with nearly zero-shrinkage upon solidification.

#### 3.2.3.1 Trials to impose larger thermal gradients

A heat transfer model, conducted by Ms. Alejandra Slagter, of the hardware displayed in Figure 3-7a and used to fabricate structures shown in Figures 3-3 to 3-6 exhibits a shallow temperature gradient at the silver solidification temperature ($\Delta T < 30$ °C across the mold) (Figure 3-7b). The model assumes thermal conductance of interfaces similar to an air gap of 10 µm, the bottom of the chamber at 80 °C and the middle part, region heated by the induction coil, initially at 1100 °C (Figure 3-7b).

A new version of the infiltration chamber that aims to achieve higher temperature gradients was conceived (chamber v2-Figure 3-7c). This new chamber contains an actuator that enables a direct contact between a cold copper chill and the alumina crucible containing the mold right after infiltration (see schematic illustration of Figure 3-7c). A heat transfer model of this chamber design displays a three times higher temperature gradient across the mold ($\Delta T \approx 100$ °C) when the solidification temperature of silver is reached (Figure 3-7d). Yet, defects due to solidification shrinkage persisted, even though this new setup showed an effect of accelerated cooling, in that compared to the earlier set-up it leads to an increased number of nucleation points along the mold, given the presence of more grains at the base of the bulk metal.

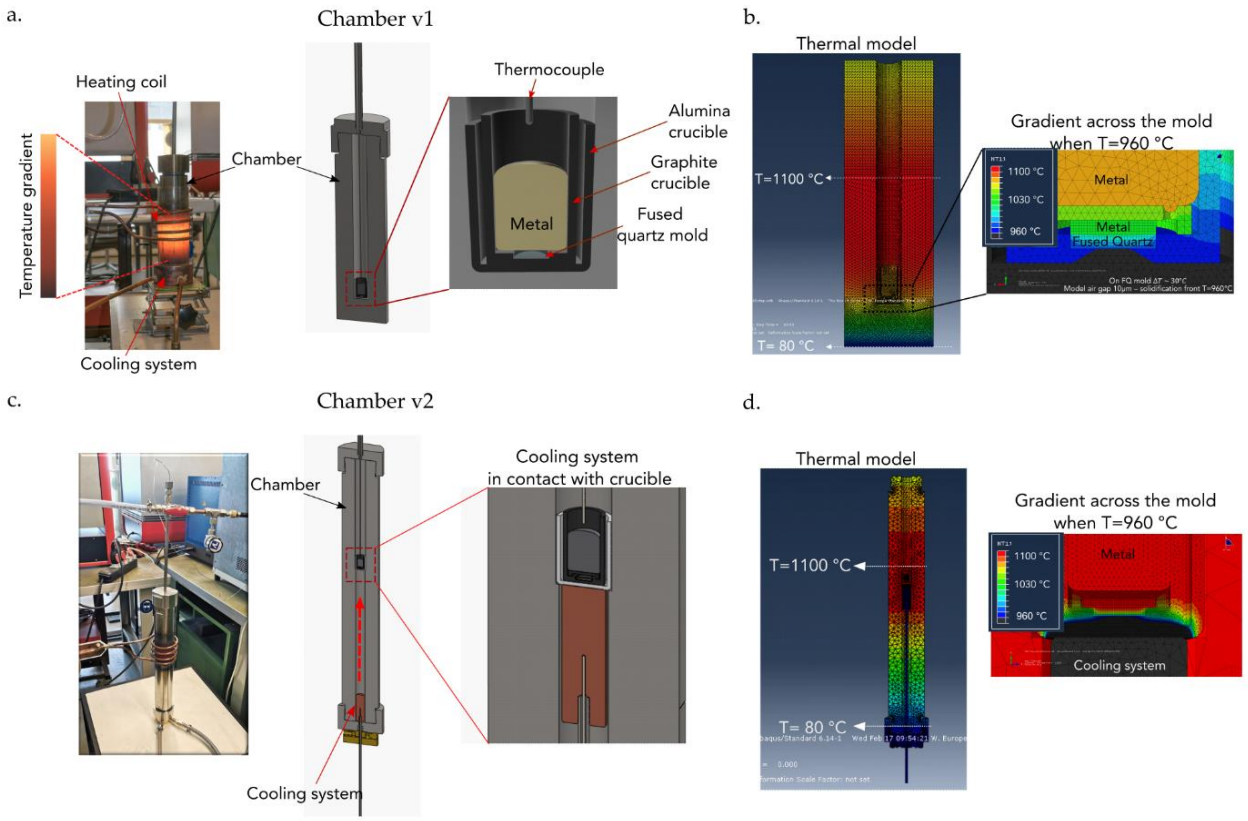


**Figure 3-7** Images of the experimental setup (chamber v1 and v2) together with thermal models, a-b) First version of the chamber, which is lowered on top of a cooling system after infiltration, the transient thermal model shows a shallow thermal gradient. c-d) Second version of the infiltration chamber in which a cold copper chill is directly put in contact with the crucible right after infiltration, the thermal model shows a higher temperature gradient.

Since monocrystalline salt molds open on both ends were found in earlier work on microcasting to produce defect-free aluminum wires, these casting conditions were replicated in the current setup. Hollow holes traversing the complete thickness of the fused quartz were produced by femtosecond laser micromaching and a new setup was developed to be able to seal such cavities and avoid flotation of the mold. Despite successful filling of open cavities, defects likely associated with solidification shrinkage continue to be present.

### 3.2.3.2 Development of nearly zero-shrinkage alloys

The volume change during solidification ($V_{sol}$-$V_{liq}$) for most pure metals is negative and usually on the order of -3 to -10 %; however, there are elements that exhibit expansion upon solidification, namely silicon,

germanium, gallium, bismuth and antimuonium [244–246]. Adding alloying elements that expand upon solidification may counterbalance the shrinkage of the matrix and thus lead to the design of alloys that exhibit no change of volume during solidification. This would be of great advantage, since a full reproduction of the mold cavities could be achieved with no major challenges in the mold design. This has been a topic of research and interest for many years [245,247–249]. For instance, a commercial lead-bismuth eutectic alloy (known as LBE) is generally used for soldering. Here, systems based on precious metals (Au or Ag) with additions of germanium are investigated due to their potential applications in the present microcasting process. Refs. [249,250] have served as points of departure of the present work.

A thermomechanical analyzer (TMA) is used in order to evaluate the alloy expansion-shrinkage upon solidification. Although this technique is generally employed to study the coefficient of thermal expansion, it has been adapted for this purpose by Dr. Ludger Weber in [249] in our laboratory. The setup consists in a hollow graphite cylinder, in which the metal sample is placed. Two graphite rods, each from one side of the cylinder, are in contact with the sample. The change in position $\Delta L$ of these rods is constantly measured and computed by the system as a function of temperature. Thus, by indicating the initial length $L_0$ it is possible to obtain curves of $\Delta L/L_0$ versus temperature.

The gold-germanium system fulfills all the requirements for being cast by microcasting due to the low melting temperature, negligible etching in high concentration HF (for both elements), and the absence of interaction with fused quartz of alloys in this binary system. The gold-germanium eutectic alloy (Au-12.5 wt.%Ge) exhibits a linear expansion of about 1.2-1.4 % upon solidification at around 360 °C (Figure 3-8a). Silver can be added to the alloy since it is able to dissolve a certain amount of germanium and to reduce the overall expansion, without a significative increase in the melting temperature. Two eutectic alloys were prepared; their compositions are, in weight percent (wt.%), 81.2Au-10.5Ge-8.3Ag (green) and 67.7Au-10Ge-22.3Ag (orange). Upon solidification, the alloy represented in green in the ternary diagram, exhibits a linear expansion in the range of 0.5 to 0.6 %, while that in orange exhibits a volume change in the range of -0.1 to 0.02 %. The latter then is an alloy with a nearly zero-shrinkage upon solidification, and his hence of interest. Note that alloys that expand upon solidification will also suppress shrinkage defects; however, the expansion may develop cracks in the fused quartz mold, which raises a problem when the substrate is to be kept.

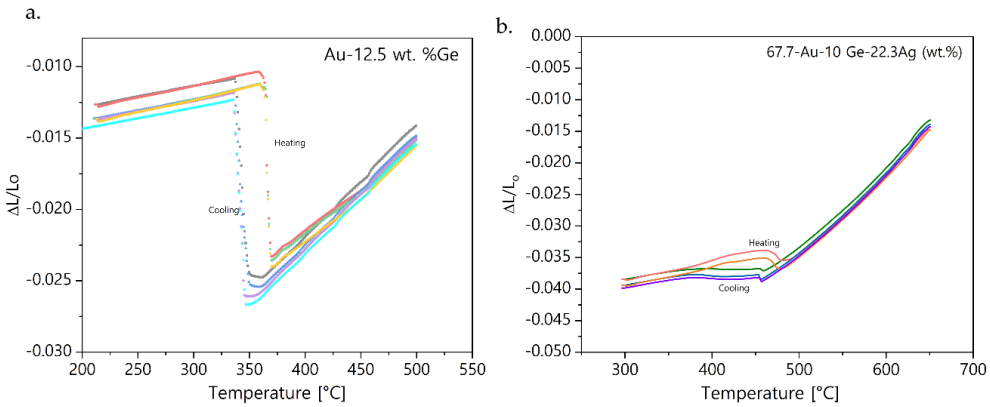


**Figure 3-8** a) Linear expansion exhibited upon solidification by the Au-Ge eutectic composition. b) A nearly-zero shrinkage/expansion exhibited upon solidification by the alloy 67.7 Au-10 Ge-22.3 Ag (wt.%).

Figure 3-9 displays 'H-shape' beams cast in different metals and alloys. Images on the left exhibit castings still embedded within the fused quartz mold, meaning right after solidification. It is clear that, for the case of pure metals (Figure 3-9a-b), surface defects are already present before mold dissolution. These depressions remain the same after dissolving the substrate in HF, as shown by SEM images on the right (Figure 3-9a-b). Note that beams on the left do not necessarily match the area imaged on the right. Beams made of gold-germanium or gold-silver-germanium alloys, with an expansion or nearly-zero shrinkage after solidification present smooth and defect-free surfaces, both before and after mold dissolution. These observations provide confirmation that such defects arise from unsuccessful metal feeding and eliminates any potential local effect of the HF etchant in the case of pure silver and gold. Figure 3-9c-d also depict the microstructure of the Au-Ge and Au-Ag-Ge alloys, with large germanium phases (dark regions) surrounded by a gold or gold-silver enriched matrix.

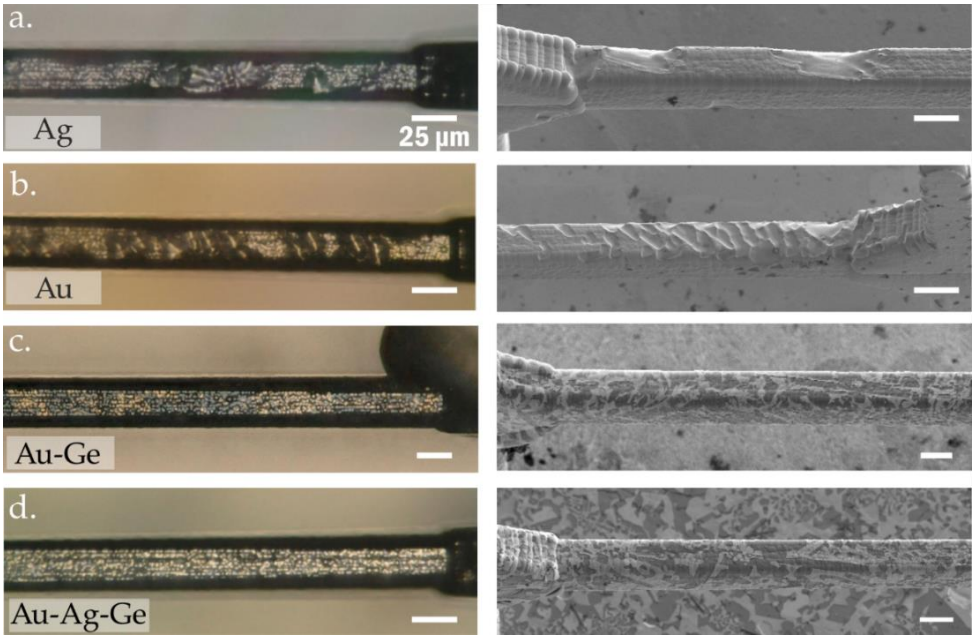


**Figure 3-9** H-shape beams, similar to those shown in Figure 3-4 still embedded within the fused quartz substrate and imaged by optical microscopy (left) and SEM images after mold dissolution in high-concentration HF (right). Structures made of pure silver (a), pure gold (b), Au-13 wt.% Ge (c) and 67.7Au-23.3Ag-10Ge (wt.%). Trusses made of silver and gold present surface defects, which are not evidenced in the case of the alloys due to expansion or nearly-zero shrinkage upon solidification. Note that beams on the left do not necessarily match the area imaged on the right. Scale bar=25 µm.

Large fused quartz substrates with multiscale features and overall dimensions in the millimeter range were femtosecond-laser machined by FEMTOprint® (Muzzano, Switzerland) and Femtika (Vilnius, Lithuania), two companies specialized in glass microfabrication using femtosecond lasers (Figure 3-10). Those are then cast using a 67.7Au-10Ge-22.3Ag (wt.%) alloy. The structures have a thickness near 0.7 mm. In this case, the excess of metal after infiltration is removed by conventional cutting and grinding, and the substrate is subsequently dissolved to obtain freestanding microstructures (similar to what is schematically shown in Figure 3-1 step 6C). Figure 3-10c-d display defect-free castings in the millimeter scale, while still reproducing accurately micrometric details present in the mold, namely the feeding channels and surface roughness. Thus, these structures demonstrate a good example of the versatility and potential of the process, which can reach multiple scales maintaining its resolution.

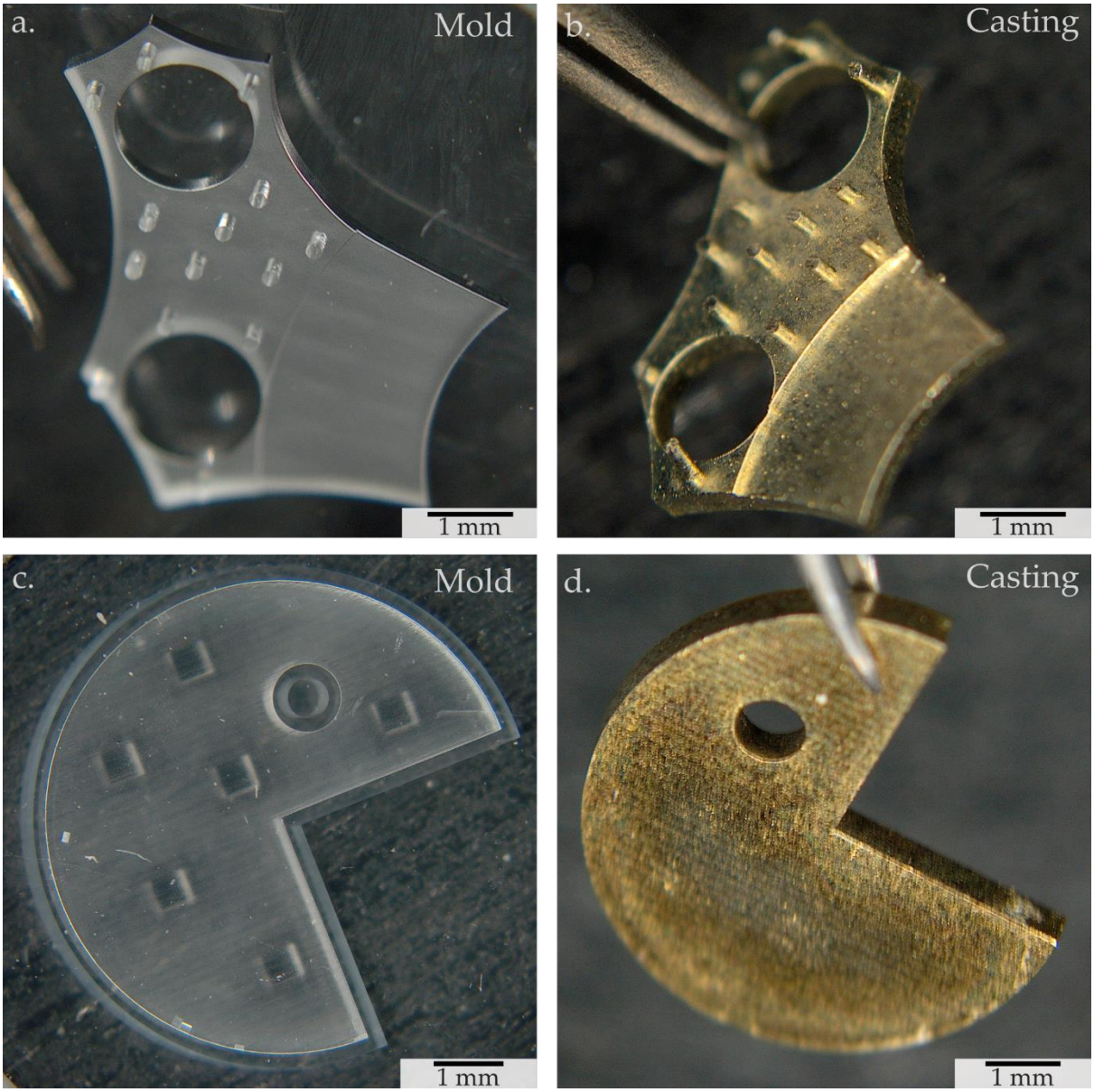


**Figure 3-10** Optical images of millimeter structures. Femtosecond-laser micromanufactured molds (left) and the resulting castings (right) made of and alloy 67.7Au-10Ge-22.3Ag (wt.%).

### 3.2.4 Glass-in-glass composites

*The same casting process can be used for infiltrating other type of material than a metal into glass. Although it is not directly connected to the scope of this thesis, the infiltration of glass-in-glass illustrates the versatility of the process and its applicability beyond metals.*

Chalcogenide glass has attracted much attention in the last few decades because of their exceptionally wide optical transmission window in the infrared and their high nonlinear refractive index [251]. Unfortunately, due to their poor mechanical properties, and weak chemical and environmental stability [252,253], three-dimensional structuring, integration, and packaging of those glasses remain challenging tasks. Current pathways to chalcogenide glass fabrication include the production of optical fibers and deposition processes. Photonic crystal fibers (PCFs) combining chalcogenide or tellurite glass into silica were produced by a pressure-infiltration technique, exploring both the process and optical properties of the resulting structures [254,255]. By this route, PCFs several centimeters long and containing chalcogenide rods down to sub-micron diameter were manufactured [254–257]. Deposition processes such as chemical vapor deposition [258], physical vapor deposition followed by glass melting over etched silicon [259], sputtering [260], and pulsed laser deposition [261] are employed in applications for optical circuits, which require planar waveguides and components. Chalcogenide glass components such as lenses are currently fabricated by glass molding [262] and high-precision diamond-turning [263], restricting shapes to specific 3D geometries [264]. Recently, attempt to 3D print chalcogenide glass using the fused-deposition technique applied to fiber preforms in $As_2S_3$ (one of the commercially available chalcogenides) has been reported [265–267].

The freeform microcasting process previously introduced also enables the fabrication of arbitrary three-dimensional glass-in-glass elements while maintaining micrometric resolution and sub-micron roughness. The two constitutive materials, fused silica and chalcogenide, offer a high index contrast combination, in geometries and size scales suited for geometrically complex 3D mid-infrared optics based on total internal reflection optical design principles. Figure 3-11 displays optical images of structures produced after pressure-assisted infiltration of $As_2S_3$ chalcogenide glass into a fused silica micro-mold fabricated by femtosecond laser machining followed by chemical etching. The substrate used is UV-grade fused silica (Corning 7980 0F). Following laser exposure, the specimen is etched in a 5 wt.% NaOH bath for several hours [268]. Then the micro-mold is positioned in a glass crucible with the chalcogenide glass $As_2S_3$ (IRG27, from Schott) to be infiltrated resting on top. The crucible-glass combination is placed in a pressure infiltration furnace, and then brought to low vacuum (~ 0.02 mbar) while the temperature is raised to 600 °C (well above the transition temperature of IRG27 at 200 °C), according to values previously reported [255]. *Note that, given that the chalcogenide glass $As_2S_3$ contains arsenic, the infiltration is a delicate process. It is important to prevent at this stage of the process any contamination of the furnace by arsenic that may have evaporated while the glass is molten.* It is therefore advised to surround the molten glass with an inner enclosure within the pressure infiltration furnace, so as to prevent any transfer of arsenic to the furnace. Then, to force the glass into the

mold, a pressure of 10 MPa is applied hydrostatically with Argon gas leaked into the chamber, causing the molten chalcogenide glass to infiltrate the cavities underneath. Finally, the sample is cooled down while maintaining the pressure. Figure 3-11a shows a set of pillars with dimensions ranging from 30 to 150 μm laterally and from 400 to 500 μm in height. The "EPFL" letters in Figure 3-11b demonstrate the production of complex geometries out of chalcogenide glass at the microscale, while the long channels in Figure 3-11c show an aspect ratio (here defined as length over thickness) of around 80, thus demonstrating a structure that might be used as an infrared waveguide embedded in a fused silica substrate.

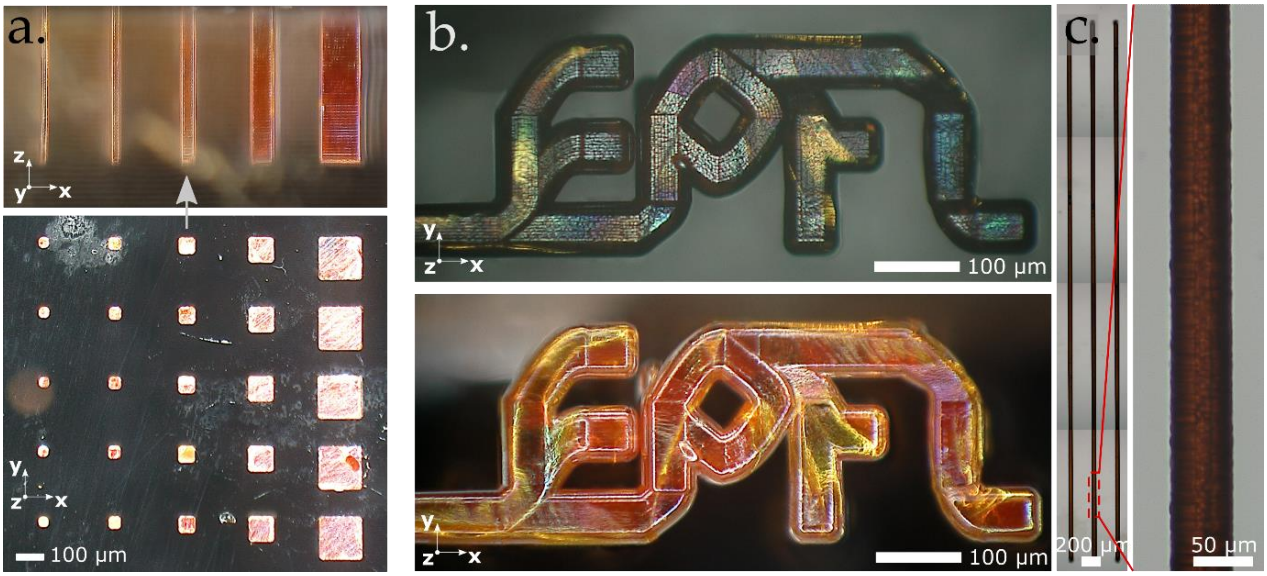


**Figure 3-11** Optical micrographs of different chalcogenide structures infiltrated into fused silica. (a) A set of pillars of different dimensions. (b) A complex 3D shape in dark and bright field illumination, and (c) overview (left) and magnification (right) of infiltrated channels 4 mm long and around 50 μm thick and wide (four micrographs are stitched together to form the figure).

Trapped gas bubbles found in earlier chalcogenide glass infiltrated PCFs [254–257] are not observed here. Yet, we note that structures infiltrated here are not as spectacularly long as those achieved in fiber infiltration and that the infiltration conditions are not the same. Namely, the mold is at constant temperature (*i.e.*, no thermal gradient is present as was the case with the long PCFs); also, the infiltration chamber is evacuated prior to melting and pressurization, so that there is no gas trapping in the present experiments. Cracks might on the other hand be present in the complex geometry samples of this work, given the changes in hue of the chalcogenide glass in Figure 3-11b. It should be mentioned that the darker lines visible in Figure 3-11a-b are typical surface texturing due to the laser machining followed by chemical etching of the glass mold and therefore likely not defects from the infiltration process. The roughness of the structures is defined by the femtosecond laser machining of the mold and depends chiefly on laser parameters and the writing strategy used. When those are optimized, an average roughness of about 100 nm can be achieved [268].

## 3.3 Discussion

Metallic structures produced in this work, of size ranging from a few tens of micrometer to a few millimeters and with features of size down to around 2 μm, are made out of engineering metals (silver, copper and gold and their alloys) that are among the best electrical conductors and the most corrosion resistant metals – features

of interest for microtechnology in general. It will easily be appreciated that producing those structures would at best be difficult using existing technology, with one exception, namely local freeform electrodeposition. Micromachining would not carve out the space between the tables and the chairs, or between them and the floor of the classroom of Figure 3-3. Layer deposition processes would not, unless the part was of dimensions far above the voxel size, produce in-plane beams of circular cross-section such as those in Figure 3-6. Processes that produce rapidly porous and/or binder-containing metal structures that require subsequent sintering and/or debinding would be unlikely to leave the thin table or chair structures unwarped after the required thermal cycle. The only process that we believe could rival or surpass what is presented here is local freeform electroplating, as this process also produces dense metal with nearly total shape flexibility (it might, however, be challenged by the sharp, 90° corner, overhangs present in structures of Figures 3-3, 3-4 or 3-6).

As with any process that aims at broad acceptance and potential industrialization, achievable production rates are important. In producing silica molds in larger quantities, the laser-exposure time is the main bottleneck. The time needed to produce the mold for samples presented here was, with laboratory tooling used in this study, on the order of a day for a part such as the Maltese cross in Figure 3-6. In our laboratory, etching represented most of this time. In a production environment, however, the etching process is low-cost and usually parallelized, such that it does not represent an intrinsic limitation on production rates. Casting, meaning pressure infiltration followed by metal solidification, is a relatively rapid process already capable of high production rates; it, too, can also be massively parallelized, since larger molds each containing many castings can be infiltrated, solidified and retrieved simultaneously. Femtosecond laser-exposure is therefore the rate-limiting step of the present process if production runs reach sufficiently high volumes.

The femtosecond laser-exposure process can be seen as moving an ellipsoid-shaped interaction zone (resulting from a non-linear laser-matter interaction) across the glass structure to be carved; in our set-up, motion is driven by linear-motor moving stages. The shape and size of the laser-affected zone within the glass depends critically on the focusing conditions, *i.e.*, the numerical aperture of the focusing objective as well as the laser wavelength and the pulse energy. With our apparatus, at the finest level of focusing, we can produce an ellipsoid of diameter ~ 2 μm on its short axes and length 8 μm on the long one. The velocity of the motorized stages is coupled to the laser pulse repetition rate to optimize the etching rate, as this depends strongly on the deposited energy (or dose, typically expressed in J $mm^{-2}$) [239]. Exposure parameters are set by several considerations. On one hand, thermal diffusion beyond the LAZ should be avoided; this limits the repetition rate to a maximum of about one MHz, which is the onset for thermal accumulation in fused silica [269]. An optimal deposited energy value of ~ 10 J $mm^{-2}$ (for HF 2.5 %vol. etching) is reported to achieve the highest etching contrast between laser affected zones and pristine material. Considering a repetition rate of 900 kHz, the maximum optimal writing speed is ~ 15 mm $s^{-1}$ [239]. This is a very high value, such that operationally it is inertia, and in turn the achievable acceleration of the motorized stages used here (maximum acceleration of ~ 50 mm $s^{-2}$) that will limit the maximum attainable speed for μm-scale patterns to values well below the

above limit. This adds a dependence of the maximum average glass pattern printing velocity on the intricacy of the pattern. For example, to pattern the structures in Figures 3-3 and 3-6, the average speeds of stages were ~ 1.0 and ~ 1.45 mm $s^{-1}$, respectively; however, these values are defined by technical limitations of the setup. Other commercial motorized stages can reach accelerations of around 10 m $s^{-2}$. This would result in average writing speeds of ~ 14.1 and ~ 20.1 mm $s^{-1}$ for the previous examples. We thus take a few tens of mm $s^{-1}$ as the upper limit of scanning speeds attainable with the present process.

Additional features of the process are also to be noted, on both fronts of limitations and potential. Pressure infiltration is, as expected, capable of intimately replicating nanometric features. The minimum channel size that can be infiltrated is ruled by the pressure required to overcome the molten metal surface tension that opposes its flow into tiny mold cavities. This is given by the Young-Laplace equation [73], according to which the capillary pressure differential roughly equals the metal surface tension divided by the channel width. Surface tensions of most metals are on the order of 1 J $m^{-2}$; hence, a pressure of 10 MPa, which is technically achievable, should drive metal into features as fine as 100 nm. This is in keeping with the observed fidelity with which the infiltrated metal reproduces the carved glass structure in samples of this work.

The present process is therefore chiefly limited in terms of resolution by the controllable size of the LAZ which, due to the non-linear nature of the process by which it is formed, can itself be significantly smaller than the optical waist at the focus of the laser beam (in our case ≈ 1.8 μm at a laser wavelength of 1030 nm) as illustrated elsewhere [270]. In its versions presented here, the minimum features size of the process is of about 2 μm; however, for these reasons, this may be reduced in future work. For example, an additional approach to reduce the laser beam waist further, and in turn, the size of the laser affected zone, is to use shorter wavelengths, for instance by frequency doubling or tripling common Ytterbium-based laser sources, reaching out to the UV exposure regime.

A limitation of the present process is that it is *a priori* not amenable to process alloys that contain elements, the oxide of which is more stable than silica (for example aluminum, titanium or magnesium) or to process metals with melting temperature higher than the mold annealing temperature, ~ 1200 °C for fused quartz. It also tends to produce large-grained structures, which has advantages (*e.g.*, high conductivity) and disadvantages (*e.g.*, absence of grain boundary hardening or the formation of visible grain boundary grooves along the metal surface; see Figure 3-6d). The process is also well suited for the production of multiscale structures (as in Figures 3-5 and 3-10) and it offers, when making multiscale structures, scope for efficiency gains in production if laser parameters are dynamically adjusted during printing. One could indeed dynamically alter lens parameters (for example by using a spatial light modulator) and beam energy, so as to vary both the laser spot shape and size while maintaining optimal exposure conditions. This possibility might largely increase the volumetric speed and so provide opportunities for the more rapid production of multiscale structures. For example, just by tuning the beam energy, the ellipsoidal LAZ can vary from ~ 1 to ~ 2.5 μm

and from ~ 8 to ~ 20 μm in short and long axis dimensions, respectively; this corresponds to an order of magnitude (dynamic) change in voxel volume [270].

Building on the extensive survey of metal freeform microfabrication that is given in Ref. [2], the production speed of the microcasting process presented here is compared, using figures for voxel size and estimated peak printing speed given above, with alternative 3D metal freeform manufacturing techniques in Figure 3-12. Specifically, in Figure 3-12a, the fabrication speed is normalized by the voxel size, which is in essentially all such processes assumed to be a cylinder with a diameter equal to the dimension read in the horizontal axis. Assuming a roughly equiaxed cylinder, one can obtain estimations of the volumetric production rate (for a more detailed description we refer to [2]). As seen, comparing feature sizes and production rates of the present process with current alternatives places it in the top right corner, showing that it stands out in terms of achievable production speeds. Such higher fabrication rates should enable the industrialization of the process and the large-scale production of 3D components. In parallel, Figure 3-12b displays a measure of the metal microstructural soundness, namely the ratio of measured to theoretical elastic modulus, for different techniques, using in this graph data and graph formats from Ref. [271], to which we have added data for our samples.

The pronounced porosity, and thus large spread in elastic properties, exhibited by most of the structures obtained by current micron-scale additive micromanufacturing processes other than local electroplating underlines a major advantage of the microcasting process, namely the metallurgical soundness of the structures that it produces. For example, the electrical or thermal conductivity in metal structures produced by the present process will be as high as in the same pristine bulk metal (or higher given the absence of grain boundaries), enabling micro-components and devices with optimal electrical or thermal performance. This is a feature that the present process only shares with electrodeposition, a process capable of finer resolution than the present process, albeit with far lower achievable production rates.

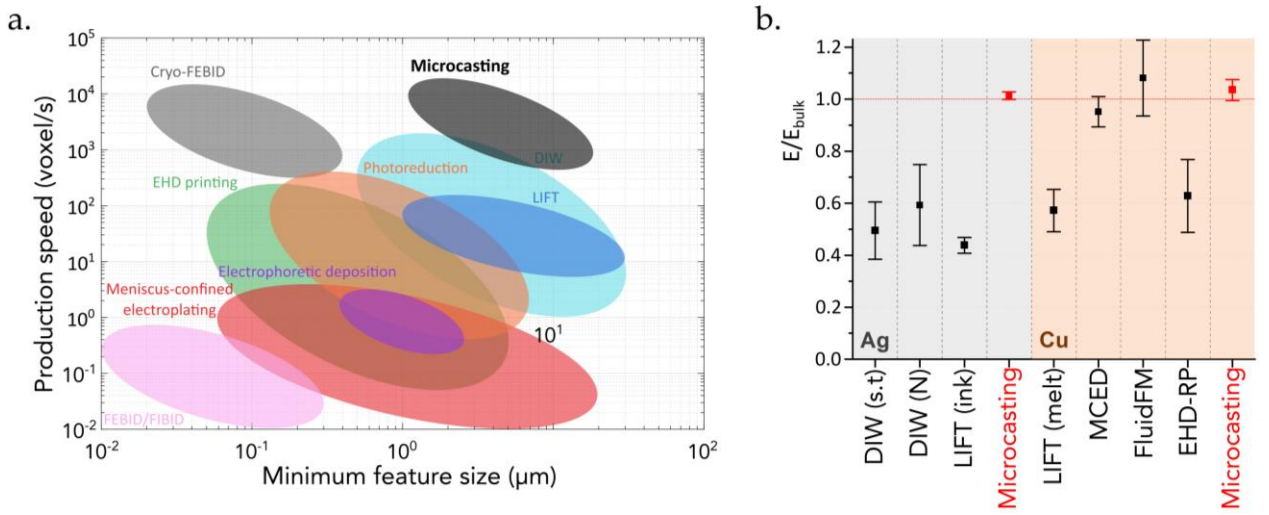


**Figure 3-12** (A) Qualitative comparison of achievable production speeds with alternative 3D freeform metal microfabrication processes (Redrawn from [2]): Direct Ink Writing (DIW), Electrohydrodynamic Printing (EHD printing), Laser-Assisted Electrophoretic Deposition, Laser-Induced Forward Transfer (LIFT), Meniscus-Confined Electroplating, Laser-Induced Photoreduction, Focused Electron/Ion Beam Induced Deposition (FEBID/FIBID), Cryo-FEBID. (B) Comparison of measured elastic modulus normalized by theoretical elastic modulus obtained by different techniques on silver and copper structures: DIW (shear thinning), DIW (Newtonian), LIFT (ink), LIFT (melt), Meniscus-confined electrodeposition (MCED), Confined electro-deposition in liquid (FluidFM), Electrohydrodynamic Redox Printing (EHD-RP). Error bars represent measured standard deviation. (Redrawn from [271]).

Moving forward, a few remaining challenges will have to be addressed for the present process to be improved or for it to enter commercial production. As seen, the pressure infiltrated metal reproduces with precision even minute details, below 100 nm in size, along the inner mold surface, see Figure 3-4; thus, improving the roughness of the molds is the next step in producing even smoother micro-cast products. A challenge, omnipresent in metal casting, is feeding solidification shrinkage of the metal. At the macro-scale there are well-known recipes to this end, directional solidification towards a riser being one of the main approaches. In present experiments, with the current setup and with the structures analyzed, the sole action of directional solidification was found not to be sufficient to move such defects out of the substrate. The development and use of nearly-zero shrinkage alloys was on the contrary found to enable the fabrication of defect-free structures in a wide range of scales. In addition, Figure 3-10, with substrates received from companies specialized in femtosecond laser machining, demonstrates that complex and millimeter-wide structures can be accomplished. This fills the gap in fabrication of components, since millimeter pieces cannot be produced by conventional casting and it would require long manufacturing times if any of the current microfabrication technique was to be employed. Finally, mastering the inner microstructural development of micron-scale cast metals and alloys is an area where much remains to be learned.

As shown in Figure 3-11, the process also enables the fabrication of three-dimensional chalcogenide structures in fused silica with micrometric precision. As a proof of concept, $As_2S_3$ is employed; microstructural examination confirms the consistency of material properties before and after the infiltration. The resulting silica-chalcogenide composites offer a high index contrast combination over a broad spectrum, with the silica mold acting as a mechanically and chemically resistant support and protection for the chalcogenide glass. This experimental result opens to innovative designs and further integration in the context of broadband photonics

by offering a means to produce sub-mm components such as 3D waveguides, tapered or not, lenses, etc. all embedded in a robust silica substrate, that itself may contain additional features such as fluidic channels [272–275] or mechanical elements [276,277]. Still, we have not explored how high the glass-forming ability needs to be for the resulting infiltrated glass to always be amorphous in structures such as those of this work. We thus believe that there is scope to transpose the same concept to other glass systems, both within and outside the chalcogenide family, provided similar limitations with respect to the ones impose when casting metals, namely lack of reactivity and working temperatures below the softening point of fused silica.

## 3.4 Conclusion

We have demonstrated that geometrically complex interconnected multiscale components up to a few millimeters in size and freely shaped to micrometric resolution can be made of fully dense metal or chalcogenide glass via a novel, freeform manufacturing process that combines fs-laser glass micromachining with pressure casting. The process is reproducible and suited for metals or ceramics that melt below roughly 1200°C and are inert in contact with silica; this includes silver, copper, gold and their alloys. We have also demonstrated that the process has the potential for higher large-scale production rates compared to existing technology for the freeform manufacturing of dense parts with micrometric precision. The resulting glass/metal or glass combinations enable new device architectures for applications in a wide range of areas in microtechnology. Alternatively, by mold dissolution, this process fills a gap in microfabrication because it gives the ability to turn, as is done at the macro-scale, to casting when monolithic metallic or glass parts of high geometrical complexity are to be produced.

# Chapter 4 Coupling Silicon Lithography with Metal Casting

In this chapter, a second novel manufacturing technique that produces micron-scale shaped structures made of silver or copper is introduced. The method is restricted to 2D or 2.5D part geometries, and combines silicon photolithographic etching with metal casting by pressure infiltration. We demonstrate the production of various structures including monocrystalline tensile specimens, of diameter selected in the range from 2.5 μm to 13 μm, whose mechanical properties are tested and discussed in following chapters.

Disclaimer: This chapter contains literal reproduction of full paragraphs and figures of the publication [278] *L. Borasi, S. Frasca, K. Nicolet-Dit-Felix, E. Charbon, A. Mortensen, Coupling silicon lithography with metal casting, Applied Materials Today. 29 (2022) 101647* to which the author has contributed. Specifically, the author contributed in the conception of the process, conducted the infiltration of the molds, and characterization of components after demolding. The micromanufacturing of the silicon wafer was performed by Dr. Simone Frasca at the EPFL Centre of MicroNanoTechnology (CMi-EPFL).

## 4.1 The process: combining silicon lithography with metal casting

Metal casting has the advantage of providing a dense component and affords considerable freedom in terms of both part geometry and alloy chemistry. There are challenges to be overcome if one is to scale metal casting down to micrometric part production, yet this is possible, as seen by the method to produce freeform shaped 3D castings presented in Chapter 3 Freeform Microcasting. Lithography is the current workhorse approach to micromanufacturing because it reproducibly provides excellent dimensional control while enabling the fabrication of many components simultaneously. Although lithography is nominally designed to fabricate 2D structures, relatively simple (generally multiple-layer composed) 2.5D shapes can also be produced, either by layering patterned materials or alternatively by modifying available layer etching and deposition methods [279,280]. Lithography-based techniques are often used to produce metallic components for microtechnology; a good example of this is given by the LIGA process introduced in Chapter 2 Literature Review, in which metal is plated into cavities produced to nanometric precision by photon- or electron-beam lithography [40,43,281,282]. Thus, a combination of both processes should provide an interesting and easily scalable approach to fabricate relatively simple structures out of metal.

The process is presented in what follows. It is depicted in Figure 4-1: its starting point is a wafer-like silicon piece that will be transformed, by means of conventional lithography adapted to produce highly anisotropic etching, into a mold that can be filled with molten metal.

As a first step, one or more surfaces of a silicon single-crystal are covered by a mask, namely a material that is more resistant, *i.e.*, has a smaller etching rate than silicon when exposed to the etchant used to pattern the silicon piece (Figure 4-1). The chip is then processed by photolithography and development, to imprint the shape of the final components into the mold using anisotropic etching techniques. Usual methods to this end include deep reactive ion etching, cryogenic etching, or ion beam etching [283]. Note that Steps 7 to 9 are only necessary to produce a particular mushroom-like shape (micropillars with large heads) that is detailed in following sections and used for tensile testing.

Once desired structures are patterned and etched into the silicon wafer, an intermediate isolating layer of silicon oxide, or other material that is inert in contact with the molten metal to be cast, is either grown by transforming the outer silicon layer by chemical reaction, or deposited by conventional conformal coating techniques, such as atomic layer deposition or low-pressure chemical vapor deposition (Figure 4-1 step 10). This layer is inserted to prevent chemical reaction between the molten metal (the infiltrant) and silicon during the infiltration process: without this layer silicon dissolves in the infiltrant, given its finite solubility in molten silver or copper and the high atom mobility characteristic of temperatures in excess of the melting point of those metals. Materials that can protect silicon from the molten metal are ones that remain solid during casting and are chemically stable when in contact with both the molten metal and silicon. Moreover, when a free-standing metallic structure is the desired final product, this layer should be leachable using an etchant in which the metal is inert: $SiO_2$ fulfills all of those requirements if the cast metal is of silver or copper.

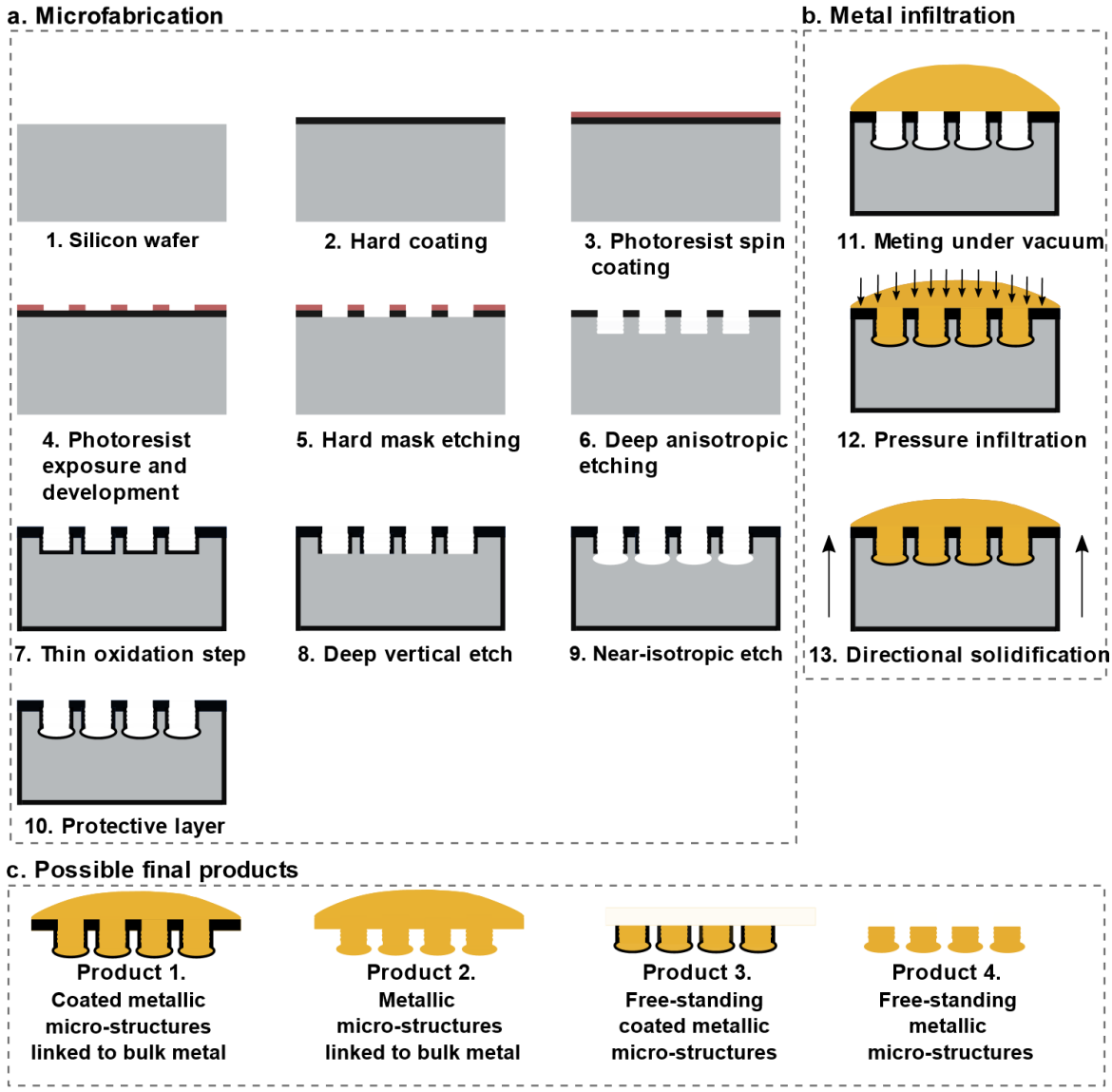


Figure 4-1 Schematic illustration of the process, which combines a first stage of lithographic microfabrication based on DRIE (a) with metal pressure infiltration (b). (c) displays the possible final products that the process can produce. Steps 7 to 9 are added to produce a particular mushroom-like shape (micropillars with large heads) that allow mechanical testing in tension.

As aforementioned, at the micro-scale the filling of mold features with molten metal is not spontaneous because it is generally opposed by capillary forces. To push the liquid metal into all open cavities of the mold, an external pressure is therefore applied (Figure 4-1 step 12). This produces a silicon mold coated with an outer layer of ceramic material that itself contains infiltrated solid metal. This component can be used as such, or further processed to retrieve small free-standing shaped parts of metal alone. For instance, after removing mechanically excess metal remaining from solidification, the silicon can be dissolved using an etchant in which the metal and the isolating layer are inert, or have a substantially lower etching rate in comparison with silicon, such as KOH. The component thus produced has the previously patterned shape and is composed of a metallic core partially surrounded by a ceramic layer (Figure 4-1 Product 3). Alternatively, if the metal alone is to be used, the protective ceramic layer can be also dissolved, as was the silicon, in a subsequent step (Figure 4-1 Product 4).

In order to produce 2.5D structures, it is possible to either carry out consecutive steps of coating, photolithography, pattern transfer to the mask (when necessary) and anisotropic etching, or it is possible to exploit aspect ratio dependent etching (ARDE [284], a property of deep reactive ion etching), as was done in Ref. [285]. By patterning hole arrays of identical pitch but different diameters, it is in this way possible to achieve different depths of etching in just one etching step (Figure 4-2). This effect, when followed by a quick isotropic etch to "merge" the holes together, is capable of creating complex 2.5D structures in just one lithographic sequence.

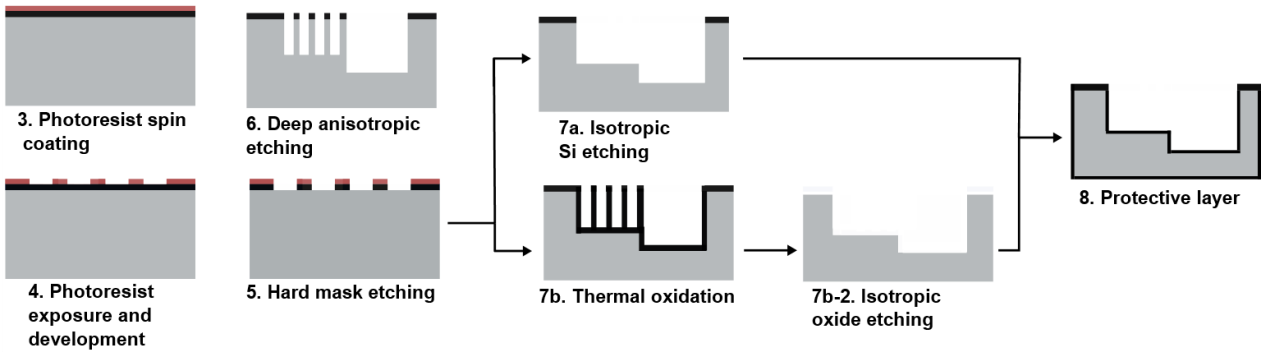


**Figure 4-2** Schematic illustration of the microfabrication of multilevel structures via a single photolithography sequence. The last step of protective layer deposition ensures a ready-to-fill, multilevel silicon mold.

### 4.1.1 Experimental implementation of the process

The mold manufacturing was conducted by Dr. Simone Frasca at the Centre of MicroNanoTechnology (CMi-EPFL). The process starts from standard 100 mm, 525 μm thick wafers of P-doped <100> oriented crystalline silicon. The <100> orientation is the standard Si crystal orientation used in electronics- and MEMS-based processes, for which all the processes described below were already optimized in our cleanrooms; this being noted however, there is to our knowledge no reason why another crystalline orientation could not be used. We grew a 2-μm thick layer of $SiO_2$ by thermal oxidation of the wafer surface; this layer was afterwards used as a hard mask. To pattern the $SiO_2$ layer, after thermal dehydration we spin-coated AZ ECI 3007 positive photoresist at 6000 RPM to reach a homogeneous coating thickness of ca. 600 nm. The photoresist was exposed by i-line photolithography ($\lambda$ = 365 nm) and then developed by AZ 726 MIF, an organic solution based on TMAH. After development, the pattern was transferred to the $SiO_2$ layer by means of fluorine plasma etching in an SPTS APS dielectric etcher, using a $He/H_2/C_4F_8$ gas mixture plasma. The patterns were then etched into Si by means of deep reactive ion etching in an Alcatel AMS200 silicon etcher. The process developed in the AMS200 is a modified Bosch process [286] consisting of alternating steps of $SF_6$, $C_4F_8$ and $O_2$ plasmas respectively to etch, coat and clean throughout the process, optimized in previous work to ensure good verticality and a high aspect ratio [287].

Variations in the fabrication of structures shown here are all in the microfabrication stage of the process, while infiltration procedures remained the same. Experimentally, this is conducted with the silicon substrate at the bottom of a graphite crucible, where the metal seals the cavities when molten. The procedure and setup are

detailed in Sections "3.1.1 Experimental implementation of the process" and "3.2.3.1 Trials to impose larger thermal gradients".

After solidification, the substrate-metal composite (as in Figure 4-1 step 13) is immersed into a 60 % KOH solution at ~ 60 °C for approximately 12 hours or until no trace of silicon is observed along the sample surface.

## 4.2 Results

Mushroom-shaped metal structures amenable to tensile testing that were produced by coupling silicon lithography with metal casting are presented in Figure 4-3. The lithographic process that was used here included steps 7 to 9 of Figure 4-1 to produce the larger mushroom-like bulges at the top of the micropillars. Unless otherwise noted, a ~1 μm $SiO_2$ layer was thermally grown over the patterned Si wafer prior to infiltration. After infiltration, solidification and etching, the exposed cast structures remain linked to the excess of infiltrant metal that lined the silicon mold surface before filling its cavities (Product 2, Figure 4-1). The infiltrant volume is always far greater than the total cavity volume of the mold since this facilitates subsequent manipulation and imaging of the casting, as well as mechanical testing, and furthermore makes the infiltration process simpler and more robust. Figure 4-3a-b display an array of 2.5D mushroom-like structures made of pure silver: those long, slender structures ending with a wider cap serve both for demonstration of process capabilities (because they would be hard to produce from the Si mold by metal deposition or by pressing solid metal) and for tensile testing, as we show below. Top and lateral cross-sections, after metallographic polishing, of silver still embedded in the silicon mold can be observed in Figure 4-3c, together with the elemental distribution maps for silicon, oxygen and silver acquired by energy dispersive spectroscopy (EDS). It is clear that the metal is pore-free and that chemical interaction between the metal and the silicon mold was prevented by the silica interlayer.

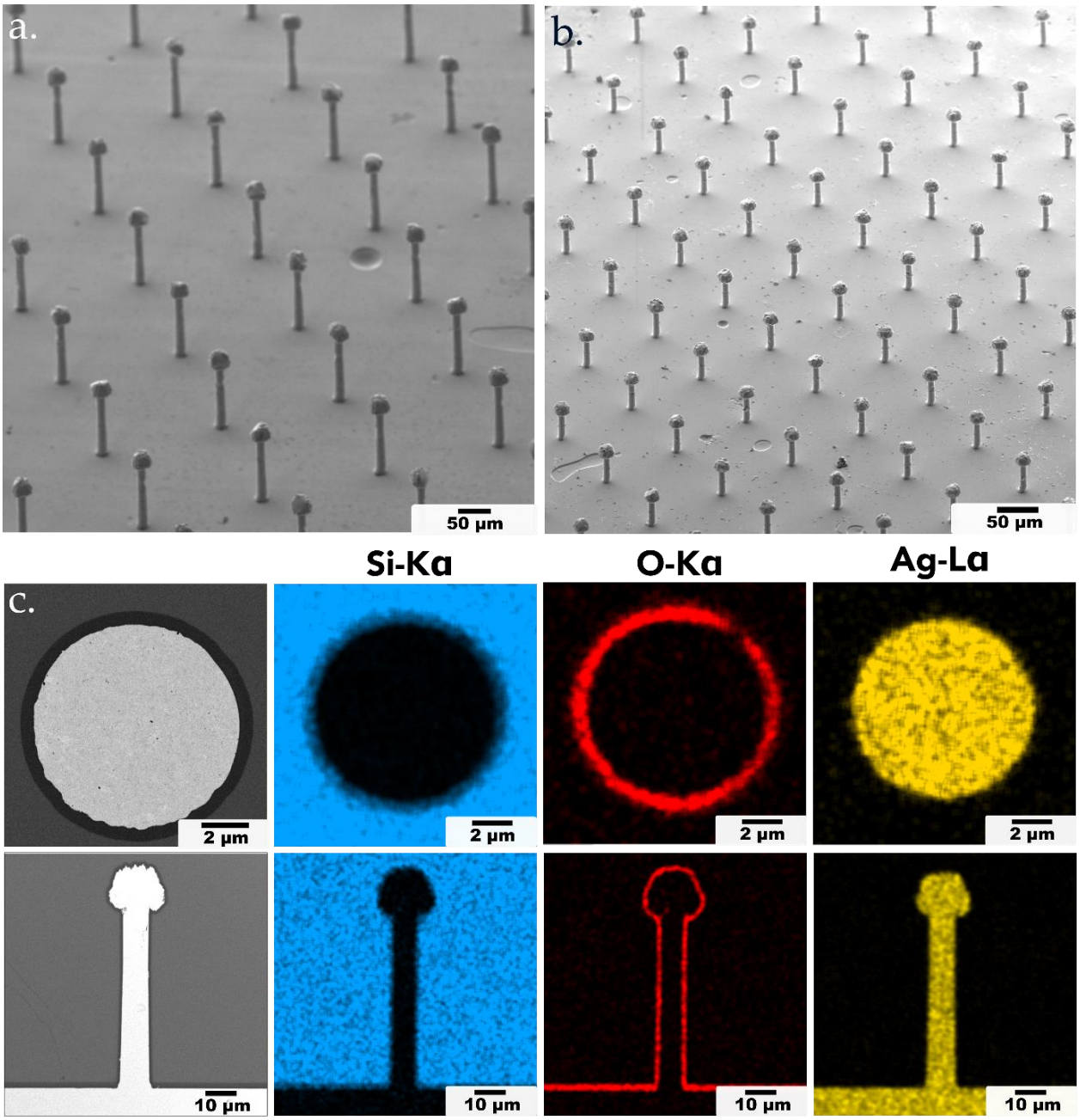


**Figure 4-3** Cast micro-structures produced by means of the proposed process. a) An array of 2.5D mushroom-like silver structures with a diameter of ~9 µm and an aspect ratio of ~5. b) An array of 2.5D mushroom-like copper structures with a diameter of ~9 µm and an aspect ratio of ~5. c) Top and lateral cross section of a silver structure along with the elemental distribution maps for silicon, oxygen and silver.

With the present approach one can also produce structures of metal coated with a ceramic, given that the etching rate of silicon in KOH exceeds greatly the etching rate of some ceramics (*e.g.,* Si etches in KOH about 140 times faster than silica) [288]. Figure 4-4 shows structures consisting of a silver core surrounded by a ceramic layer (Figure 4-1, Product 1). Figures 4-4a-c exhibit 2.5D pillars with a diameter of approximately 5 µm and an aspect ratio of ~7.5. These structures, as shown by the FIB-milled top cross section and the elemental distribution maps displayed in the inset of Figure 4-4c, consist of a pore-free, dense silver core surrounded by a silicon nitride layer 470 nm thick, which features a sharp interface with the metal. These architectures were produced by depositing, via low pressure chemical vapor deposition (LPCVD), a silicon nitride coating over the silicon substrate (at step 10 in Figure 4-1) prior to pressure infiltration with silver followed by silicon dissolution in KOH.

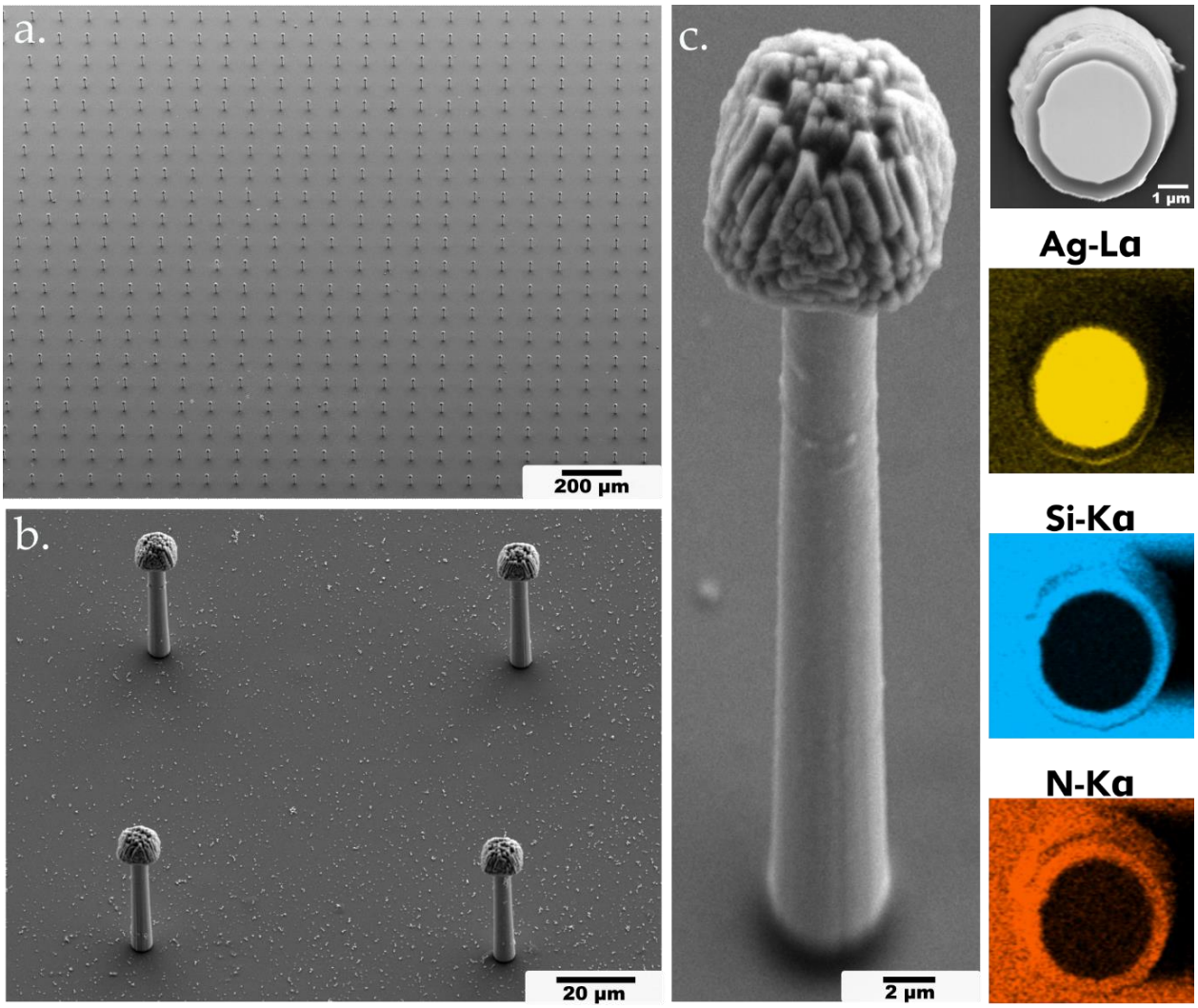


**Figure 4-4** SEM images of cast silver micropillar structures (from low to high magnification), covered by a ~ 470 nm silicon nitride layer. Micropillars have a diameter of 5 µm an aspect ratio of ~ 7.5. A FIB-milled top cross section of a single pillar with the elemental distribution maps for silver, silicon and nitrogen is displayed in c).

Figure 4-5a-b show an example of a multilevel silicon substrate after patterning and thermal oxidation. Figure 4-5c-d present a free-standing multilevel silver gear that was cast into a similarly patterned Si mold, after which excess silver along the mold surface was removed by grinding before mold dissolution (Figure 4-1, Product 4). As shown by electron backscatter diffraction (EBSD) in the inset of Figure 4-5c, the gear is monocrystalline. Large metal grains were found in all microcomponents produced by the present process: castings were either monocrystalline (this being by far the most frequent case) or composed of only a few grains.

In patterning multilevel structures such as these, the use of a single photolithography sequence (Figure 4-2) speeds up mold fabrication and prevents misalignment problems; however, the segmentation of different sections into arrays of holes has an impact on the final surface roughness of the substrate, and therefore defines the precision to which finer features are produced. This is because part voxel resolution and surface roughness are commensurate with the radius of the holes, in the mold and hence in the final metal structure, given that pressure infiltration faithfully replicates mold features. This can be seen in higher magnification images of the

silicon mold (Figure 4-5b) and of the cast metal gear surface (Figure 4-5d): an array of holes finer than those used here would therefore have to be used in industrial microgear production. Figures 4-5e-f represent a system of small gears, made of silver-copper alloy (Ag-9 wt.%Cu), still linked to the bulk metal.

Provided reaction between the metal and silicon is either inoperative (because it is too slow or because silicon is stable in contact with the infiltrant) or can be prevented (as demonstrated here via silica coating), essentially any alloy can be used since it suffices to pre-alloy the metal before infiltration to obtain the desired composition.

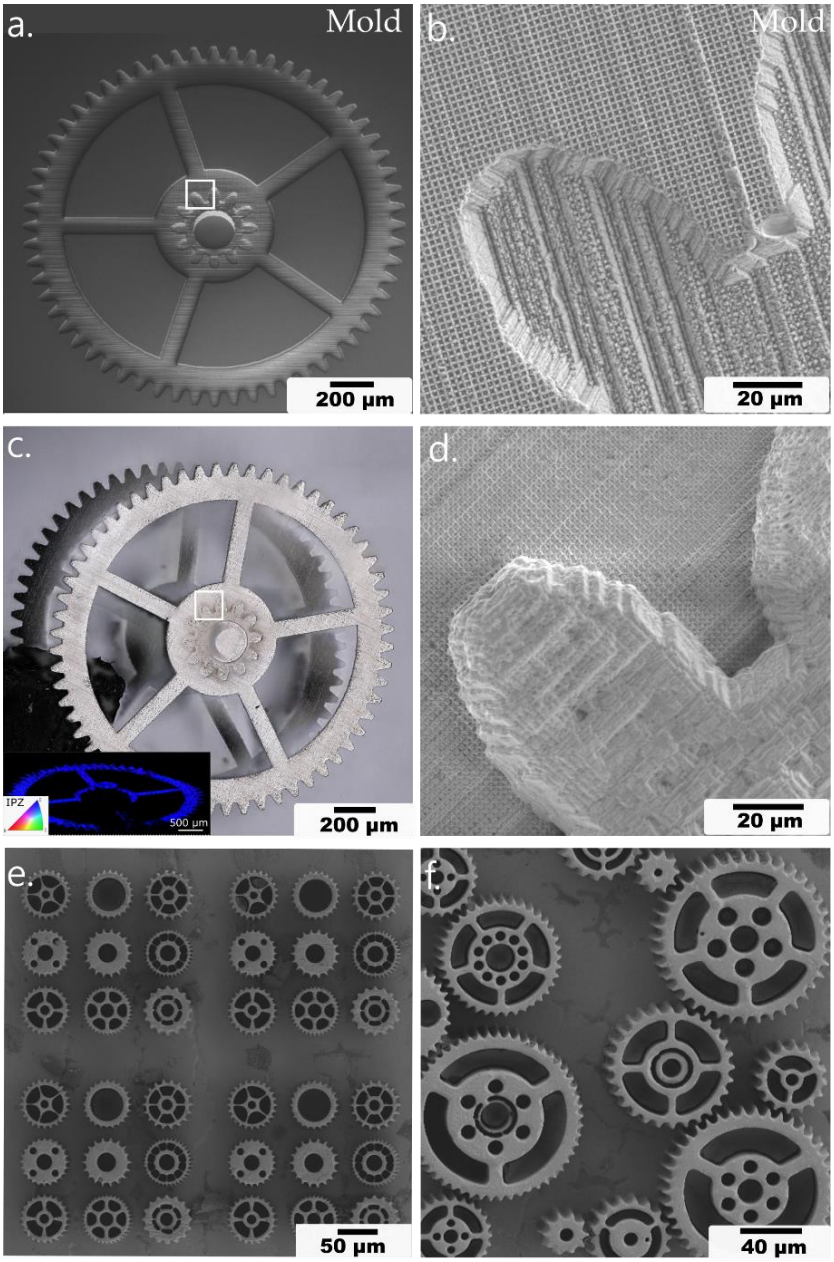


**Figure 4-5** a-b) Multilevel silicon substrate produced by a single photolitography sequence. b) A binocular image of the resulting free-standing multilevel silver gear produced after infiltration and separation of the mold in a), where the inset is an EBSD grain orientation map showing that the wheel is monocrystalline. d) SEM image of the free-standing multilevel silver gear showing that all small details present on the substrate b) are fully reproduced thanks to pressure infiltration. Rectangles drawn in a) and c) indicate the area of interest in the following image. e-f) SEM images of gears made of silver alloyed with 9 wt.% copper (which are here still attached to the bulk metal).

## 4.3 Discussion

Results show that 2D and 2.5D dense metal microcomponents can be produced in large numbers out of pure silver or copper by means of a process that uses lithographic silicon nanofabrication to manufacture molds into which molten metal is cast. Structures with sizes ranging from 2.5 μm up to a millimeter, including structures with high aspect ratios and strongly reentrant geometries, can be produced by this approach, unlike other metal shaping processes that replicate silicon lithography structures. This method inherits attributes from both lithography and casting, namely excellent dimensional control, high reproducibility, full density, the possibility to alloy with great freedom the infiltrant alloy composition, and a capacity to replicate essentially any continuous shaped hollow. A proof-of-concept alloy, namely silver-copper, is demonstrated here. Among other advantages of the process is the fact that it uses currently widespread silicon microfabrication facilities, and the fact that an isolating silica layer contouring the mold surface is easily produced and has been shown to provide the chemical stability necessary to enable casting at high temperatures with weakly-oxidizing engineering metals such as silver and copper. Unless the patterned silicon mold is to form part of the final component, reutilization of the silicon substrate, as can be done in other processes (such as nanoimprinting) [34,35], is not possible here because the mold has to be dissolved to free the metallic pieces; however, silicon volumes utilized here are small, and given that many closely spaced castings can be produced with a single thin wafer, this should not be much of a limitation.

The approach to create patterns on a substrate in the process presented here holds similarities with the LIGA process in that it produces both 2D and 2.5D structures, however, there is a difference in that in metal mold production LIGA patterns the photoresist while we pattern silicon. Methods based on patterning of a photoresist offer the possibility to fabricate inclined structures [42,279], which is not possible on silicon, because strongly directional, anisotropic plasma etching of silicon can only occur in one direction, namely towards the RF bias power source. Still, microfabrication of silicon does provide the possibility to achieve multilevel 2.5D structures in a single sequence. Moreover, filling cavities by metal casting is substantially faster than electroplating, offers a different variety of possible metals or alloys, and enables a wider range of 2.5D structures since high aspect-ratio and re-entrant structures generally cannot be filled by electroplating. Some aspects regarding size limitations for the process introduced here should be noted. Photolithography was conducted in this work using a flood-illuminated mask (no direct writing); this provides for a rapid lithographic step but limits the size resolution to ≈1 μm. Lithography can, however, reach nanometric resolution, for instance by means of e-beam lithography, while pressure infiltration can infiltrate features far smaller than 1 μm if the pressure is sufficient (the Young-Laplace equation, $P \approx \frac{\sigma}{R}$, implies that pressures on the order of 10 MPa, which can be produced industrially, will infiltrate features 100 nm wide). The main limitation to the production of nanometric structures is thus in mold dissolution and manipulation of dissolved metal structures, particularly if freestanding structures are to be produced.

The level of part shape flexibility afforded by lithographic etching processes is limited when compared with an alternative microcasting approach that uses femtosecond laser micromachining of silica to produce the molds [230]; however, the present molding process has the advantage of delivering smoother metal surfaces with higher in-plane resolution. In addition, since each individual step in the process, namely lithography, casting and chemical demolding, is easily parallelized, the present process is likely to be economical since it is possible to manufacture a large number of components in a single fabrication sequence. Another attractive feature of the present process is that the etchant used here, namely KOH, is less aggressive than HF; this opens up high-precision microcasting to metals and alloys that are attacked by HF but not by KOH.

The large metal grain size found here parallels what has been reported for other metal microcasting processes [81,230], or for solid state metal forming coupled with silicon lithography [34,36]. This may prove a limitation in some cases, given the potential for inhomogeneous deformation that comes with single or large-grained metal structures; on the other hand, an absence of grain boundaries within the metal reduces the propensity for time-dependent deformation including creep, and produces metal with a greater electrical conductivity. Among other structures, the process can produce mushroom-like samples, shown in Figures 4-3 and 4-4, that are amenable to micro-tensile testing; it thus provides a new pathway for the production of micron-scale mechanical test specimens. From an industrial applications standpoint it provides a way to produce, with massive parallelization, conductive structures out of strong metal for the MEMS industry; examples are antennas, electrodes, and photonic crystal structures such as metasurfaces.

In summary, the present approach pushes the limits of micromanufacturing, since it enables the production, out of dense metal, of a wide range of shapes with good surface definition and at high production rates. Any 2.5D component made of pure metal or alloy that melts at a temperature below the melting point of silicon (1414 °C) can, in essence, be fabricated if one can identify a ceramic layer that can be coated onto silicon and is inert with the metal in question. This barrier can serve not only to prevent dissolution of the silicon by the molten metal but it can also, after properly conducted metal infiltration and silicon etching, act as a thin protective coating around the metal in the final product, raising for example its modulus or surface hardness. All steps in the process can be highly parallelized and are already practiced industrially; as such, the process presented here has tangible potential for industrial impact.

# Chapter 5 Mechanical Behavior of Microcast Structures at Room Temperature

In this chapter, the mechanical behavior of monocrystalline 2.5D microcastings made of silver or copper, of diameter selected in the range from 2.5 μm to 13 μm, is investigated by means if *in-situ* tensile tests on samples produced by the process described in the previous chapter.

Disclaimer: This chapter contains literal reproduction of full paragraphs and figures of the publication [278] *L. Borasi, S. Frasca, K. Nicolet-Dit-Felix, E. Charbon, A. Mortensen, Coupling silicon lithography with metal casting, Applied Materials Today. 29 (2022) 101647*, and of a manuscript to be submitted, entitled *"The Effect of Size, Orientation and Temperature on the Deformation of Microcast Silver Crystals"* to which the author has contributed. Specifically, the author contributed to the conception of the process, and conducted the infiltration of the molds, the characterization of components after demolding and contributed to the data curation and data analysis together with Prof. Andreas Mortensen. Dr. Simone Frasca conducted the microfabrication of silicon substrates.

## 5.1 Materials and Methods

### 5.1.1 Sample preparation

An array of cylindrical mushroom-shaped structures is prepared by the microcasting process described in more detail in Ref. [289] and Chapter 4 Coupling Silicon Lithography with Metal Casting. The process combines silicon-based mold microfabrication with pressure infiltration and is summarized in Figure 5-1. In summary, once lithographic steps are performed, to prevent chemical reaction between silicon and molten metal during the infiltration process, wafers are subjected to thermal oxidation in air in order to create a protective $SiO_2$ layer (~1 $\mu$m) on the walls of the patterned holes. Finally, wafers are diced for separation into substrates of area ~ 9x9 $mm^2$.

Once it is manufactured, each 9x9 $mm^2$ mold is pressure infiltrated with pure molten silver (Figure 5-1 step 2) at ~ 1000 °C using argon gas (~ 15 bar). A detailed description of the hardware and infiltration cycle that were used can be found in Chapter 3 -Section "3.1.1 Experimental implementation of the process". After solidification, mold and metal are immersed into a 60 %KOH solution at ~ 60 °C (Figure 5-1 step 3) for approximately 12 hours or until no trace of silicon or $SiO_2$ is observed. This step selectively dissolves the

mold, leaving all microstructures exposed and linked to a bulk (roughly 1 cm wide) solidified button of metal (Figure 5-1 step 4). Pure silver or pure copper (99.99 wt.%) granules are used during infiltration. Copper microstructures containing 1 wt.%Si were produced by a partial reaction of the mold with the copper, leaving alloyed wires along the remaining area, presumably due to localized fracture of the silicon dioxide during that particular infiltration experiment. In addition, $Si_xN_y$-coated silver structures, such as those introduced in Chapter 4, Figure 4-4 are produced by removing samples out of the KOH once the silicon is etched away and before dissolution of the oxide, given the etching contrast between these two. Most data are for silver; however, a few copper specimens are also tested to validate both the fabrication process and testing procedure.

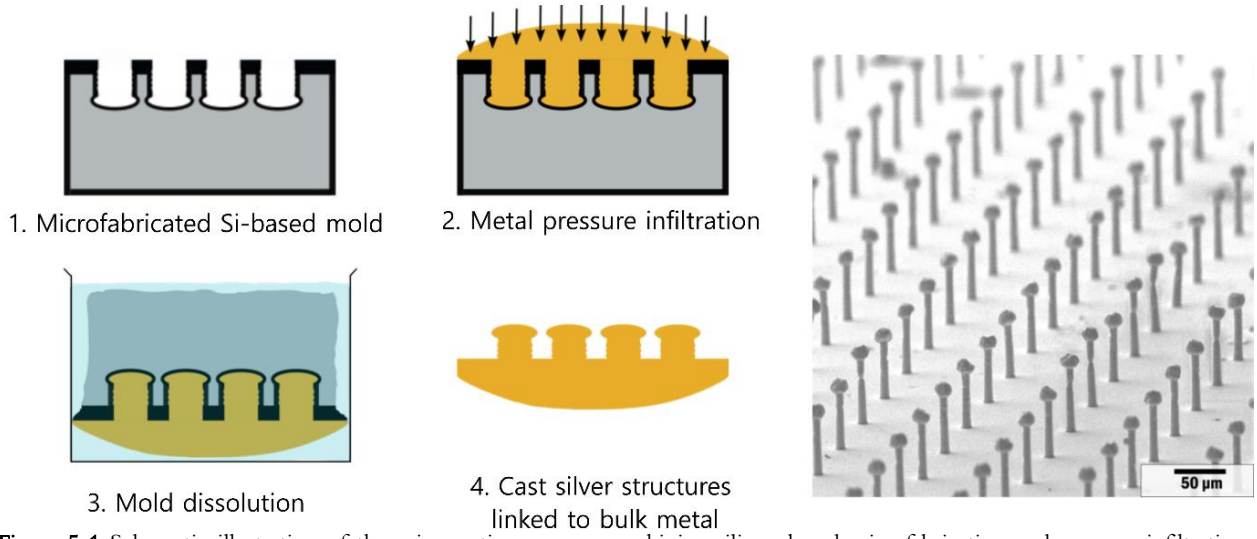


**Figure 5-1** Schematic illustration of the microcasting process combining silicon-based microfabrication and pressure infiltration, together with an array of resulting cast silver microstructures suitable for tensile testing.

To prevent the deformation of samples having a diameter below 5 µm, which are delicate and easily deformed during handling and processing, a cylindrical four-wall shield is added around every single wire. This avoids bending or other deformation of the wire that may be caused by capillary or viscous forces during mold dissolution, cleaning or drying (Figure 5-2). The four sides of this shield are then bent away from the wires before testing, giving access to grip the microwire. This is done simply by compressing the walls of the ring with the micromechanical system before gripping and testing the sample.

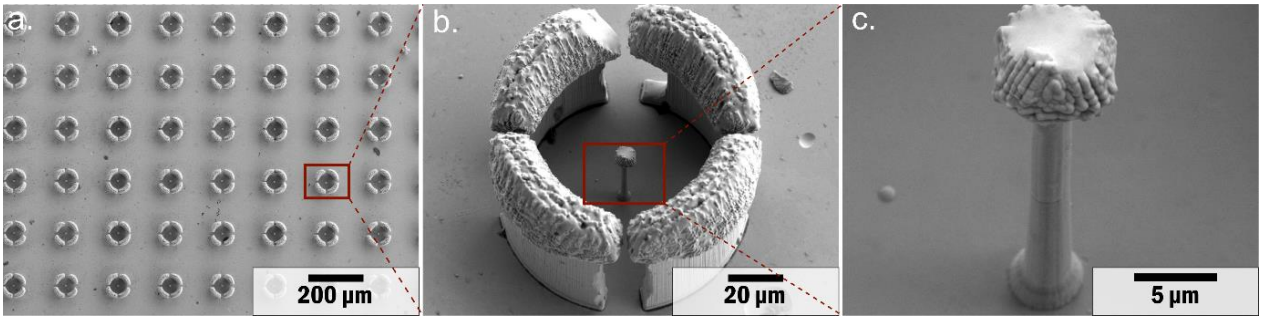


**Figure 5-2** An array of specimens with a diameter of 2.5 µm protected by an outer shield. a) Top view of the bulk showing multiple cylinders. b) A cylindrical sample with an outer shield. c) A close image of a cylindrical structure with a diameter of 2.5 µm.

Each pressure-infiltrated casting contains several thousand (~ 8000) randomly oriented thin cylindrical silver monocrystals linked to bulk silver of dimensions around 9x9x1.5 $mm^3$ in size. Mushroom-shaped tensile micro-specimens have a selected uniform diameter (either 13 μm, 8 μm, 3.7 μm or 2.5 μm) with an aspect ratio (length divided by sample diameter) kept in the present experiments between four and ten and are evenly distributed in a square array with a mutual spacing of 100 μm. The surface quality, as well as the sample diameter and length, are examined by scanning electron microscopy (Zeiss® GeminiSEM 300; Oberkochen, Germany) prior to testing.

### 5.1.2 Crystal orientation of microwires

Since the grain size of the bulk silver button is on the order of a few millimeters and since the same grains extend through both the Ag button and the microsamples, many neighboring wires have the same crystal orientation. Figure 5-3 presents a schematic illustration (not to scale) of an array of six tensile specimens linked to bulk metal, together with an EBSD image of an actual sample showing grains on the bulk metal surface. As seen, metal grains are in the millimeter range. Note that each colored area on the EBSD image contains many small dark spots; those mark the position of individual tensile specimens: as shown schematically, the dark region around each wire is the consequence of signal shading caused by the "head" of the pillars. Since each tensile specimen is a prolongation of the underlying bulk crystal to which it is attached, it is evident that many microtensile specimens with the same crystal orientation are obtained in each casting.

The crystallographic orientation of both the wires and the underlying substrate are analyzed for each casting by means of electron backscattering diffraction (EBSD). This is performed with a Zeiss® Gemini450 (Oberkochen, Germany) scanning electron microscope (SEM) equipped with a symmetry CMOS and operating with the Aztec acquisition and data treatment software (Oxford Instruments, UK). The precise crystallographic axes are obtained by means of the ARPGE software [290].

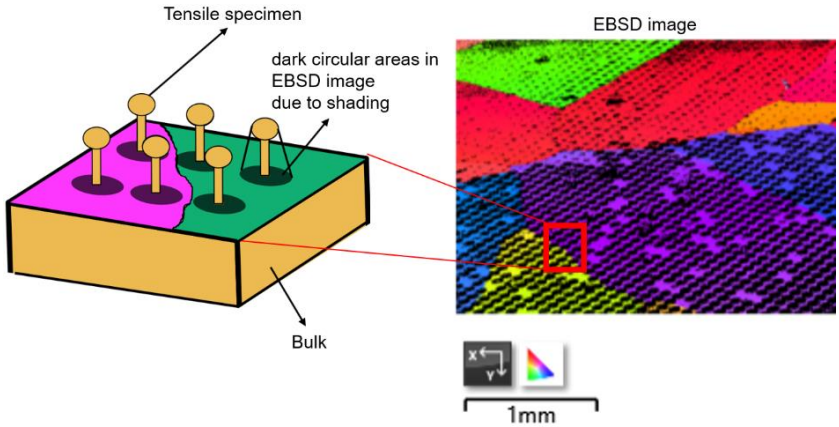


**Figure 5-3** A schematic illustration (not to scale) of an array of tensile specimens linked to bulk metal, showing the shadowing of specimens during EBSD analysis (left). EBSD image of a bulk showing multiple grains with sizes on the order of the millimeter and with several tensile specimens on each grain (right).

### 5.1.3 Casting of silver wires in the millimeter range

In the case of silver, for comparison of microsample data with the behavior of macroscopic samples, considerably larger monocrystalline silver wires, of diameter in the millimeter range and of high aspect ratio (>10), are also produced by pressure infiltration using fused silica capillary tubes as a mold. The process is outlined in Figure 5-4. It begins by placing capillary tubes within a graphite crucible together with silver pellets. The ensemble is then heated under vacuum (~ 0.06 mbar) in order to melt the silver. The liquid then seals all evacuated tube entries (Figure 5-4 step 1). Subsequently, argon gas is bled into the chamber to increase the pressure until a level of ~5 bar to create, similar to what was previously mentioned for the microcasting process, a pressure differential that drives the liquid upwards, filling the tubes (Figure 5-4 step 2). Once the metal has filled the glass molds, the silver is directionally solidified by placing the infiltration chamber on top of a water-refrigerated copper chill. After solidification, the silver is removed from the crucible and tubes are cut and immersed in high-concentration hydrofluoric acid (46 %) in order to selectively dissolve the fused quartz (Figure 5-4 step 3) and obtain a free-standing monocrystalline silver wire (Figure 5-4 step 4).

The surface quality, diameter, and orientation of those larger crystals are also evaluated by means of SEM and EBSD.

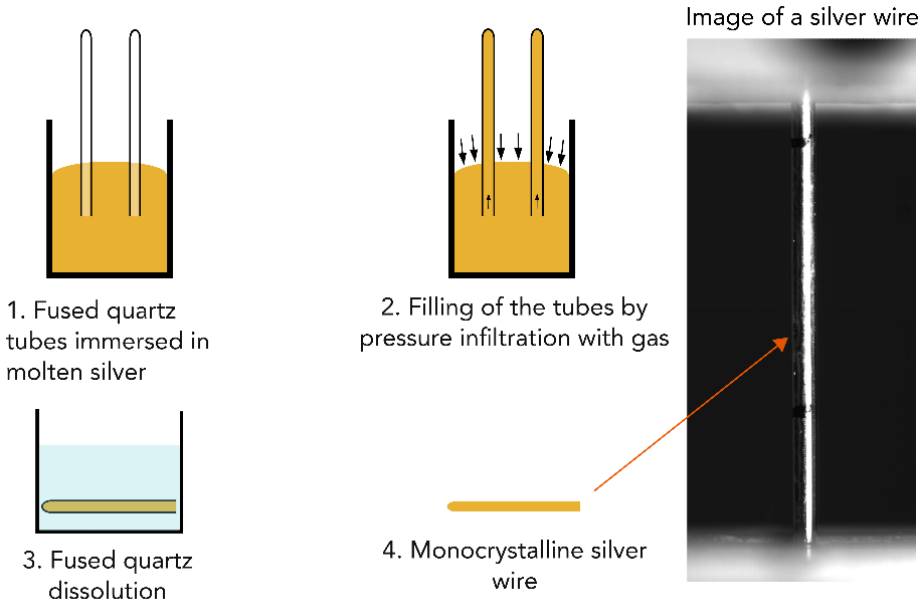


**Figure 5-4** Schematic illustration of the pressure infiltration of fused quartz capillary tubes together with an image of a silver wire cast by means of that method ($D$ = 1 mm).

### 5.1.4 In-situ SEM microtensile testing and data treatment

In-situ SEM uniaxial tensile experiments are performed on micropillars by means of a FT-NMT04 Nanomechanical Testing System (FemtoTools, Buchs, Switzerland). All tests are carried out at a nominal strain rate of $10^{-3}$ $s^{-1}$ in intrinsically displacement-controlled mode (*i.e.*, with a stiff load train and without the

need for a force feedback loop), using a linear piezo-scanner. This stage is coupled with microforce sensing probes based on microelectromechanical (MEM) systems. These silicon probes have a specific keyhole-shaped grip with a sensing load of up to 200 mN. Since the width of the mouth of those grips is initially 5 μm, it is widened by means of FIB milling for probes used to test bigger pillars. The setup is tilted ~ 15° with respect to the sample stage in order for the electron beam to access the wires and allow imaging during testing.

The resolved shear stress (RSS-$\tau$) is calculated from the stress ($\sigma$) and Schmid factor ($S$, relative to the wire orientation) as $\tau = \sigma \cdot S$, considering the measured diameter and wire orientation, under the assumption that the wires deform along the slip system that experiences the highest resolved stress. All elastic contributions from both sample and load train are subtracted from the total displacement to compute the load point displacement ($\Delta l$) corresponding to purely plastic strain. In doing so, the machine *cum* wire compliance is assessed as the inverse of the slope of the linear loading portion along force-displacement curves for each test. The plastic shear strain is then computed as $\gamma = \Delta l/(l_0.S)$.

Data are collected at 96 kHz, while all resolved shear stress vs. shear strain plots are produced using data at 1 kHz. To this end, raw data are reduced by merging data points using Origin (Pro) Version 2021 software (OriginLab Corporation, Northampton, MA, USA).

Experiments are stopped when necking is observed, or just before sample fracture to avoid having to clean the grip after testing. Complete datasets can be found at 10.5281/zenodo.7373750 and 10.5281/zenodo.6641562. All videos in the Supplementary material are accelerated by a factor of 15.

Separately cast macroscopic single crystals one millimeter in diameter are tested *ex-situ* at room temperature by means of an RSA 50 tensile test machine (Walter+Bai A.G.; Löhningen, Switzerland) at a nominal strain rate of $10^{-3}$. Data are collected and treated as described above for microwires.

## 5.2 Results

All tested samples are monocrystalline and results are therefore plotted in terms of resolved shear stress versus resolved plastic shear strain. Representative curves of resolved shear stress vs. resolved plastic shear strain at room temperature are presented in Figure 5-5. This includes representative curves of macroscopic (Ø 1mm) crystals cast from the same silver metal (Figure 5-5a) as well as results from in-situ testing of micro-specimens of various diameters (13 μm, 8 μm, 3.7 μm or 2.5 μm) and crystal orientations (displayed within the stereographic triangle inset) (Figure 5-5b-e). Two experiments were performed for each combination of orientation, diameter, and temperature, since results were shown to be reproducible, such that their average did not vary significantly when performing more tests (as seen for green and purple curves in Figure 5-5c).

Representative sample surface features of slip in these displacement-controlled small-scale uniaxial experiments are displayed in Figure 5-6.

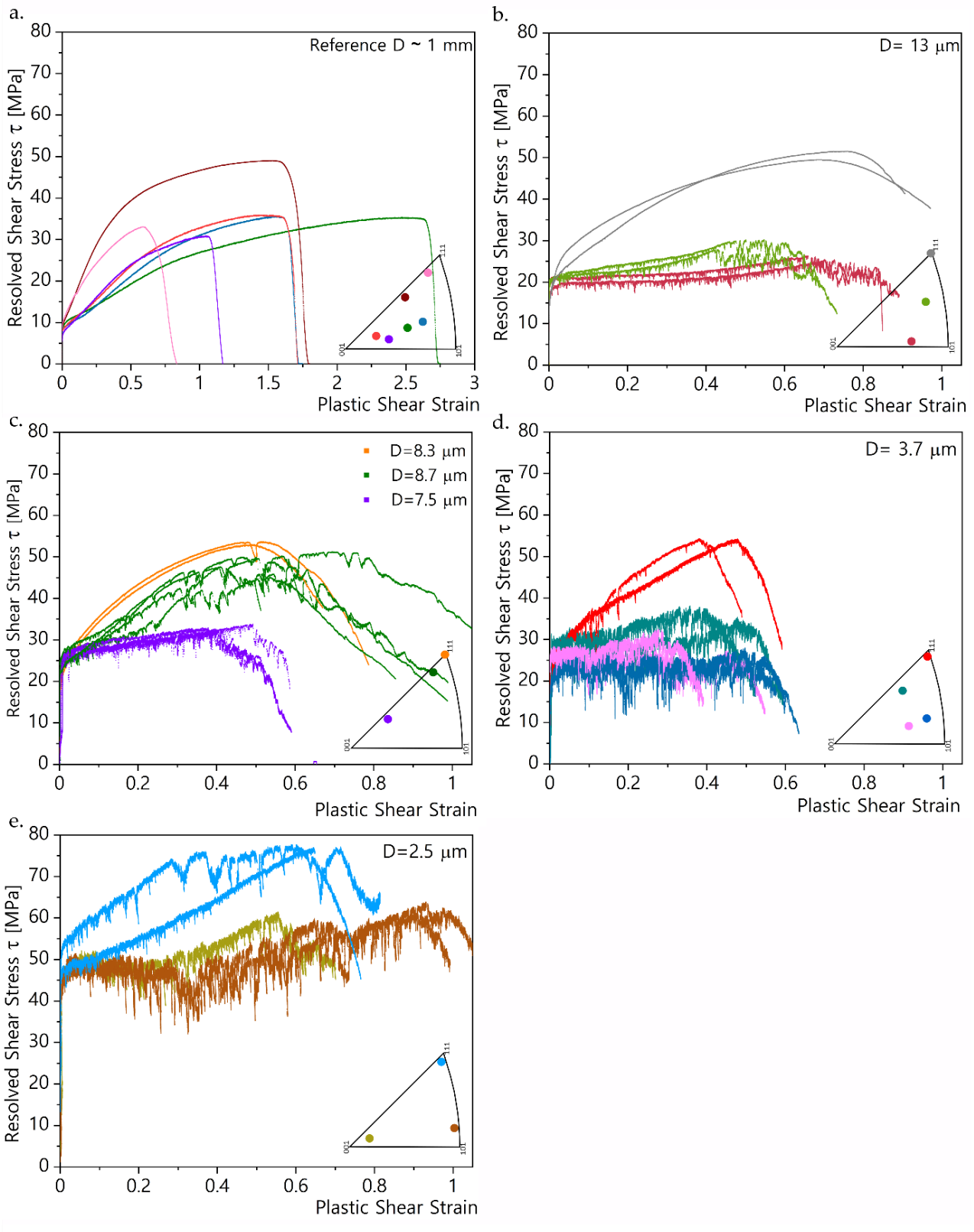


**Figure 5-5** Resolved shear stress vs. shear strain curves at room temperature of: a) wires in the millimeter range ($D$ = 1 mm), b) $D$ = 13 µm microwires, c) $D$ = 8 µm (with four curves in green and five curves in purple), d) $D$ = 3.7 µm, e) $D$ = 2.5 µm.

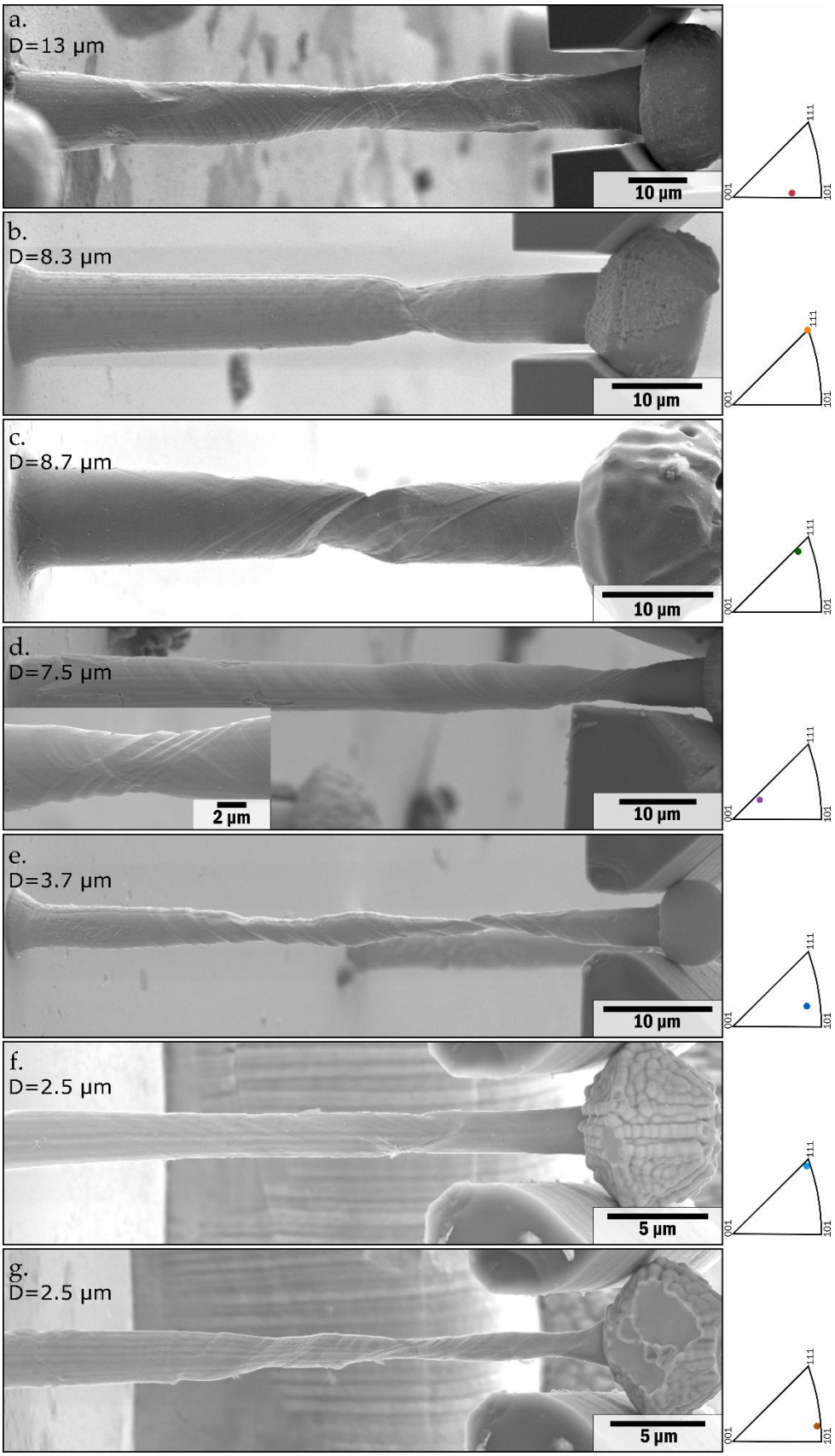


**Figure 5-6** Representative *in-situ* scanning electron microscopy images of microcastings with different sizes and crystal orientation after tensile testing at room temperature. Points within stereographic triangles indicate the initial crystal orientation with respect to the tensile axis.

In addition to silver specimens, the mechanical behavior of copper (Figure 5-7a), copper alloyed with 1 wt.% silicon (Figure 5-7b), and silver coated with silicon nitride (Figure 5-7c) is tested. SEM images given in the insets show specimens after loading.

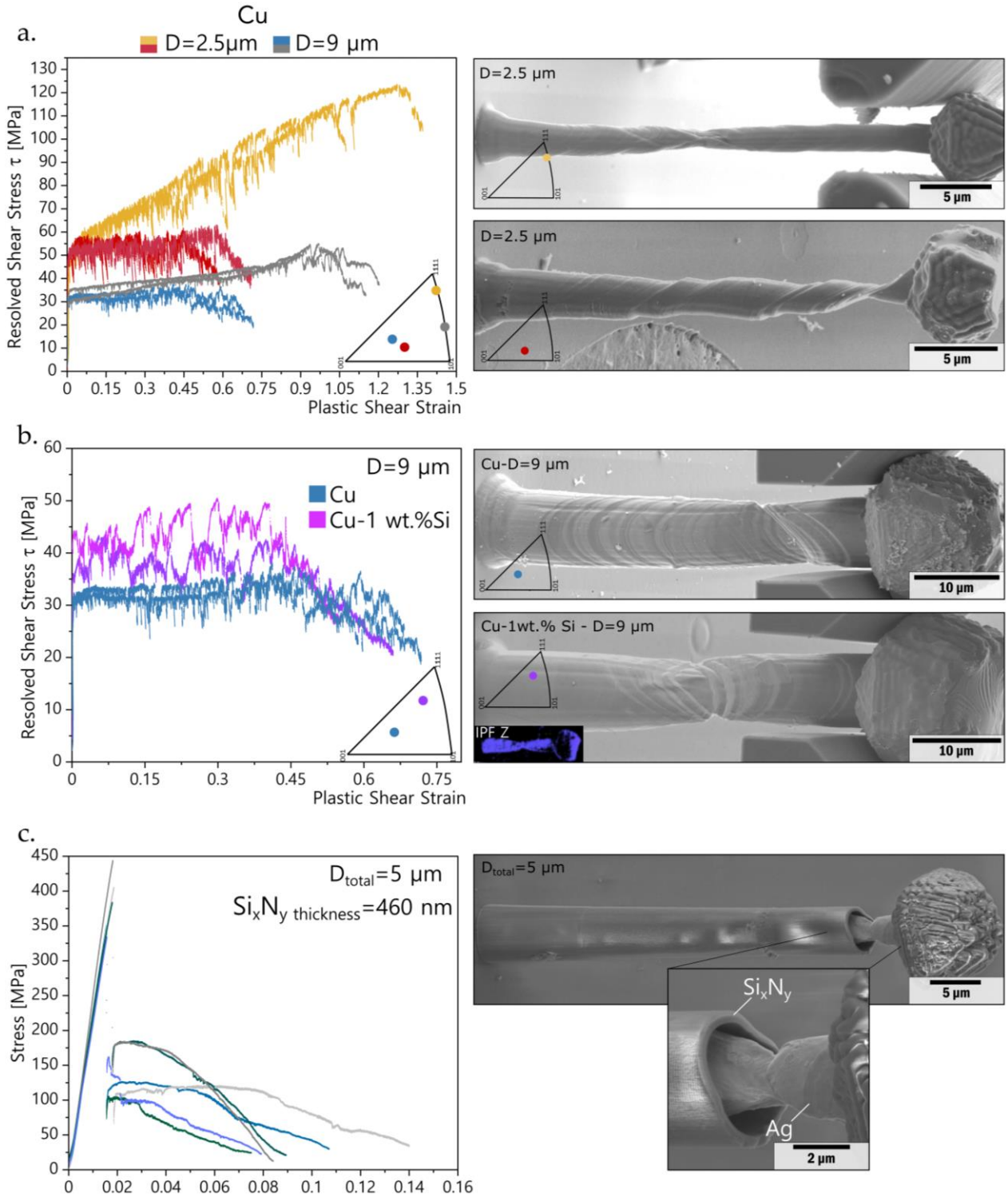


**Figure 5-7** Representative results from in-situ SEM tensile testing of single-crystalline structures. a-b) show curves of resolved shear stress (RSS) vs. plastic shear strain for: a) copper microwires $D$ = 9 μm and $D$ = 2.5 μm, b) copper and alloyed (1 wt.%Si) copper specimens $D$ = 9 μm. c) shows stress-strain curves of silver micropillars surrounded by a silicon nitride layer.

Principal characteristics of the tensile deformation of microcast face-centered cubic crystals produced via the present process can be listed as follows:

1 –Although there are sample-to-sample variations in the collected signal, the reproducibility of tensile properties is sufficiently good for the influence of parameters such as the sample orientation or diameter to be measured.

2 – The critical resolved shear stress (CRSS) for initial yield is predominantly determined by the sample diameter; it increases as the sample diameter decreases.

3 – The rate of work hardening, and the strain-dependent flow stress after deformation, are predominantly influenced by the orientation of the crystal. Samples with (or close to) a <111> crystal orientation display a finite and gradually decreasing work hardening rate ($\theta = \frac{\Delta\tau}{\Delta\gamma}$), while samples oriented for single slip (namely, those with a crystal orientation lying within the stereographic triangle, which is the case for a majority of the samples), show little or no work hardening within experimental uncertainty.

4 - All tested microcastings are ductile: the extent of resolved shear plastic deformation before fracture reaches at least ~50 % (tensile elongations are from 0.27 to 0.5 of the resolved shear strains, depending on the crystal orientation); however, they show less deformation before fracture than do bulk counterparts. Final rupture is by strain localization and ductile rupture, with localized crystal thinning proceeding in some samples very far before the final rupture of the sample (Supplementary video 1 provides an example of this).

5 – Plastic deformation proceeds with a high degree of intermittency, concomitant with the formation of localized, often high-amplitude (micrometric), slip steps along the gage length surface. Their formation is associated with load drops sufficiently strong to be visible on the tensile test curves. Large slip steps are seen to form gradually, for all samples, by successive glide events along the same direction and in the same location. Distributed steps, for crystals initially oriented for single slip, are usually observed along the primary system until advanced deformation, corresponding to > 30% plastic shear strain, after which glide activation of the secondary slip system occurs. The initiation of glide on a secondary glide system, evidenced in the inset SEM images or in videos by the presence of localized slip steps on new glide planes, frequently assists localization of deformation and necking (*e.g.,* Supplementary video 2).

6 - None of the silver or copper castings examined by EBSD after tensile testing exhibited indications of twinning as a deformation mechanism (see, for instance, the inverse pole figure displayed in the inset of Figure 5-7b).

7 - The addition of 1 wt.% silicon to copper increases the CRSS from ≈30 to ≈40 MPa (Figure 5-7b) for wires of diameter 9 μm without a substantial reduction in ductility. Comparing samples of pure Cu and Cu-

1wt.%Si oriented for single slip, one can notice that more pronounced and localized slip steps are observed on samples that contain silicon (See supplementary videos 2 & 3, together with Figure 5-7).

8 - Silver specimens coated with silicon nitride (Figure 5-7c) show elastic loading, up to comparatively high tensile (not resolved) stress (≈ 400 MPa), followed by sudden unloading. The sharp stress drop is associated with local rupture of the ceramic layer at the corner marking the transition between the pillar and its head. This leaves the metallic wire at that location exposed and bearing the load by itself (See supplementary video 4), causing a localization of deformation in the metal near that region, followed by rapid failure.

## 5.3 Discussion

### 5.3.1 Yield

Tensile samples produced in this way are single-crystalline and free of surface alterations that come with the use of focused ion beam milling (FIB), which is commonly used in microsample fabrication and produces samples with a surface that has been modified by gallium ion-implantation [17–19]. Compared with other FIB-free microsample fabrication methods, which include selective etching [31,32,291], hot-embossing [34,36], electroplating [43,45,46], microcasting into single-crystalline salt molds [81,82] or into femtosecond laser micromachined glass, together with silver nanocube precipitation [138,292,293], the present process has as its main virtue that it produces simultaneously many samples of micrometric (yet not nanometric) diameter. Among test specimen weaknesses, it must be noted that, despite their low taper angle (<1°), given the high gage section aspect ratio (>10 for $D$ = 2.5 μm), the difference between the area at the base and that at the head of the specimen is not negligible (the cross-sectional area is augmented by ≈ 80 % from top to base in a sample with a 1° taper and an aspect ratio of 10). Given this variation in cross-sectional area, it is interesting to note that tensile failure did not occur systematically in the region near the head of the column in (uncoated) fully metallic samples. Similarly, although sometimes the first glide steps appear near the sample heads and spread out from there throughout the length of the wire towards its base (see Supplementary video 1), this was not systematically observed. Stochastic factors that operate in micron-scale metals are thus as important as the stress level in dictating the onset or localization of plastic deformation within metallic structures produced by microcasting.

As mentioned above, the resolved initial yield stress is primarily a function of the diameter of the tensile micropillars and depends less on their orientation. Figure 5-8 plots the yield stress of the present microcrystals, defined as their CRSS at a plastic strain of 2 % and made dimensionless by division with the shear modulus of the metal, $\mu$ (as mentioned in previous sections, an appropriate value for $\mu$ in anisotropic crystals is the Reuss average [91,101]- $\mu_{Ag\text{-}bulk}$ = 25.6 GPa and $\mu_{Cu\text{-}bulk}$ = 48.3 GPa) [91,294], plotted versus the burgers vector $b$ (= 2.88 Å and 2.55 Å for Ag and Cu, respectively) [295] divided by the micropillar diameter $D$. The plot also contains tensile yield data from microcast pure aluminum from Ref. [81].

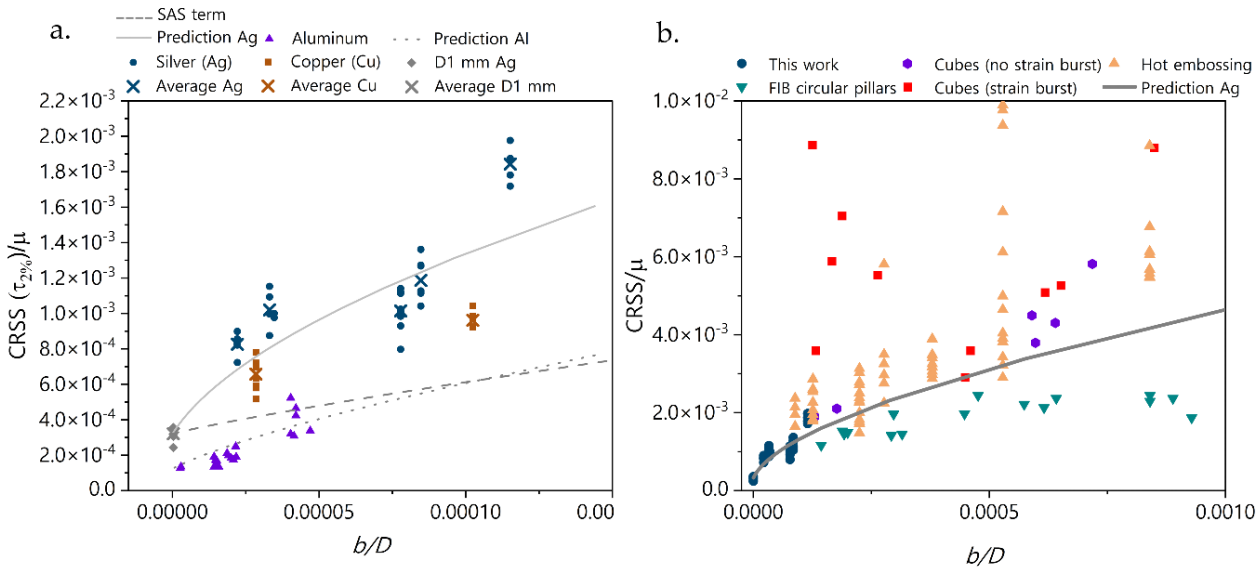


**Figure 5-8** a) The yield stress of the present microcrystals defined as their CRSS at a plastic strain of 2% and made dimensionless by division with the shear modulus of the metal, together with similar data for aluminum redrawn from Ref. [65]. Solid and dotted lines represent values predicted for silver and aluminum respectively by Equation 5-1, while the dashed line refers to the value predicted by its first (SAS) term, with $L=D/3$ and $N = 16.4$ in Equation 5-4. b) Resolved room-temperature shear stress made dimensionless by division with the shear modulus vs. $b/D$ of silver microcastings (this work), together with data for silver from the literature [36,138]. The solid grey line is the same as that in (a).

The line in the graph is the yield stress predicted by the expression:

$$\tau = \tau_{SAS} + \tau_{forest} = \alpha_1 \mu (b/L) + \alpha_2 \mu b \rho_f^{1/2} \quad \text{Equation 5-1}$$

for the flow stress of a thin FCC crystal containing a density $\rho_f$ of forest dislocations, the deformation of which is governed by the motion of a SAS dislocation of length $L$ through the dislocation forest. $\alpha_1$ is given as [81,103,296]:

$$\alpha_1 = 0.12 \ln\left(L/b\right) \quad \text{Equation 5-2}$$

This simple model has been found to give overall good agreement with both the output of discrete dislocation simulations of small crystal deformation [81,297] and experimental data for microcast Al, Ag, and Cu [81,82,289] or FIB-carved micropillars of various metals [20,144,146,182,298]. Given that the present samples are clearly not dislocation starved and in keeping with previous work [81,139], we take $L = D/3$. If anything, this will slightly overestimate the contribution of the first term in Equation 5-1.

The second term on the right-hand of Equation 5-1 corresponds, according to the derivation in Ref. [144], to forest hardening ($\tau_{forest}$). According to Equation 2-13 in Section "

2.4 Dislocations in face-centered cubic metals" $\alpha_2$ can be considered as:

$$\alpha_2 = 0.35 \frac{\ln\left(b\sqrt{\rho_f}\right)}{\ln\left(b\sqrt{\rho_o}\right)} \quad \text{Equation 5-3}$$

where $\rho_o$ is a reference dislocation density equal to $10^{12}$ m$^{-2}$ [299].

As seen with the dashed line in Figure 5-8a, even with $L = D/3$, the first term ($\tau_{SAS}$) underpredicts the observed rate of increase of the flow stress with decreasing $D$. This observation has been reported before [81,82,297], and suggests that in the present samples there is an additional factor that increases the flow stress as $D$ decreases. A likely mechanism comes from the fact that present samples have cooled in their mold from the melting point of the metal (*i.e.*, silver) to room temperature. Prior to mold dissolution and tensile testing, the metal was therefore subjected to thermal mismatch stresses, induced by the growing difference, with decreasing temperature, in thermal contraction between the mold and the cast metal. If resulting thermal stresses are relieved by the emission of dislocations, as is the case for metal matrix composites [300], replicated microcellular aluminum [301], or hot-embossed silver micropillars [36], then there will be a contribution to the forest dislocation density from geometrically necessary dislocations that have been emitted in the silver microsamples to compensate for this differential shrinkage. One can therefore expect that $\rho_f$ be, in present samples, the sum of:

(i) a scale-independent, density $\rho_{f,0}$ of dislocations characteristic of bulk silver cast under present conditions. This we estimate from the CRSS of the 1 mm diameter castings (or 100 μm for the case of Al), $\tau_{bulk} = \alpha_2 \mu b {\rho_{f,0}}^{1/2}$, and

(ii) a scale-dependent density $\rho_{f,D}$ of dislocations emitted to compensate for differential thermal shrinkage between the silicon mold and the silver microcasting:

$$\rho_{f,D} = N \frac{\Delta\alpha \Delta T}{bD} \qquad \text{Equation 5-4}$$

where $\Delta\alpha$ is the difference in thermal expansion coefficient between silicon and silver, and $\Delta T$ is the thermal excursion experienced during cooldown from casting temperatures. Fitting this equation to data (Appendix 1) yields a value of parameter $N$ equal to 16.4 for Ag and 1.7 for Al. For silver the value is a little high; for both, however, it is for both of a realistic magnitude. For copper, with only two sizes investigated data were insufficient to credibly deduce a value for $N$.

Writing $\rho_f = \rho_{f,0} + \rho_{f,D}$, with $\rho_{f,D}$ from Equation 5-4 and with the above values for $N$ one obtains the continuous and dotted lines in Figure 5-8a for silver and aluminum respectively. Equations 5-1 to 5-4 thus capture, using reasonable values for all parameters, trends in the present data.

Present data are overall consistent with predictions of Equation 5-1, despite its assumptions (such as simply adding hardening contribution from forest dislocations to those resulting from proximity of source pinning points to a free surface despite the fact that both mechanisms operate similarly and simultaneously), exception made for microcast silver data at the lowest values of $D$ investigated, namely for $D \leq 3$ μm, Figure 5-8a. A similar upward deviation of the flow stress from predictions of a single-arm dislocation source hardening

expression close to that in Equation 5-1 was also found for nickel at $D \leq 5$ μm by Norfleet *et al.* [146] and for microcast aluminum at $D \leq 7$ μm [81,82].

If one looks at the magnitude of the initial yield CRSS (instead of its dependence on $D$), one finds that resolved yield stress values for cast copper of this work exceed those reported in the literature for FIB-milled tensile specimens of the same size (30 MPa for FIB-milled tensile specimens of diameter close to 3 μm, compared with 50 MPa for present samples of diameter 2.5 μm) [168]. The difference might reflect (i) a difference in initial dislocation density, which could be raised in microcast samples by differential thermal contraction during sample cooldown in the Si mold, and/or (ii) an effect of gallium implantation in samples that were produced by FIB milling (a higher strength was similarly observed in lithographically-produced silicon pillars compared with their FIB-milled counterparts [47,49]).

Focusing on silver, Figure 5-8b adds data from other studies of the deformation of microscale silver, all of which are for $D < 2.5$ μm ($b/D > 1.15\ 10^{-4}$). Literature data are highly scattered; also, they differ according to each sample type and thus point to the importance of processing on the properties of microscale metals. Recrystallized hot-embossed pillars (for which resolved shear stress were deduced here assuming a Taylor factor of 3 [36]) and also pristine precipitated nanocubes, evidence a higher rate of increase in flow stress with $b/D$ than is predicted by Equations 5-1 to 5-4: a transition at $b/D \approx 10^{-4}$ from source-control to dislocation nucleation control of the flow stress is a possible reason for this, since both structures are ones in which the initial dislocation density is likely far lower than in microcastings. Also, hot-embossed pillars contained grain boundaries and twins, which may also have raised the yield stress compared to the present, single-crystalline twin-free samples. Pillars FIB-milled from nanocubes [138] (inverted cyan triangle) present a lower yield stress and a lower rate of increase of stress with decreasing size than do other samples. This is likely because the flow stress of those samples is that of a composite of relatively dislocation-free metal surrounded by a layer of material containing defects that were introduced during FIB milling, which likely eases the nucleation of slip across the softer core.

Alloying copper with 1 wt.% silicon increases, in samples oriented for easy glide, the CRSS from roughly 30 to 40 MPa. This illustrates the potential of alloying for the strengthening of microcast metal components noting, however, that precipitation hardening is likely to be a better approach to this end. No influence of the silicon addition on the rate of work hardening can be noted. The flow stress displays in this alloyed sample a greater degree of fluctuation than it does for pure copper. This might be related to the known role of silicon in lowering the stacking fault energy of copper, influencing in turn mechanisms that trigger and/or terminate strain jumps [81,302,303].

Microcast silver coated with silicon nitride demonstrates the potential of coated structures to sustain considerably higher stresses than their metallic counterparts: dividing the load drop experienced by the samples upon fracture of the coating by its cross-sectional area returns peak stress values in the ceramic that

exceed 1 GPa. Following the failure of the coating, the sample flow stress falls to a far lower value, in the range 100-150 MPa if stress is computed with reference to the total sample cross-sectional area. This rises to the range from roughly 150 to 250 MPa if the load is divided only by the metal cross-sectional area. The CRSS at initial yield of microcast silver of roughly similar diameter (4 μm) is on the order of 28 MPa (Figure 5-5), corresponding to a tensile yield stress in the range of 56 to 100 MPa depending on the initial crystal orientation (the Schmid factor is in the range 0.27-0.5). This difference between the coated metal flow stress right after the rupture of the nitride coating and the uncoated metal yield stress gives a rough measure of the interfacial strength of the metal/ceramic interface if we assume that the two apparent tensile yield stresses differ by a hydrostatic stress equal to the lateral metal/ceramic interfacial tensile stress. This gives an interfacial tensile strength on the order of 100 MPa, denoting a relatively strong bond between the silver core and silicon nitride coating.

### 5.3.2 Work hardening rate and slip characteristics

Upon tensile deformation, microcast silver and copper samples display typical attributes of microsample plasticity, namely intermittency and a size-dependent flow stress. Resolved stress-strain curves furthermore exhibit the strong dependence on crystal orientation that is typical of macroscopic face centered cubic (FCC) single crystals [91,109,304]. Thus, for both silver and copper, samples oriented for multiple slip show far higher rates of work hardening than do samples oriented for single slip, Figures 5-5 and 5-7. There are also attributes of microsample plasticity in the orientation-dependent deformation of the present micropillars, notably a far greater extent of Stage I, *aka* easy glide, deformation than one observes in bulk crystals [81–83,118,304].

Samples of Ag or Cu oriented for multiple slip generally show homogeneous deformation, with less visible and multiply oriented slip steps. Failure of those samples is by necking and ductile rupture. Castings oriented for single slip exhibit more localized slip, with clearly visible, often rather large, parallel slip steps, as seen on right-hand pictures of Figure 5-6 and consistent with data for aluminum in Ref. [81] or copper in Ref. [305].

The dimensionless rate of work hardening ($\theta$), defined as $\theta = \frac{d\tau}{d\gamma}$ was calculated by taking for each tested sample the slope of a straight line fitted through resolved stress-strain data between $\gamma = 0.1$ and $\gamma = 0.3$. Results are plotted in Figure 5-9 for each sample tested versus the sample diameter $D$ together with an indication, by means of color, of the sample orientation on the stereographic triangle. As seen, the dimensionless work hardening rate depends strongly on crystal orientation and less so on sample diameter. This reflects the dominant importance, in the work hardening of these FCC metals, of dislocation interactions across different glide planes. Usual values measured in bulk FCC crystals are $\theta \approx 3\ 10^{-3}\mu$ to $10^{-2}\,\mu$ for Stage II and $\theta \approx 10^{-4}\,\mu$ to $5\ 10^{-4}\,\mu$ for Stage I (easy glide) [109,112,306,307]. Present data for microcast samples oriented near <111>, which display from the onset of deformation shallower and multiply oriented slip steps characteristic of multiple slip, give $\theta_{II}$ in the range from 1.4 to $2.7\ 10^{-3}\,\mu$ for silver, and $\approx 1.25\ 10^{-3}\,\mu$ for

copper, *i.e.,* slightly below the usual range for FCC crystals or, more specifically, the work hardening rate measured on bulk silver crystals ($\approx 3.1\ 10^{-3}\,\mu$). This observation parallels results obtained in Ref. [109], where the work hardening of copper crystals was found to decrease for wires of diameter falling below $D$ = 200 μm. It has as its most obvious reason a reduced rate of dislocation accumulation due to dislocation escape through the surface. Samples oriented for single slip and showing a single set of parallel slip steps show work hardening rates so low as to not be distinguishable from zero as a result of the highly intermittent nature of plastic flow in such orientations. The best one can therefore conclude for samples oriented for easy glide is that data are not incompatible with hardening rates generally observed in Stage I of FCC crystal deformation.

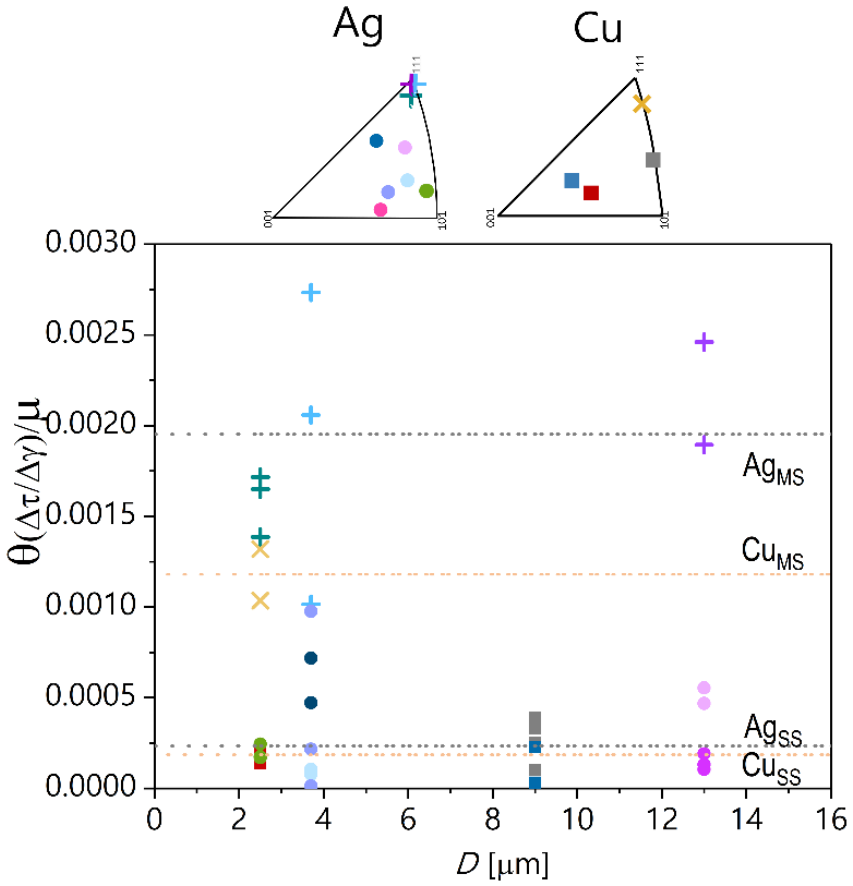


**Figure 5-9** The dimensionless rate of work hardening($\theta$), defined as $\theta = \frac{d\tau}{d\gamma}$ adimenzionallized by the shear modulus $\mu$ vs. sample diameter of silver (circles and +) and copper (squares and X) microstructures. The color of each point corresponds to the initial sample orientation on the stereographic triangle. Horizontal dotted lines give average values for samples respectively oriented for single (SS) or multiple slip (MS).

## 5.4 Conclusions

In-situ SEM microtensile tests performed on microcast silver and copper specimens lead to the following conclusions:

(i) The yield stress of silver microcastings is affected by $D$, while no evident effect of the crystal orientation is observed, irrespective of the sample size.

(ii) The flow stress predicted by the single arm source analytical expression in Equation 5-1 underpredicts the observed rate of increase of the flow stress with decreasing $D$ if one only considers the effect of

single arm source length $L$. The discrepancy is explained if the forest dislocation density includes a scale-dependent population of geometrically necessary dislocations, the likely source of which is compensation for differential thermal shrinkage between the silicon mold and silver microcastings during cooldown after casting and solidification.

(iii) The rate of work hardening depends chiefly on the crystal orientation, with wires oriented for single slip presenting an extended easy-glide stage, and microcastings oriented for multiple slip deforming as expected directly in Stage II but with a lower work hardening rate than their bulk counterparts.

(iv) Samples oriented for multiple slip deform homogeneously while localized deformation and discernible slip steps are evident on crystals oriented for single slip, particularly when $D < 5$ μm. Post-test examination reveals an absence of twins.

# Chapter 6 Mechanical Behavior of Microcast Silver Structures at Elevated Temperatures

In this chapter, displacement-controlled *in-situ* tensile tests at elevated temperatures (200 °C and 400°C) are conducted on silver microstructures; results are compared with data from the previous chapter as concerns yield and work hardening, while features of intermittent plasticity are entirely shown and discussed here.

Disclaimer: This chapter contains literal reproduction of full paragraph and figures of a publication entitled "*The Effect of Size, Orientation and Temperature on the Deformation of Microcast Silver Crystals*", which is in the process of submission to a refereed journal and to which the author has contributed. Specifically, the author contributed in the conception of the process, conducted the infiltration of the molds, characterization of components after demolding and was part of the data curation and data analysis, together with Prof. Andreas Mortensen. Dr. Simone Frasca fabricated the silicon substrates.

## 6.1 Materials and Methods

A full description of the sample preparation, experiments and data curation are provided in Section "5.1 Materials and Methods". All tests are carried out at the same nominal strain rate of $10^{-3}$ $s^{-1}$ as at room temperature, in intrinsically displacement-controlled mode and using the same testing apparatus fitted with a high-temperature stage (FT-SEM-HT04, FemtoTools), which enables tensile tests at elevated temperatures. This stage is coupled with microelectromechanical (MEM) system based microforce sensing probes (FT-S200'000-HT) that feature integrated tip heating. This enables temperature matching between sample and tip before testing, so as to ensure isothermal conditions along the sample length. Cooling of the equipment is achieved by a solid copper heat sink, which is coupled with an active fan, ensuring the integrity of the equipment and a constant signal noise floor even at high temperatures.

### 6.1.2 Load drop detection and analysis

Plastic deformation at the microscale generally displays an intermittent series of load drops (or strain bursts in load-controlled testing systems). Raw data are collected at 96 kHz. The signal is filtered by means of a moving average filter with a window size of 250, applied twice. A detailed description of the implementation of this type of filter for the analysis of intermittent deformation can be found in Ref. [80]. To evaluate the standard deviation on the load signal, tests in which the microforce sensing probe is compressed against a silver matrix

and held during 10 s show that, after filtering, the standard deviation on the load-signal remains consistently below 4 μN, regardless of the test temperature.

Drops in the load signal are extracted using Python v4.0 (Python Software Foundation). A drop in the load signal is taken to start when the difference between two consecutive points is positive; it ends when this difference becomes negative. Since this definition would also include any downward variation of the signal due to noise, the load drop is only considered and recorded as such if its amplitude exceeds 15 μN, which is close to four times the measured standard deviation of the load-signal. In addition, during a drop any intermediate upward fluctuation in load of extent below 20 (96 kHz) datapoints, thus lasting less than ≈ 0.2 ms, is viewed as inconsequential and considered to be part of a single strain burst event. When a detected drop in load complies with these requirements, its amplitude, duration, onset, end time and end force are recorded.

## 6.2 Results

### 6.2.1 The influence of temperature on the tensile behavior

Figure 6-1 plots resolved stress-strain curves for wires of diameter 13 μm, ~8 μm, 3.7 μm and 2.5 μm, for specific crystal orientations, at room temperature (RT), $T$ = 200 °C and 400 °C. These temperatures correspond for silver to homologous temperature $T/T_m$ values (where $T_m$ is the melting point) of 0.24, 0.38 and 0.54 respectively. As seen, no sample shows a strong alteration of the shape of its resolved stress-strain curve at any of these temperatures, while the flow stress, the apparent rate of work hardening and the strain to (ductile) failure all decrease as $T$ increases.

The work hardening rate (WHR), defined as $\theta = d\tau/d\gamma$ is, given the highly jagged shape of the curves collected from microcast samples, hard to compute, variable, and low for samples that are initially oriented for single slip. For castings oriented close to the <111> corner of the stereographic triangle, $\theta$ is better defined and computed for each tested sample as the slope of a straight line fitted through resolved stress-strain data between $\gamma = 0.1$ and $\gamma = 0.3$. Results are reported in Table 6-1.

**Table 6-1** Work hardening rate ($\theta$), defined as $\theta = d\tau/d\gamma$, for castings oriented close to <111> corner as a function of diameter and temperature.

| D [μm] | Temperature [°C] | $\theta$ [MPa] | Reference |
|---|---|---|---|
| Bulk (D1 mm-yet not <111>) | RT | ~75 | Chapter 5 |
| 13 | RT | 50-62 | Fig. 6-1a |
| | 200 | 40-42 | |
| | 400 | 10-15 | |
| 8 | RT | 63.5-67 | Fig. 6-1d |
| | 200 | 37-56 | |
| | 400 | 15-16 | |
| 3.7 | RT | 53-72 | Fig. 6-1f |
| | 200 | 25.5-26 | |
| | 400 | 10-12 | |
| 2.5 | RT | 44-52 | Fig. 6-1k |
| | 200 | 26.5-47 | |
| | 400 | 1-30 | |

**Table 6-2** Summary of the influence of temperature on microcast tensile sample slip traces along the sample surface classified according to the sample diameter and initial crystal orientation.

| $D \geq 7$ μm | | $D \leq 4$ μm | |
|---|---|---|---|
| **Single Slip (Figure 6-1b-c & e)** | **Multiple Slip (Figure 6-1 a & d)** | **Single Slip (Figure 6-1 g-i, j & l)** | **Multiple Slip (Figure 6-1 f & k)** |
| Spacing of slipped regions increases with increasing $T$ (Figures 6-2 a-d Supplementary videos 5,6&7) | No evident alteration as $T$ increases (Supplementary videos 8,9&10) | Slipped regions gradually narrow and are further spaced apart with increased $T$, leading to a concentration of deformation along selected single slip planes (Figures 6-2 e-f and i-j and Supplementary videos 11,12&13) | Onset of strain localization, still on multiple slip systems, increases with increased $T$ (Figures 6-2 g-h and Supplementary videos 14,15&16) |

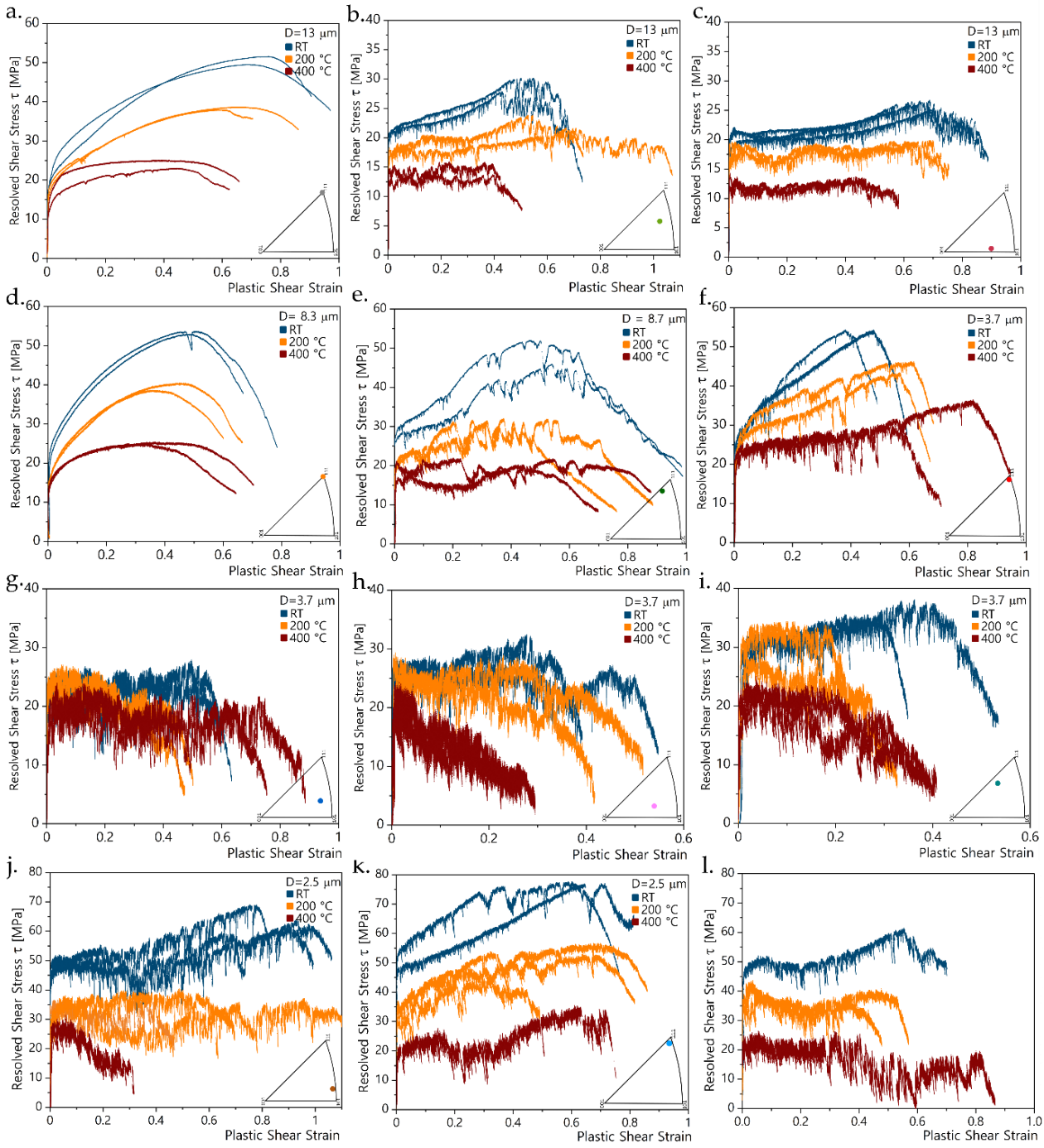


**Figure 6-1** Resolved shear stress vs. plastic shear strain for wires of $D$ = 13 µm, $D$ ~ 8 µm, $D$ = 3.7 µm and $D$ = 2.5 µm, with particular crystal orientations, at room temperature (RT-blue), 200 °C (orange) and 400 °C (red). Inset shows the sample orientation within the stereographic triangle, with the color referring to that of the room temperature curve in Figure 5-5 of Chapter 5).

The influence of temperature on general wire deformation characteristics is summarized in Table 6-2. Present tests being conducted *in-situ* in the SEM, one can observe the evolution of slip steps along the sample surface (albeit at a lower frequency of observation than load drop recordings). Figure 6-2 displays images of microcastings after tensile testing at 200 °C and 400 °C, to be compared with those reported in Chapter 5, Figure 5-5 and Figure 5-6.

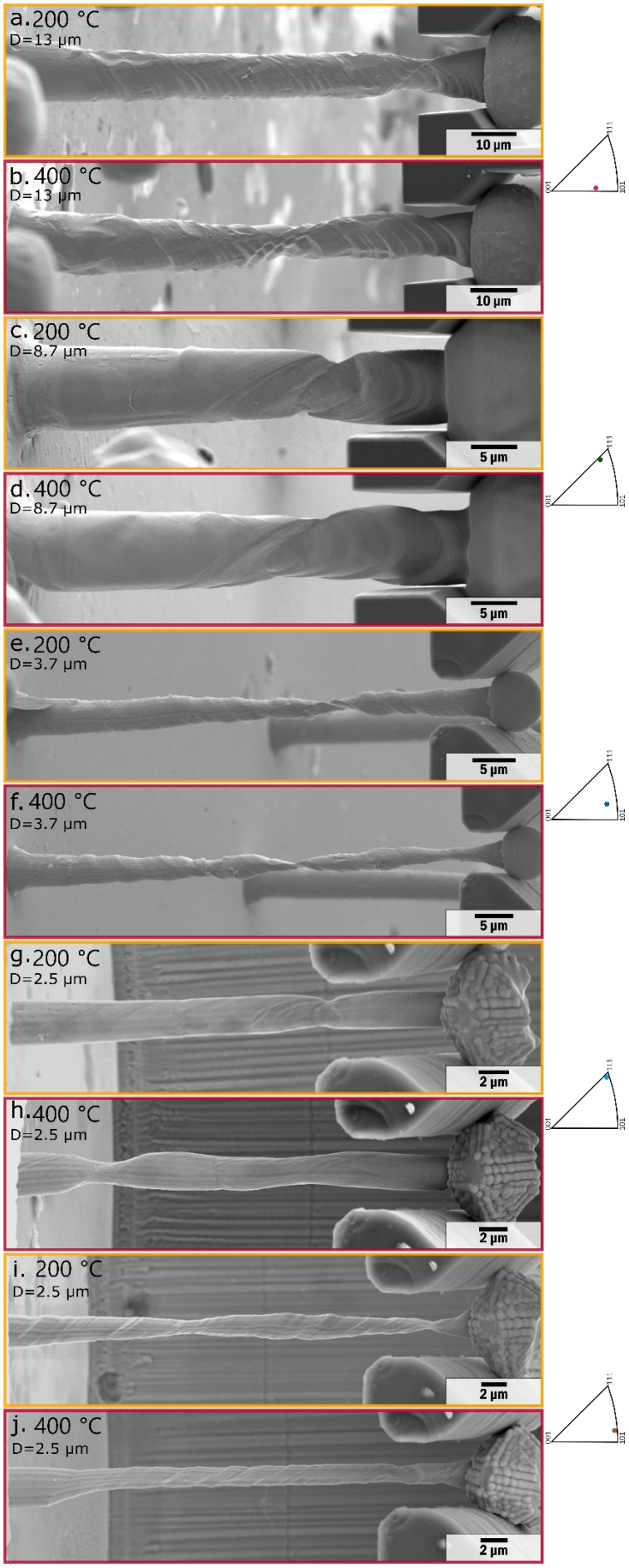


**Figure 6-2** Representative SEM images of microcastings with different sizes and crystal orientation after tensile testing at 200 °C (orange image border) and 400 °C (red image border). Point within stereographic triangles indicates the initial crystal orientation with respect to the tensile axis, with the color referring to that of the room temperature tensile curve in Figure 5-5 of Chapter 5.

## 6.2.2 Intermittency

Strain bursts, characteristic of confined plasticity, are amply present in the deformation of the microcast samples, Figure 6-1. Quantification of their magnitude has been conducted in the literature by various means: by acoustic emission [205,207,213–215], image-based analysis [218], by analyzing their duration time, by recording the axial displacement during each event [201,219,220], or as in the present work, by measuring the magnitude of the load drop [81,149,204]. The magnitude of each corresponding resolved slip displacement can then be deduced as:

$$s = \frac{\Delta F\, K}{S} \qquad \text{Equation 6-1}$$

where $K$ is the system compliance [μm/μN], $\Delta F$ is the measured load drop and $S$ is the Schmid factor for the active glide system(s) [81,204].

Measured distributions of the strain burst (resolved) displacement amplitude $s$ in the slip plane and direction are plotted in Figure 6-3 as complementary cumulative distribution functions (CCDF) P(s), giving the emission probability of a strain burst of amplitude greater than $s$, with $s \geq s_{min}$ taken to equal four times the signal noise level of the present micro-mechanical system. $s_{min}$ varies in the range 1.5-6 nm because it depends on $S$ and on $K$. Complete datasets can be found at 10.5281/zenodo.7373750.

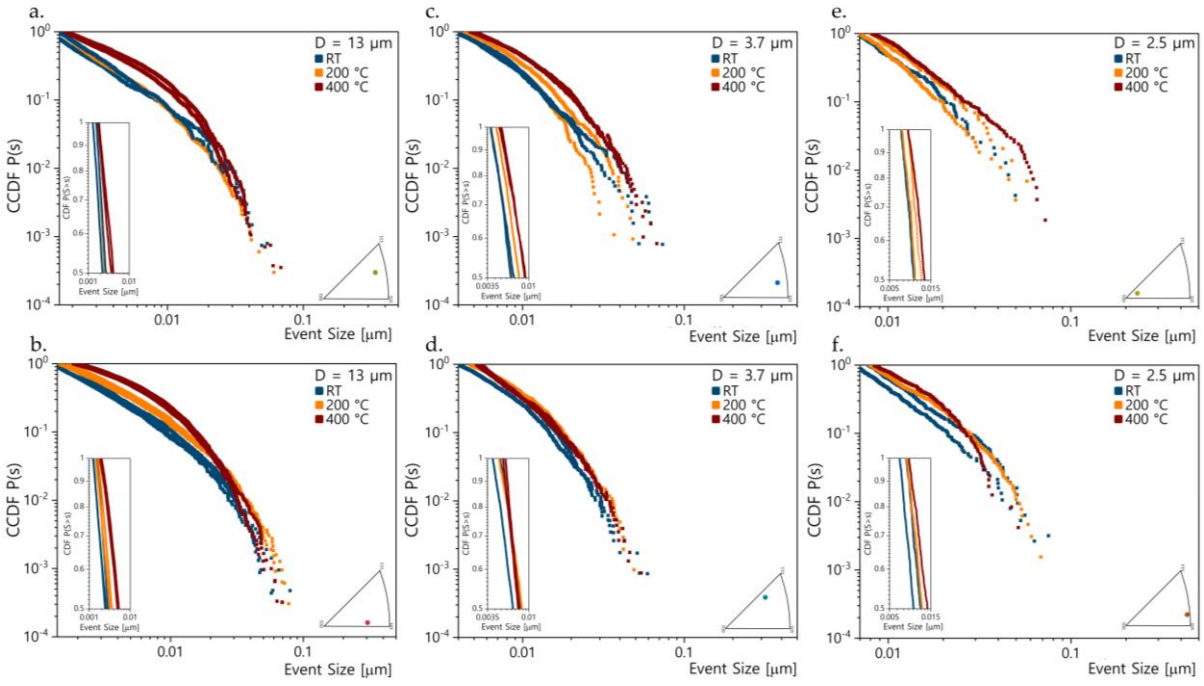


**Figure 6-3** Complementary cumulative distribution function of slip events as a function of temperature (RT-blue; 200 °C-orange; 400 °C-red) for D13 μm, D3.7 μm and D2.5 μm plotted in log-log coordinates. Insets display linear portions of the CDF at small event sizes.

## 6.3 Discussion

### 6.3.1 Yield

Data in Figure 6-1 confirm what was reported earlier for the room-temperature deformation of microcast metal tensile samples [81,82,289], namely that:

(i) reducing the sample diameter $D$ raises the critical resolved shear stress (CRSS) for initial yield, with little evident effect of the crystal orientation on the CRSS, while

(ii) past yield the crystal orientation influences strongly the work hardening rate of the material and hence its flow stress, with a clear separation between samples initially oriented for single or for multiple slip.

We extend here those observations to 200 and 400 °C. Unlike what has been concluded for the microcompression of copper pillars [194], the strength of present silver samples decreases with increasing temperature (Figure 6-1). The decrease reaches, at 400 °C, ≈ 40 % of the room-temperature CRSS, in overall good agreement with data reported for bulk silver crystals [308]. The low difference in initial yield strength between castings oriented for single or multiple slip is maintained at elevated temperature.

Figure 6-4 displays the measured CRSS, made dimensionless by division with the shear modulus of silver, $\mu$, for each of the three temperatures, plotted versus the ratio of the burgers vector $b$ to the sample diameter $D$. As in Section "5.3.1 Yield" of Chapter 5, the shear modulus $\mu$ is the Reuss average. This gives $\mu$ = 25.6 GPa for silver at room temperature [299], with a variation as a function of temperature that is given in Ref. [309]. The ratio $b/D$ is computed at room temperature by taking $b$ = 2.88 Å [295] and is assumed not to vary since both lengths increase similarly upon heating (the linear thermal expansion coefficient of the sample is roughly the same as that of the average interatomic bond length).

Figure 6-4 shows that, exception made for the finest ($D$ = 2.5 μm) samples deformed at room temperature, division of the resolved flow stress by $\mu$ brings all data points within the same range. The temperature dependence of the flow stress that is observed in Figure 6-1 can thus entirely be attributed to variations in the stiffness of atomic bonds. The implication is that between 20 and 400 °C the mechanisms that govern plastic flow are likely the same and that there is no visible influence of thermally activated phenomena, such as the propensity for cross-slip or for dislocation release from locks, on the yield stress of microcast silver for all except $D$ = 2.5 μm room-temperature data.

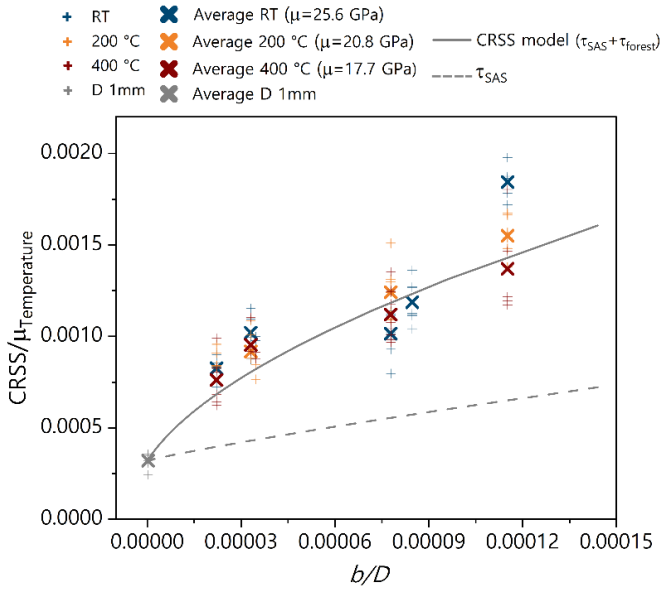


**Figure 6-4** Ratio of the critical resolved shear stress (CRSS) at a plastic strain of 2% to the shear modulus μ of silver at the corresponding temperature vs. b/D, with D the tensile specimen diameter, for the tensile deformation of microcast silver at all three temperatures. Vertical crosses are datapoints from individual samples; larger diagonal crosses are averages of those points for each value of temperature and sample diameter. Data points are also given for cast crystals 1 mm in diameter of the same pure silver (points close to b/d=0). Solid and dashed lines represent values predicted by the single arm source model, introduced in Section "5.3.1 Yield".

### 6.3.2 Work hardening and slip

Post-test EBSD examination of silver microcast sample surfaces reveals a uniform crystal orientation throughout the gauge length, with no sign of twins. Plastic deformation of the present microcast samples is thus entirely driven by slip. This is similar to what is reported for nanopillars of gold (of SFE similar to that of silver) [44,22], but differs from observations on polycristalline silver pillars produced by hot embossing: these contained preexisting twin boundaries produced during recrystallization after embossing, such that their deformation was driven by both dislocation slip and twinning [36].

Slip steps in microcast silver samples (particularly for $D > 8$ μm) are small in comparison with large slip traces observed in microcast aluminum of similar size (6 to 25 μm), also tested in tension [81,82,310]. Two explanations for this difference can be advanced. The first is that present tests were conducted with a far stiffer load train than were tests of Ref. [81,85]. This leads the resolved shear stress to decrease much faster during a strain burst in the present silver samples than in microcast aluminum tensile tests (see next section). The second explanation is linked to the presence of a nanometric oxide scale on the cast aluminum wires. This is known to create a barrier to dislocation escape along the sample surface [82,83]: gliding dislocations therefore need to pile up at the oxide-aluminum interface before they collectively break the oxide layer and escape through the surface, explaining in turn why slip steps may tend to be larger in aluminum than in a noble metal such as silver.

In microcast crystals oriented for multiple slip, as the temperature increases, $\theta_{II}$ decreases, and in crystals oriented for single slip with $D \leq 3.7$ μm even changes sign, (Figure 6-1). Variations of $\theta_{II}$ with temperature are stronger than the rate of decrease of elastic moduli, unlike data for low-SFE bulk FCC single crystals, which tend to vary with temperature in proportion with $\mu$ [311]. Comparing work hardening rates with the

evolution of stiffness, one finds that multiple slip values at room temperature, which are roughly centered around $\theta_{II,RT} \sim 60$ MPa, correspond to $\theta_{II,RT} \sim 2.3\ 10^{-3}\ \mu$, (with $\mu \sim 25.6$ GPa at room temperature), while $\theta_{II,400\,°C} \sim 15$ MPa represents $8.4\ 10^{-4}\ \mu$, given that $\mu \sim 17.7$ GPa at 400 °C. $\theta_{II}$ thus decreases faster with increasing temperature than does $\mu$. The same can be said for samples oriented for single (Stage I) glide, given that $\theta_I$ is found to even change sign as the deformation temperature is raised, Figure 6-1. Thus, unlike the yield stress, the observed variation of $\theta$ with temperature suggests that there is an evolution, with increasing $T$, in mechanisms that govern dislocation accumulation within the present samples. One explanation for this can be found in the fact that, as the deformation temperature rises, so does the contribution of intermittent deformation (of amplitude above the present measurement threshold) to the overall microcast sample deformation. This is shown by computing the sample elongation caused, over each tensile test, by summation of all detected sudden strain burst events, where the elongation ($\Delta l$) due to each sudden event ($s$) is given by $\Delta l = s.S$ (with $S$ being the Schmid factor). The result, given in Table 6-3, shows the percentage of the total elongation that can be attributed to detected strain burst events in samples oriented for single slip. Although the variation with $D$ at fixed temperature lies within scatter, it is evident that the contribution of intermittent deformation to the overall sample elongation increases with increasing temperature. That an increased proportion of larger amplitude strain bursts comes with a lower average recorded rate of work hardening suggests that strain bursts in microcast crystals lead on average too little, or no, dislocation accumulation. Such is, for instance, the case if a significant fraction of strain bursts results from the repeated operation of single arm sources.

**Table 6-3** Contribution of (recorded) intermittent deformation to the overall sample elongation in samples oriented for single slip.

| | % of deformation due to sudden events | | |
|---|---|---|---|
| D [μm] | RT | 200 °C | 400 °C |
| 13 | 16-18 | ~31 | 33-56 |
| | 12-15 | 35-40 | 44-52 |
| 3.7 | 8-11 | 11-18 | 33-38 |
| | 37-40 | 50-54 | 58-67 |
| | 37-40 | ~44 | 60-85 |
| 2.5 | ~19 | 20-35 | ~49 |
| | 21-26 | 28-38 | ~50 |

Increasing the temperature causes no change in the operative slip systems (Figure 6-2) but, similar to the effect of a decrease in $D$ and in line with a greater proportion of slip occurring in bursts as $T$ rises, this increases slip localization, Table 6-2 and Figure 6-2. As a result, individual slip steps along the sample surface are larger after deformation at elevated temperatures (this is visible if one compares Figure 5-6 and Figure 6-2). The ensuing localization of slip in selected regions of the samples may be sufficient to rotate significantly the glide plane towards the tensile axis, causing a new source to be activated in a different non-deformed region, such that the wire continues to deform instead of fracturing in shear. More localized deformation also

comes with a reduction in area where the sample deforms; this likely contributed to the negative $\theta$ values displayed in some experiments (Figure 6-1).

### 6.3.3 Intermittency

It has been amply documented that the complementary cumulative probability distribution of strain burst amplitudes recorded in the deformation of small-scale samples follows, in a range of amplitudes just above the noise level and below a cut-off value ($s_c$) that limits the size of avalanches, a power-law distribution such that $P(s) \propto s^{-\lambda}$, where $\lambda$ is an exponent predicted by mean field theory to equal 1/2 [198,200,201,204,220]. This is tested in Figure 6-5, which plots $P(s)$ versus $s^{-1/2}$ (this plot has the advantage that it gives equal weight to each data point, unlike the more usual plots of log (P(s)) versus log($s$), which bundle low-intensity drops into the upper left-hand corner of the plot as the one shown in Figure 6-3). As seen, exception made for some of the 400 °C data, the curves are linear or nearly so over a range of the CCDF that extends immediately above $s_{min}$ from $P(s)= 1$ to a value of $P(s)$ situated between 0.25 and 0.5. Between one-half and 75 % of recorded bursts thus agree with the lower-intensity power-law regime predicted by mean-field theory. It is furthermore seen that, for a given sample, the slope of the line in this power-law regime remains the same at all three temperatures. This, in turn, suggests that dislocation mechanisms that govern strain bursts remain the same between 20 and 400 °C, similarly to what is found for the yield stress (see Section "6.3.1 Yield").

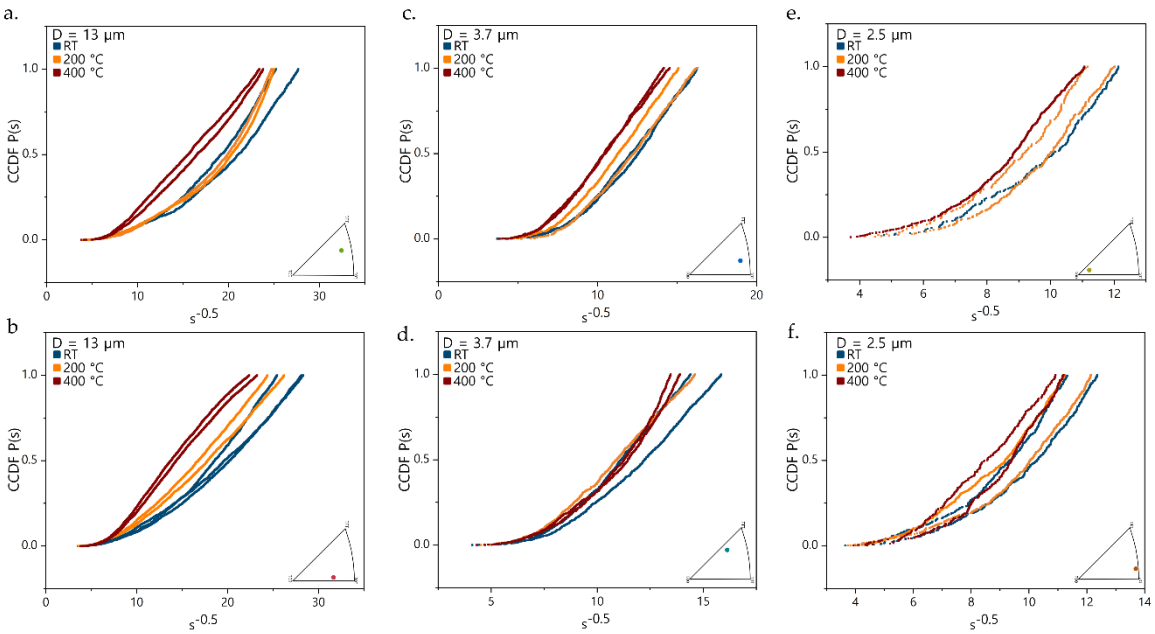


**Figure 6-5** Plots of measured complementary cumulative distribution functions (CCDF) P(s) for samples of different size and orientation tested at three different temperatures, plotted versus the inverse square root of the resolved strain burst amplitude $s$. A straight line corresponds to $\boldsymbol{P(s) \propto s^{-1/2}}$.

At burst amplitudes exceeding roughly $s$ = 0.01 µm, $P(s)$ deviates from this power-law, Figure 6-5. Plotting now the same data in semi-logarithmic coordinates, Figure 6-6, one obtains relatively straight lines at higher strain burst amplitudes for nearly all samples. In the higher-amplitude, cut-off, regime, data thus conform with a simple exponential decay of the CCDF. The same result was found for microcast aluminum in Ref.

[81], ice crystals [213,229], and also for a high-entropy alloy in Ref. [220] (Eq. 2 and Fig.3 in [220]). An exponential decay of the CCDF also agrees with what was observed for copper and aluminum nanopillars in Ref. [204] (J. Alcalá and J. Ocenasek, private communication: the best fit with data is found with n = 0.8 in Eq. 3 of Ref. [204]; however those data are also compatible with $n = 1$). In other words, our data and those of three other studies conform with:

$$P(s) \propto s^{-0.5}\, e^{-\left(\frac{s}{s_c}\right)} \qquad \text{Equation 6-1}$$

This expression and present data are at variance with the more usually adopted cutoff expression given in Refs. [198,200,312], namely

$$\frac{dP(s)}{ds} = p_{(s)} \propto s^{-1.5}\, e^{-\left(\frac{s}{s_c}\right)^2} \qquad \text{Equation 6-2}$$

since, unlike present data, in semi-logarithmic coordinates the relation in Equation 6-2 does not produce a linear CCDF (Appendix 1- Zaiser-Nikitas expression for the complementary cumulative distribution function).

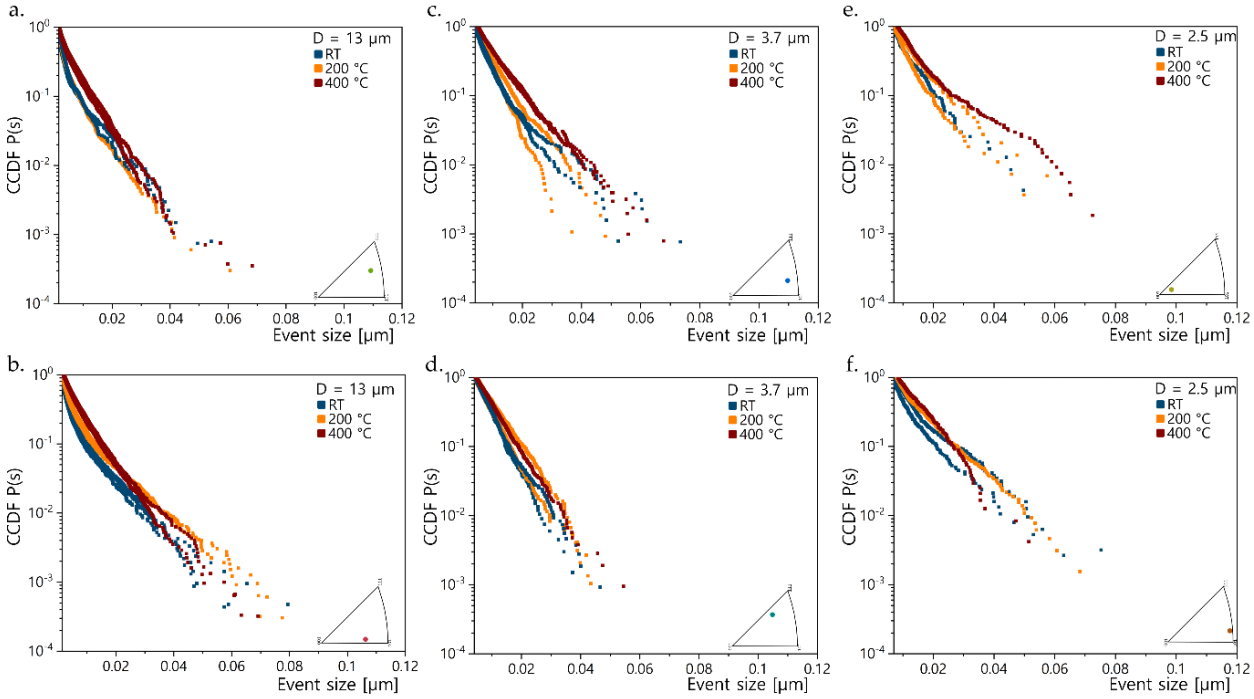


**Figure 6-6** Complementary cumulative distribution function of slip events (CDF) as a function of temperature (RT-blue; 200 °C-orange; 400 °C-red) for D13 µm, D3.7 µm and D2.5 µm plotted in log-linear coordinates. A straight line corresponds to $\boldsymbol{P(s) \propto e^{-\left(\frac{s}{s_c}\right)}}$.

Another observation that emerges from Figure 6-6 is that recorded strain burst amplitudes are all smaller than 0.1 µm and are thus well below the size of observed slip steps in deformed samples oriented for single glide. The implication, which was confirmed by *in-situ* observation of the sample surfaces during tests, is that the largest slip steps along deformed crystals oriented for single glide are the result of a sequence of several far

smaller strain burst events along the same plane, an observation that was also recently reported for slip in FCC high-entropy alloy nanopillars [220]. In consequence one must exert caution when equating final slip step amplitudes along the surface of a deformed sample with burst event amplitudes.

Equation 6-1 reduces to $P(s) \propto e^{-\left(\frac{s}{s_c}\right)}$ when $s$ exceeds the cut-off value $s_c$. Values for $s_c$, computed by a linear fit (as in Refs. [81,204]) of data for $P(s) > 0.1$ in the semi-logarithmic plots in Figure 6-6 are presented in Table 6-4 for each sample size and orientation. Assuming that larger slip events are generated by the operation of a single arm source, their amplitude then corresponds in present samples to a characteristic number of arm turns $\bar{N}$ ($= s_c/b$) that is in the range from 20 to 60 (Table 6-4).

Plots in Figure 6-6 show that, within experimental uncertainty, the slope of lines in each plot, and therefore the characteristic burst size distribution, does not vary much with temperature. Since the same observation holds for the power-law regime of burst intensities, one can conclude that across the entire range of measured strain burst amplitudes there is no sign of a change in the underlying mechanism as the temperature varies from 20 to 400 °C. In this regard, present data again agree with findings in Ref. [204] for FIB-milled copper nanopillars oriented for multislip, also tested between 20 and 400 °C using a rigid strain-controlled nanoindentation apparatus, where $\bar{N}$ values were in the same range, $\bar{N}$ = 4 to 44, and did not vary significantly with temperature.

Microcast aluminum wires produced $\bar{N}$ values in the range of 300 to 900 [81]. We can propose two explanations for this large difference between $s_c$ values measured here for silver (or in Ref. [204] for copper nanopillars), and values for microcast aluminum [81]. The first takes the view that larger strain bursts are mainly produced by a rotating single-arm source. This is consistent with the fact that large strain bursts were observed generally to come with the growth of large slip steps at a few well-defined locations. In that view, a strain burst event distribution that obeys $P(s) \propto e^{-\left(\frac{s}{s_c}\right)}$ is the signature of a single-arm source (SAS) that operates with a constant probability $e^{-\left(\frac{b}{s_c}\right)}$ that its operation will remain active after each turn of the arm. The probability that the SASs stop at any given turn is then on the order of $1- e^{-\left(\frac{b}{s_c}\right)} = 0.025 \approx \left(\frac{b}{s_c}\right)$, which is here roughly ten times higher than was found for aluminum. A potential explanation for this could be that, because the stacking fault energy is far lower in silver (and copper) than in aluminum, the propensity for lock formation is far higher, leading to a far more frequent blockage of SAS activity in low stacking fault FCC metals by interference from cross-cutting dislocations.

**Table 6-4** Average cut-off values of the CCDF for different sample sizes and temperatures, from the slope of curves in Figure 6-6.

| D [µm] | Temperature | $s_c$ [µm] | $\bar{N}$ | Crystal orientation |
|---|---|---|---|---|
| 13 | RT | 0.011-0.015 | 41-52 | 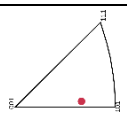 |
| | 200 °C | 0.0149-0.155 | 51-53 | |
| | 400°C | 0.009-0.011 | 34-39 | |
| 13 | RT | 0.009-0.0116 | 32-40 | 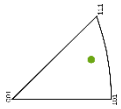 |
| | 200 °C | ≈0.012 | ≈42 | |
| | 400°C | 0.0085-0.009 | 29-32 | |
| 3.7 | RT | 0.01-0.016 | 35-55 | 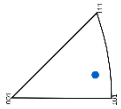 |
| | 200 °C | 0.05-0.096 | 19-33 | |
| | 400 °C | 0.01-0.011 | 34-39 | |
| 3.7 | RT | 0.006-0.0082 | 22-28 | 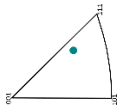 |
| | 200 °C | 0.006-0.0075 | 22-26 | |
| | 400 °C | ≈0.008 | ≈28 | |
| 2.5 | RT | ≈0.0126 | ≈44 | 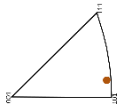 |
| | 200 °C | 0.012-0.015 | 42-52 | |
| | 400 °C | ≈0.0169 | ≈59 | |
| 2.5 | RT | ≈0.0138-0.019 | ≈48-66 | 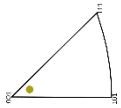 |
| | 200 °C | ≈0.012 | 42 | |
| | 400 °C | ≈0.008 | ≈30 | |

The second explanation that can be proposed for the difference between data for microcast aluminum and silver can be found in the proposal by Zaiser and Nikitas [200] that the mechanism limiting the size of a dislocation avalanche is the decrease, with the progression of slip, in the effective stress that drives dislocations during a slip event. From results of a continuum model for slip avalanches (with periodic boundary conditions) [200,312], Zaiser *et al.* predict that :

$$s_c = \frac{Cb\mu}{M + H} \qquad \text{Equation 6-3}$$

where $C \approx 5$ [200], $H$ is the work hardening rate and $M$ the system-*cum*-sample rigidity (meaning the inverse of the load train and sample compliance). In present experiments $H$ is far smaller than $M$, while $M$ is given by the measured stiffness $J$ displayed by the force-displacement curve, according to $M = \frac{JDS^2}{A_0}$ with $S$ the Schmid factor, $A_o$ the cross sectional area of the tensile sample and $D$ the sample diameter (see Section 2.2 in the Supplementary Material of Ref. [81]). Parameters for some experiments are given in Table 6-5, together with $s_c$ values predicted by Equation 6-3. The equation proposed by Zaiser *et al.* overestimates data somewhat, but gives values for $s_c$ that are of the right order of magnitude, regardless of the testing temperature, for both the present samples and for aluminum data of Ref. [81], where the largest avalanche sizes were an order of magnitude higher than here, as was the load train compliance (see Section 2.3 in the Supplementary Material of Ref. [81]). The Zaiser-Nikitas equation thus proves, across both studies, to be a reliable predictor

of the slip burst cut-off amplitude $s_c$ (even though the burst size distribution observed here and in Ref. [81] do not have the form given by Zaiser *et al.* [198,200,312]).

**Table 6-5** General parameters of tested microcastings showing sample diameter, testing temperature, stiffness (J), machined stiffness (M) from Ref. [200], measured work hardening rate (H), cutoff predicted by Equation 6-3 ($s_c$ predicted), and $s_c$ from Figure 6-6 ($s_c$ measured).

| Sample diameter [μm] | Testing Temperature [°C] | $J$ [μN/μm] | $M$ [MPa] | $H$ [MPa] | $s_c$ predicted (Eq. 6-3) [μm] | $s_c$ measured [μm] |
|---|---|---|---|---|---|---|
| 13 | RT | 24100 | 500 | 7 | 0.084 | 0.015 |
| 13 | RT | 20700 | 429 | 7 | 0.097 | 0.0143 |
| 13 | 200 | 19700 | 408 | - | 0.085 | 0.012 |
| 13 | 400 | 17700 | 367 | - | 0.080 | 0.011 |
| 3.7 | RT | 8300 | 647 | - | 0.066 | 0.016 |
| 3.7 | 200 | 7200 | 561 | - | 0.052 | 0.0096 |
| 3.7 | 400 | 6300 | 491 | - | 0.070 | 0.011 |
| 2.5 | RT | 4500 | 444 | - | 0.096 | 0.015-19 |
| 2.5 | 200 | 4200 | 414 | - | 0.071 | 0.012 |
| 2.5 | 400 | 4000 | 394 | - | 0.075 | 0.008 |

In our view, the present data do not allow us to go further in interpretation without entering speculation. Let us therefore simply note that the two views, of a SAS that operates with a constant probability of ceasing activity, and dislocation flow that ceases due to a decrease in the effective stress driving dislocation motion during a strain burst, are not mutually incompatible. Suppose for instance that the probability for a new burst to be triggered (for whatever reason) at a given SAS while the sample is reloaded after cessation of the previous strain burst at that source, be constant. If the stress at which the SAS ceases to function remains the same, then a steady burst initiation probability upon reloading will translate, upon SAS activation and consequent sample unloading, into a SAS that has at each turn a constant probability of stopping. This view, analogous to that of a helical spring that is wound an evenly distributed random number of turns before it is released to stop at the same spring tension value, will also produce a burst size CCDF that has constant probability of stopping at any given turn, translating into an exponential burst size CCDF. If then the probability of a burst being triggered while reloading is only a function of stress, then the load point displacement corresponding to each strain burst, and hence $s_c$, will be proportional to the load train compliance, as predicted in Equation 6-3.

## 6.4 Conclusions

*In-situ* SEM uniaxial tensile tests are conducted at 20 °C, 200 °C and 400 °C on cast micron-scale samples of single-crystalline silver, evaluating the effect of sample diameter $D$, orientation, and temperature $T$ on the flow stress, work hardening rate, strain intermittency, and deformation characteristics. Main conclusions are:

(i) The yield stress of silver microcastings is affected by both $D$ and $T$, while no evident effect of the crystal orientation is observed irrespective of the sample size. The decrease of the yield stress at elevated temperatures can fully be attributed to the concomitant decrease in shear modulus. This suggests that the mechanisms that govern the initiation of plastic flow in microcast silver are likely the same from 20 °C up to 400 °C.

(ii) A substantial decrease in the work hardening rate is found with increasing the deformation temperature. This decrease exceeds that of the shear modulus, brings the rate of work hardening near zero at 400 °C and is accompanied by a higher contribution of intermittent deformation to the overall sample elongation.

(iii) Increasing the temperature brings no change in the operative slip system(s) but leads to deformation gradually narrowing and concentrating in just a few pronounced slip bands.

(iv) Large slip steps along deformed crystals oriented for single glide are the result of a sequence of several smaller strain burst events along the same plane.

(v) Resolved intermittent strain burst amplitude complementary cumulative distributions display at low burst amplitudes the power-law distribution expected from mean-field theory, while at higher burst amplitudes the distribution agrees well with an exponential cumulative distribution, in line with data in Refs. [81,204,213,220,229].

(vi) Burst amplitude cutoff values do not vary, within scatter, with either $D$ or $T$, agree with data in Ref. [204] for copper between 20 and 400 °C, are an order of magnitude lower than was measured at room temperature for aluminum in Ref. [81], and agree with the expression proposed by Nikitas and Zaiser [200].

# Chapter 7 Conclusion

In the present work, structures made of silver, copper, gold and their alloys, from several to a few micrometers in size, demonstrate that metal casting offers a tangible path into the field of microtechnology. Downscaled versions of this ancient process fill a gap in microfabrication because they give the ability to turn, as is done at the macro-scale, to casting when shaped monolithic metallic microparts are to be produced. Two alternative manufacturing techniques are employed during the stage of molding, namely femtosecond laser micromachining and silicon microfabrication. Capillary forces preventing the liquid metal to flow in narrow cavities are overcome by pressure infiltration, whereas demolding is accomplished by chemical dissolution (*i.e.*, selective etching). Microcasting inherits attributes from its counterpart in the macro scale, namely excellent dimensional control, high reproducibility, full density, the possibility to alloy with great freedom the infiltrant alloy composition, and a capacity to replicate to high precision essentially any continuous shaped hollow, which can be reproduced with a resolution finer than 100 nm. Microcasting additionally offers a novel route towards the production of samples of metal of micrometric dimensions that are amenable to mechanical testing; in this work this opportunity is exploited towards the characterization of micron-size metals in uniaxial tension.

Some of the main conclusions to come out of this work are summarized in what follows.

## 7.1 Processing

Fused quartz or monocrystalline silicon substrates are attractive molding materials for microcasting because of the absence of grain boundaries in the mold, and the existence of shaping processes for each of those materials.

The fabrication of molds via femtosecond laser micromachining provides essentially full freedom of design of interconnected three-dimensional structures made of metal, that are either freestanding or embedded in the mold material. This freeform manufacturing approach opens up the possibility to fabricate geometrically complex structures, difficult or even impossible to produce by other means, and at comparatively attractive rates by comparison to bottom-up approaches. The process is shown to produce structures of dense metal that replicate with high precision hollow shapes created by femtosecond micromachining; however, challenges exist. One is the formation of cracks in the glass substrate, after solidification and during cooling. These cracks develop due to the action of thermal stresses associated with the difference in coefficients of thermal expansion between metal and substrate, especially when casting larger, millimetric structures. Another challenge is the elimination of surface porosity linked with solidification shrinkage. This was addressed in this work by the development of nearly-zero solidification shrinkage alloys, which are shown to enable the fabrication of defect-free structures over a wide range of scales, free of surface defects associated with solidification shrinkage.

Mold fabrication using single-crystalline silicon wafers, previously etched by conventional lithographic processes and coated with an intermediate layer, enables the use of conventional cleanroom processes to pattern micrometric structures; geometries are however confined to 2D or 2.5D designs. Thus, the level of part shape flexibility afforded is limited when compared with femtosecond laser micromachining of silica. Lithographic processes are, however, widespread and provide excellent dimensional control, high reproducibility, and the possibility for all steps in the process to be highly paralleled, leading to very high part production rates. In addition, it is shown that this approach introduces a new pathway to efficiently produce a large number of micron-scale specimens that are amenable to tensile testing while being free of artefacts that come with conventional FIB-based microsample fabrication. This process thus has the potential to also be of interest to the micro- and nano-scale testing community.

After infiltration and solidification, demolding is achieved by chemical dissolution, either by use of hydrofluoric acid or of potassium hydroxide to selectively dissolve fused quartz or silicon, respectively. This, together with the requirements imposed by the need for chemical stability between mold and metal at casting temperatures, narrows the list of metals that can be microcast via these processes to relatively noble metals and alloys. Given that such alloys are good conductors of heat and electricity, are chemically stable in usual working environments and can be made to have attractive mechanical properties, the two microcasting approaches developed in this work have the potential to find application in MEMS technology.

## 7.2 Deformation of microcastings

Monocrystalline microwires of aspect ratio > 4.5 were produced via microcasting, with a diameter as small as 2.5 μm. The mechanical response of microcast silver or copper, either bare or coated with ceramic, is investigated by conducting *in-situ* tensile tests under the scanning electron microscope at room- and elevated temperatures. In summary it is found that:

- The yield stress of microcastings is affected by both size and temperature, while no evident effect of the crystal orientation is observed irrespective of the sample size.
- Yield stress values at room- and elevated temperatures agree with the single arm source model such that their temperature-dependence is governed by variations in the shear modulus, and provided that the density of forest dislocations comprises a scale-dependent component likely resulting from thermal mismatch stresses during sample cooldown after solidification.
- The rate of work hardening of microcastings is, as in bulk crystals, strongly influenced by the initial crystal orientation while exhibiting lower values than their bulk counterparts, in both Stage I and Stage II of deformation.
- The decrease of this lowered work hardening rate with increasing deformation temperature exceeds that of the elastic modulus, and is accompanied by a higher contribution of intermittent deformation to the overall sample elongation.

- The statistics of strain burst amplitudes agree with an exponentially truncated power-law distribution, with the power-law exponent expected from mean-field theory and a cutoff amplitude that depends little on sample diameter or test temperature.

## 7.3 Perspectives for future work

The potential of microcasting has certainly not been fully uncovered here and several topics remain for future investigation. These include research on processing, microstructure and deformation; suggestions for work that would complement the work presented here are introduced in what follows.

Given that metal pressure-infiltration is shown to fill with great accuracy sub-micron cavities or surface features, molds with finer and smoother features including nanometric structures could be explored. Such molds can be fabricated via e-beam lithography or by downscaling, with a finer laser spot size, the femtosecond laser machining of fused silica. Similarly, further development of femtosecond laser machining to pattern alternative materials, namely sapphire or silicon, could open the process to cast other metals, or to demold by means of other etching media.

So far, monocrystalline randomly orientated microcast structures are obtained; however, alternatives to control the crystal orientation (*i.e.*, by strategically placing a seed crystal) or to fabricate nanocrystalline structures (*i.e.*, by coating cavities with a nucleation agent) could be investigated. It should be noted, however, that the latter could lead to the formation of grain boundary grooves along the metal surface if grain boundary regions are not properly fed with liquid metal during solidification.

Surface defects likely associated with solidification shrinkage have been the main processing challenge faced in this work. This issue was addressed by the development of specific alloys for microcasting, with particular requirements with respect to the melting temperature, reactivity and volume contraction upon solidification. Much more remains to be learned and achieved on this front. Nearly zero solidification shrinkage alloys are produced by adding elements such as germanium or silicon, which usually are prone to lower the mechanical properties, in particular by reducing the elongation to fracture. Thus, mastering and tailoring the chemical composition and material microstructure of such alloys are areas for future development, as is the pursuit of other approaches towards feeding solidification shrinkage in microcast metals and alloys.

Finally, in terms of processing, in this work demolding is performed by chemical dissolution, currently employing aggressive solutions. Strategies that allow to extract differently (or faster) microcastings out of their host substrate could expand the process to metals and alloys that are currently not feasible because they are degraded during mold removal.

The straightforward production of several monocrystalline metal microstructures by microcasting opens up the possibility for numerous studies in microplasticity. Microcasting enables to easily modify the metal

chemical composition within the range of metals that presently can be microcast using processes developed here. On can, for instance, investigate different strengthening mechanisms for microscale metallic components, namely i) the effect of solid solution elements on yield and plastic flow of small-sized samples, ii) the effect of precipitates, their size, distribution, or iii) the plasticity of microcast high-entropy alloys.

In addition, since many wires with the same crystal orientation and size are obtained via the silicon-based lithographic process, tests at different strain rates or stress relaxation tests can be performed to investigate activation volumes and the kinetics of plastic deformation or strain burst initiation. Similarly, the effect of different initial dislocation densities could be studied (*i.e.*, by annealing and/or cooling the casting down into nitrogen before demolding).

Eventually, since the deformation of crystals has been largely considered over the last decades, enabling the fabrication of microcast bicrystals could benefit the micro- and nano-scale testing community towards the analysis of confined plasticity in the presence of grain boundaries.

# Appendix 1- Zaiser-Nikitas expression for the complementary cumulative distribution function

A series of events of intensity ($s$) ranging from 0.002 up to 0.12 µm separated by steps of 0.0005 were given an occurrence probability ($p(s)$) of:

$$p(s) = Ks^{-1.5}\exp\left(\left[-\frac{s}{s_0}\right]^2\right) \qquad \text{Equation A1}$$

with $s_0$ given four values in the range from 0.1 to 0.16. The resulting plots of probability (p(s)) are shown in double logarithmic coordinates in Figure A1.1.

Data were then integrated numerically with Python, to yield the CCDF $P(S \geq s)$:

$$P(S \geq s) = \int_s^{\infty} p(s).ds \qquad \text{Equation A2}$$

After normalization by its maximum value so that $P(s_{min})=1$, the resulting CCDF $P(S \geq s)$ is displayed in Figure A1.1 in linear, logarithmic and semilogarithmic coordinates.

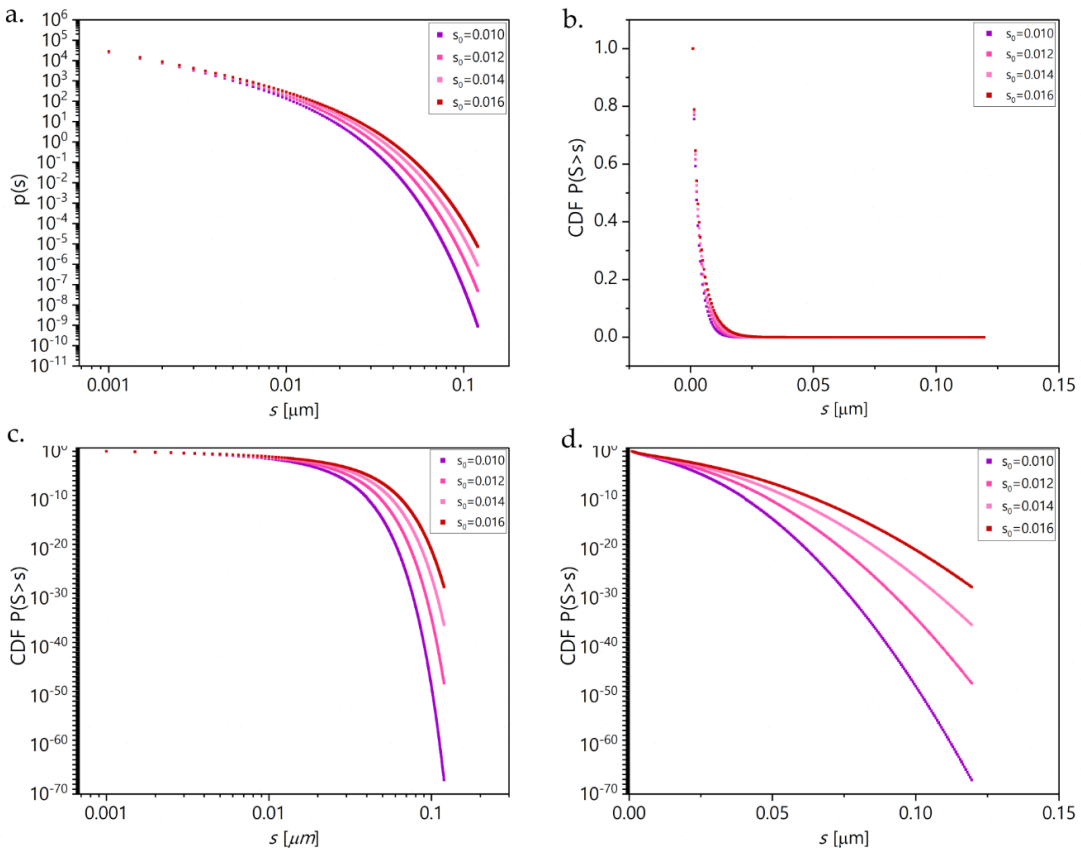


**Figure A1.1** a) The probability of size events p(s) according to the Zaiser-Nikitas expression. b-d) the complementary cumulative distribution function CCDF P(S>s) obtained after integration of Zaiser-Nikitas expression plotted with linear, linear, logarithmic and semilogarithmic coordinates respectively.

Figure A1.1d shows that Equation A1 does not produce, in semi-logarithmic coordinates, a linear CCDF. This is not unexpected: integration of $p(s)$ as given in Equation A1 according to Equation A2 to produce the corresponding CCDF does not yield an exponential function. Using Mathematica (Wolfram Alpha LLC, Champaign US) the corresponding CCDF is given as:

$$P(S \geq s) = \int_s^{\infty} K s^{-1.5} \exp\left(\left[-\frac{s}{s_0}\right]^2\right) . ds = \frac{0.5\left(\frac{s^2}{s_0}\right)^{0.25} \Gamma\left[-0.25, \frac{s^2}{s_0}\right]}{s^{0.5}} \qquad \text{Equation A3}$$

# Appendix 2-Finding *N* in Equation 5-4

Figure A2.1 is a plot of the dislocation density suggested by Equation 5-4 of the main text, namely $\{[\tau/\mu - \alpha_1(b/L)]/[\alpha_2 b \mu]\}^2$, plotted versus $b/D$ with $L = D/3$, with $\alpha_2$ kept at a constant value of 0.25 for silver (appropriate for dislocation densities in the vicinity of the range relevant to present data, namely $10^{14}$ $m^{-2}$), and containing data at room- and elevated temperatures. There is significant scatter in the data, but if one sets aside outlier data from room temperature tests of the finest ($D$ = 2.5 μm) tensile bars, points roughly delineate a straight line with a finite positive slope and a positive intercept with the ordinate axis. The line in Figure A2.1 is a least-squares fit through the data, with $\rho_{f,o} = 1.44\ 10^{13}$ $m^{-2}$ corresponding to the intercept of the line with the ordinate axi. This gives $N = 16.4$ since $\Delta\alpha = 1.6\ 10^{-5}$ $K^{-1}$ if one takes $\Delta T = 700$ K under the assumption that vacancy-driven silver deformation ceases during cooldown roughly around 700°C. A similar procedure was performed for Al microwires using data from Ref. [81] and assuming $\Delta T = 300$ K, with $\Delta\alpha = 2.1\ 10^{-5}$ $K^{-1}$. This yielded $N = 1.7$.

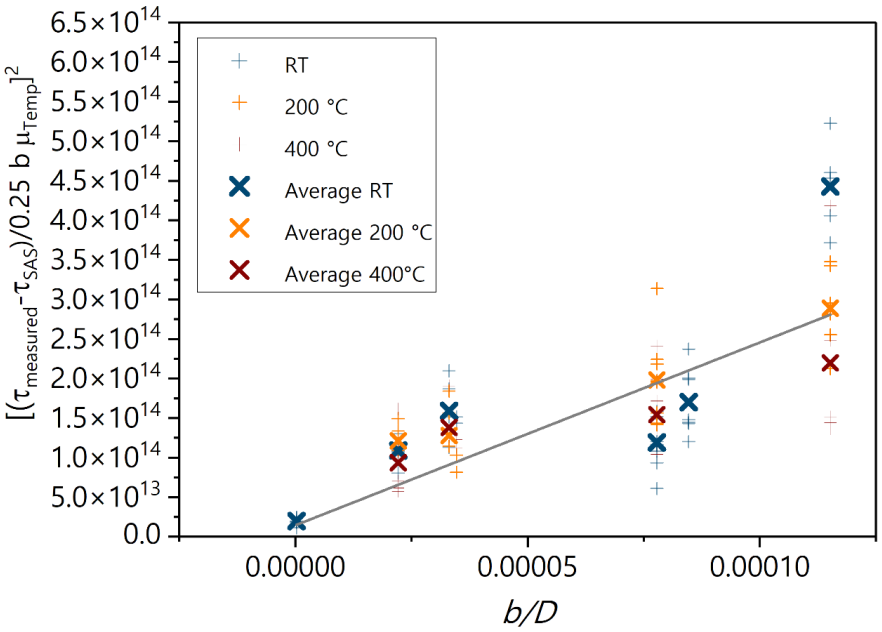


**Figure A2.1** Estimated dislocation density from Equation 5-4 assuming $\alpha_1 = 0.25$ vs. b/D. Vertical crosses are datapoints from individual samples; larger diagonal crosses are averages of those points for each value of temperature and sample diameter. Data points are also given for cast crystals 1 mm in diameter of the same pure silver (points close to b/D = 0). The straight line is a least-squares fit through data points and corresponds to N=16.4 in Equation 5-4.

# References


[1] M.K. Mishra, V. Dubey, P.M. Mishra, I. Khan, MEMS Technology: A Review, JERR. (2019) 1–24. https://doi.org/10.9734/jerr/2019/v4i116891.

[2] L. Hirt, A. Reiser, R. Spolenak, T. Zambelli, Additive Manufacturing of Metal Structures at the Micrometer Scale, Adv. Mater. 29 (2017) 1604211. https://doi.org/10.1002/adma.201604211.

[3] A. Reiser, L. Koch, K.A. Dunn, T. Matsuura, F. Iwata, O. Fogel, Z. Kotler, N. Zhou, K. Charipar, A. Piqué, P. Rohner, D. Poulikakos, S. Lee, S.K. Seol, I. Utke, C. Nisselroy, T. Zambelli, J.M. Wheeler, R. Spolenak, Metals by Micro-Scale Additive Manufacturing: Comparison of Microstructure and Mechanical Properties, Adv. Funct. Mater. 30 (2020) 1910491. https://doi.org/10.1002/adfm.201910491.

[4] S. Reyntjens, R. Puers, A review of focused ion beam applications in microsystem technology, J. Micromech. Microeng. 11 (2001) 287–300. https://doi.org/10.1088/0960-1317/11/4/301.

[5] C.A. Volkert, A.M. Minor, Focused Ion Beam Microscopy and Micromachining, MRS Bulletin. 32 (2007) 389–399. https://doi.org/10.1557/mrs2007.62.

[6] K. Gamo, S. Namba, Microfabrication using focused ion beams, Euro III-Vs Review. 3 (1990) 41–42. https://doi.org/10.1016/0959-3527(90)90205-8.

[7] M.D. Uchic, Sample Dimensions Influence Strength and Crystal Plasticity, Science. 305 (2004) 986–989. https://doi.org/10.1126/science.1098993.

[8] M.D. Uchic, D.M. Dimiduk, A methodology to investigate size scale effects in crystalline plasticity using uniaxial compression testing, Materials Science and Engineering: A. 400–401 (2005) 268–278. https://doi.org/10.1016/j.msea.2005.03.082.

[9] M.D. Uchic, D.M. Dimiduk, J.N. Florando, W.D. Nix, Exploring specimen size effects in plastic deformation of Ni3(Al, Ta), MRS Online Proceedings Library. 753 (2003) 14. https://doi.org/10.1557/PROC-753-BB1.4.

[10] Z.W. Shan, R.K. Mishra, S.A. Syed Asif, O.L. Warren, A.M. Minor, Mechanical annealing and source-limited deformation in submicrometre-diameter Ni crystals, Nature Mater. 7 (2008) 115–119. https://doi.org/10.1038/nmat2085.

[11] H. Zhang, B.E. Schuster, Q. Wei, K.T. Ramesh, The design of accurate micro-compression experiments, Scripta Materialia. 54 (2006) 181–186. https://doi.org/10.1016/j.scriptamat.2005.06.043.

[12] B. Kondori, A. Needleman, A. Amine Benzerga, Discrete dislocation simulations of compression of tapered micropillars, Journal of the Mechanics and Physics of Solids. 101 (2017) 223–234. https://doi.org/10.1016/j.jmps.2017.01.015.

[13] G. Dehm, B.N. Jaya, R. Raghavan, C. Kirchlechner, Overview on micro- and nanomechanical testing: New insights in interface plasticity and fracture at small length scales, Acta Materialia. 142 (2018) 248–282. https://doi.org/10.1016/j.actamat.2017.06.019.

[14] D. Kiener, W. Grosinger, G. Dehm, On the importance of sample compliance in uniaxial microtesting, Scripta Materialia. 60 (2009) 148–151. https://doi.org/10.1016/j.scriptamat.2008.09.024.

[15] D. Kiener, Z. Zhang, S. Šturm, S. Cazottes, P.J. Imrich, C. Kirchlechner, G. Dehm, Advanced nanomechanics in the TEM: effects of thermal annealing on FIB prepared Cu samples, Philosophical Magazine. 92 (2012) 3269–3289. https://doi.org/10.1080/14786435.2012.685966.

[16] D. Kiener, C. Motz, G. Dehm, Micro-compression testing: A critical discussion of experimental constraints, Materials Science and Engineering: A. 505 (2009) 79–87. https://doi.org/10.1016/j.msea.2009.01.005.

[17] D. Kiener, C. Motz, M. Rester, M. Jenko, G. Dehm, FIB damage of Cu and possible consequences for miniaturized mechanical tests, Materials Science and Engineering: A. 459 (2007) 262–272. https://doi.org/10.1016/j.msea.2007.01.046.

[18] J. Hütsch, E.T. Lilleodden, The influence of focused-ion beam preparation technique on microcompression investigations: Lathe vs. annular milling, Scripta Materialia. 77 (2014) 49–51. https://doi.org/10.1016/j.scriptamat.2014.01.016.

[19] Y. Xiao, J. Wehrs, H. Ma, T. Al-Samman, S. Korte-Kerzel, M. Göken, J. Michler, R. Spolenak, J.M. Wheeler, Investigation of the deformation behavior of aluminum micropillars produced by focused ion beam machining using Ga and Xe ions, Scripta Materialia. 127 (2017) 191–194. https://doi.org/10.1016/j.scriptamat.2016.08.028.

[20] J. Liu, R. Niu, J. Gu, M. Cabral, M. Song, X. Liao, Effect of Ion Irradiation Introduced by Focused Ion-Beam Milling on the Mechanical Behaviour of Sub-Micron-Sized Samples, Sci Rep. 10 (2020) 10324. https://doi.org/10.1038/s41598-020-66564-y.

[21] S. Lee, J. Jeong, Y. Kim, S.M. Han, D. Kiener, S.H. Oh, FIB-induced dislocations in Al submicron pillars: Annihilation by thermal annealing and effects on deformation behavior, Acta Materialia. 110 (2016) 283–294. https://doi.org/10.1016/j.actamat.2016.03.017.

[22] J.R. Greer, W.D. Nix, Nanoscale gold pillars strengthened through dislocation starvation, Phys. Rev. B. 73 (2006) 245410. https://doi.org/10.1103/PhysRevB.73.245410.

[23] A.T. Jennings, J.R. Greer, Tensile deformation of electroplated copper nanopillars, Philosophical Magazine. 91 (2011) 1108–1120. https://doi.org/10.1080/14786435.2010.505180.

[24] S. Shim, H. Bei, M.K. Miller, G.M. Pharr, E.P. George, Effects of focused ion beam milling on the compressive behavior of directionally solidified micropillars and the nanoindentation response of an electropolished surface, Acta Materialia. 57 (2009) 503–510. https://doi.org/10.1016/j.actamat.2008.09.033.

[25] M. Dietiker, S. Buzzi, G. Pigozzi, J.F. Löffler, R. Spolenak, Deformation behavior of gold nano-pillars prepared by nanoimprinting and focused ion-beam milling, Acta Materialia. 59 (2011) 2180–2192. https://doi.org/10.1016/j.actamat.2010.12.019.

[26] A. Delobbe, O. Salord, T. Hrncir, A. David, P. Sudraud, F. Lopour, High Speed TEM Sample Preparation by Xe FIB, Microscopy and Microanalysis. 20 (2014) 298–299. https://doi.org/10.1017/S1431927614003213.

[27] A.D. Smith, J. Donoghue, A. Garner, B. Winiarski, E. Bousser, J. Carr, J. Behnsen, T.L. Burnett, R. Wheeler, K. Wilford, P.J. Withers, M. Preuss, On the Application of Xe+ Plasma FIB for Micro-fabrication of Small-scale Tensile Specimens, Exp Mech. 59 (2019) 1113–1125. https://doi.org/10.1007/s11340-019-00528-w.

[28] T.L. Burnett, R. Kelley, B. Winiarski, L. Contreras, M. Daly, A. Gholinia, M.G. Burke, P.J. Withers, Large volume serial section tomography by Xe Plasma FIB dual beam microscopy, Ultramicroscopy. 161 (2016) 119–129. https://doi.org/10.1016/j.ultramic.2015.11.001.

[29] Y. Xiao, V. Maier-Kiener, J. Michler, R. Spolenak, J.M. Wheeler, Deformation behavior of aluminum pillars produced by Xe and Ga focused ion beams: Insights from strain rate jump tests, Materials & Design. 181 (2019) 107914. https://doi.org/10.1016/j.matdes.2019.107914.

[30] H. Bei, S. Shim, G.M. Pharr, E.P. George, Effects of pre-strain on the compressive stress–strain response of Mo-alloy single-crystal micropillars, Acta Materialia. 56 (2008) 4762–4770. https://doi.org/10.1016/j.actamat.2008.05.030.

[31] H. Bei, S. Shim, E. George, M. Miller, E. Herbert, G. Pharr, Compressive strengths of molybdenum alloy micro-pillars prepared using a new technique, Scripta Materialia. 57 (2007) 397–400. https://doi.org/10.1016/j.scriptamat.2007.05.010.

[32] H. Bei, E.P. George, Microstructures and mechanical properties of a directionally solidified NiAl–Mo eutectic alloy, Acta Materialia. 53 (2005) 69–77. https://doi.org/10.1016/j.actamat.2004.09.003.

[33] F. Mompiou, M. Legros, A. Sedlmayr, D.S. Gianola, D. Caillard, O. Kraft, Source-based strengthening of sub-micrometer Al fibers, Acta Materialia. 60 (2012) 977–983. https://doi.org/10.1016/j.actamat.2011.11.005.

[34] S. Buzzi, F. Robin, V. Callegari, J.F. Löffler, Metal direct nanoimprinting for photonics, Microelectronic Engineering. 85 (2008) 419–424. https://doi.org/10.1016/j.mee.2007.08.001.

[35] S. Buzzi, M. Galli, M. Agio, J.F. Löffler, Silver high-aspect-ratio micro- and nanoimprinting for optical applications, Appl. Phys. Lett. 94 (2009) 223115. https://doi.org/10.1063/1.3142426.

[36] S. Buzzi, M. Dietiker, K. Kunze, R. Spolenak, J.F. Löffler, Deformation behavior of silver submicrometer-pillars prepared by nanoimprinting, Philosophical Magazine. 89 (2009) 869–884. https://doi.org/10.1080/14786430902791748.

[37] L. Romano, J. Vila-Comamala, M. Kagias, K. Vogelsang, H. Schift, M. Stampanoni, K. Jefimovs, High aspect ratio metal microcasting by hot embossing for X-ray optics fabrication, Microelectronic Engineering. 176 (2017) 6–10. https://doi.org/10.1016/j.mee.2016.12.032.

[38] E.W. Backer, W. Ehrfeld, D. Münchmeyer, H. Betz, A. Heuberger, S. Pongratz, W. Glashauser, H.J. Michel, R. v. Siemens, Production of separation-nozzle systems for uranium enrichment by a combination of X-ray lithography and galvanoplastics, Naturwissenschaften. 69 (1982) 520–523. https://doi.org/10.1007/BF00463495.

[39] H. Lorenz, M. Despont, N. Fahrni, N. LaBianca, P. Renaud, P. Vettiger, SU-8: a low-cost negative resist for MEMS, J. Micromech. Microeng. 7 (1997) 121–124. https://doi.org/10.1088/0960-1317/7/3/010.

[40] H. Lorenz, M. Despont, P. Vettiger, P. Renaud, Fabrication of photoplastic high-aspect ratio microparts and micromolds using SU-8 UV resist, Microsystem Technologies. 4 (1998) 143–146. https://doi.org/10.1007/s005420050118.

[41] G. Genolet, H. Lorenz, UV-LIGA: From Development to Commercialization, Micromachines. 5 (2014) 486–495. https://doi.org/10.3390/mi5030486.

[42] C. Beuret, G.-A. Racine, J. Gobet, R. Luthier, N.F. de Rooij, Microfabrication of 3D multidirectional inclined structures by UV lithography and electroplating, in: Proceedings IEEE Micro Electro Mechanical Systems An Investigation of Micro Structures, Sensors, Actuators, Machines and Robotic Systems, IEEE, Oiso, Japan, 1994: pp. 81–85. https://doi.org/10.1109/MEMSYS.1994.555602.

[43] M.J. Burek, J.R. Greer, Fabrication and Microstructure Control of Nanoscale Mechanical Testing Specimens via Electron Beam Lithography and Electroplating, Nano Lett. 10 (2010) 69–76. https://doi.org/10.1021/nl902872w.

[44] J.R. Greer, W.C. Oliver, W.D. Nix, Size dependence of mechanical properties of gold at the micron scale in the absence of strain gradients, Acta Materialia. 53 (2005) 1821–1830. https://doi.org/10.1016/j.actamat.2004.12.031.

[45] A.T. Jennings, M.J. Burek, J.R. Greer, Microstructure versus Size: Mechanical Properties of Electroplated Single Crystalline Cu Nanopillars, Phys. Rev. Lett. 104 (2010) 135503. https://doi.org/10.1103/PhysRevLett.104.135503.

[46] D. Jang, X. Li, H. Gao, J.R. Greer, Deformation mechanisms in nanotwinned metal nanopillars, Nature Nanotech. 7 (2012) 594–601. https://doi.org/10.1038/nnano.2012.116.

[47] M. Chen, L. Pethö, A.S. Sologubenko, H. Ma, J. Michler, R. Spolenak, J.M. Wheeler, Achieving micron-scale plasticity and theoretical strength in Silicon, Nature Communications. 11 (2020) undefined-undefined. https://doi.org/10.1038/s41467-020-16384-5.

[48] H.V. Jansen, M.J. de Boer, S. Unnikrishnan, M.C. Louwerse, M.C. Elwenspoek, Black silicon method: X. A review on high speed and selective plasma etching of silicon with profile control: an in-depth comparison between Bosch and cryostat DRIE processes as a roadmap to next generation equipment, J. Micromech. Microeng. 19 (2009) 033001. https://doi.org/10.1088/0960-1317/19/3/033001.

[49] M. Chen, J. Wehrs, A.S. Sologubenko, J. Rabier, J. Michler, J.M. Wheeler, Size-dependent plasticity and activation parameters of lithographically-produced silicon micropillars, Materials & Design. 189 (2020) 108506. https://doi.org/10.1016/j.matdes.2020.108506.

[50] B. Moser, K. Wasmer, L. Barbieri, J. Michler, Strength and fracture of Si micropillars: A new scanning electron microscopy-based micro-compression test, J. Mater. Res. 22 (2007) 1004–1011. https://doi.org/10.1557/jmr.2007.0140.

[51] A.R. Razali, Y. Qin, A Review on Micro-manufacturing, Micro-forming and their Key Issues, Procedia Engineering. 53 (2013) 665–672. https://doi.org/10.1016/j.proeng.2013.02.086.

[52] J.D. Patel, K.D. Maniya, A Review on: Wire cut electrical discharge machining process for metal matrix composite, Procedia Manufacturing. 20 (2018) 253–258. https://doi.org/10.1016/j.promfg.2018.02.037.

[53] K.H. Ho, S.T. Newman, S. Rahimifard, R.D. Allen, State of the art in wire electrical discharge machining (WEDM), International Journal of Machine Tools and Manufacture. 44 (2004) 1247–1259. https://doi.org/10.1016/j.ijmachtools.2004.04.017.

[54] R.R. Gattass, E. Mazur, Femtosecond laser micromachining in transparent materials, Nature Photon. 2 (2008) 219–225. https://doi.org/10.1038/nphoton.2008.47.

[55] Y. Bellouard, The Femtoprint Project, JLMN. 7 (2012) 1–10. https://doi.org/10.2961/jlmn.2012.01.0001.

[56] Y. Bellouard, A. Said, M. Dugan, P. Bado, Fabrication of high-aspect ratio, micro-fluidic channels and tunnels using femtosecond laser pulses and chemical etching, Opt. Express. 12 (2004) 2120. https://doi.org/10.1364/OPEX.12.002120.

[57] A. Champion, Local effective volume changes in fused silica induced by femtoscecond laser irradiation., Technische Universiteit Eindhoven., 2015.

[58] M.P. Echlin, A.T. Polonsky, J. Lamb, R. Geurts, S.J. Randolph, A. Botman, T.M. Pollock, Recent Developments in Femtosecond Laser-Enabled TriBeam Systems, JOM. 73 (2021) 4258–4269. https://doi.org/10.1007/s11837-021-04919-0.

[59] T. Schubert, F. Zhou, R. Pero, N. Randall, T. Bernthaler, G. Schneider, Fast Fabrication of Micropillars for Micromechanical Testing Using a Combined fs-Laser – FIB/SEM Approach, Microscopy and Microanalysis. 28 (2022) 892–895. https://doi.org/10.1017/S1431927622003932.

[60] F. Madani-Grasset, Y. Bellouard, Femtosecond laser micromachining of fused silica molds, Opt. Express. 18 (2010) 21826. https://doi.org/10.1364/OE.18.021826.

[61] E. Casamenti, S. Pollonghini, Y. Bellouard, Few pulses femtosecond laser exposure for high efficiency 3D glass micromachining, Opt. Express, OE. 29 (2021) 35054–35066. https://doi.org/10.1364/OE.435163.

[62] S. Rajesh, Y. Bellouard, Towards fast femtosecond laser micromachining of fused silica: The effect of deposited energy, Opt. Express. 18 (2010) 21490. https://doi.org/10.1364/OE.18.021490.

[63] R.N. Widmer, D. Bischof, J. Jurczyk, M. Michler, J. Schwiedrzik, J. Michler, Smooth or not: Robust fused silica micro-components by femtosecond-laser-assisted etching, Materials & Design. 204 (2021) 109670. https://doi.org/10.1016/j.matdes.2021.109670.

[64] S.I. Nazir, C.E. Athanasiou, Y. Bellouard, On the uniaxial static stress relaxation in fused silica at room temperature, (2022). https://doi.org/10.48550/arXiv.2201.06571.

[65] S.Y. Chin, V. Dikshit, B. Meera Priyadarshini, Y. Zhang, Powder-Based 3D Printing for the Fabrication of Device with Micro and Mesoscale Features, Micromachines. 11 (2020) 658. https://doi.org/10.3390/mi11070658.

[66] P.-W. Wu, W. Cheng, I.B. Martini, B. Dunn, B.J. Schwartz, E. Yablonovitch, Two-Photon Photographic Production of Three-Dimensional Metallic Structures within a Dielectric Matrix, Advanced Materials. 12 (2000) 1438–1441. https://doi.org/10.1002/1521-4095(200010)12:19<1438::AID-ADMA1438>3.0.CO;2-Y.

[67] T. Tanaka, A. Ishikawa, S. Kawata, Two-photon-induced reduction of metal ions for fabricating three-dimensional electrically conductive metallic microstructure, Appl. Phys. Lett. 88 (2006) 081107. https://doi.org/10.1063/1.2177636.

[68] M.S. Saleh, C. Hu, R. Panat, Three-dimensional microarchitected materials and devices using nanoparticle assembly by pointwise spatial printing, Sci Adv. 3 (2017) e1601986. https://doi.org/10.1126/sciadv.1601986.

[69] G. Ercolano, T. Zambelli, C. van Nisselroy, D. Momotenko, J. Vörös, T. Merle, W.W. Koelmans, Multiscale Additive Manufacturing of Metal Microstructures, Advanced Engineering Materials. 22 (2020) 1900961. https://doi.org/10.1002/adem.201900961.

[70] A. Reiser, M. Lindén, P. Rohner, A. Marchand, H. Galinski, A.S. Sologubenko, J.M. Wheeler, R. Zenobi, D. Poulikakos, R. Spolenak, Multi-metal electrohydrodynamic redox 3D printing at the submicron scale, Nat Commun. 10 (2019) 1853. https://doi.org/10.1038/s41467-019-09827-1.

[71] T.M. Braun, D.T. Schwartz, The Emerging Role of Electrodeposition in Additive Manufacturing, Interface Magazine. 25 (2016) 69–73. https://doi.org/10.1149/2.F07161if.

[72] M. Sahoo, S. Sahu, Principles of metal casting, Third ed, McGraw-Hill Education, New York, 2014.

[73] N. Eustathopoulos, M.G. Nicholas, B. Drevet, Wettability at High Temperatures, Pergamon Press, Inc., 1999. https://www.elsevier.com/books/wettability-at-high-temperatures/eustathopoulos/978-0-08-042146-9 (accessed April 27, 2020).

[74] G. Baumeister, J. Hausselt, R. Ruprecht, Microcasting of parts made of metal alloys, Microsystem Technologies. 10 (2004) 261–264. https://doi.org/10.1007/s00542-003-0363-2.

[75] G. Baumeister, S. Rath, J. Hausselt, Microcasting of Al bronze and a gold base alloy improved by plaster-bonded investment, Microsyst Technol. 12 (2006) 773–777. https://doi.org/10.1007/s00542-006-0105-3.

[76] G. Baumeister, K. Mueller, R. Ruprecht, J. Hausselt, Production of metallic high aspect ratio microstructures by microcasting, Microsystem Technologies. 8 (2002) 105–108. https://doi.org/10.1007/s00542-001-0132-z.

[77] G. Baumeister, R. Ruprecht, J. Hausselt, Replication of LIGA structures using microcasting, Microsystem Technologies. 10 (2004) 484–488. https://doi.org/10.1007/s00542-004-0377-4.

[78] S. Rath, G. Baumeister, J. Hausselt, Investments for casting micro parts with base alloys, Microsyst Technol. 12 (2006) 258–266. https://doi.org/10.1007/s00542-005-0047-1.

[79] G. Baumeister, D. Buqezi-Ahmeti, J. Glaser, H.-J. Ritzhaupt-Kleissl, New approaches in microcasting: permanent mold casting and composite casting, Microsyst Technol. 17 (2011) 289–300. https://doi.org/10.1007/s00542-011-1237-7.

[80] S.G.A. Verheyden, Thermal Activation, Intermittency and Size Effects in the Plastic Deformation of Cast Aluminium Microwires, EPFL, 2018.

[81] J. Krebs, S.I. Rao, S. Verheyden, C. Miko, R. Goodall, W.A. Curtin, A. Mortensen, Cast aluminium single crystals cross the threshold from bulk to size-dependent stochastic plasticity, Nature Mater. 16 (2017) 730–736. https://doi.org/10.1038/nmat4911.

[82] S. Verheyden, L. Pires Da Veiga, L. Deillon, A. Mortensen, The effect of size on the plastic deformation of annealed cast aluminium microwires, Scripta Materialia. 161 (2019) 58–61. https://doi.org/10.1016/j.scriptamat.2018.10.009.

[83] S.G.A. Verheyden, L. Deillon, A. Mortensen, The thermally activated deformation behaviour of single-crystalline microcast aluminium wires, Acta Materialia. 234 (2022) 118037. https://doi.org/10.1016/j.actamat.2022.118037.

[84] J. Krebs, Cast aluminium microwires:processing and plastic deformation, (n.d.) 157.

[85] S. Verheyden, L. Deillon, A. Mortensen, Stress relaxation in the presence of sudden strain bursts: Methodology and stress relaxation data of microcast aluminium microwires, Data in Brief. 21 (2018) 2134–2141. https://doi.org/10.1016/j.dib.2018.11.047.

[86] N. Kleger, S. Fehlmann, S.S. Lee, C. Dénéréaz, M. Cihova, N. Paunović, Y. Bao, J.-C. Leroux, S.J. Ferguson, K. Masania, A.R. Studart, Light-Based Printing of Leachable Salt Molds for Facile Shaping of Complex Structures, Advanced Materials. 34 (2022) 2203878. https://doi.org/10.1002/adma.202203878.

[87] F.R.N. Nabarro, Z.S. Basinski, D.B. Holt, The plasticity of pure single crystals, Advances in Physics. 13 (1964) 193–323. https://doi.org/10.1080/00018736400101031.

[88] R.W.K. Honeycombe, The plastic deformation of metals, 2nd ed., Baltimore - Md.& Caulfield East : Arnold, 1984.

[89] G. Dieter, Mechanical Metallurgy, 3rd edition, McGraw-Hill Education, New York, 1986.

[90] R.E.R.-H.R. Abbaschian, Physical Metallurgy Principles, REZA ABBASCHIAN & ROBERT E. REED-HILL, 2008.

[91] L. Kubin, Dislocations, Mesoscale Simulations and Plastic Flow, 1st edition, Oxford University Press, Oxford, United Kingdom, 2013.

[92] W.F. Hosford, Mechanical Behavior of Materials, 2nd ed., Cambridge University Press, Cambridge, 2009. https://doi.org/10.1017/CBO9780511810923.

[93] Introduction to Dislocations - 5th Edition, (n.d.). https://www.elsevier.com/books/introduction-to-dislocations/hull/978-0-08-096672-4 (accessed August 16, 2022).

[94] Theory of Dislocations | Materials science, Cambridge University Press. (n.d.). https://www.cambridge.org/ch/academic/subjects/engineering/materials-science/theory-dislocations-3rd-edition, https://www.cambridge.org/ch/academic/subjects/engineering/materials-science (accessed August 16, 2022).

[95] D. Caillard, J.L. Martin, Thermally Activated Mechanisms in Crystal Plasticity, Elsevier, 2003.

[96] D. Caillard, J.L. Martin, Some aspects of cross-slip mechanisms in metals and alloys, (n.d.) 20.

[97] P. Rohith, G. Sainath, S. Goyal, A. Nagesha, V.S. Srinivasan, Role of axial twin boundaries on deformation mechanisms in Cu nanopillars, Philosophical Magazine. 100 (2020) 529–550. https://doi.org/10.1080/14786435.2019.1695163.

[98] R.L. Fleischer, Cross slip of extended dislocations, Acta Metallurgica. 7 (1959) 134–135. https://doi.org/10.1016/0001-6160(59)90122-1.

[99] D. Hull, D.J. Bacon, Chapter 3 - Movement of Dislocations, in: D. Hull, D.J. Bacon (Eds.), Introduction to Dislocations (Fifth Edition), Butterworth-Heinemann, Oxford, 2011: pp. 43–62. https://doi.org/10.1016/B978-0-08-096672-4.00003-7.

[100] D. Hull, D.J. Bacon, Chapter 7 - Jogs and the Intersection of Dislocations, in: D. Hull, D.J. Bacon (Eds.), Introduction to Dislocations (Fifth Edition), Butterworth-Heinemann, Oxford, 2011: pp. 137–155. https://doi.org/10.1016/B978-0-08-096672-4.00007-4.

[101] M. Sauzay, L.P. Kubin, Scaling laws for dislocation microstructures in monotonic and cyclic deformation of fcc metals, Progress in Materials Science. 56 (2011) 725–784. https://doi.org/10.1016/j.pmatsci.2011.01.006.

[102] M.D. Uchic, P.A. Shade, D.M. Dimiduk, Plasticity of Micrometer-Scale Single Crystals in Compression, Annu. Rev. Mater. Res. 39 (2009) 361–386. https://doi.org/10.1146/annurev-matsci-082908-145422.

[103] S.I. Rao, D.M. Dimiduk, M. Tang, M.D. Uchic, T.A. Parthasarathy, C. Woodward, Estimating the strength of single-ended dislocation sources in micron-sized single crystals, Philosophical Magazine. 87 (2007) 4777–4794. https://doi.org/10.1080/14786430701591513.

[104] C. Zhou, I.J. Beyerlein, R. LeSar, Plastic deformation mechanisms of fcc single crystals at small scales, Acta Materialia. 59 (2011) 7673–7682. https://doi.org/10.1016/j.actamat.2011.08.032.

[105] D. Hull, D.J. Bacon, Chapter 8 - Origin and Multiplication of Dislocations, in: D. Hull, D.J. Bacon (Eds.), Introduction to Dislocations (Fifth Edition), Butterworth-Heinemann, Oxford, 2011: pp. 157–169. https://doi.org/10.1016/B978-0-08-096672-4.00008-6.

[106] L.H. Friedman, D.C. Chrzan, Continuum analysis of dislocation pile-ups: Influence of sources, Philosophical Magazine A. 77 (1998) 1185–1204. https://doi.org/10.1080/01418619808214247.

[107] W. Cai, V.V. Bulatov, J. Chang, J. Li, S. Yip, Chapter 64 - Dislocation Core Effects on Mobility, in: F.R.N. Nabarro, J.P. Hirth (Eds.), Dislocations in Solids, Elsevier, 2004: pp. 1–80. https://doi.org/10.1016/S1572-4859(05)80003-8.

[108] W. Cai, V.V. Bulatov, J. Chang, J. Li, S. Yip, Dislocation Core Effects on Mobility, in: Dislocations in Solids, Elsevier, 2004: pp. 1–80. https://doi.org/10.1016/S1572-4859(05)80003-8.

[109] J.G. Sevillano, Flow Stress and Work Hardening, in: Flow Stress and Work Hardening, American Cancer Society, 2006. https://doi.org/10.1002/9783527603978.mst0049.

[110] A.D. Rollett, U.F. Kocks, A Review of the Stages of Work Hardening, SSP. 35–36 (1993) 1–18. https://doi.org/10.4028/www.scientific.net/SSP.35-36.1.

[111] F.R.N. Nabarro, Work Hardening of Face-Centered Cubic Single Crystals, in: H.J. McQUEEN, J.-P. Bailon, J.I. Dickson, J.J. Jonas, M.G. Akben (Eds.), Strength of Metals and Alloys (ICSMA 7), Pergamon, 1986: pp. 1667–1700. https://doi.org/10.1016/B978-0-08-031640-6.50009-8.

[112] U.F. Kocks, H. Mecking, Physics and phenomenology of strain hardening: the FCC case, Progress in Materials Science. 48 (2003) 171–273. https://doi.org/10.1016/S0079-6425(02)00003-8.

[113] F.D. Rosi, Stress-Strain Characteristics and Slip-Bond Formation In Metal Crystals: Effect of Crystal Orientation, (n.d.) 12.

[114] G.I. Taylor, The mechanism of plastic deformation of crystals. Part I.—Theoretical, Proceedings of the Royal Society of London. Series A, Containing Papers of a Mathematical and Physical Character. 145 (1934) 362–387. https://doi.org/10.1098/rspa.1934.0106.

[115] A. Argon, Strengthening Mechanisms in Crystal Plasticity, 2008. https://doi.org/10.1093/acprof:oso/9780198516002.001.0001.

[116] F. Prinz, A.S. Argon, Dislocation cell formation during plastic deformation of copper single crystals, Phys. Stat. Sol. (a). 57 (1980) 741–753. https://doi.org/10.1002/pssa.2210570234.

[117] F.J. Worzala, W.H. Robinson, Dislocation distributions during stage I deformation of silver single crystals, The Philosophical Magazine: A Journal of Theoretical Experimental and Applied Physics. 15 (1967) 939–957. https://doi.org/10.1080/14786436708221638.

[118] F.R.N. Nabarro, Surface effects in crystal plasticity – overview from the crystal plasticity standpoint, in: Surface Effects in Crystal Plasticity, Nato Advanced Study Institute Series, Series E – Applied Science No. 17, Noordhoff, Leiden, NL, 1977: pp. 49–125.

[119] E.N. da C. Andrade, C. Henderson, The mechanical behaviour of single crystals of certain face-centred cubic metals, Phil. Trans. R. Soc. Lond. A. 244 (1951) 177–203. https://doi.org/10.1098/rsta.1951.0019.

[120] H. Suzuki, S. Ikeda, S. Takeuchi, Deformation of Thin Copper Crystals, J. Phys. Soc. Jpn. 11 (1956) 382–393. https://doi.org/10.1143/JPSJ.11.382.

[121] H. Mecking, U.F. Kocks, Kinetics of flow and strain-hardening, Acta Metallurgica. 29 (1981) 1865–1875. https://doi.org/10.1016/0001-6160(81)90112-7.

[122] E. Orowan, Problems of plastic gliding, Proc. Phys. Soc. 52 (1940) 8–22. https://doi.org/10.1088/0959-5309/52/1/303.

[123] V.I. Dotsenko, Stress Relaxation in Crystals, Phys. Stat. Sol. (b). 93 (1979) 11–43. https://doi.org/10.1002/pssb.2220930102.

[124] R.A. Mulford, Analysis of strengthening mechanisms in alloys by means of thermal-activation theory, Acta Metallurgica. 27 (1979) 1115–1124. https://doi.org/10.1016/0001-6160(79)90129-9.

[125] P. Spätig, J. Bonneville, Martin, JL, A new method for activation volume measurements: application to Ni3(A1,Hf), Materials Science and Engineering: A. 167 (1993) 73–79. https://doi.org/10.1016/0921-5093(93)90339-G.

[126] M. Cagnon, The role of entropy in thermally activated deformation: Application to the study of irradiation hardening in LiF, Philosophical Magazine. 24 (1971) 1465–1476. https://doi.org/10.1080/14786437108217425.

[127] S. Mishra, M. Yadava, K.N. Kulkarni, N.P. Gurao, Stress relaxation behavior of an aluminium magnesium silicon alloy in different temper condition, Mechanics of Materials. 125 (2018) 80–93. https://doi.org/10.1016/j.mechmat.2018.07.010.

[128] A. Seeger, J. Diehl, S. Mader, H. Rebstock, Work-hardening and work-softening of face-centred cubic metal crystals, Philosophical Magazine. 2 (1957) 323–350. https://doi.org/10.1080/14786435708243823.

[129] B.J. Diak, K.R. Upadhyaya, S. Saimoto, Characterization of thermodynamic response by materials testing, Progress in Materials Science. 43 (1998) 223–363. https://doi.org/10.1016/S0079-6425(98)00007-3.

[130] F.R.N. Nabarro, Cottrell-stokes law and activation theory, Acta Metallurgica et Materialia. 38 (1990) 161–164. https://doi.org/10.1016/0956-7151(90)90044-H.

[131] O. Kraft, P.A. Gruber, R. Mönig, D. Weygand, Plasticity in Confined Dimensions, Annu. Rev. Mater. Res. 40 (2010) 293–317. https://doi.org/10.1146/annurev-matsci-082908-145409.

[132] J.R. Greer, J.Th.M. De Hosson, Plasticity in small-sized metallic systems: Intrinsic versus extrinsic size effect, Progress in Materials Science. 56 (2011) 654–724. https://doi.org/10.1016/j.pmatsci.2011.01.005.

[133] R. Maaß, P.M. Derlet, Micro-plasticity and recent insights from intermittent and small-scale plasticity, Acta Materialia. 143 (2018) 338–363. https://doi.org/10.1016/j.actamat.2017.06.023.

[134] R. Dou, B. Derby, A universal scaling law for the strength of metal micropillars and nanowires, Scripta Materialia. 61 (2009) 524–527. https://doi.org/10.1016/j.scriptamat.2009.05.012.

[135] S. Brinckmann, J.-Y. Kim, J.R. Greer, Fundamental Differences in Mechanical Behavior between Two Types of Crystals at the Nanoscale, Phys. Rev. Lett. 100 (2008) 155502. https://doi.org/10.1103/PhysRevLett.100.155502.

[136] D. Kiener, A.M. Minor, Source Truncation and Exhaustion: Insights from Quantitative in situ TEM Tensile Testing, Nano Lett. 11 (2011) 3816–3820. https://doi.org/10.1021/nl201890s.

[137] J. Senger, D. Weygand, C. Motz, P. Gumbsch, O. Kraft, Aspect ratio and stochastic effects in the plasticity of uniformly loaded micrometer-sized specimens, Acta Materialia. 59 (2011) 2937–2947. https://doi.org/10.1016/j.actamat.2011.01.034.

[138] C. Griesbach, S.-J. Jeon, D.F. Rojas, M. Ponga, S. Yazdi, S. Pathak, N. Mara, E.L. Thomas, R. Thevamaran, Origins of size effects in initially dislocation-free single-crystal silver micro- and nanocubes, Acta Materialia. (2021) 117020. https://doi.org/10.1016/j.actamat.2021.117020.

[139] S.I. Rao, D.M. Dimiduk, T.A. Parthasarathy, M.D. Uchic, M. Tang, C. Woodward, Athermal mechanisms of size-dependent crystal flow gleaned from three-dimensional discrete dislocation simulations, Acta Materialia. 56 (2008) 3245–3259. https://doi.org/10.1016/j.actamat.2008.03.011.

[140] J.A. El-Awady, Unravelling the physics of size-dependent dislocation-mediated plasticity, Nat Commun. 6 (2015) 5926. https://doi.org/10.1038/ncomms6926.

[141] D.M. Dimiduk, M.D. Uchic, T.A. Parthasarathy, Size-affected single-slip behavior of pure nickel microcrystals, Acta Materialia. 53 (2005) 4065–4077. https://doi.org/10.1016/j.actamat.2005.05.023.

[142] B. von Blanckenhagen, P. Gumbsch, E. Arzt, Dislocation sources and the flow stress of polycrystalline thin metal films, Philosophical Magazine Letters. 83 (2003) 1–8. https://doi.org/10.1080/0950083021000050287.

[143] D. Kiener, C. Motz, T. Schöberl, M. Jenko, G. Dehm, Determination of Mechanical Properties of Copper at the Micron Scale, Adv. Eng. Mater. 8 (2006) 1119–1125. https://doi.org/10.1002/adem.200600129.

[144] T.A. Parthasarathy, S.I. Rao, D.M. Dimiduk, M.D. Uchic, D.R. Trinkle, Contribution to size effect of yield strength from the stochastics of dislocation source lengths in finite samples, Scripta Materialia. 56 (2007) 313–316. https://doi.org/10.1016/j.scriptamat.2006.09.016.

[145] S.H. Oh, M. Legros, D. Kiener, G. Dehm, In situ observation of dislocation nucleation and escape in a submicrometre aluminium single crystal, Nature Mater. 8 (2009) 95–100. https://doi.org/10.1038/nmat2370.

[146] D.M. Norfleet, D.M. Dimiduk, S.J. Polasik, M.D. Uchic, M.J. Mills, Dislocation structures and their relationship to strength in deformed nickel microcrystals, Acta Materialia. 56 (2008) 2988–3001. https://doi.org/10.1016/j.actamat.2008.02.046.

[147] K.S. Ng, A.H.W. Ngan, Breakdown of Schmid's law in micropillars, Scripta Materialia. 59 (2008) 796–799. https://doi.org/10.1016/j.scriptamat.2008.06.019.

[148] J. Gil Sevillano, I. Ocaña Arizcorreta, L.P. Kubin, Intrinsic size effects in plasticity by dislocation glide, Materials Science and Engineering: A. 309–310 (2001) 393–405. https://doi.org/10.1016/S0921-5093(00)01733-0.

[149] J. Alcalá, J. Očenášek, K. Nowag, D.E. los Ojos, R. Ghisleni, J. Michler, Strain hardening and dislocation avalanches in micrometer-sized dimensions, Acta Materialia. 91 (2015) 255–266. https://doi.org/10.1016/j.actamat.2015.02.027.

[150] D. Kiener, P.J. Guruprasad, S.M. Keralavarma, G. Dehm, A.A. Benzerga, Work hardening in micropillar compression: In situ experiments and modeling, Acta Materialia. 59 (2011) 3825–3840. https://doi.org/10.1016/j.actamat.2011.03.003.

[151] C.A. Volkert, E.T. Lilleodden, Size effects in the deformation of sub-micron Au columns, Philosophical Magazine. 86 (2006) 5567–5579. https://doi.org/10.1080/14786430600567739.

[152] C.P. Frick, B.G. Clark, S. Orso, A.S. Schneider, E. Arzt, Size effect on strength and strain hardening of small-scale [111] nickel compression pillars, Materials Science and Engineering: A. 489 (2008) 319–329. https://doi.org/10.1016/j.msea.2007.12.038.

[153] S.S. Brenner, Tensile Strength of Whiskers, Journal of Applied Physics. 27 (1956) 1484–1491. https://doi.org/10.1063/1.1722294.

[154] C. Herring, J.K. Galt, Elastic and Plastic Properties of Very Small Metal Specimens, Phys. Rev. 85 (1952) 1060–1061. https://doi.org/10.1103/PhysRev.85.1060.2.

[155] O. Kraft, R. Schwaiger, W.D. Nix, Measurement of Mechanical Properties in Small Dimensions by Microbeam Deflection, MRS Online Proceedings Library (OPL). 518 (1998) 39. https://doi.org/10.1557/PROC-518-39.

[156] M.F. Pantano, H.D. Espinosa, L. Pagnotta, Mechanical characterization of materials at small length scales, J Mech Sci Technol. 26 (2012) 545–561. https://doi.org/10.1007/s12206-011-1214-1.

[157] V. Jayaram, Small-Scale Mechanical Testing, Annu. Rev. Mater. Res. 52 (2022) 473–523. https://doi.org/10.1146/annurev-matsci-080819-123640.

[158] W.C. Oliver, G.M. Pharr, An improved technique for determining hardness and elastic modulus using load and displacement sensing indentation experiments, Journal of Materials Research. 7 (1992) 1564–1583. https://doi.org/10.1557/JMR.1992.1564.

[159] A.C. Fischer-Cripps, Nanoindentation of Thin Films and Small Volumes of Materials, in: A.C. Fischer-Cripps (Ed.), Nanoindentation, Springer, New York, NY, 2011: pp. 147–161. https://doi.org/10.1007/978-1-4419-9872-9_8.

[160] T.P. Weihs, S. Hong, J.C. Bravman, W.D. Nix, Mechanical deflection of cantilever microbeams: A new technique for testing the mechanical properties of thin films, Journal of Materials Research. 3 (1988) 931–942. https://doi.org/10.1557/JMR.1988.0931.

[161] M.G. Mueller, M. Fornabaio, G. Žagar, A. Mortensen, Microscopic strength of silicon particles in an aluminium–silicon alloy, Acta Materialia. 105 (2016) 165–175. https://doi.org/10.1016/j.actamat.2015.12.006.

[162] M.G. Mueller, V. Pejchal, G. Žagar, A. Singh, M. Cantoni, A. Mortensen, Fracture toughness testing of nanocrystalline alumina and fused quartz using chevron-notched microbeams, Acta Materialia. 86 (2015) 385–395. https://doi.org/10.1016/j.actamat.2014.12.016.

[163] G. Žagar, V. Pejchal, M.G. Mueller, L. Michelet, A. Mortensen, Fracture toughness measurement in fused quartz using triangular chevron-notched micro-cantilevers, Scripta Materialia. 112 (2016) 132–135. https://doi.org/10.1016/j.scriptamat.2015.09.032.

[164] W. Suwito, M.L. Dunn, S.J. Cunningham, Elastic moduli, strength, and fracture initiation at sharp notches in etched single crystal silicon microstructures, (n.d.) 17.

[165] D.S. Gianola, C. Eberl, Micro- and nanoscale tensile testing of materials, JOM. 61 (2009) 24–35. https://doi.org/10.1007/s11837-009-0037-3.

[166] G. Žagar, V. Pejchal, M.G. Mueller, A. Rossoll, M. Cantoni, A. Mortensen, The local strength of microscopic alumina reinforcements, Acta Materialia. 100 (2015) 215–223. https://doi.org/10.1016/j.actamat.2015.08.026.

[167] V. Pejchal, M. Fornabaio, G. Žagar, A. Mortensen, The local strength of individual alumina particles, Journal of the Mechanics and Physics of Solids. 109 (2017) 34–49. https://doi.org/10.1016/j.jmps.2017.08.005.

[168] D. Kiener, W. Grosinger, G. Dehm, R. Pippan, A further step towards an understanding of size-dependent crystal plasticity: In situ tension experiments of miniaturized single-crystal copper samples, Acta Materialia. 56 (2008) 580–592. https://doi.org/10.1016/j.actamat.2007.10.015.

[169] J.-Y. Kim, J.R. Greer, Tensile and compressive behavior of gold and molybdenum single crystals at the nano-scale, Acta Materialia. 57 (2009) 5245–5253. https://doi.org/10.1016/j.actamat.2009.07.027.

[170] J.M. Wheeler, D.E.J. Armstrong, W. Heinz, R. Schwaiger, High temperature nanoindentation: The state of the art and future challenges, Current Opinion in Solid State and Materials Science. 19 (2015) 354–366. https://doi.org/10.1016/j.cossms.2015.02.002.

[171] J.M. Wheeler, J. Michler, Elevated temperature, nano-mechanical testing *in situ* in the scanning electron microscope, Review of Scientific Instruments. 84 (2013) 045103. https://doi.org/10.1063/1.4795829.

[172] B.D. Beake, J.F. Smith, High-temperature nanoindentation testing of fused silica and other materials, Philosophical Magazine A. 82 (2002) 2179–2186. https://doi.org/10.1080/01418610208235727.

[173] A.C. Lund, A.M. Hodge, C.A. Schuh, Incipient plasticity during nanoindentation at elevated temperatures, Appl. Phys. Lett. 85 (2004) 1362–1364. https://doi.org/10.1063/1.1784891.

[174] C.A. Schuh, J.K. Mason, A.C. Lund, Quantitative insight into dislocation nucleation from high-temperature nanoindentation experiments, Nature Mater. 4 (2005) 617–621. https://doi.org/10.1038/nmat1429.

[175] J.K. Mason, A.C. Lund, C.A. Schuh, Determining the activation energy and volume for the onset of plasticity during nanoindentation, Phys. Rev. B. 73 (2006) 054102. https://doi.org/10.1103/PhysRevB.73.054102.

[176] C.A. Schuh, C.E. Packard, A.C. Lund, Nanoindentation and contact-mode imaging at high temperatures, Journal of Materials Research. 21 (2006) 725–736. https://doi.org/10.1557/jmr.2006.0080.

[177] X. Huang, J. Nohava, B. Zhang, A.G. Ramirez, Nanoindentation of NiTi shape memory thin films at elevated temperatures, International Journal of Smart and Nano Materials. 2 (2011) 39–49. https://doi.org/10.1080/19475411.2011.558179.

[178] S. Korte, W.J. Clegg, Micropillar compression of ceramics at elevated temperatures, Scripta Materialia. (2009) 5.

[179] K.V. Rajulapati†, M.M. Biener, J. Biener, A.M. Hodge, Temperature dependence of the plastic flow behavior of tantalum, Philosophical Magazine Letters. 90 (2010) 35–42. https://doi.org/10.1080/09500830903356893.

[180] A.S. Schneider, C.P. Frick, E. Arzt, W.J. Clegg, S. Korte, Influence of test temperature on the size effect in molybdenum small-scale compression pillars, Philosophical Magazine Letters. 93 (2013) 331–338. https://doi.org/10.1080/09500839.2013.777815.

[181] A.S. Schneider, D. Kaufmann, B.G. Clark, C.P. Frick, P.A. Gruber, R. Mönig, O. Kraft, E. Arzt, Correlation between Critical Temperature and Strength of Small-Scale bcc Pillars, Phys. Rev. Lett. 103 (2009) 105501. https://doi.org/10.1103/PhysRevLett.103.105501.

[182] O. Torrents Abad, J.M. Wheeler, J. Michler, A.S. Schneider, E. Arzt, Temperature-dependent size effects on the strength of Ta and W micropillars, Acta Materialia. 103 (2016) 483–494. https://doi.org/10.1016/j.actamat.2015.10.016.

[183] S.-W. Lee, W.D. Nix, Size dependence of the yield strength of fcc and bcc metallic micropillars with diameters of a few micrometers, Philosophical Magazine. 92 (2012) 1238–1260. https://doi.org/10.1080/14786435.2011.643250.

[184] N.K. Aragon, S. Yin, H. Lim, I. Ryu, Temperature Dependent Plasticity in BCC Micropillars, Materialia. (2021) 101181. https://doi.org/10.1016/j.mtla.2021.101181.

[185] Y. Lu, X. Shu, X. Liao, Size effect for achieving high mechanical performance body-centered cubic metals and alloys, Sci. China Mater. 61 (2018) 1495–1516. https://doi.org/10.1007/s40843-018-9313-2.

[186] J. Ast, J.J. Schwiedrzik, J. Wehrs, D. Frey, M.N. Polyakov, J. Michler, X. Maeder, The brittle-ductile transition of tungsten single crystals at the micro-scale, Materials & Design. 152 (2018) 168–180. https://doi.org/10.1016/j.matdes.2018.04.009.

[187] R. Soler, J.M. Wheeler, H.-J. Chang, J. Segurado, J. Michler, J. Llorca, J.M. Molina-Aldareguia, Understanding size effects on the strength of single crystals through high-temperature micropillar compression, Acta Materialia. 81 (2014) 50–57. https://doi.org/10.1016/j.actamat.2014.08.007.

[188] S. Korte, J.S. Barnard, R.J. Stearn, W.J. Clegg, Deformation of silicon – Insights from microcompression testing at 25–500°C, International Journal of Plasticity. 27 (2011) 1853–1866. https://doi.org/10.1016/j.ijplas.2011.05.009.

[189] J.M. Wheeler, C. Niederberger, C. Tessarek, S. Christiansen, J. Michler, Extraction of plasticity parameters of GaN with high temperature, in situ micro-compression, International Journal of Plasticity. 40 (2013) 140–151. https://doi.org/10.1016/j.ijplas.2012.08.001.

[190] J.M. Wheeler, R. Raghavan, J. Michler, Temperature invariant flow stress during microcompression of a Zr-based bulk metallic glass, Scripta Materialia. (2012) 4.

[191] S. Korte, R.J. Stearn, J.M. Wheeler, W.J. Clegg, High temperature microcompression and nanoindentation in vacuum, J. Mater. Res. 27 (2012) 167–176. https://doi.org/10.1557/jmr.2011.268.

[192] G. Mohanty, J.M. Wheeler, R. Raghavan, J. Wehrs, M. Hasegawa, S. Mischler, L. Philippe, J. Michler, Elevated temperature, strain rate jump microcompression of nanocrystalline nickel, Philosophical Magazine. 95 (2015) 1878–1895. https://doi.org/10.1080/14786435.2014.951709.

[193] A. Wimmer, W. Heinz, A. Leitner, T. Detzel, W. Robl, C. Kirchlechner, G. Dehm, Micro-tension study of miniaturized Cu lines at variable temperatures, Acta Materialia. 92 (2015) 243–254. https://doi.org/10.1016/j.actamat.2015.03.056.

[194] J.M. Wheeler, C. Kirchlechner, J.-S. Micha, J. Michler, D. Kiener, The effect of size on the strength of FCC metals at elevated temperatures: annealed copper, Philosophical Magazine. 96 (2016) 3379–3395. https://doi.org/10.1080/14786435.2016.1224945.

[195] M. Newman, Power laws, Pareto distributions and Zipf's law, Contemporary Physics. 46 (2005) 323–351. https://doi.org/10.1080/00107510500052444.

[196] D.M. Dimiduk, M.D. Uchic, S.I. Rao, C. Woodward, T.A. Parthasarathy, Overview of experiments on microcrystal plasticity in FCC-derivative materials: selected challenges for modelling and simulation of plasticity, Modelling Simul. Mater. Sci. Eng. 15 (2007) 135–146. https://doi.org/10.1088/0965-0393/15/2/009.

[197] D.M. Dimiduk, C. Woodward, R. LeSar, M.D. Uchic, Scale-Free Intermittent Flow in Crystal Plasticity, Science. 312 (2006) 1188–1190. https://doi.org/10.1126/science.1123889.

[198] F.F. Csikor, C. Motz, D. Weygand, M. Zaiser, S. Zapperi, Dislocation Avalanches, Strain Bursts, and the Problem of Plastic Forming at the Micrometer Scale, Science. 318 (2007) 251–254. https://doi.org/10.1126/science.1143719.

[199] K.S. Ng, A.H.W. Ngan, Stochastic nature of plasticity of aluminum micro-pillars, Acta Materialia. 56 (2008) 1712–1720. https://doi.org/10.1016/j.actamat.2007.12.016.

[200] M. Zaiser, N. Nikitas, Slip avalanches in crystal plasticity: scaling of the avalanche cut-off, (2007) 11.

[201] M. Zaiser, J. Schwerdtfeger, A.S. Schneider, C.P. Frick, B.G. Clark, P.A. Gruber, E. Arzt, Strain bursts in plastically deforming molybdenum micro- and nanopillars, Philosophical Magazine. 88 (2008) 3861–3874. https://doi.org/10.1080/14786430802132522.

[202] M. Zaiser, P. Moretti, Fluctuation phenomena in crystal plasticity—a continuum model, J. Stat. Mech. 2005 (2005) P08004–P08004. https://doi.org/10.1088/1742-5468/2005/08/P08004.

[203] P.D. Ispánovity, L. Laurson, M. Zaiser, I. Groma, S. Zapperi, M.J. Alava, Avalanches in 2D Dislocation Systems: Plastic Yielding Is Not Depinning, Phys. Rev. Lett. 112 (2014) 235501. https://doi.org/10.1103/PhysRevLett.112.235501.

[204] J. Alcalá, J. Očenášek, J. Varillas, J. A. El-Awady, J.M. Wheeler, J. Michler, Statistics of dislocation avalanches in FCC and BCC metals: dislocation mechanisms and mean swept distances across microsample sizes and temperatures, Sci Rep. 10 (2020) 19024. https://doi.org/10.1038/s41598-020-75934-5.

[205] P.D. Ispánovity, D. Ugi, G. Péterffy, M. Knapek, S. Kalácska, D. Tüzes, Z. Dankházi, K. Máthis, F. Chmelík, I. Groma, Dislocation avalanches are like earthquakes on the micron scale, Nat Commun. 13 (2022) 1975. https://doi.org/10.1038/s41467-022-29044-7.

[206] P. Bak, C. Tang, K. Wiesenfeld, Self-organized criticality, Phys. Rev. A. 38 (1988) 364–374. https://doi.org/10.1103/PhysRevA.38.364.

[207] M.-C. Miguel, A. Vespignani, S. Zapperi, J. Weiss, J.-R. Grasso, Intermittent dislocation flow in viscoplastic deformation, Nature. 410 (2001) 667–671. https://doi.org/10.1038/35070524.

[208] M. Zaiser, Scale invariance in plastic flow of crystalline solids, Advances in Physics. 55 (2006) 185–245. https://doi.org/10.1080/00018730600583514.

[209] P. Hähner, K. Bay, M. Zaiser, Fractal Dislocation Patterning During Plastic Deformation, Phys. Rev. Lett. 81 (1998) 2470–2473. https://doi.org/10.1103/PhysRevLett.81.2470.

[210] M. Zaiser, K. Bay, P. Hähner, Fractal analysis of deformation-induced dislocation patterns, Acta Materialia. 47 (1999) 2463–2476. https://doi.org/10.1016/S1359-6454(99)00096-8.

[211] J.G. Sevillano, E. Bouchaud, L.P. Kubin, The fractal nature of gliding dislocation lines, Scripta Metallurgica et Materialia. 25 (1991) 355–360. https://doi.org/10.1016/0956-716X(91)90192-4.

[212] K.A. Dahmen, Y. Ben-Zion, J.T. Uhl, Micromechanical Model for Deformation in Solids with Universal Predictions for Stress-Strain Curves and Slip Avalanches, Phys. Rev. Lett. 102 (2009) 175501. https://doi.org/10.1103/PhysRevLett.102.175501.

[213] T. Richeton, J. Weiss, F. Louchet, Dislocation avalanches: Role of temperature, grain size and strain hardening, Acta Materialia. 53 (2005) 4463–4471. https://doi.org/10.1016/j.actamat.2005.06.007.

[214] J. Weiss, J.-R. Grasso, M.-C. Miguel, A. Vespignani, S. Zapperi, Complexity in dislocation dynamics: experiments, Materials Science and Engineering: A. 309–310 (2001) 360–364. https://doi.org/10.1016/S0921-5093(00)01633-6.

[215] T. Richeton, P. Dobron, F. Chmelik, J. Weiss, F. Louchet, On the critical character of plasticity in metallic single crystals, Materials Science and Engineering: A. 424 (2006) 190–195. https://doi.org/10.1016/j.msea.2006.03.072.

[216] M. Zaiser, F.M. Grasset, V. Koutsos, E.C. Aifantis, Self-Affine Surface Morphology of Plastically Deformed Metals, Phys. Rev. Lett. 93 (2004) 195507. https://doi.org/10.1103/PhysRevLett.93.195507.

[217] J. Weiss, M. Montagnat, Long-range spatial correlations and scaling in dislocation and slip patterns, Philosophical Magazine. 87 (2007) 1161–1174. https://doi.org/10.1080/14786430600936439.

[218] Y. Hu, L. Shu, Q. Yang, W. Guo, P.K. Liaw, K.A. Dahmen, J.-M. Zuo, Dislocation avalanche mechanism in slowly compressed high entropy alloy nanopillars, Commun Phys. 1 (2018) 1–8. https://doi.org/10.1038/s42005-018-0062-z.

[219] B. Devincre, T. Hoc, L. Kubin, Dislocation Mean Free Paths and Strain Hardening of Crystals, 320 (2008) 6.

[220] Q. Rizzardi, P.M. Derlet, R. Maaß, Microstructural signatures of dislocation avalanches in a high-entropy alloy, Phys. Rev. Materials. 5 (2021) 043604. https://doi.org/10.1103/PhysRevMaterials.5.043604.

[221] J. Weiss, F. Lahaie, J.R. Grasso, Statistical analysis of dislocation dynamics during viscoplastic deformation from acoustic emission, Journal of Geophysical Research: Solid Earth. 105 (2000) 433–442. https://doi.org/10.1029/1999JB900312.

[222] J.P. Sethna, K.A. Dahmen, C.R. Myers, Crackling noise, Nature. 410 (2001) 242–250. https://doi.org/10.1038/35065675.

[223] J. Weiss, J.-R. Grasso, Acoustic Emission in Single Crystals of Ice, J. Phys. Chem. B. 101 (1997) 6113–6117. https://doi.org/10.1021/jp963157f.

[224] J. Weiss, T. Richeton, F. Louchet, F. Chmelik, P. Dobron, D. Entemeyer, M. Lebyodkin, T. Lebedkina, C. Fressengeas, R.J. McDonald, Evidence for universal intermittent crystal plasticity from acoustic emission and high-resolution extensometry experiments, Phys. Rev. B. 76 (2007) 224110. https://doi.org/10.1103/PhysRevB.76.224110.

[225] J. Weiss, D. Marsan, Three-Dimensional Mapping of Dislocation Avalanches: Clustering and Space/Time Coupling, Science. 299 (2003) 89–92. https://doi.org/10.1126/science.1079312.

[226] R. Maaß, M. Wraith, J.T. Uhl, J.R. Greer, K.A. Dahmen, Slip statistics of dislocation avalanches under different loading modes, Phys. Rev. E. 91 (2015) 042403. https://doi.org/10.1103/PhysRevE.91.042403.

[227] H. Song, D. Dimiduk, S. Papanikolaou, Universality Class of Nanocrystal Plasticity: Localization and Self-Organization in Discrete Dislocation Dynamics, Phys. Rev. Lett. 122 (2019) 178001. https://doi.org/10.1103/PhysRevLett.122.178001.

[228] Y. Cui, G. Po, P. Srivastava, K. Jiang, V. Gupta, N. Ghoniem, The role of slow screw dislocations in controlling fast strain avalanche dynamics in body-centered cubic metals, International Journal of Plasticity. 124 (2020) 117–132. https://doi.org/10.1016/j.ijplas.2019.08.008.

[229] T. Richeton, J. Weiss, F. Louchet, Breakdown of avalanche critical behaviour in polycrystalline plasticity, Nature Mater. 4 (2005) 465–469. https://doi.org/10.1038/nmat1393.

[230] L. Borasi, E. Casamenti, R. Charvet, C. Dénéréaz, S. Pollonghini, L. Deillon, T. Yang, F. Ebrahim, A. Mortensen, Y. Bellouard, 3D metal freeform micromanufacturing, Journal of Manufacturing Processes. 68 (2021) 867–876. https://doi.org/10.1016/j.jmapro.2021.06.002.

[231] A. Mortensen, Y. Bellouard, R. Charvet, C. Dénéréaz, Small-scale metal castings, small-scale metal/transparent composite structures and process to produce same, WO2017081635A1, 2017. https://patents.google.com/patent/WO2017081635A1/pt (accessed June 25, 2020).

[232] E. Casamenti, G. Torun, L. Borasi, M. Lautenbacher, M. Bertrand, J. Faist, A. Mortensen, Y. Bellouard, Glass-in-glass infiltration for 3D micro-optical composite components, Opt. Express, OE. 30 (2022) 13603–13615. https://doi.org/10.1364/OE.451026.

[233] Y. Kondo, J. Qiu, T. Mitsuyu, K. Hirao, T. Yoko, Three-Dimensional Microdrilling of Glass by Multiphoton Process and Chemical Etching, Jpn. J. Appl. Phys. 38 (1999) L1146–L1148. https://doi.org/10.1143/JJAP.38.L1146.

[234] A. Marcinkevičius, S. Juodkazis, M. Watanabe, M. Miwa, S. Matsuo, H. Misawa, J. Nishii, Femtosecond laser-assisted three-dimensional microfabrication in silica, Opt. Lett. 26 (2001) 277. https://doi.org/10.1364/OL.26.000277.

[235] Y. Bellouard, A. Said, M. Dugan, P. Bado, Fabrication of high-aspect ratio, micro-fluidic channels and tunnels using femtosecond laser pulses and chemical etching, Opt. Express. 12 (2004) 2120. https://doi.org/10.1364/OPEX.12.002120.

[236] D. Du, X. Liu, G. Korn, J. Squier, G. Mourou, Laser-induced breakdown by impact ionization in $SiO_2$ with pulse widths from 7 ns to 150 fs, Appl. Phys. Lett. 64 (1994) 3071–3073. https://doi.org/10.1063/1.111350.

[237] E.N. Glezer, M. Milosavljevic, L. Huang, R.J. Finlay, T.-H. Her, J.P. Callan, E. Mazur, Three-dimensional optical storage inside transparent materials, Opt. Lett. 21 (1996) 2023. https://doi.org/10.1364/OL.21.002023.

[238] S. Kiyama, S. Matsuo, S. Hashimoto, Y. Morihira, Examination of Etching Agent and Etching Mechanism on Femotosecond Laser Microfabrication of Channels Inside Vitreous Silica Substrates, J. Phys. Chem. C. 113 (2009) 11560–11566. https://doi.org/10.1021/jp900915r.

[239] S. Rajesh, Y. Bellouard, Towards fast femtosecond laser micromachining of fused silica: The effect of deposited energy, Opt. Express. 18 (2010) 21490. https://doi.org/10.1364/OE.18.021490.

[240] K. Hasse, G. Huber, C. Kränkel, Selective etching of fs-laser inscribed high aspect ratio microstructures in YAG, Opt. Mater. Express. 9 (2019) 3627. https://doi.org/10.1364/OME.9.003627.

[241] A. Schaap, Y. Bellouard, Molding topologically-complex 3D polymer microstructures from femtosecond laser machined glass, Opt. Mater. Express. 3 (2013) 1428. https://doi.org/10.1364/OME.3.001428.

[242] B. Wu, A. Heidelberg, J.J. Boland, J.E. Sader, Sun, Li, Microstructure-Hardened Silver Nanowires, Nano Lett. 6 (2006) 468–472. https://doi.org/10.1021/nl052427f.

[243] J. Dolbow, M. Gosz, Effect of out-of-plane properties of a polyimide film on the stress fields in microelectronic structures, Mechanics of Materials. 23 (1996) 311–321. https://doi.org/10.1016/0167-6636(96)00021-X.

[244] P. Hicter, Y. Malmejac, Quelques aspects de la transition solide-liquide, Centre d'etudes Nucléaires de Saclay. Rapport C E A R 275 (1965).

[245] M. Rittich, The volume change during solidification, (1985).

[246] O. Kubaschewski, The change of entropy, volume and binding state of the elements on melting, Trans. Faraday Soc. 45 (1949) 931. https://doi.org/10.1039/tf9494500931.

[247] W.E. Goodrich, Volume changes during the solidification of metals and alloys of low melting-point, Transactions of the Faraday Society. 25 (1929) 531–569.

[248] OECD, Nuclear Energy Agency, Handbook on Lead-bismuth Eutectic Alloy and Lead Properties, Materials Compatibility, Thermalhydraulics and Technologies, OECD, 2015. https://doi.org/10.1787/42dcd531-en.

[249] T. Pachova, L. Weber, Development of a new alloy with zero shrinkage on solidification, École Polytechnique Fédérale de Lausanne, 2016.

[250] O. Gross, Precious metal based bulk glass-forming liquids: Development, thermodynamics, kinetics and structure, (n.d.) 160.

[251] B.J. Eggleton, B. Luther-Davies, K. Richardson, Chalcogenide photonics, Nature Photon. 5 (2011) 141–148. https://doi.org/10.1038/nphoton.2011.309.

[252] M.F. Churbanov, V.S. Shiryaev, V.V. Gerasimenko, A.A. Pushkin, I.V. Skripachev, G.E. Snopatin, V.G. Plotnichenko, Stability of the Optical and Mechanical Properties of Chalcogenide Fibers, Inorganic Materials. 38 (2002) 1063–1068. https://doi.org/10.1023/A:1020593708749.

[253] O. Mouawad, C. Strutynski, J. Picot-Clémente, F. Désévédavy, G. Gadret, J.-C. Jules, F. Smektala, Optical aging behaviour naturally induced on As_2S_3 microstructured optical fibres, Opt. Mater. Express. 4 (2014) 2190. https://doi.org/10.1364/OME.4.002190.

[254] M.A. Schmidt, N. Granzow, N. Da, M. Peng, L. Wondraczek, P.St.J. Russell, All-solid bandgap guiding in tellurite-filled silica photonic crystal fibers, Opt. Lett. 34 (2009) 1946. https://doi.org/10.1364/OL.34.001946.

[255] N. Da, L. Wondraczek, M.A. Schmidt, N. Granzow, P.St.J. Russell, High index-contrast all-solid photonic crystal fibers by pressure-assisted melt infiltration of silica matrices, Journal of Non-Crystalline Solids. 356 (2010) 1829–1836. https://doi.org/10.1016/j.jnoncrysol.2010.07.002.

[256] J. Kobelke, R. Spittel, D. Hoh, K. Schuster, A. Schwuchow, F. Jahn, F. Just, C. Segel, A. Hartung, J. Kirchhof, H. Bartelt, Preparation and characterization of microstructured silica holey fibers filled with high-index glasses, in: F. Baldini, J. Homola, R.A. Lieberman, K. Kalli (Eds.), Prague, Czech Republic, 2011: p. 80732F. https://doi.org/10.1117/12.886243.

[257] R. Spittel, J. Kobelke, D. Hoh, F. Just, K. Schuster, A. Schwuchow, F. Jahn, J. Kirchhof, M. Jäger, H. Bartelt, Arsenic chalcogenide filled photonic crystal fibers, Journal of Non-Crystalline Solids. 377 (2013) 231–235. https://doi.org/10.1016/j.jnoncrysol.2013.01.043.

[258] C.C. Huang, D.W. Hewak, J.V. Badding, Deposition and characterization of germanium sulphide glass planar waveguides, Opt. Express. 12 (2004) 2501. https://doi.org/10.1364/OPEX.12.002501.

[259] S. Serna, H. Lin, C. Alonso-Ramos, C. Lafforgue, X. Le Roux, K.A. Richardson, E. Cassan, N. Dubreuil, J. Hu, L. Vivien, Engineering third-order optical nonlinearities in hybrid chalcogenide-on-silicon platform, Opt. Lett. 44 (2019) 5009. https://doi.org/10.1364/OL.44.005009.

[260] W.C. Tan, M.E. Solmaz, J. Gardner, R. Atkins, C. Madsen, Optical characterization of a-As2S3 thin films prepared by magnetron sputtering, Journal of Applied Physics. 107 (2010) 033524. https://doi.org/10.1063/1.3295908.

[261] K.E. Youden, T. Grevatt, R.W. Eason, H.N. Rutt, R.S. Deol, G. Wylangowski, Pulsed laser deposition of Ga-La-S chalcogenide glass thin film optical waveguides, Appl. Phys. Lett. 63 (1993) 1601–1603. https://doi.org/10.1063/1.110730.

[262] X.H. Zhang, Y. Guimond, Y. Bellec, Production of complex chalcogenide glass optics by molding for thermal imaging, Journal of Non-Crystalline Solids. 326–327 (2003) 519–523. https://doi.org/10.1016/S0022-3093(03)00464-2.

[263] J.D. Owen, M.A. Davies, D. Schmidt, E.H. Urruti, On the ultra-precision diamond machining of chalcogenide glass, CIRP Annals. 64 (2015) 113–116. https://doi.org/10.1016/j.cirp.2015.04.065.

[264] S. Saini, K. Kritika, D. Devvrat, M.D. Sharma, Survey of chalcogenide glasses for engineering applications, Materials Today: Proceedings. 45 (2021) 5523–5528. https://doi.org/10.1016/j.matpr.2021.02.297.

[265] E. Baudet, Y. Ledemi, P. Larochelle, S. Morency, Y. Messaddeq, 3D-printing of arsenic sulfide chalcogenide glasses, Opt. Mater. Express. 9 (2019) 2307. https://doi.org/10.1364/OME.9.002307.

[266] J. Carcreff, F. Cheviré, E. Galdo, R. Lebullenger, A. Gautier, J.L. Adam, D.L. Coq, L. Brilland, R. Chahal, G. Renversez, J. Troles, Mid-infrared hollow core fiber drawn from a 3D printed chalcogenide glass preform, Opt. Mater. Express. 11 (2021) 198. https://doi.org/10.1364/OME.415090.

[267] J. Carcreff, F. Cheviré, R. Lebullenger, A. Gautier, R. Chahal, J.L. Adam, L. Calvez, L. Brilland, E. Galdo, D. Le Coq, G. Renversez, J. Troles, Investigation on Chalcogenide Glass Additive Manufacturing for Shaping Mid-infrared Optical Components and Microstructured Optical Fibers, Crystals. 11 (2021) 228. https://doi.org/10.3390/cryst11030228.

[268] E. Casamenti, S. Pollonghini, Y. Bellouard, Few pulses femtosecond laser exposure for high efficiency 3D glass micromachining, Opt. Express. 29 (2021) 35054. https://doi.org/10.1364/OE.435163.

[269] Y. Bellouard, M.-O. Hongler, Femtosecond-laser generation of self-organized bubble patterns in fused silica, Opt. Express. 19 (2011) 6807. https://doi.org/10.1364/OE.19.006807.

[270] Y. Bellouard, E. Barthel, A.A. Said, M. Dugan, P. Bado, Scanning thermal microscopy and Raman analysis of bulk fused silica exposed to low-energy femtosecond laser pulses, Opt. Express, OE. 16 (2008) 19520–19534. https://doi.org/10.1364/OE.16.019520.

[271] A. Reiser, L. Koch, K.A. Dunn, T. Matsuura, F. Iwata, O. Fogel, Z. Kotler, N. Zhou, K. Charipar, A. Piqué, P. Rohner, D. Poulikakos, S. Lee, S.K. Seol, I. Utke, C. Nisselroy, T. Zambelli, J.M. Wheeler, R. Spolenak, Metals by Micro-Scale Additive Manufacturing: Comparison of Microstructure and Mechanical Properties, Adv. Funct. Mater. 30 (2020) 1910491. https://doi.org/10.1002/adfm.201910491.

[272] Y. Bellouard, A. Said, M. Dugan, P. Bado, Fabrication of high-aspect ratio, micro-fluidic channels and tunnels using femtosecond laser pulses and chemical etching, Opt. Express. 12 (2004) 2120. https://doi.org/10.1364/OPEX.12.002120.

[273] Y. Cheng, K. Sugioka, K. Midorikawa, Microfluidic laser embedded in glass by three-dimensional femtosecond laser microprocessing, Opt. Lett. 29 (2004) 2007. https://doi.org/10.1364/OL.29.002007.

[274] C. Hnatovsky, R.S. Taylor, E. Simova, V.R. Bhardwaj, D.M. Rayner, P.B. Corkum, Polarization-selective etching in femtosecond laser-assisted microfluidic channel fabrication in fused silica, Opt. Lett. 30 (2005) 1867. https://doi.org/10.1364/OL.30.001867.

[275] T.N. Kim, K. Campbell, A. Groisman, D. Kleinfeld, C.B. Schaffer, Femtosecond laser-drilled capillary integrated into a microfluidic device, Appl. Phys. Lett. 86 (2005) 201106. https://doi.org/10.1063/1.1926423.

[276] Y. Bellouard, A.A. Said, P. Bado, Integrating optics and micro-mechanics in a single substrate: a step toward monolithic integration in fused silica, Opt. Express. 13 (2005) 6635. https://doi.org/10.1364/OPEX.13.006635.

[277] V. Tielen, Y. Bellouard, Three-Dimensional Glass Monolithic Micro-Flexure Fabricated by Femtosecond Laser Exposure and Chemical Etching, Micromachines. 5 (2014) 697–710. https://doi.org/10.3390/mi5030697.

[278] L. Borasi, S. Frasca, K. Nicolet-Dit-Felix, E. Charbon, A. Mortensen, Coupling silicon lithography with metal casting, Applied Materials Today. 29 (2022) 101647. https://doi.org/10.1016/j.apmt.2022.101647.

[279] M. Han, W. Lee, S.-K. Lee, S.S. Lee, 3D microfabrication with inclined/rotated UV lithography, Sensors and Actuators A: Physical. 111 (2004) 14–20. https://doi.org/10.1016/j.sna.2003.10.006.

[280] S. Ni, E.J.W. Berenschot, P.J. Westerik, M.J. de Boer, R. Wolf, H. Le-The, H.J.G.E. Gardeniers, N.R. Tas, Wafer-scale 3D shaping of high aspect ratio structures by multistep plasma etching and corner lithography, Microsystems & Nanoengineering. 6 (2020) 1–11. https://doi.org/10.1038/s41378-020-0134-6.

[281] E.W. Becker, W. Ehrfeld, P. Hagmann, A. Maner, D. Münchmeyer, Fabrication of microstructures with high aspect ratios and great structural heights by synchrotron radiation lithography, galvanoforming, and plastic moulding (LIGA process), Microelectronic Engineering. 4 (1986) 35–56. https://doi.org/10.1016/0167-9317(86)90004-3.

[282] Fundamentals of Microfabrication : The Science of Miniaturization, Second Edition, CRC Press, 2018. https://doi.org/10.1201/9781482274004.

[283] J. Parasuraman, A. Summanwar, F. Marty, P. Basset, D.E. Angelescu, T. Bourouina, Deep reactive ion etching of sub-micrometer trenches with ultra high aspect ratio, Microelectronic Engineering. 113 (2014) 35–39. https://doi.org/10.1016/j.mee.2013.06.010.

[284] R.A. Gottscho, C.W. Jurgensen, D.J. Vitkavage, Microscopic uniformity in plasma etching, Journal of Vacuum Science & Technology B: Microelectronics and Nanometer Structures Processing, Measurement, and Phenomena. 10 (1992) 2133–2147. https://doi.org/10.1116/1.586180.

[285] J. Kiihamäki, H. Kattelus, J. Karttunen, S. Franssila, Depth and profile control in plasma etched MEMS structures, Sensors and Actuators A: Physical. 82 (2000) 234–238. https://doi.org/10.1016/S0924-4247(99)00336-2.

[286] M.A. Blauw, G. Craciun, W.G. Sloof, P.J. French, E. van der Drift, Advanced time-multiplexed plasma etching of high aspect ratio silicon structures, J. Vac. Sci. Technol. B. 20 (2002) 3106. https://doi.org/10.1116/1.1518018.

[287] S. Frasca, R.C. Leghziel, I.N. Arabadzhiev, B. Pasquier, G.F.M. Tomassi, S. Carrara, E. Charbon, The Michelangelo step: removing scalloping and tapering effects in high aspect ratio through silicon vias, Scientific Reports. 11 (2021) 3997. https://doi.org/10.1038/s41598-021-83546-w.

[288] K.R. Williams, K. Gupta, M. Wasilik, Etch rates for micromachining processing-part II, J. Microelectromech. Syst. 12 (2003) 761–778. https://doi.org/10.1109/JMEMS.2003.820936.

[289] L. Borasi, S. Frasca, K. Nicolet-Dit-Felix, E. Charbon, A. Mortensen, Coupling silicon lithography with metal casting, Applied Materials Today. 29 (2022) 101647. https://doi.org/10.1016/j.apmt.2022.101647.

[290] C. Cayron, ARPGE: a computer program to automatically reconstruct the parent grains from electron backscatter diffraction data, J Appl Cryst. 40 (2007) 1183–1188. https://doi.org/10.1107/S0021889807048777.

[291] F. Mompiou, M. Legros, Plasticity Mechanisms in Sub-Micron Al Fiber Investigated by In Situ TEM, Advanced Engineering Materials. 14 (2012) 955–959. https://doi.org/10.1002/adem.201200020.

[292] S.-J. Jeon, J.-H. Lee, E.L. Thomas, Polyol synthesis of silver nanocubes via moderate control of the reaction atmosphere, Journal of Colloid and Interface Science. 435 (2014) 105–111. https://doi.org/10.1016/j.jcis.2014.08.039.

[293] R. Thevamaran, O. Lawal, S. Yazdi, S.-J. Jeon, J.-H. Lee, E.L. Thomas, Dynamic creation and evolution of gradient nanostructure in single-crystal metallic microcubes, Science. 354 (2016) 312–316. https://doi.org/10.1126/science.aag1768.

[294] W.F. Gale, T.C. Totemeier, eds., 15 - Elastic properties, damping capacity and shape memory alloys, in: Smithells Metals Reference Book (Eighth Edition), Butterworth-Heinemann, Oxford, 2004: pp. 15–1. https://doi.org/10.1016/B978-075067509-3/50018-X.

[295] W.F. Gale, T.C. Totemeier, eds., 4 - X-ray analysis of metallic materials, in: Smithells Metals Reference Book (Eighth Edition), Butterworth-Heinemann, Oxford, 2004: pp. 4–1. https://doi.org/10.1016/B978-075067509-3/50007-5.

[296] B. Pichaud, F. Minari, J. Kellerhals, Calculation of critical shapes and stresses of surface sources of dislocations, Philosophical Magazine A. 38 (1978) 593–602. https://doi.org/10.1080/01418617808239257.

[297] S.I. Rao, C. Woodward, B. Akdim, E. Antillon, T.A. Parthasarathy, J.A. El-Awady, D.M. Dimiduk, Large-scale dislocation dynamics simulations of strain hardening of Ni microcrystals under tensile loading, Acta Materialia. 164 (2019) 171–183. https://doi.org/10.1016/j.actamat.2018.10.047.

[298] C. Zhou, I.J. Beyerlein, R. LeSar, Plastic deformation mechanisms of fcc single crystals at small scales, Acta Materialia. 59 (2011) 7673–7682. https://doi.org/10.1016/j.actamat.2011.08.032.

[299] L. Kubin, Dislocations, Mesoscale Simulations and Plastic Flow, Oxford University Press, Oxford, U.k., 2013.

[300] N. Chawla, K.K. Chawla, Metal Matrix Composites, Springer, New York, NY, 2013. https://doi.org/10.1007/978-1-4614-9548-2.

[301] R. Goodall, J.-F. Despois, A. Mortensen, The plasticity size effect in replicated microcellular aluminium, Scripta Materialia. 69 (2013) 469–472. https://doi.org/10.1016/j.scriptamat.2013.05.044.

[302] J.H. Foley, R.W. Cahn, G.V. Raynor, Stacking fault densities in the copper-germanium, copper-silicon and copper-germanium silicon alloys, Acta Metallurgica. 11 (1963) 355–360. https://doi.org/10.1016/0001-6160(63)90160-3.

[303] T.V. Nordstrom, C.R. Barrett, The stacking fault energy of some copper silicon alloys, Acta Metallurgica. 17 (1969) 139–146. https://doi.org/10.1016/0001-6160(69)90134-5.

[304] R.W.K. Honeycombe, The plastic deformation of metals, Second, Edward Arnold, London, U.K., 1984.

[305] D. Kiener, P. Kaufmann, A.M. Minor, Strength, Hardening, and Failure Observed by In Situ TEM Tensile Testing, Advanced Engineering Materials. 14 (2012) 960–967. https://doi.org/10.1002/adem.201200031.

[306] J. Weertmann, J.R. Weertmann, Mechanical Properties, Mildly Temperature-Dependent, Edited by R.W. Cahn and P. Haasen, in: Physical Metallurgy, Third, Revised and Enlarged Edition, Elsevier Science Publishers, Amsterdam NL, 1983: pp. 1259–1307.

[307] A. Argon, Strengthening Mechanisms in Crystal Plasticity, Oxford University Press, Oxford, U.K., 2007.

[308] K. Lücke, S. Bühler, High Temperature plasticity of face centred cubic single crystals, The Relation Between the Structure and Mechanical Properties of Metals: Proceedings. (1963) 83–97.

[309] H. Mecking, B. Nicklas, N. Zarubova, U.F. Kocks, A "universal" temperature scale for plastic flow, Acta Metallurgica. 34 (1986) 527–535. https://doi.org/10.1016/0001-6160(86)90088-X.

[310] L. Deillon, S. Verheyden, D. Ferreira Sanchez, S. Van Petegem, H. Van Swygenhoven, A. Mortensen, Laue microdiffraction characterisation of as-cast and tensile deformed Al microwires, Philosophical Magazine. 99 (2019) 1866–1880. https://doi.org/10.1080/14786435.2019.1605220.

[311] T.E. Mitchell, P.R. Thornton, The work-hardening characteristics of Cu and α-brass single crystals between 4•2 and 500°K, The Philosophical Magazine: A Journal of Theoretical Experimental and Applied Physics. 8 (1963) 1127–1159. https://doi.org/10.1080/14786436308207340.

[312] M. Zaiser, P. Moretti, Fluctuation phenomena in crystal plasticity—a continuum model, J. Stat. Mech. 2005 (2005) P08004. https://doi.org/10.1088/1742-5468/2005/08/P08004.

# LUCIANO **BORASI**

luciano.borasi@epfl.ch
luchoborasi@gmail.com

## EDUCATION

| | |
|---|---|
| Since Oct. 2018 | **PhD candidate in Materials Science and Engineering**<br>École Polytechnique Fédérale de Lausanne (EPFL),<br>Laboratory of Mechanical Metallurgy (LMM)<br>Lausanne Switzerland |
| Sep. 2016-Aug.2018 | **Advanced Materials Science and Engineering Master Program (AMASE)**<br>Double Master Degree<br>Luleå Tekniska Universitet (LTU); Luleå,Sweden<br>Universitat Politècnica de Catalunya (UPC); Barcelona, Spain<br>*under an Erasmus Mundus Scholarship sponsorship |
| Jan. 2011- Mar. 2016 | **Materials Engineering**<br>Universidad Nacional de La Plata (UNLP); La Plata, Argentina<br>*awarded as the best graduated in Materials Engineering at UNLP in 2016 by the "*Colegio de Ingenieros*". |

## RESEARCH EXPERIENCE

**Laboratory of Mechanical Metallurgy (LMM-EPFL) / PhD Candidate /** Since Oct. 2018
Development of new pathways to the micromanufacturing of metallic components and investigation of the mechanical behavior of microcastings by in-situ micromechanical testing. Supervised by Prof. Andreas Mortensen and Prof. Yves Bellouard.

**Luleå Tekniska Universitet (LTU) / Semester Project & Master Thesis /** Sep. 2017-Aug. 2018
Investigation of the effect of different "quenching and partitioning" parameters on the mechanical properties of AHSS. Supervised by Prof. Farnoosh Forouzan and Prof. Esa Vuorinen

**Laboratory of Physical Metallurgy (LIMF-UNLP)/Scientific research assistant**/Feb. 2013-Aug. 2016
Failure analysis & microstructural/ mechanical characterization of metals and alloys for external companies. Supervised by Prof. Pablo Bilmes.
Investigation of coatings on titanium and titanium alloys for biomedical applications, supervised by Prof. Adriana Kang.
Responsible of equipment for DSC, TGA and OES analysis.
TA duties in "Behavior of Materials II", "Characterization of Materials" and "Structure and Properties of Alloys"

## PUBLICATIONS

**L. Borasi**, S. Frasca, E. Charbon, A. Mortensen, *The Effect of Size, Orientation and Temperature on the Deformation of Microcast Silver Crystals*, submitted Dec. 2022.

**L. Borasi**, S. Frasca, K. Nicolet-Dit-Felix, E. Charbon, A. Mortensen, *Coupling silicon lithography with metal casting*, Applied Materials Today. 29 (2022) 101647. https://doi.org/10.1016/j.apmt.2022.101647

E. Casamenti, G. Torun, **L. Borasi**, M. Lautenbacher, M. Bertrand, J. Faist, A. Mortensen, Y. Bellouard, *Glass-in-glass infiltration for 3D micro-optical composite components*, Opt. Express, OE. 30 (2022) 13603–13615. https://doi.org/10.1364/OE.451026

**L. Borasi**, E. Casamenti, R. Charvet, C. Dénéréaz, S. Pollonghini, L. Deillon, T. Yang, F. Ebrahim, A. Mortensen, Y. Bellouard, *3D metal freeform micromanufacturing*, Journal of Manufacturing Processes. 68 (2021) 867–876. https://doi.org/10.1016/j.jmapro.2021.06.002

F. Forouzan, **L. Borasi,** E. Vuorinen, F. Mücklich, *Process control maps to design an ultra-high strength-ductile steel, Materials Science and Technology*. 35(10) (2019) 1173-1184. https://doi.org/10.1080/02670836.2019.1615752

# LUCIANO **BORASI**

F. Forouzan, **L. Borasi**, E. Vuorinen, F. Mücklich, *Optimization of quenching temperature to minimize the micro segregation induced banding phenomena in quenching and partitioning (Q&P) steels*, Steel Research International. 90(1) (2019) 1800281. https://doi.org/10.1002/srin.201800281

## SELECTED CONFERENCES

**L. Borasi**, S. Frasca, E. Charbon, A. Mortensen, *Coupling silicon lithography with metal casting*, 19th International Conference on Strength of Materials (ICSMA); Metz (France), 2022

(Poster) **L. Borasi**, S. Frasca, E. Charbon, A. Mortensen, *The Effect of Size, Crystal Orientation and Temperature on the Deformation of Cast Microwires*, Nanomechanical Testing in Materials Research and Development VIII (ECI Conference Series); Split (Croatia), 2022. (3rd best poster award)

**Borasi, L.**; Casamenti, E.; Charvet; R. Dénéréaz, C.; Pollonghini, S.; Deillon, L.; Bellouard, Y.; Mortensen, A., *Freeform microcasting*, Euromat 2021, online live presentation, September 2021.

## ADDITIONAL INFORMATION

- Part of the project "*Materializando el futuro*" (2015), to encourage high-school students to follow Materials Engineering studies.
- Scholarship awarded by the Roberto Rocca Education Program (2014-2015).
- Student representative of Materials Engineering at UNLP (2014-2015).
- Best presentation award at the "Young Professionals Conference AUGM"; La Plata, Argentina (2015).

## LANGUAGUES

- SPANISH
- ENGLISH
- FRENCH